DENSE DEFORMATION FIELD ESTIMATION FOR ATLAS REGISTRATION USING THE ACTIVE CONTOUR FRAMEWORK

THÈSE N^{O} 3979 (2007)

PRÉSENTÉE LE 19 DÉCEMBRE 2007
À LA FACULTÉ DES SCIENCES ET TECHNIQUES DE L'INGÉNIEUR
LABORATOIRE DE TRAITEMENT DES SIGNAUX 5
PROGRAMME DOCTORAL EN INFORMATIQUE, COMMUNICATIONS ET INFORMATION

ÉCOLE POLYTECHNIQUE FÉDÉRALE DE LAUSANNE

POUR L'OBTENTION DU GRADE DE DOCTEUR ÈS SCIENCES

PAR

Valérie DUAY

ingénieure électricienne diplômée EPF
de nationalité suisse et originaire d'Orsières (VS)

acceptée sur proposition du jury:

Prof. K. Aminian, président du jury
Prof. J.-Ph. Thiran, directeur de thèse
Dr M. Bach Cuadra, rapporteur
Dr C. Barillot, rapporteur
Dr X. Bresson, rapporteur

ÉCOLE POLYTECHNIQUE
FÉDÉRALE DE LAUSANNE

Suisse
2008

A tous ceux qui ont rendu ceci possible,
en particulier à mes parents.

Contents

Remerciements

Ouf! Le parcours pour passer de maîtresse d'école primaire à Docteur ès Sciences n'a pas toujours été un long fleuve tranquille. Certaines personnes m'avaient pourtant prévenue que j'allais m'attaquer à l'Everest le jour où j'ai pris la décision d'entreprendre des études d'ingénieur à l'EPFL. Finalement l'Everest a été vaincu et j'ai même été un petit peu plus haut dans les nuages. :-) Mais tout cela n'aurait pas été possible sans les nombreux encouragements et le soutient des personnes que j'ai croisées sur ma route et que j'aimerais remercier ici.

Mes premiers remerciements vont à mon directeur de thèse, le Professeur Jean-Philippe Thiran, pour m'avoir transmis sa passion pour l'analyse automatique d'images et permis de faire mes premiers pas dans le monde de la recherche. Merci infiniment Jean-Phi pour tes judicieux conseils, tes nombreux encouragements, ton côté toujours prêt à faire tout ce qui est en ton pouvoir pour aider tes élèves, doctorants ou post-doctorants ainsi que pour ton caractère très chaleureux et joviale.

Je voudrais également remercier le Professeur Murat Kunt, directeur de l'institut de recherche du traitement du signal (ITS), pour offrir à ses chercheurs et apprentis chercheurs un environnement de travail de haute qualité. De plus l'atmosphère multiculturelle qui règne à l'ITS a été une expérience très enrichissante pour la petite Valaisanne que je suis. Je suis très heureuse d'avoir eu l'honneur de faire partie des tous derniers doctorants de votre laboratoire et je vous souhaite une très belle et heureuse retraite.

J'aimerais aussi remercier les membres de mon jury de thèse.

Tout d'abord, je remercie le Dr Meritxell Bach Cuadra pour m'avoir suivie tout au long de cette thèse et assisté à ma défense. Un grand merci Meri pour tes critiques toujours constructives qui m'ont permis à améliorer la qualité de mes publications et du manuscrit de cette thèse. Merci également pour ton amitié et pour ce côté protecteur que tu adoptes naturellement avec les étudiants ou doctorants que tu suis.

Je remercie ensuite le Dr Xavier Bresson d'avoir bien voulu accepté de faire partie de mon jury malgré la naissance imminente de sa petite fille. Merci beaucoup Xavier pour tes conseils mathématiques éclairés qui m'ont été très utiles tout au long de ma thèse et pour toutes tes judicieuses remarques concernant la rédaction de mes papiers et de ma thèse.

Je remercie finalement le Dr Christian Barillot pour s'être déplacé depuis Rennes afin d'assister à ma défense privée. Merci pour les commentaires très motivants que vous m'avez donnés ce jour là sur mon travail de recherche.

Je tiens également à remercier le Professeur Kamiar Aminian pour avoir présidé mon jury et dont le sourire communicatif a contribué à me mettre en confiance pendant cette impressionnante épreuve qu'est la défense privée.

Dans mon domaine de recherche, une place importante est consacrée à l'informatique. J'aimerais remercier les preux chevaliers, Ruth Campos, Gilles Auric, Nicolas Aspert, Vincent Nicolas, Gaël Bourgeois et Simon Chatelain pour avoir volé maintes fois à mon secours contre les terribles virus et sautes d'humeur de mes ordinateurs ainsi que pour leurs conseils.

Merci aussi à toi, Marianne Marion pour ta précieuse aide concernant le côté administratif de l'ITS et ainsi que pour les merveilleux récits de tes voyages d'aventure que tu nous fais souvent partager à la pause café.

Je remercie les membres réguliers ou occasionnels du "club tupper", Meritxell Bach Cuadra, Maria Eugenia Cabot, Elisa Drelie Gelasca, Nawal Houhou, Ruth Campos, Leila Camoun, Dragana Viceic, Patricia Besson et Marie Shaer pour toutes ces longues discussions sur des problèmes fondamentaux de la vie et surtout pour nos nombreux fous rires.

Merci également aux autres membres du labo ou de l'EPFL qui ont participé directement ou indirectement à la réussite de ma thèse, Olivier Cuisenaire, Francesco Javier Sánchez Castro, Claudio Pollo, David Marimón Sanjuán, Torsten Butz, Matteo Sorci, Yannick Maret, Olivier Steiger, Julien Meynet, Patrick Hagmann, Vlad Popovici, Pierre Vandergheynst, Sara Luti, Gloria Menegaz, Dominique Zosso, Alexandre Alahi, Xavier Gigandet, Mihai Gurban, Laura Gui, Alessandro Crespi, Valérie Bresson, Carole Cardou, Olivier Cardou, ...

Un merci tout spécial à mes deux chères amies et confidentes que j'ai rencontré pendant mes études, Sonya Florey et Cécile Levasseur et qui sont toutes les deux sur le point de terminer leur thèse. Bonne chance et bon courage à vous deux pour cette toute dernière ligne droite!

Merci aussi a Myriam et Philippe Budry pour avoir pris de mes nouvelles pendant tout le temps de la réaction de ma thèse et pour leur gentil mot d'encouragement le jour de ma défense.

L'année précédant le début de ma thèse, j'ai eu la chance de pouvoir m'initier à la recherche au laboratoire de traitement d'images médicales de l'université Vanderbilt à Nashville, USA. Je remercie le Prof. Benoit Dawant pour tout ce qu'il m'a appris et tout ce qu'il a fait pour moi. Je remercie également les personnes que j'ai connues là-bas, Ebru Cetinkaya, Pierre-François D'Haese, Zhujiang Cao, Joshi Pallavi, Rui Li, ... qui ont contribué à ce que cette année aux USA reste inoubliable.

Un grand merci à mes collègues et amis du Laboratoire de télécomunication et de télédétection, UCL Belgique en particulier le Prof. Benoit Macq, Mathieu De Craene, Daniela Travisan, Aloys du Bois D'Aische et Vincent Nicolas que j'ai eu de la chance de rencontrer à la fin de mon travail de diplôme d'ingénieur et que j'ai revu régulièrement tout au long de ma thèse lors de conférences ou de meetings Similar.

Je tiens particulièrement à remercier ma professeur de mathématiques de l'école normale du Valais Romand, Mme Hedwige Aymon, pour avoir cru en mes possibilités et encouragée lorsque je prétendais vouloir faire l'EPFL après ma formation d'institutrice.

Je remercie également ma famille pour leurs constants encouragements et soutient durant toutes ces années. En particulier, un grand merci à ma grand-maman Madeleine qui s'est occupée de moi pendant mes études d'ingénieur et qui malheureusement est partie trop tôt pour me voir achever cette thèse. Je me souviendrais toujours de ce qu'elle m'a dit au sujet de la recherche: "Tu sais Valérie, il ne suffit pas de chercher, il faut aussi trouver!". Egalement un grand merci à ma tante et marraine Marie-Hélène Roth qui m'a aidée à trouver ce petit studio dans lequel je me suis sentie si bien pendant toute la durée de ma thèse et avec qui je rentrais souvent en Valais le week-end. Finalement, je suis extrêmement reconnaissante envers mes parents pour m'avoir encouragée, soutenue dans les moments difficiles, tout fait pour que mes études puissent se passer dans les meilleures conditions possibles et pour tout leur amour.

Ma dernière pensée va à celui qui partage maintenant ma vie et qui m'a énormément soutenue pendant ma dernière année de thèse. Merci Alain pour ton "thèse, thèse" de rappel à chaque fois que j'avais tendance à l'oublier, pour tes bons petits plats réconfortants pendant la rédaction de mes chapitres, pour cette soirée passée à imprimer ma thèse la veille de sa soumission et à trier les pages des six versions que le clown que je suis avait imprimées en même temps. Merci pour tout l'amour que tu me donnes.

Abstract

A key research area in computer vision is *image segmentation.* Image segmentation aims at extracting *objects of interest* in images or video sequences. These objects contain relevant information for a given application. For example, a video surveillance application generally requires to extract moving objects (vehicles, persons or animals) from a sequence of images in order to check that their path stays conformed to the regulation rules set for the observed scene.

Image segmentation is not an easy task. In many applications, the contours of the objects of interest are difficult to delineate, even manually. The problems linked to segmentation are often due to low contrast, fuzzy contours or too similar intensities with adjacent objects. In some cases, the objects to be extracted have no real contours in the image. This kind of objects is called *virtual objects.* Virtual objects appear especially in medical applications. To draw them, medical experts usually estimate their position from surrounding objects.

The problems related to image segmentation can be greatly simplified with information known in advance on the objects to be extracted (*the prior knowledge*). A widely used method consists to extract the needed prior knowledge from *a reference image* often called *atlas.* The goal of the atlas is to describe the image to be segmented like a map would describe the components of a geographical area. An atlas can contain three types of information on each object being part of the image: an estimation of its position in the image, a description of its shape and texture, and the features of its adjacent objects. The atlas-based segmentation method is rather used when the atlas can characterize a range of images. This method is thus especially adapted to medical images due to the existing consistency between anatomical structures of same type.

There exist two types of atlas: the determinist atlas and the statistical atlas. The determinist atlas is an image which has been selected or computed, to be the most representative of an image category to be segmented. This image is called *intensity atlas.* The contours of the objects of interest (the objects to be extracted in images of the same type) have been traced manually on the intensity atlas, or by using a semi-automatic method. A label is often attributed to each one of these objects in order to differentiate them. In this way, we obtain a labeled version of the atlas called *labeled atlas.* The statistical atlas is an atlas created from a database of images in order to be the most representative of a certain type of images to be segmented. In this atlas, the position and the features of the objects of interest depend on statistical measures. In this thesis, we are focused on the use of determinist atlases for image segmentation.

The segmentation process with a determinist atlas consists to deform the objects delineated in the atlas in order to better align them with their corresponding objects in the image to be segmented. To perform this task, we have distinguished two types of approaches in the literature. The first approach consists to reduce the segmentation problem in an image registration problem. First of all, a *dense deformation field* that registers (i.e. puts in point-to-point spatial correspondence) the atlas to the image to be segmented, is explicitly computed. Then, this transformation is used to project the assigned labels onto each atlas structure on the image to be segmented. The advantage of this approach is that the deformation field computed from the registration of visible contours allows to easily estimate the position of virtual objects or objects with fuzzy contours. However, the methods currently used for the atlas registration are often only based on the intensity atlas. That means that they do not exploit the *object-based information* that can be obtained by combining the intensity atlas with its labeled version. In the second approach, the atlas contours selected by the labeled atlas are directly deformed without using a geometrical deformation. For that, this approach is based on matching contour techniques, generally called *deformable models*. In this thesis, we are interested to a particular type of deformable models, which are the *active contour segmentation models*. The advantage of the active contour method is that this segmentation technique has been designed to exploit the image information directly linked to the object to be delineated. By using object-based information, active contour models are frequently able to extract regions where the atlas-based segmentation method by registration fails. On the other hand, the result of this local segmentation method is very sensitive to the initial atlas contour position regarding to the target contours. On the other hand, this local segmentation method is very sensitive to the initial position of the atlas contours: the closer they are to the contours to be detected, the more robust the active contour-based segmentation will be. Besides, this segmentation technique needs prior shape models to be able to estimate the position of virtual objects.

The main objective of this thesis is to design an algorithm for atlas-based segmentation which combines the advantages of the dense deformation field computed by the registration algorithms, with local segmentation constraints coming from the active contour framework. This implies to design a model where the registration and segmentation by active contours are jointly performed. The atlas registration algorithm that we propose is based on a formulation allowing the integration of any segmentation or contour regularization forces derived from the theory of the active contours in a *non parametric registration process*. Our algorithm led us to introduce the concept of *hierarchical atlas registration*. Its principle is that the registration of the main image objects helps the registration of depending objects. This allows to bring progressively the atlas contours closer to their target and thus, to limit the risk to be stuck in a local minimum. Our model had been designed to be easily adaptable to various types of segmentation problems. At the end of the thesis, we present several examples of atlas registration applications in medical imaging. These applications highlight the integration of manual constraints in an atlas registration process, the modeling of a tumor growth in the atlas, the labelization of the thalamus for a statistical study on neuronal connections, the localization of the subthalamic nucleus (STN) for deep brain stimulation (DBS) and the compensation of intra-operative brain shift for neuronavigation systems.

Key Words: Atlas-based segmentation, joint registration and segmentation model, hierarchical atlas registration, active contours, level set representation.

Version Abrégée

Un important domaine de recherche en vision assistée par ordinateur est la *segmentation d'images*. Celle-ci a pour but d'extraire des *objets d'intérêt* d'une série d'images ou séquence vidéo. Ces objets contiennent de l'information significative pour une application donnée. Par exemple, une application de vidéo surveillance nécessite généralement d'extraire les objets mobiles d'une séquence d'images (véhicules, personnes ou animaux) afin de pouvoir contrôler que leur trajectoire reste bien conforme aux règles définies pour la scène observée.

La segmentation d'images est loin d'être une tâche facile. Dans beaucoup d'applications, les contours des objets d'intérêt sont difficiles à définir, même manuellement. Les problèmes liés à la segmentation d'images sont souvent dus à un faible contraste, à des contours flous ou à des intensités trop similaires aux objets avoisinants. Dans certains cas, les objets à extraire n'ont pas de contours réels dans l'image. Ce genre d'objet est appelé *objets virtuels*. Les objets virtuels apparaissent surtout dans des applications de segmentation en imagerie médicale. Afin de pourvoir les dessiner, les experts médicaux estiment généralement leur position d'après les objets environnant.

Les problèmes de segmentation peuvent être grandement simplifiés avec de l'information connue à l'avance sur les objects à extraire (*l'information à priori*). Une méthode largement utilisée consiste à extraire cette information d'une *image de référence* souvent appelée *atlas*. Le but de l'atlas est de décrire l'image à segmenter comme une carte décrirait les éléments d'une région géographique. Un atlas peut contenir trois types d'information sur chacun des objets de l'image : une estimation de sa position dans l'image, une description de sa forme et de sa texture ainsi que les caractéristiques des objets qui l'entourent. La méthode de segmentation basée sur l'atlas est surtout utilisée lorsque l'atlas peut décrire une série d'images. Cette méthode est donc particulièrement adaptée aux images médicales en raison de la consistance existante entre des structures anatomiques de même type.

Il existe deux types d'atlas: l'atlas déterministe et l'atlas statistique. L'atlas déterminise correspond à une image qui a été sélectionnée ou calculée pour être la plus représentative possible d'une catégorie d'images à segmenter. Cette image est appelée *atlas d'intensité*. Les contours des objets d'intérêt (les objets à extraire dans des images de même type) sont ensuite tracés sur cet atlas d'intensité, manuellement ou à l'aide d'une méthode semi-automatique. Un label est généralement attribué à chacun des objets délimités de manière à pouvoir les différencier. De cette manière, nous obtenons une version labellisée de l'atlas appelée *atlas labellisé*. L'atlas statistique est un atlas créé à partir d'une base de données d'images de façon à ce qu'il soit le plus representatif possible d'un certain type d'images à segmenter. Dans cet atlas, la position et les caractéristiques des objets d'intérêt dépendent de mesures statistiques. Dans cette thèse, nous nous sommes concentrés sur l'utilisation des atlas déterministes en segmentation d'images.

Le processus de segmentation basé sur un atlas déterministe consiste à déformer les objets délimités dans l'atlas de manière à les aligner au mieux avec leurs objets correspondant dans l'image à segmenter. Pour effectuer cette tâche, nous avons distingués deux types d'approche dans la

littérature.

La première approche consiste à réduire le problème de segmentation en un problème de recalage. Tout d'abord, un *champ de déformation dense* recalant (c'est-à-dire mettant en correspondance spatiale point par point) l'atlas sur l'image à segmenter, est explicitement calculé. Ensuite, cette transformation est utilisée pour projeter les labels assignés à chaque objet de l'atlas sur l'image à segmenter. Dans cette approche, le champ de déformation calculé à partir du recalage de contours visibles permet d'estimer facilement la position d'objets virtuels ou d'objets avec des contours flous. Ceci représente un avantage appréciable. Cependant, les méthodes couramment utilisées pour le recalage d'atlas sont souvent uniquement basées sur l'atlas d'intensité. Cela signifie qu'ils n'exploitent pas l'*information basée objet* qui pourrait être obtenue en combinant l'atlas d'intensité avec sa version labellisée.

Dans la deuxième approche, les contours de l'atlas d'intensité sélectionnés par l'atlas labellisé sont directement déformés sans passer par une déformation géométrique. Pour cela, cette approche est basée sur des techniques de correspondance de contours généralement appelées *modèles déformables*. Dans cette thèse, nous nous sommes intéressés à un type particulier de modèles déformables, les *modèles de segmentation par contours actifs*. L'avantage de la méthode des contours actifs réside dans le fait que cette technique de segmentation a été conçue pour exploiter l'information de l'image directement liée à l'objet à segmenter. En utilisant l'information basée sur l'objet, les modèles de contours actifs peuvent souvent extraire des régions où la segmentation basée sur l'atlas utilisant le recalage échoue. Par contre, le résultat de cette méthode de segmentation locale est très sensible à la position initiale des contours de l'atlas par rapport à celle des contours cibles. Plus les contours initiaux sont proches des contours devant être détectés, plus la segmentation basée sur les contours actifs sera robuste. De plus, cette technique de segmentation a besoin d'a priori de forme pour pouvoir estimer la position d'objets virtuels.

L'objectif essentiel de cette thèse est la conception d'un algorithme pour la segmentation basée sur un atlas qui combinerait les avantages des champs de déformation denses des algorithmes de recalage et les contraintes locales de segmentation de la théorie des contours actifs. Ceci revient à concevoir un modèle où le recalage et la segmentation par contours actifs s'effectueraient de façon jointe. L'algorithme de segmentation d'atlas que nous proposons est basé sur une formulation permettant d'intégrer des forces de segmentation ou de lissage de contours provenant de la théorie des contours actifs dans un processus de *recalage non paramétrique*. Notre algorithme nous a conduit à introduire le concept du *recalage hiérarchique d'atlas*. Son principe est que le recalage des objets principaux de l'image aide au recalage d'objets qui en sont dépendants. Cela permet de rapprocher progressivement les contours de l'atlas de leur cible et de limiter ainsi les risques de mauvaise convergence de l'algorithme. Notre modèle de recalage d'atlas a été conçu pour être facilement adaptable à différents types de problèmes en segmentation d'image. A la fin de cette thèse nous présentons plusieurs exemples d'applications en imagerie médicale utilisant le recalage d'atlas. Les applications présentées mettent en évidence l'intégration de contraintes manuelles dans un processus de recalage d'atlas, la modélisation de la croissance d'une tumeur dans l'atlas, la labellisation de la surface du thalamus (une petite structure du cerveau) pour une étude statistique des connections neuronales, la localisation des noyaux sous-thalamique pour la stimulation cérébrale profonde et la compensation de la déformation naturelle du cerveau pendant une opération chirurgicale pour les systèmes de neuronavigation.

Mots Clés: Segmentation basée atlas, modèle joint de recalage et de segmentation, recalage hiérarchique d'atlas, contours actifs, représentation implicite de contours par la méthode des courbes de niveaux.

List of Figures

List of Tables

Part I

Introduction

Atlas-Based Segmentation

1

1.1 Introduction

The registration algorithm we propose in this thesis is dedicated to atlas-based segmentation. This chapter introduces the notion of atlas-based segmentation of images, which is a supervised segmentation method[*] that exploits prior knowledge coming from a reference image (atlas). First, we bring out the importance of spatial prior knowledge in the image segmentation task (Section 1.2). Then, we present the two existing types of digital atlas (Section 1.3). Finally, we describe the two families of atlas-based segmentation approaches (Section 1.4). The first one is based on the registration techniques that are detailed in Chapter 2. The second one is based on the active contour techniques that are presented in Chapter 3. After that, Sections 1.5 and 1.6 respectively describe the objectives and the contributions of this thesis. Finally, the organization of the dissertation can be found in Section 1.7.

1.2 Segmentation and Spatial Prior Knowledge

Digital image analysis consists in extracting meaningful information from images. This information can simply correspond to the position of the objects of interest in the image or to a set of features characterizing these objects (shape, size, texture, color, ...). The position information permits, for example, one to localize anatomical structures in medical images or to track moving objects (vehicles, people, etc.) in a video sequence. Feature information can be used to identify a person from his face or to detect anomalies in a material. To extract the information needed by a particular application, the first step generally consists of delineating the objects of interest in the image. This operation is called segmentation.

Image segmentation is often a challenging task. In most cases, it is very hard to separate the objects of interest from the image background or from other objects in the image. The segmentation problems are often due to the low contrast of the objects to segment, their weak boundaries or the

---

[*] Here supervised designs a method that it is based on prior knowledge.

similar intensities of adjacent objects. Sometimes it is even difficult to do the segmentation manually. For example in image 1.1(a), it is not straightforward to draw the boundaries separating the three young birds. In image 1.1(b), the intensities of some parts of the shark are so similar to those of the background that portions of its contour are fuzzy. The computed tomography (CT) image 1.1(c) shows a slice of the neck. This image contains three different types of object. First there are the well contrasted objects, which consequently have contours easy to delineate. In 1.1(c), these objects correspond to the external contour of the neck, the trachea (in black) and the bones (in white). Second, some objects are more difficult to distinguish because of their lower contrast. Here, these objects are the muscles and the arteria located in the gray area of the neck. Finally, there are the virtual objects that have a meaning for an application, but no real boundaries in the image. In image 1.1(c), these objects are delineated by red contours. They are used, for instance, to localize regions to irradiate or to protect during radiotherapy treatment. To draw such virtual structures, medical experts usually estimate their position from surrounding objects.


(a) (b) (c)

Figure 1.1: Image segmentation is often a challenging task. (a) The boundary between the three birds is not well defined. Note that this image comes from [1]. (b) The whole contour of this shark is partially fuzzy because some of its intensities are very similar to those of the background. (c) The contour of well contrasted structures (bone, vertebra, trachea, external contour) are easier to delineate than those of lower contrasted structures (muscles, arteria) or virtual regions (red contours).

Segmentation problems can be simplified by using prior knowledge. Atlas-based segmentation has become a standard paradigm for exploiting spatial prior knowledge in image segmentation, mainly in medical image segmentation. It relies on the existence of a reference image. The reference image is also called the atlas and the image to segment is often called the target image. The goal of the atlas is to describe the image to segment like a map would describe the components of a geographical area (Figure 1.2).

In an atlas, we can find three types of information on each object contained in the image:

1. **An estimation of its position in the image** Thanks to this information, a lot of processing time can be saved in the localization of the object. It also allows to distinguish the objects of interest from others with similar features.

2. **Its features** The features describe its texture (intensity distribution, mean, variance, entropy, ...) or its shape (mean contour, principal components (PCA), local curvature, ...). This information is used to detect the object contours in the area of interest.

3. **Its neighbours** With the atlas, we can know the position and the features of the surrounding

(a) (b)

Figure 1.2: The atlas describes the image to segment like a map would describe the components of a geographical area. (a) Satellite image of the Federal Polytechnic School of Lausanne. (b) Geographical map corresponding to the satellite image. Note that these figures are reproduced from [59].

objects. This information helps to better distinguish an object of interest from its neighborhood.

1.3 Digital Atlas

The term atlas is mainly used in geography and in biology. It refers to a collection of maps that are symbolized representations of a given space. Each map highlights the relationship between the components of the modeled space (their localization, their size, their position relative to the neighbours, etc.) according to a particular theme (for geographical maps: political, climatic, etc., for anatomical maps: anatomical, functional, etc.). Until recently, all atlases were paper-based. In Figure 1.3, we can see two examples of geographical and anatomical paper-based atlases. Panel 1.3(a) shows a world map from the first modern atlas dating from 1570 and panel 1.3(b) shows a slice of the brain atlas of Talairach and Tournoux [163]. The development of digital image processing techniques allowed the creation of digital versions of these atlases. Digital atlases have an increased potential: they provide a lot of details and may be used in a number of embedded software-based or computer-based applications (examples for geographical maps: gps, weather forecast, etc., for anatomical maps: computer assisted diagnosis, planning and guidance of surgical procedures, etc.). The main difference between geographical and anatomical atlases is that a geographical atlas can represent only one geographical region while an anatomical atlas can characterize a group of individuals. This is due to the consistence between anatomical structures of a same type. Biological images, especially medical images, are thus particularly well suited for atlas-based segmentation methods. This explains why the majority of the studies done on this technique have medical applications. We would like to emphasize here that other areas in computer vision, like video tracking, use segmentation methods very close to the atlas-based segmentation method. However, these methods are described rather as supervised segmentation methods based on a reference image.

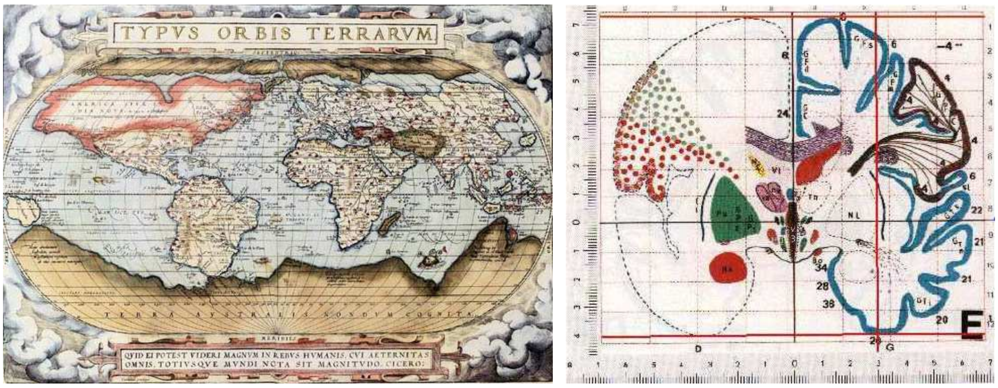

(a) (b)

Figure 1.3: Some examples of paper-based atlas. (a) World map from the first modern atlas dating from 1570. (b) A slice of the brain atlas of Talairach. Note that these figures are respectively reproduced from [173] and [59].

1.3.1 Types of Digital Atlas

There exist two types of digital atlas: the determinist and the statistical atlas. Both types of atlas are described below.

Determinist Atlas

This type of atlas corresponds to an image that has been selected among a data set to be representative of the objects to segment in other images (average size, shapes or intensity). The objects of interest are carefully delineated in this reference image, manually or with a semi-automatic method. Finally, a particular label is assigned to each of the extracted objects in order to differentiate them. This way we obtain a labeled image of the atlas. In medicine, one of the first determinist digital atlases was proposed by the Visible Human Project of the National Library of Medicine [2]. The goal of this project is the creation of complete and detailed three-dimensional anatomical representations of the normal male and female human bodies. These representations were obtained from the acquisition of transverse CT, MR and cryosection high resolution images of representative male and female cadavers. However, the frozen brain sections appear compressed and there is not much intensity contrast in the MR images since they scanned the brains after death. An example of determinist digital atlas, used in some applications presented in this thesis, is shown in Figure 1.4. This brain atlas is available on the web site of the Surgical Planning Laboratory of the Harvard medical school [101]. It was obtained from a Magnetic Resonance image (shown in Figure 1.4(a)) segmented by medical experts. Figure 1.4(b) shows its corresponding labeled image. In Figure 8.1b) we can see a 3D view of some of these labeled structures: ventricles in green, central nuclei in red and thalamus in blue.

We would like to point out here that the atlas is not always a single image selected and labeled in a pre-processing step. In some applications, the atlas/reference image changes during the segmentation process. It can correspond to the neighboring slice of a 3D image (Figure 5.22) or to the previous image in a temporal sequence (Figure 1.12). Generally, an image becomes an atlas when it has just been segmented by the algorithm. This method permits one to reduce the temporal or spatial variability between the reference image and the image to segment. Its drawback is that the prior

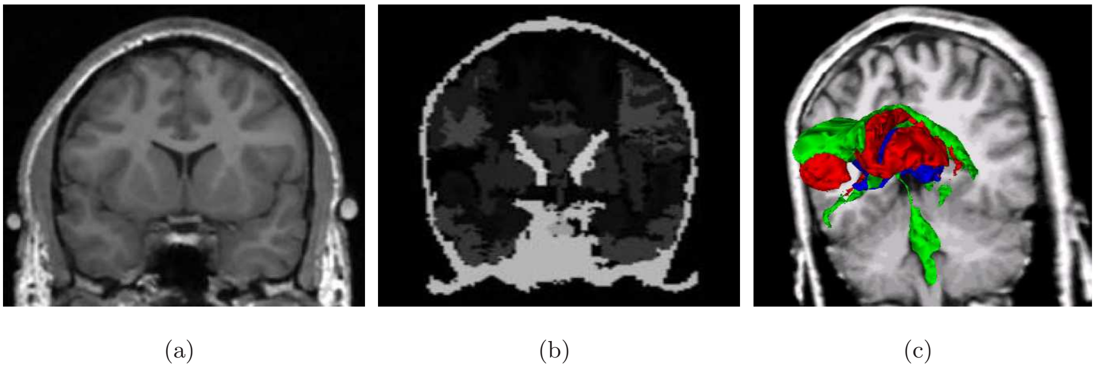
(a) (b) (c)

Figure 1.4: Digital brain atlas of the Surgical Planning Laboratory of Harvard Medical School: (a) Magnetic resonance image of the atlas. (b) Atlas with all labeled brain structures. (c) 3D view of some labeled structures: ventricles (green), central nuclei (red) and thalamus (blue). Note that these figures are reproduced from [12].

knowledge depends on the accuracy of the previous segmentation. This method is mostly used to segment a 3D image slice by slice [120] or temporal images like a video sequence [94]. For the segmentation of a 3D volume, it is often used to interpolate the segmentation between two slices segmented by the user. This permits one to speed up the manual segmentation task while preserving the accuracy of the prior knowledge [178].

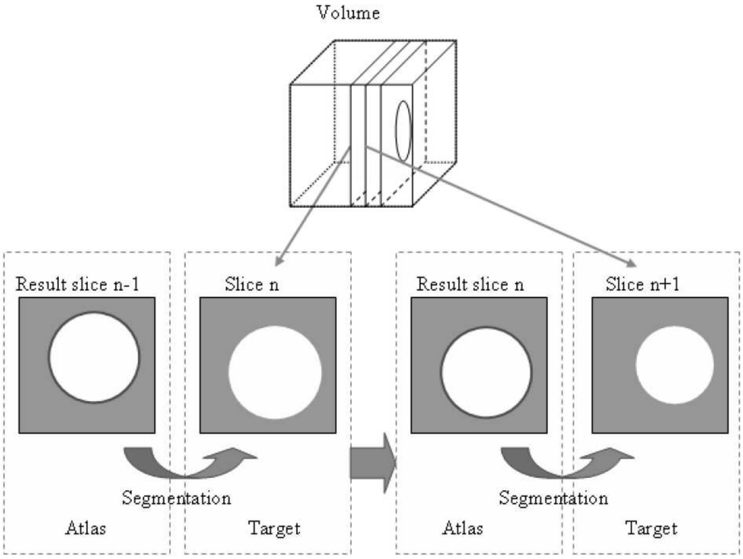

Figure 1.5: Slice by slice segmentation of a 3D volume with the atlas-based method. After the segmentation of slice n, this slice becomes the atlas. It is then used for the segmentation of the slice n+1, the new target image. Note that these figures are reproduced from [120].

Statistical Atlas

In principle, a single image is not representative of a data set. To better characterize the possible variability of the objects contained in a particular type of image, some techniques have been developed to generate an atlas from statistical measures done on a training set. The first attempt to generate this type of atlas was presented by Hohne et al. for medical applications [90]. Statistical atlases are in continuous evolution since new images can be easily incorporated in their training sets. Also, the population that a statistical atlas represents can be easily subdivided into groups according to specific criteria (age, sex, handedness, etc.). Statistical atlases can also be based on representative subgroups of some disease instead of using a healthy representative group of subjects. This is a disease-based atlas. For instance, functional and morphological atlases for Alzheimer's Disease, Parkinson's Disease, or schizophrenia are increasingly of research interest [119] [66]. Such atlases would provide the way to examine the history and evolution (due to natural disease evolution or reaction to clinical treatment) of a specific disease.

1.4 Atlas-based Segmentation Process

We describe below the two families of atlas-based segmentation approaches that we can usually find in the literature.

1.4.1 Atlas-based Segmentation seen as a Registration Problem

This technique is widely used in medical image analysis (see [118] and [116] for reviews). Figure 1.6 illustrates the atlas-based segmentation process using registration.

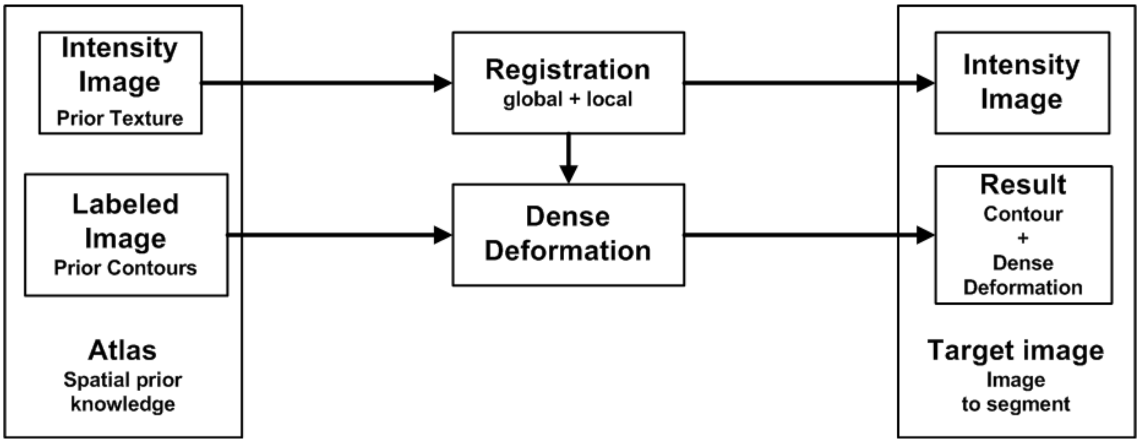

Figure 1.6: Atlas-based segmentation process using registration.

To segment a new image (the target image), a dense deformation field that registers (i.e. puts in point-to-point spatial correspondence) the atlas to the target image is first computed. This transformation is then used to project the labels assigned to structures from the atlas onto the target image to be segmented. This way, the segmentation problem is reduced to a registration problem. The registration process is usually performed in two steps. First, the atlas is globally registered to the volume of interest in order to compensate for the difference of position, orientation and possibly size between both images. In the second step, a more local registration is performed to

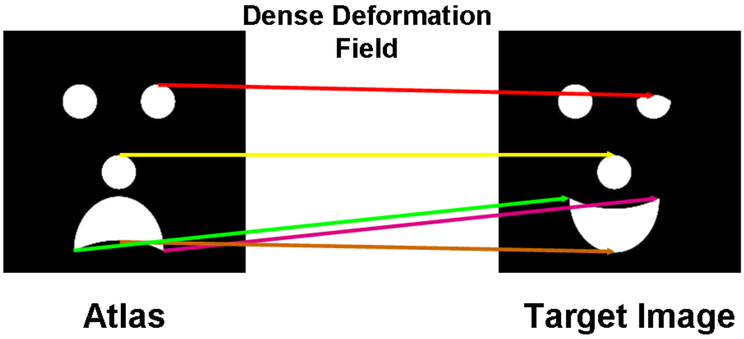

Figure 1.7: Point to point correspondence between two images.

compensate for the variability between both images. See Chapter 2 for a description of the different types of registration algorithms that can be used to perform these two steps.

The main advantage of this approach is that the dense deformation field, interpolated on the whole image from the registration of visible image features, allows to easily estimate, in the target image, the position of structures with fuzzy or not visible contours. Moreover, this approach allows to segment at the same time several contours of any types (closed, open, connected or disconnected). Figure 1.8 shows segmentation results obtained on a brain MR image with this atlas registration method.

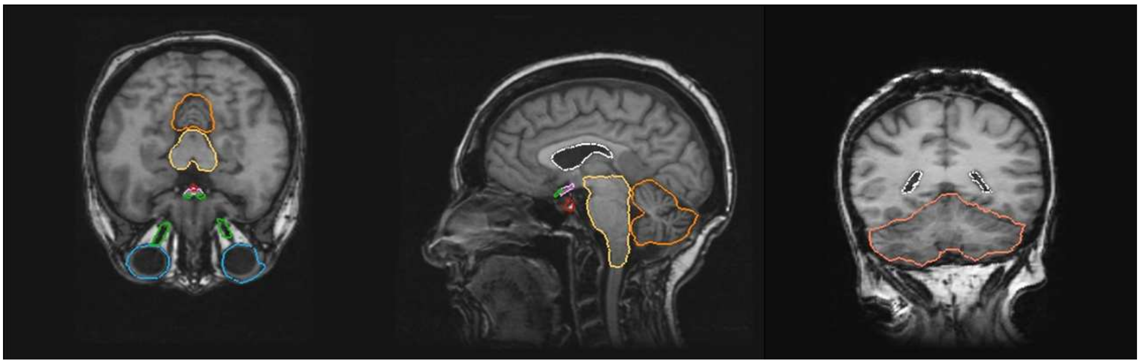

Figure 1.8: Segmentation of deep brain structures on an MR image with the atlas registration method: ventricles (white) brainstem (yellow), cerebellum (orange), chiasm (pink), pituitary (red), eyes (blue), optical nerves (green). This result comes from a study on the use of the atlas-based segmentation method for radiation therapy planning [57].

However, the majority of the approaches used so far to warp the atlas to a patient image are general registration methods. That means that they have not been specially designed to exploit the information contained in an atlas. To compute the deformation field, they generally use some global information coming from the atlas intensity image. They do not exploit the object-based information that can be obtained by combining the atlas intensity image with its labeled version. Moreover, a main limitation of these methods is that they often lead to a compromise between the accuracy of the registration and the smoothness of the deformation. When at some places the registration is not accurate enough, a widely-used solution is to globally or locally allow more variability in the registration model in order to obtain more local deformation, but with the risk of creating irregularities in the deformation field. Also, this does not assure that the desired level of precision will be obtained. To cope with this problem, local constraints should be included in the registration process.

A constraint of the atlas-based segmentation process using registration is that the images to segment are assumed to be as consistent as possible with the atlas. Possible inconsistencies between two images to be registered are of two types: intensity-based or content-based. Figure 1.9 shows some examples of intensity-based inconsistencies due to different intensity ranges (images 1.9(a) and 1.9(b)), different modalities (images 1.9(c) and 1.9(d)) or the presence of a contrast agent (image 1.9(e)). Figure 1.10 shows some examples of content inconsistencies in brain images due to normal anatomical differences between minor cortical sulcal patterns (image 1.10(b)) or to a pathology (image 1.10(b)).

(a) (b) (c) (d) (e)

Figure 1.9: Intensity inconsistencies. a),b) Eye image with different intensity ranges, c),d) MR brain images with different modalities (T1 and T2). e) Brain image with contrast product.

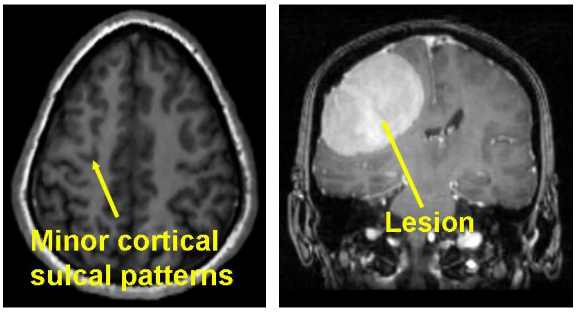

(a) (b)

Figure 1.10: Shape inconsistencies between brain images due to: a) the normal anatomical difference between minor cortical sulcal patterns, b) the presence of a pathology.

Trying to find a point to point correspondence between inconsistent images is a challenging task. In the literature several methods have been proposed to remove these inconsistencies. For example, different intensity ranges or the presence of a bias field in the luminance of the target images can be corrected in a pre-processing step by an histogram equalization [161] or a bias correction algorithm [105]. Some similarity measures as gradient-based, joint-entropy or mutual information permit the registration of images from different modalities or containing a contrast product (see Chapter 2).

For content-based inconsistencies, geometrical models have been proposed either to introduce the inconsistent object in the atlas (see [13] for a short survey on atlas registration on pathological brain images) or to force corresponding objects to match (see for instance [113] for cortical constraints in brain image registration).

1.4.2 Atlas-based Segmentation seen as a Contour Morphing Problem

The second type of atlas-based segmentation method does not explicitly compute the deformation between the atlas and the target image [8, 31, 57, 63, 120]. In this method the target image is segmented by a morphing contour technique often called *deformable models*. Some examples of deformable models are active contour models [98], active shape models [48] or active appearance models [49]. In this thesis we will focus on atlas-based segmentation using active contour models. This morphing contour technique is described in detail in Chapter 3.

Figure 1.11 illustrates the atlas-based segmentation process using active contours. First, the atlas is put in global correspondence with the image to segment. Sometimes an approximative local registration is performed to bring the atlas contour closer to the target contour. Then, the original shape of the active contour is deformed by global transformation. Finally the active contour segments the target image by combining the information given by the deformed atlas intensity image and the target image. The advantage of this technique is its computational cost, which is much lower than the previous atlas-based segmentation approach. This is due to the fact that it computes the deformation of the contours of interest only, not of the whole image. Also, as it deforms the contours, it is directly designed to use local contour-based information. However, we will see that with this method, the segmentation of several contours, open contours or not visible contours is not straightforward. The atlas-based segmentation via contour morphing is often used in the analysis of video sequence [78]. Figure 1.12 shows an example in face tracking. In this method, the first frame 3.1(a) is segmented by the user. Then, the segmentation of the next frames are successively deduced by contour matching from the segmentation of their previous frame. Atlas-based segmentation by active contour is sometimes used to improve the segmentation results obtained with the registration of an atlas [57]. Figure 1.12 shows the correction of the cerebellum contours on a brain MR image. The dotted line shows the contour obtained with atlas-based segmentation via registration. The gray line shows the contour obtained with the active contour method. We can see that the contours

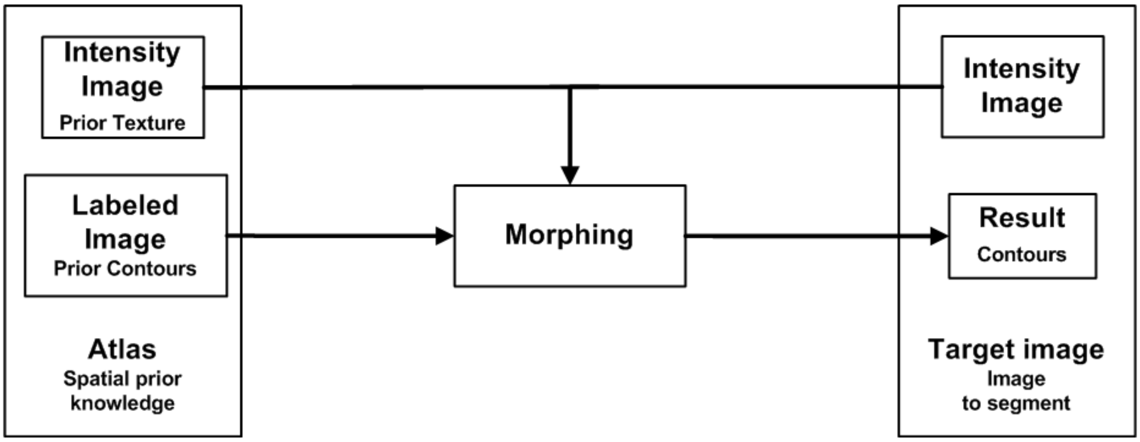

Figure 1.11: Atlas-based segmentation process using active contours.

produced by this algorithm tend to follow the sinuous contour of this brain structure. The desired cerebellum envelope (white line) is obtained by morphological operations.

Figure 1.12: Face tracking. The contour of reference of the frame 3.1(a) was initialized by the user. Then, for each frame, the contour of reference is automatically deduced from the contour of the previous frame by contour matching. Note that these Figures are reproduced from [78].

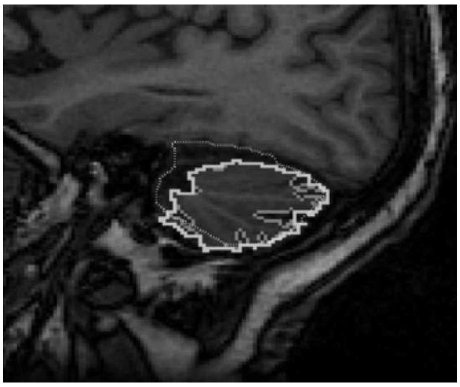

(a)

Figure 1.13: Correction of a cerebellum contour on a MR brain image. Dotted line: original contours obtained with atlas registration; gray line: contours obtained with a morphing method; white line: final cerebellum envelope obtained by morphological operations. Note that this figure is reproduced from [57].

1.5 Aims of this Thesis

In this chapter, we showed the importance of prior knowledge in segmentation tasks. The registration algorithm that we propose in this thesis uses prior knowledge coming from a reference image (the atlas). We focus on the segmentation methods using a determinist digital atlas: either a single atlas to segment a set of images of the same type or reference images to segment slice by slice an image volume or temporal images. We saw that there exist two families of atlas-based segmentation approaches. The first one reduces the segmentation problem to a registration problem. It can segment all the contours of the images simultaneously. Thanks to the deformation field interpolation, the position of fuzzy or virtual contours based on visible contours can be estimated. However, it is very sensitive to the possible inconsistencies between the atlas and the target image and does not exploit local contour-based information. The second approach considers the segmentation problem as a contour morphing problem. This technique is faster and more accurate than the segmentation method via atlas registration because it segments only the objects of interest that are consistent between both images. Moreover, it is directly designed to use object-based information. However it can delineate visible contours only. The main objective of this thesis is to combine the advantages of the point to point correspondence established by registration algorithms with the local segmentation constraints of active contour methods in an algorithm especially designed for atlas registration. This leads to design a *joint registration and segmentation model*.

1.6 Main Contributions

The main contributions of this thesis can be summarized as follows:

1. **A Joint Registration and Segmentation Model** Our atlas registration algorithm is derived from the combination of the *optical flow model* (a registration technique) and *active contour segmentation models*. It is based on a formulation allowing the integration of any contour regularization force or segmentation forces derived from the theory of the active contours, in a non parametric registration process. Moreover it allows to base the atlas registration on particular regions selected in the atlas.
2. **A Multi-Phase Active Contour Representation** Through the design of our model, we have elaborated a new type of implicit representation of active contours allowing the modeling of connected regions.
3. **A Hierarchical Atlas Registration Approach** Our algorithm led us to introduce the concept of hierarchical atlas registration. Its principle is that the registration of the most contrasted and rigid structures help to the registration of the structures that depend on them. This allows to bring progressively the atlas contour closer to their target and thus, to limit the risk to be stuck in a local minima.
4. **An Analogy to the Demons of the Thirion's Algorithm** We also show that the integration in the registration process of the region-based forces (particular forces of the active contours framework), joins the Demons concept of the non rigid registration algorithm proposed by Thirion (an algorithm widely used in atlas registration) [166].
5. **Supervised Segmentation Forces based on Information Theory** After the description of our atlas registration model, we present a study on supervised forces based on marginal and joint prior probability distribution. The idea behind this work is to integrate such supervised forces into our model in order to drive the registration of an atlas.

1.7 Organization of the Text

Figure 7.1 illustrates the organization of this dissertation. It is divided in five parts.

1. **Introduction** In the current Chapter, we have presented the motivation and the objective of this thesis.
2. **Background** Chapter 2 to 4 present the theoretical background of this thesis. Chapter 2 contains a short survey on the image registration techniques and Chapter 3 describes the active

contours segmentation framework. In Chapter 4, we can found a description of the models recently proposed to combine the advantages of the image registration with those of the segmentation by active contours.

3. **Contributions** Chapter 5 and 6 are dedicated to our contributions. First, Chapter 5 introduces the general formulation of our active contour-based registration model. Then, Chapter 6 presents two types of supervised segmentation forces derived from the active contours framework and the information theory.

4. **Applications** Chapter 7 shows the ability of our algorithm in the registration of various types of medical atlases. The atlas-based applications that we present are listed below:

    - Integration of manual constraints in the registration process.
    - Modeling of a tumor growth in the atlas.
    - Labelization of the thalamus for a statistical study on neuronal connections.
    - Localization of the subthalamic nucleus (STN) deep brain stimulation (DBS).
    - Compensation of intra-operative brain shift.
    - Illustrative examples of the hierarchical atlas registration approach.

5. **Conclusions** Finally, general conclusions and future works are presented in Chapter 8.

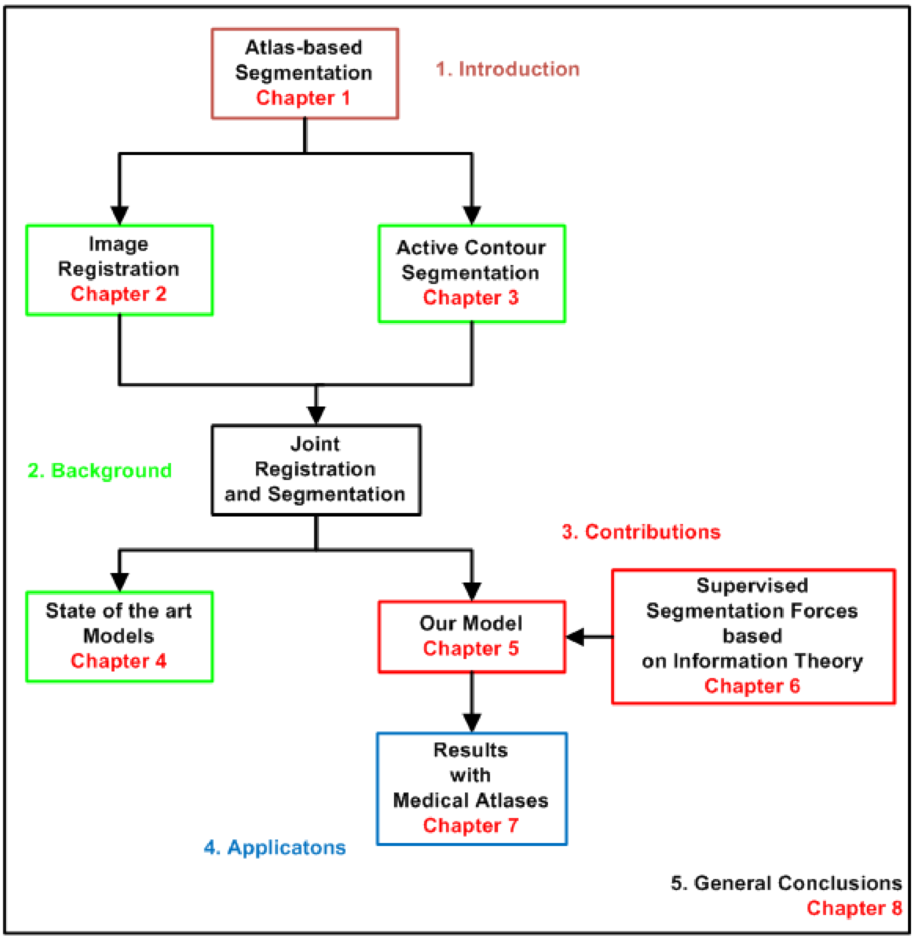

Figure 1.14: Organization of this dissertation.

Part II

Background

Image Registration

2

2.1 Introduction

We saw in Chapter 1 that atlas-based segmentation can be seen as a registration problem. This chapter presents a brief survey of the existing methods in image registration. First we describe the image registration problem in computer vision (Section 2.2). Then we present the main components of the registration framework (Section 3.3). After that we intend to classify the registration algorithms according to their feature space (Section 3.6) and their search space (Section 3.4). Simultaneously we highlight the advantages and the limitations of each approach. Then, in Sections 5.7 and 2.7, we present the regularization constraints and the multiresolution approaches. Finally these different registration techniques are discussed in Section 5.10.

2.2 Image Registration Problem in Computer Vision

Spatial registration techniques aim at establishing a point-to-point correspondence between two images. The images can have been taken at different times, from different viewpoints, and/or by different sensors. The registration concept is schematically represented in Figure 2.1. In the most general case, the point-to-point correspondence is given by a dense vectorial field also called deformation field. Once computed, this deformation field can be used to detect and quantify differences between two images, to combine their information (fusion) or to interpolate intermediate sequences. Image registration has a wide range of potential applications in image or video analysis including image or video restoration, tracking and motion analysis, automatic image segmentation based on a reference image, statistical studies, stereo and animation or augmented reality. We refer the reader to [181] for a good survey of image registration techniques and their application. Generally, the terms *registration* and *matching* are both used to refer to any process that deforms one data set to another one in order to determine a point-to-point correspondence between them. On the other hand, the term *morphing* can also refer to a process that deforms one data set to another one but it does not necessary compute explicitly the corresponding geometric deformation (definition inspired from [168]). Thus the registration problem is usually a problem more constrained than the morphing problem. In a registration problem, we track the displacement of image features (surfaces, lines, points) and the set of these displacements has to stay morphologically realistic, i.e. without singularity (pixel cross-over). In a morphing problem, we generally do not need to know the displacement of each image pixel but only the final position of the deformed image contours (or the successive positions in case of an animation).

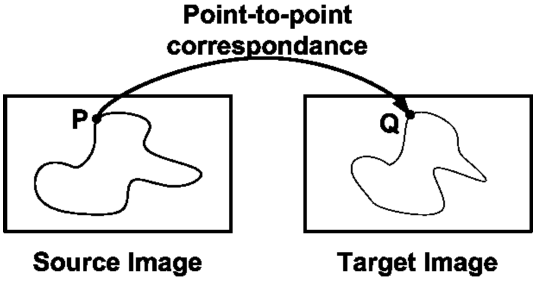

Figure 2.1: Image registration is the task of finding a point-to-point correspondence between two images.

2.3 Components of the Registration Methods

The registration problem is treated as an optimization problem. Its goal is to find the transformation (or spatial mapping) that will bring a *source image* (the moving image) into alignment with a *target image* (the fixed image). In [26], the registration methods are viewed as different combinations of choices for the four components described below. The interconnections between these four components are shown in Figure 2.2. Note that the choice of these components depends often of the application.

Feature Space The *feature space* is the class of features that can be extracted from the input images. A feature is an intermediate data containing a particular information on the image. Registering two images consists to align their corresponding *features*.

Search Space The *search space* is defined by the parameters of the type of transformation selected to align the images.

Search Strategy The *search strategy* (or optimizer) decides which is the next transformation from the search space that has to be tested in the search for the optimal transformation. An *interpolator* is used to evaluate the intensities of the source image deformed by the current transformation, at non-grid positions. The most used interpolators are the linear (respectively bi- or trilinear) for the deformation of intensity images and the nearest neighbor for the deformation of labeled or binary images.

Similarity Metric The *similarity metric* (or cost function) provides a measure of how well the target image is matched by the deformed source image. This measure is the quantitative criterion to be optimized by the *search strategy* over the *search space*.

The registration problem is solved iteratively. The process stops when the *similarity metric* satisfies the stopping criterion.

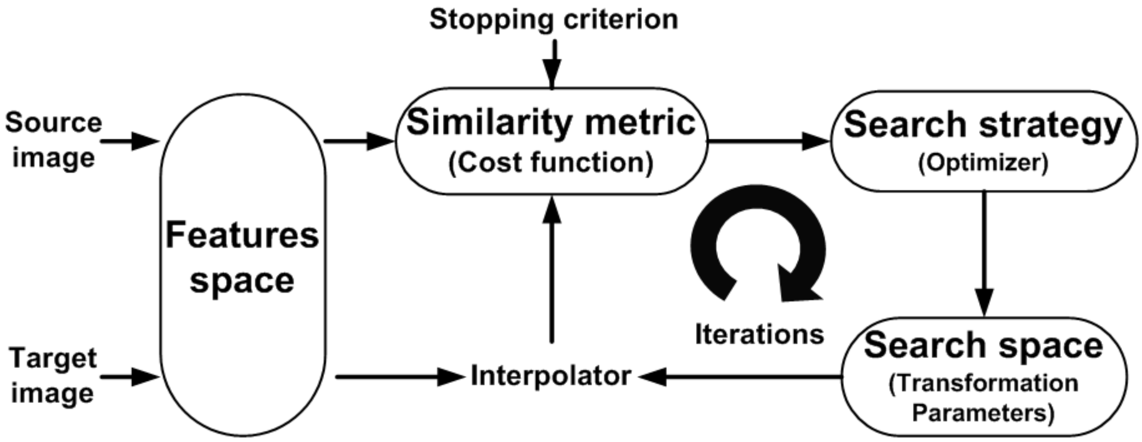

Figure 2.2: The four components of the registration framework. Note that this figure is inspired from [104].

There exists many ways to categorize the multitude of existing registration algorithms. In this section we chose to follow the classification system used by Brown et al. in [26]. They propose in particular to classify the registration algorithms by the *feature space* and the *search space* they use.

2.4 Feature space

According to the feature space employed, we can identify three classes of registration approaches: *pixel-based*, *geometrical object-based* and the *hybrid approaches*. Figure 2.3 summarizes this classification.

2.4.1 Pixel-based Approaches

Pixel-based models operate directly on the pixel intensity [14, 43, 166, 168].

The Pixel-based Approaches allow:

- to consider all the pixels of the images and thus implicitly all the geometrical objects[*] contained in the images.

Their Limitations

- They do not take into account that some objects can differ or be inconsistent between both images and thus provoke disturbances in the registration process.

2.4.2 Geometrical Object-based Approaches

The geometrical object-based approach consists first to reduce the data (only the source image or both the source and the target image) to a set of geometrical objects. These objects can be points/landmarks [19, 148], contours [15, 53, 60] or surfaces [70, 71, 106, 122, 177]. They are extracted from the image either manually or with an automatic method. Then these geometric objects are matched and the resulting deformation is propagated trough the whole image. This

---

[*] In this thesis, we consider as geometrical objects, points, lines or surfaces.

propagation is performed either by interpolation functions (basis function [19, 148] or finite-element models [70, 71, 122]) or by diffusion (PDE models [166])).

The Geometrical Object-based Approaches allow:

- to base the registration process on selected objects. These features are often chosen to be consistent between the images to match.
- to impose constraints in the registration process by forcing some source and target points to correspond.

Their Limitations

- They necessitate a previous geometrical objects extraction step.
- The quality of the registration depends not only on the geometrical objects matching but also on the quality of the segmentation of these objects.
- The computation of the transformation is only based on some objects of interest. Thus the probability of registration errors increases, the further one is from these objects. In fact, the level of accuracy is highly dependent on the number of considered objects.

2.4.3 Hybrid Approaches

The last class of registration algorithms tends to combine the advantages of both pixel-based and geometrical features-based techniques [11, 86, 89, 96]. Those algorithms use the pixel-based technique to consider implicitly all the image features in the registration and the geometrical features technique to impose local registration constraints on selected geometrical features.

The Hybrid Approaches allow:

- to introduce local constraint in the registration process.
- to get an accurate registration on the contours selected to drive the registration and far away from these contours.

Their Limitations

- They necessitate to extract the geometrical objects in a previous step. However, recent algorithms propose to perform the image segmentation (only in the source image or in both images) jointly in the registration process. Indeed segmentation and registration are closely related. The segmentation of the source and target images permits to remove the inconsistencies and thus to improve their registration. Inversely a better segmentation of these images may be obtained by combining information from the source and target image. In order to best combine this information, the images need to be perfectly aligned. So far two types of approaches have been proposed to perform this joint segmentation and registration task. The first one consists to couple active contour segmentation to registration in a variational framework [168, 177]. In the second approach, a labellisation of the source and target image is combined to the registration task by using Markov random fields [174, 175].

2.4.4 Similarity Metrics

The quality of registration is measured by a similarity metric. The similarity metric is linked to the type of feature used. We distinguish two types of metric as illustrated in Figure 2.4.

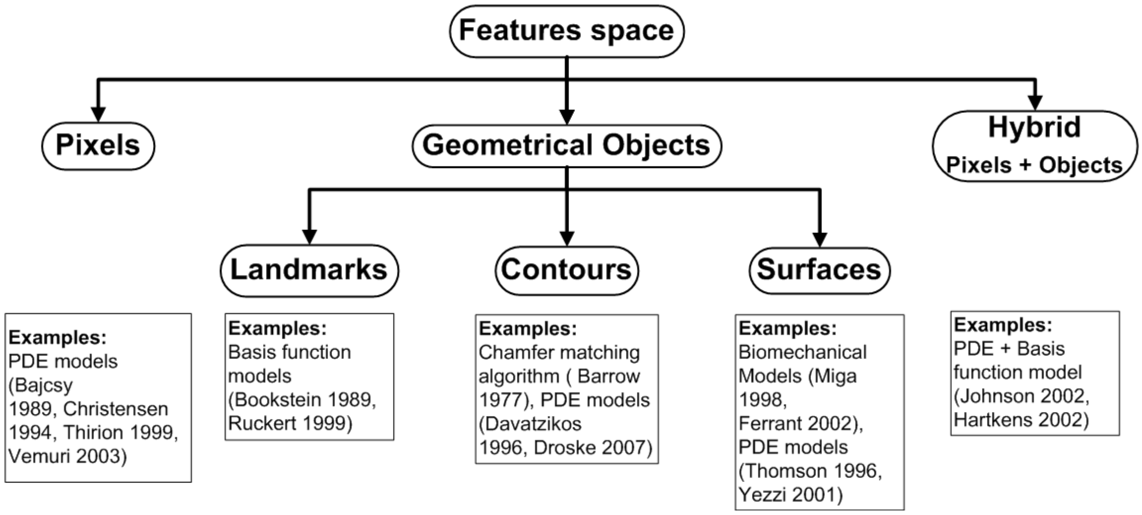

Figure 2.3: Classification of the registration algorithms according to their feature space.

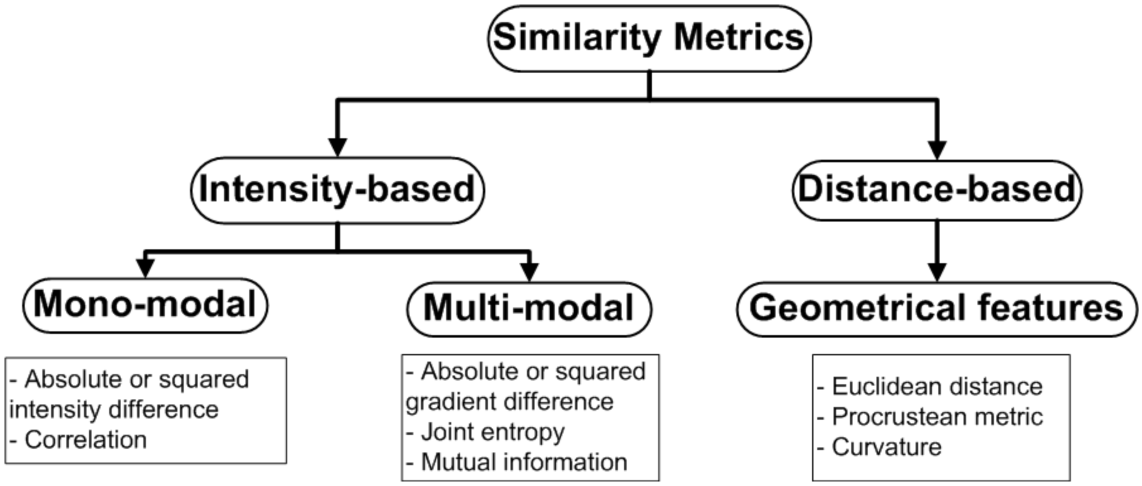

Figure 2.4: Classification of the registration algorithms according to their similarity metrics.

Intensity-based Metrics

This metric measures the intensity similarity between the source and the target images after warping. In the intensity-based algorithms, this similarity is most often expressed using their absolute (l1 norm) or squared intensity difference (l2 norm) [45]. Correlation, especially normalized cross-correlation [14] is another important cost function because of its probabilistic interpretation. However it is rather costly to evaluate and sensitive to noise. The mutual information is a powerful criterion especially to measure the global similarity between multi-modal images [115, 171]. The gradient difference [27] or the joint-entropy [47, 162] have also been proposed to register images with different intensities. We note that for some application the similarity criterion is computed locally in a window or a mask. In this case the neighborhood size must be properly chosen.

Distance-based Metrics

These metrics are used when we have geometric feature segmented in the source and target images. The cost function measures the mean distance between these corresponding features after warping. If the pairing between source and target features is not known, the iterative closest point algorithm [39] can be used to determine it. Some examples of these distance metrics are the Euclidean distance [52], the Procrustean metric [84], or the curvature [53].

2.5 Search Space

Registration algorithms can also be categorized by the *search space* they use. In this section, the registration models are classified according to their transformation representation, the number of transformation parameters and the image domain deformed by the variation of one single parameter. The search strategy used with the different transformation representation will be also mentioned. Figure 2.5 summarizes this classification.

2.5.1 Parametric Models

These registration models are based on a prior transformation model. They have a limited number of parameters to optimize. Following the number of parameters we define two categories.

Global Models The most common global parametric models are the rigid or affine transformation. For example, in 2 dimensions, the rigid model has 3 parameters to optimize (2 for the translation and 1 for the rotation). The affine model contains 7 parameters (3 for the rigid transformation, 2 for the scaling and 2 for the shearing). Because of their few number of liberty degrees, the rigid and affine models are frequently used to globally register the images, i.e. to compensate the difference of position between both images.

Non Rigid Models Beyond the global registration model, we find more sophisticated models that can compensate more local geometrical variabilities. The transformation is modeled as a linear combination of basis functions. These methods are control point-based. That means that their transformation is calculated at some points and the continuity of the transformation to the rest of the image is ensured by interpolation functions. The number of parameters is strictly dependent on the number of control points. There exists two categories of model regarding to the type of basis function used.

Semi-Local Models These models use basis functions that are defined on the whole image. The displacement of one single control point is thus propagated on the whole image. To cope with local transformation, the control points of this model has to be well distributed on the whole image in order to prevent deformation where no change is desired. Some of these basis functions as Bsplines [148] must to be placed on a regular grid and others as radial basis functions (RBF) (thin-plate splines [19], Gaussian, ...) may be placed on a non-uniform grid.

Local models The basis functions used in these models interpolate the displacement on a limited image domain. This permits the local registration of images. These basis functions are either RBF with finite support (ψ-functions of Wendland [75], Wu's function [145], ...) or shape functions ([71], [18]).

Parametric Models allow:

- to recover small and large transformations.
- to have an implicit regularization of the transformation (see Section 5.7).

Their Limitations

- They are limited to recover deformations that match the prior transformation model.
- For the local transformation, the choice of the number of control points, their positions and their ray of interpolation influence (for the RBF with finite support), is critical in the registration process.

The limited number of parameters of these methods permits to optimize their similarity metric with a wide range of optimization methods : gradient descent, Brent-Powell method [20], conjugated gradients, quasi-Newton methods [133], stochastic methods [82, 160], ...

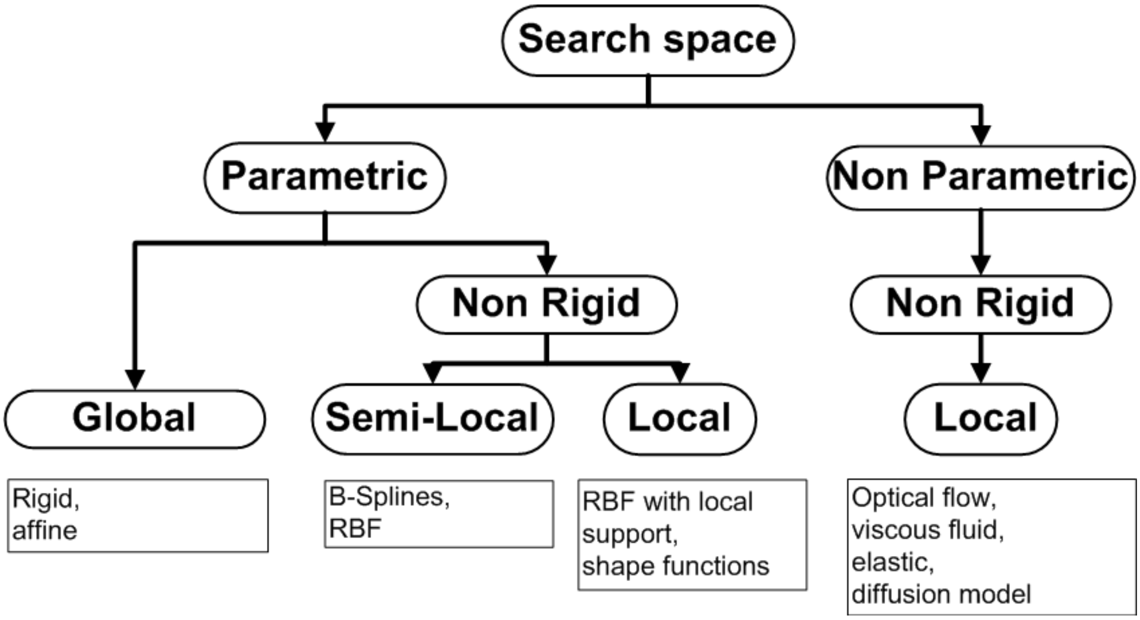

Figure 2.5: Classification of the registration algorithms according to their search space.

2.5.2 Non Parametric Models

In N dimensions, these models address the estimation of a dense deformation field, considering independently the N components displacement at each pixel. To compare them with the parametric models, the non parametric models have to optimize N parameters of each image pixel. Due to their large amount of liberty degrees, these models belong to the non rigid registration approaches. Variational methods, estimating incrementally a dense deformation field bringing the two images to the closest local minimum of the metric, are the only option for addressing such a huge dimension of the search space. The theory beyond these algorithms is related to functional analysis and Euler-Lagrange equations. Note that the active contours segmentation models that we will describe in Chapter 3 also optimize its parameters with this theory.

Non Parametric Models allow:

- to model any type of transformation because there is no a priori in the representation of their transformation.

Their Limitations

- Due to the large amount of liberty degrees, these models need an additional constraint to get a realistic deformation field, i.e. without singularity (see Section 5.7).
- Most of these approaches are limited to recover small deformations.

2.6 Regularization

In the parametric transformations with a few number of parameters, the cost function is often only defined by a similarity criteria (either intensity or distance-based). When the complexity of the transformation is high because of a large number of parameters (semi-local transformation with a large number of control points or non parametric transformation), the non rigid registration problems becomes ill-posed in the sense that the problem is not enough constraint and thus leads to a number of possible solutions (here transformations). To solve these problems numerically, one must introduce in the cost function an additional constraint concerning the regularity of the deformation field. There exist two types of regularization constraints.

2.6.1 Smoothing Constraint

The smoothing constraint imposes that the deformation field is morphologically realistic, i.e. without singularity (pixel cross-over, tearing or folding) and that the smoothness of the contours are conserved. Regularization terms are also used to express a priori knowledge on the type of transformation. The non parametric techniques mainly differ by the choice of the regularizer. The elastic [14] and fluid [44, 45] models restrict their transformations to the possible deformations of an elastic material or a fluid. In diffusion registration [166], the forces are computed only on the contour points and extended on the whole image by diffusion. The regularization is thus not based on physical properties of the object to be deformed. Diffusion registration is so far the fastest non-parametric registration technique. This makes it very attractive in particular for the registration of high-dimensional image data.

2.6.2 Bijectivity Constraint

The bijectivity constraint imposes that the direct and reverse transformation between two images are inverse of one other. The smoothing constraint is sufficient for registration applications that require only a good contour-to-contour correspondences. On the other hand when we need to estimate the position of non visible or fuzzy contours from the position of visible contours or the position of particular points on a visible contour, a good estimation of the point-to-point correspondence is important. Consequently, a bijectivity constraint has to be included in the registration process. Two types of techniques have already been proposed to compute bijective transformations. The first type is based on the analyze of the Jacobian (the determinant of the Jacobian matrix of the deformation). According the laws of continuum mechanics, if the Jacobian is positive at a particular point, this implies that the deformation is locally one-to-one and, therefore has a local inverse. Thus the method consists to control at each iteration locally the Jacobian and to enforce it to be positive (see [43] or [25]). In [42], Christensen et al. present an improvement of this method. They propose to estimate the forward and the backward transformations simultaneously and to enforce at each iteration the consistency between these two transformations with the Jacobian constraint. The main drawback of this method is that to only verify the positivity of the Jacobian at each iteration already drastically increases the computation time of the algorithm. In [165], Thirion et al. propose another type of technique, simplest but much faster to constraint the deformation to be bijective. Following the approach suggested by Burr et al. [30], they propose to compute at each iteration the forward and the backward transformations but independently. Then their compatibility is maintained by equally distributing the residual deformation onto the two deformation fields.

2.7 Multiresolution Approaches

A multiresolution scheme helps to speed up the registration process to avoid to fall in a local minima (missmatching) or to increase its ability to recover large differences between the source and the target image. It consists to solve the registration problem in a hierarchical way. First the registration problem is reduced to a simpler problem. For that, we can either reduce the feature space and/or the search space. The methods developed to reduce the features space belongs to the scale space theory [112]. The common one used in registration consists to work with a coarsest image resolution [14, 164] (Figure 2.6). The search space can be reduced by optimizing a lower number of parameters. For example, we can optimize first, only the translation parameters in an affine model or we can work with a lower number of control nodes in a non rigid parametric model. Then the solution is used as initial condition for a more complex problem, i.e. with more features to register and/or parameters to optimize. The process is repeated until the original image resolution and/or number of parameters is reached.

2.8 Conclusions

In this section, we have compared the different families of registration methods according to their feature space and their warping space. Concerning the feature space, we saw that the limitations of the pixel-based approaches can be solved by the geometrical object-based approaches and conversely. Pixel-based methods consider all the geometrical features contained in the image but in the other hand they are very sensitive to eventual inconsistencies between the images to register. The geometrical features-based approaches select consistent objects between the images to match but the accuracy of their registration decreases far away from the considered contours. In this

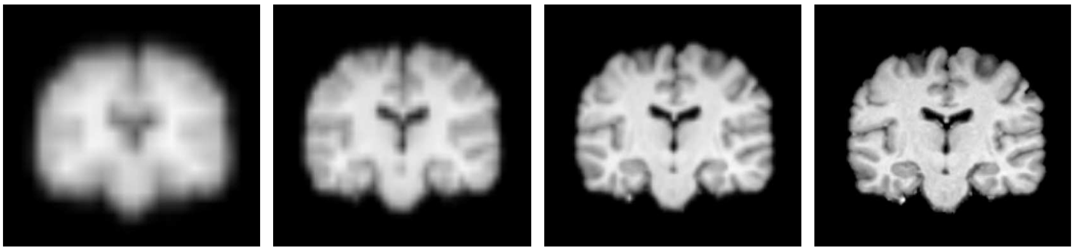

(a) (b) (c) (d)

Figure 2.6: Resolution pyramid of an MR brain image. The registration is performed by increasing progressively the image size: a) Step 1: 32x32x20, b) Step 2: 64x64x40, c) Step 3: 128x128x80, d) Step 4: 256x256x160. Note that these images are reproduced from [12].

thesis, we present a registration method that combines pixel-based with geometrical-features-based forces. This way we have the benefit of both approaches. The registration forces of our model are derived from the active contour (AC) framework [98]. With this framework we can design attractive forces that attract the moving image contours to the target image contours and regularization forces that smooth the moving image contours during their evolution. In the attractive forces we will see that we refind the forces used in common registration algorithms as the pixel-based or the distance-based forces. We find also another type of attractive forces, the object-based forces. These forces are computed from the contour or the texture of the objects selected in the moving image to drive the registration. They correspond to the typical segmentation forces of the AC models. We propose to use the object-based and regularization forces of the AC framework to constraint locally an atlas registration process. Concerning the search space, we saw that the main advantage of the parametrical approaches is the implicit regularization of their transformation. On the other hand these models are limited to their prior transformation. Moreover the setting of their parameters (number of control points, their position, the ray of influence of the interpolation) is critical in their registration process. The non parametrical method can model any types of transformation but they need additional regularization constraints. We chose to design our model following the non parametric approach. Thus, the registration results will be not dependent on the transformation parametrization. Moreover we found more realistic and more convenient to compute the attractive forces on the whole contours of the objects selected to drive the registration instead of having to represent them by control points as in [149]. In the next Chapter, we introduce the different families of AC segmentation models.

Active Contour Segmentation

3

3.1 Introduction

We saw in Chapter 1 that atlas-based segmentation can be seen as contour morphing problem. This chapter aims to present contour morphing by active contours. First, the variational methods in image segmentation are presented in Section 3.2. Then the main components of the active contour segmentation framework are described in Section 3.3. We will see that this image analysis technique although designed for segmentation has a lot of similarities with the image registration model introduced in Chapter 2. To better draw a parallel between both approaches, we intend to classify the different families of active contour segmentation models like the registration algorithms, i.e. according to their search space (Section 3.4), their search strategy (Section 3.5) and, their feature space and similarity metrics (Section 3.6). Simultaneously, we bring out the advantages and the limitations of each approach. Then the Section 5.7 is dedicated to the contour regularization technique that constitutes an important advantage of the segmentation using active contour compared to other segmentation methods. Finally, the multi-resolution approaches proposed for this segmentation model are described in Section 3.8.

3.2 Variational Methods in Image Segmentation

In image segmentation, most of the methods such the thresholding approach, the region growing or the watershed segmentation are formulate in a discrete setting, which makes them dependent to the grid of digital images. In the late 80's, a new type of image segmentation model, based on the variational approach, has been introduced. The basic idea of the variational methods is to formulate a problem of interest as an optimization problem. The problem is solved by minimizing a cost function or energy functional E. Even if the segmentation methods are developed to process digital/discrete images, the variational segmentation models are defined in a continuous formulation. This permits to better study them mathematically since continuous mathematics are more developed than their discrete version. The main advantages of the variational segmentation models compared to other segmentation models are:

1. The possibility to integrate easily in the segmentation various types of information on the object to segment (unsupervised/supervised boundary-based or region-based).
2. Their regularization techniques that permit to obtain smooth segmentation results. Contour regularization is one of the main limitation of other segmentation techniques.
3. The possibility to demonstrate mathematically that the model will converge to a unique solution in some cases.

Two well-known variational image segmentation models are the Mumford-Shah (MS) model [128, 129] and the active contour (AC) method [98].

The Mumford-Shah model was the first variational model proposed for image segmentation. Its objective is to partition an image into distinct homogeneous/piecewise-smooth regions. The MS functional is defined as follows:

$$E_{MS}(C) = \int_{\Omega} |I - I_0|^2 dx + \mu \int_{\Omega \setminus C} |\nabla I|^2 dx + \nu |C| dx, \tag{3.1}$$

where I corresponds to a piecewise smooth approximation of the image to segment I_0. μ and ν are positive parameters weighting the three terms of the functional F_{MS}. C is the edges of I and $|C|$ is the length of C. The first term of (3.1) assures that the smooth image I will stay as similar as possible to the image to segment I_0. At the beginning of the process, $I = I_0$. The second term smooths the function I inside the region delimited by the edges $\Omega \setminus C$. The last term imposes that the edges C stay smooth during the segmentation process by minimizing their length. The MS model can efficiently realize the segmentation of an image in homogenous regions but it is limited to extract a particular object of interest. Moreover an object of interest can be composed of several homogeneous regions. This limitation is solved in the active contour method. The active contour method was first introduced by Kass et al. in [98]. It aims at detecting a particular object in an image from an initial estimation of its contours. Figure 3.1 shows the segmentation results obtained on the same image by the MS model and the AC method.

In the next sections, we will start to present the AC framework in general. The particularities of the AC model proposed by Kass and of the multitude of models derived from it will be discussed more in details in Section 3.6. Especially, we will see that a well-known AC model, *the Active Contour without Edges model*, combines the original AC model of Kass with the MS approach.

3.3 Components of the Active Contour Models

We saw in the previous section that like the registration model, the active contour models treats the segmentation problem as an optimization problem. Their objective is to bring by contour morphing the *active contour* (also called moving or deformable contour) into alignment with its corresponding *target contour* in the image to segment.

Active contour segmentation methods can be viewed as the combinations of the four components described below.

Feature space The active contour models aim to delineate in the target image two or several regions that correspond to particular *features*.

Search space The *search space* is defined by the parameters of the contour representation. These parameters set the position of the active contour. The initial position can be provided either by the user or by an automatic method.

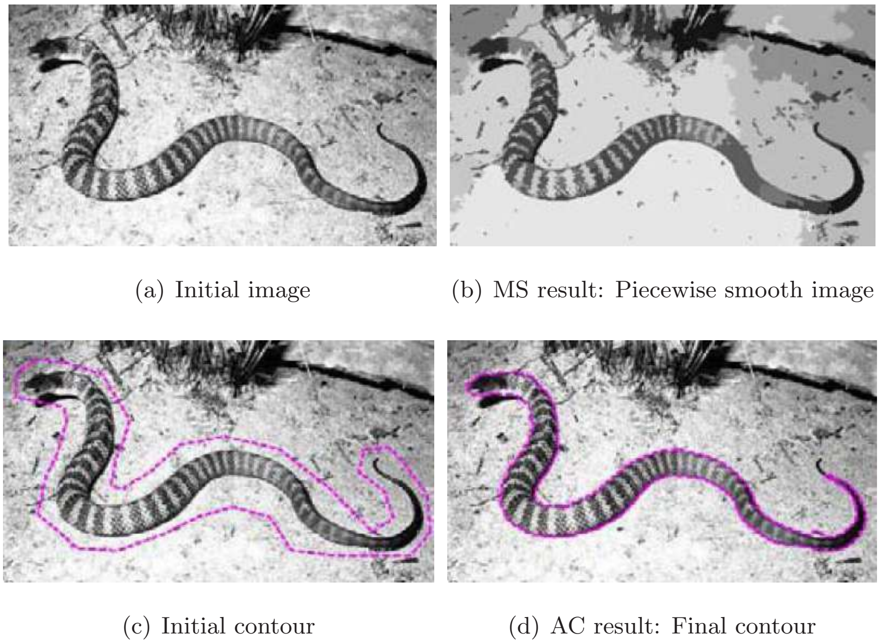

(a) Initial image (b) MS result: Piecewise smooth image

(c) Initial contour (d) AC result: Final contour

Figure 3.1: Snake image segmentation with two well-known variational image segmentation models. Row 1: Mumford-Shah (MS) model. Row 2: Active contour (AC) method. Note that these images are reproduced from [21].

Search strategy The *search strategy* (or optimizer) is the variational approach. We will see that some active contour models are built following a PDE-based approach.

Cost function The *cost function* provides a measure of how well the target image is segmented by the current position of the active contour. This measure forms the quantitative criterion to be optimized by the *search strategy* over the *search space*.

The interconnections between these four components are shown in Figure 3.2.

The segmentation problem is solved iteratively. The process stops when the *similarity metric* satisfy the stopping criterion.

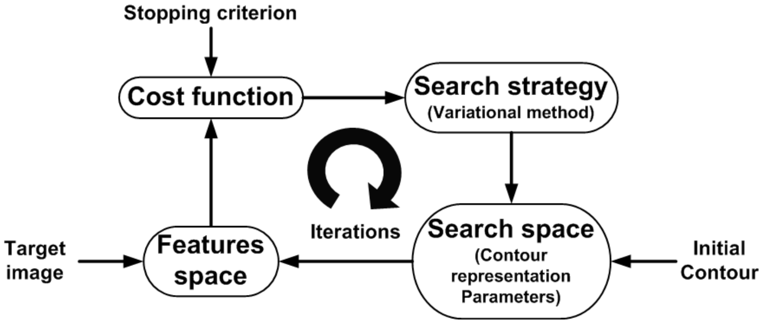

Figure 3.2: The four components of the active contour segmentation models. Note that this figure is inspired from [104].

Mathematically the segmentation problem by active contour can be formulated as follows:

$$u^* = \underset{u \in S}{min} E(u), \tag{3.2}$$

where u is the active contour representation defined in an appropriate search space S, u^* is the optimal solution of the energy functional E to minimize. The differences between the multitude of existing active contour segmentation models rely on the definition of the energy functional $F(.)$ and on the contour representation u.

In Sections 3.4 to 3.6, we classify the AC models according to their *search space*, their *search strategy*, and their *feature space* and *similarity metric*.

3.4 Search Space

In the active contour framework, three types of contour representation were defined to model the contour: *the parametric/explicit representation*, *the non-parametric/implicit representation* and *the constraint-based implicit representation.* Figure 3.3 summarizes the classification of the active contour models done from these three classes.

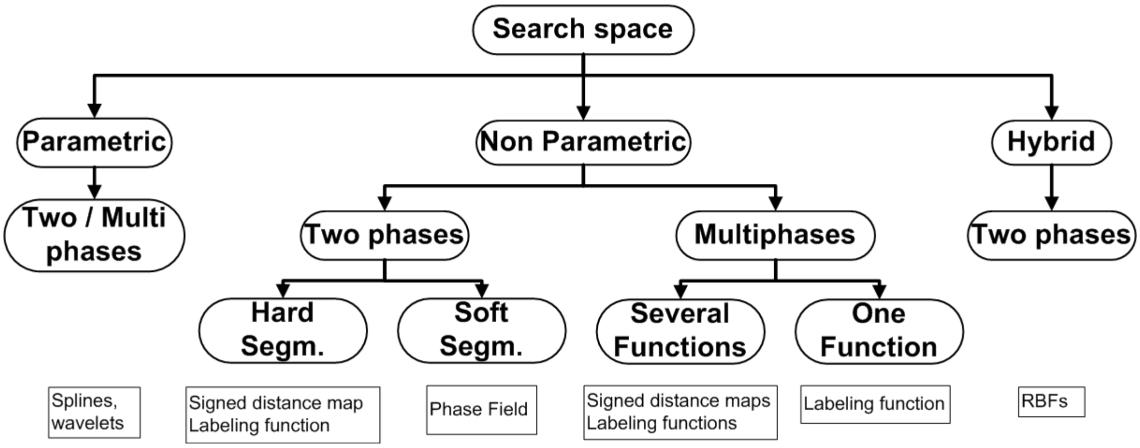

Figure 3.3: Classification of the active contour models according to their search space.

3.4.1 The Parametric/Explicit Representation

The parametric representation was the first method proposed to model the active contour [98]. The contour is represented by a linear combination of basis functions (e. g. splines, wavelets, ...) as in Equation 3.3. This technique was called *the snake method* because the deformable contour looks like a snake when it evolutes during the segmentation process.

$$C(q) = \sum_{i=0}^{K} p_i b_i(q), \tag{3.3}$$

where $C(q)$ is the curve parameterized by q, p_i are the control points, b_i the basis functions and K the number of control points/basis functions. The evolution of the snake is given by displacement vectors computed at its control points by the following evolution equation:

$$\frac{\partial C(q,t)}{\partial t} = -v(C(q,t))\mathcal{N}, \tag{3.4}$$

v is the velocity of the flow (or speed function) and $\mathcal{N}$ is the unit normal to the curve C. We will see in Section 3.5 the v can be either derived from a functional F (variational approach) or designed directly from (5.17) (PDE-based approach).

Advantages of the Parametric Representation

- This representation is compact and thus efficient in memory.
- It makes the segmentation model fast because the displacements have only to be computed at control points.
- It can model closed and open curves.
- The position of the contour can easily be modified by user interaction.
- It does not need a special scheme to partition the image in more than two regions.

Its Limitations

- The control points have to be distributed in a previous step at strategic points along the curve (generally curve points with high curvature). This can be done either manually or with an automatic method.
- The accuracy of the segmented contour is strongly depending on the initial position of the active contour, on the number of control points and on their position along the curve.
- Numerical instabilities can happen if the points on the curve get clustered during the segmentation process.
- This representation does not allow changes of topology, i.e. the final curve keeps the same topology as the initial one. Thus this model does not permit to segment disjoint objects or objects with holes.
- The speed function v depends on the parametrization of the curve C. This means that different parameterizations of the curve may give different solutions for the same initial condition.

3.4.2 The Non-Parametric/Implicit Representation

The second approach consists to represent implicitly a contour with a function of higher dimension ϕ ([135], [152], [134]). This function is called *level set function* because the inside of the shape, the outside of the shape and usually the modeled contour are put at different level. The original idea of the level set representation is to sign a given function in order to separate the image domain Ω into two disjoint regions.

The level set function ϕ is a Lipschitz continuous function that usually satisfies:

$$\begin{cases} \phi(x) = 0 & x \in C \\ \phi(x) > 0 & x \in \Omega_{in} \\ \phi(x) < 0 & x \in \Omega_{out}, \end{cases} \tag{3.5}$$

where x is an image point, Ω_{in} is the image area inside the contour and Ω_{out} is the image area outside the contour. Note that the sign makes the function derivable around its zero level (also called interface).

In order to derive the motion equation link to the level set representation, the level set values of the evolutive contour $C(t)$ are constrained to always remain zero:

$$\phi(C(t), t) = 0. \tag{3.6}$$

By deriving (3.6) with the chain rule and by combining the result with the snake evolution equation (5.17), we obtain the standard active contour evolution equation in the level set representation:

$$\underbrace{\frac{\delta\phi}{\delta C}}_{\nabla\phi}\underbrace{\frac{\partial C}{\partial t}}_{-F\mathcal{N}}+\frac{\partial\phi}{\partial t} = 0 \Rightarrow \phi_t = F|\nabla\phi|, \tag{3.7}$$

where $\phi_t := \frac{\partial\phi}{\partial t}$. Here the unit normal vector $\mathcal{N}$ is defined at each image point as follows:

$$\mathcal{N} = \frac{\nabla\phi}{|\nabla\phi|}. \tag{3.8}$$

We can see in the evolution equation (5.8), that the motion of the modeled contour depends on the gradient $\nabla\phi$. The level set function has thus not to be too steep or too flat near its interface.

During the solving process of (5.8), the zero level set evolves by moving ϕ up or down at different location with the following equation derived from the discretization of $\frac{\partial\phi(x,t)}{\partial t}$:

$$\phi(x, t + \Delta t) = \phi(x, t) + \Delta t\frac{\partial\phi(x, t)}{\partial t}. \tag{3.9}$$

where Δt is the time step.

Advantages of the Non-Parametric Representation

- Due to its non parametric nature this representation can model very accurately any type of shapes.
- This representation is more realistic than control points, since most real objects have continuous contours.
- It allows topological changes over the evolution of the curves such as breaking or merging.
- The solution of the segmentation problem does not depend on the parametrization of the curve.

Its Limitations

- This representation makes the segmentation model slower than those using the parametrical representation. Indeed, the curve displacement require to store and calculate a large number of points even by using a special scheme to speed up the process as the narrow-band method [3, 117], the fast marching methods [152], or the sparse-field methods [172].

We describe below three different types of level set functions.

a) The Signed Distance Map Function

Most often, the level set function is given by a signed distance map to the interface as follows:

$$\phi_d(x) = \begin{cases} 0 & x \in C \\ +d(x) & x \in \Omega_{in} \\ -d(x) & x \in \Omega \setminus \Omega_{in}, \end{cases} \tag{3.10}$$

where d is the Euclidean distance to the closest contour point on C.

Advantages of the Signed Distance Map Function

- It was the first implicit representation proposed. All the families of active contour models are adapted to this representation.

Its Limitations

- To keep its continuity around the zero level set, a level set function can model only closed and disconnected curves.
- The level set function loses progressively its properties of signed distance map during its evolution and this can provoke numerical instabilities. To maintain the level set function as close as possible to a distance map, the common method is to recompute it periodically from the current contour [41].

b) The Labeling Function

Some models represent the active contour by a signed labeling function ϕ_l instead of the classical signed distance map ϕ_d. This labeling function is also called binary or piecewise constant function. It takes the value 1 in one region and -1 in the other region. These labels are maintained during the evolution of the active contour by forcing ϕ_l to satisfy the condition $\phi_l^2 = 1$. In this representation, the interface does not correspond anymore to the zero level set as in the signed distance function but to the discontinuities of the labeling function.

This representation was initially proposed by Song et al. in [159] to speed up the resolution of the Chan and Vese functional [35]. The Chan and Vese model is an active contour model derived from the Mumford-Shah functional (see Section 3.6). The Song's method consists to check if the energy decreases or not when the sign of the binary function at a given point is changed. With good initial conditions, this technique permits to solve the minimization problem in one sweep. Another advantage is the gradient of the functional is not needed.

In [50], Cremers et al. use the same type of labeling function to indicate the image regions where to apply a shape prior. However in their approach, the active contour is still represented by a signed distance map function.

In [110], inspired by the method of Song et al., Lie et al. integrate the binary function in the Chan and Vese model but adapt the functional to solve it in the classic way. Through their work, the authors wanted to remove the connection established between the level set function and the signed distance function.

Advantages of the Labeling Function

- It removes the computational difficulties associated to the reinitialization of the signed distance function.
- It avoids the non-differentiability associated with the Heaviside and Deta functions used in level set formulations:

  With the signed distance function ϕ_d, the two regions in competition are identified in the energy function by using the Heaviside function $H(\phi_d)$:

$$\begin{array}{lll} H(\phi_d) = 1 & if & \phi_d \geq 0 \\ 1 - H(\phi_d) = 1 & if & \phi_d < 0. \end{array} \tag{3.11}$$

  The Delta function $\delta(\phi_d)$ is also used to select the interface in order to minimize its length:

$$|\delta\Omega| = \int_{\Omega} \delta(\phi_d)|\nabla\phi|dx. \tag{3.12}$$

The limitation of both these functions is there are not differentiable. To do so they have to be regularized (see [35] for different approximations of $H(\phi_d)$ and $\delta(\phi_d)$).

The representation of the active contour by labeling function permits to remove these functions from the functional. The two regions are thus identified by:

$$\begin{array}{lll} \frac{1}{2}(\phi_l + 1) = 1 & if & \phi_l \geq 0 \\ -\frac{1}{2}(\phi_l - 1) = 1 & if & \phi_l < 0. \end{array} \tag{3.13}$$

The interface corresponds to the image point where the gradient is not null. Its length corresponds to

$$|\delta\Omega_i| = \int_{\Omega} |\nabla\phi_l|dx. \tag{3.14}$$

Its Limitations

- As the signed distance function, it can only model closed and disconnected curves.

c) The Phase Field Representation

The phase-field representation is a mathematical model used in thermodynamic to describe the process of phase transition in a material (e.g. from a liquid to solid). The main advantage of this approach is that it permits to represent a diffuse interface between phases. In contrast, other methods assume this interface to be sharp, i.e. each point in the material is either fully solid or fully liquid. The phase-field method consists to attribute a phase value to each point in the volume of material, from 0.0 (pure liquid) to 1.0 (pure solid).

Inspired by this model, Ambrosio et al. propose in [6] to represent the edge set of a given image by a phase field $z \in [0, 1]$. $z = 1$ almost everywhere and sharply drops down to 0 in a neighborhood around the edges. In [65, 154], Esedoglu and Shen propose another type of phase field representation. Their approach consists to model the image edges as the transition of a phase field having two distinct phases. In [155], the segmentation by signed distance or labeling function is called hard segmentation because the level set function defines clear cut boundaries between the regions. The pixel classification is done through an interface. In the opposite, the segmentation by phase field is called soft segmentation. The pixel classification is done through their probabilities to belong to a particular region. Segmentation models using this representation extract all the objects of the image corresponding to the desire features. The soft segmentation is thus not as local as the hard segmentation.

Advantages of the Phase Field Representation

- It is not limited to closed curves.
- It permits to classify the image pixel without needing to move an interface as it is the case for the snake or classical level set method. This leads to faster segmentation models.

Its Limitations

- It can not extract a particular object of interest among objects having the same features.

3.4.3 The Constraint-Based Implicit Representation

Recently, a new type of representation combining the advantages of the explicit and implicit models have been proposed in [126, 127, 157]. This technique consists to model a level set function by a linear combination of radial basis functions (RBFs). To solve a segmentation problem, the active contour is deformed by moving the control points of the RBFs. This segmentation model is called *constraint-based implicit active contour.*

Advantages of the Constraint-Based Implicit Representation

- It uses a sparse, compact representation like the parametric approach. It requires thus low storage.
- As other implicit active contours, there is no finite-element representation, so it can easily adapt to non-simple or changing topologies.

Its Limitations

- The accuracy of the segmented contour is strongly depending on the number of control points and on their distribution on the image.
- So far this representation was only developed to partition the image in two regions.
- It is limited to closed curves.

3.4.4 Multiphase Segmentation Models

The basic active contour segmentation model is a 2 phase model. That means that its objective is to partition a given image into two regions (or classes), one representing the objects to detect, and the second one representing the background. The active contour is given by the boundary separating these two regions. To segment more than two regions (multi-phase), the implicit active contour model needs a special scheme. We describe below the two multiphase approaches proposed so far. The first one uses signed distance map functions and the second one labeling functions.

Signed Distance Map Function

In [179], Zhao et al. propose to solve the multi-phase segmentation problem by coupling the evolution of several level set functions. Their approach consists to use as many level set functions as region to segment. The main limitation of this method is that it necessitates additional constraints to prevent regions for overlapping and the development of a vacuum.

In [169, 170], Vese et al. propose another type of multiphase level set formulation which automatically avoids the problems of vacuum and overlap. Their approach consists to use n level sets functions to defined 2^n regions. For that they use the following vector level set function:

$$\phi(x) = (\phi_1(x), ..., \phi_n(x)), \tag{3.15}$$

and its derived vector Heaviside function:

$$H(\phi(x)) = (H(\phi_1(x)), ..., H(\phi_n(x))). \tag{3.16}$$

The phases in the image domain Ω are defined in the following way: two pixels (x_1, y_1) and (x_2, y_2) in Ω belong to the same phase if and only if $H((x_1, y_1)) = H((x_2, y_2))$. In other words, one phase contains the pixels (x,y) of Ω having the same value for $H(\phi(x))$. In 2D, according to the Four-Color Theorem [76], only two level set functions (4 regions) are needed to represent any partition. The four-color theorem (also known as the four color map theorem) states that given any plane separated into regions, such as a map of the states of a country, the regions may be colored using no more than four colors in such a way that no two adjacent regions receive the same color.

Labeling Function

a. Several Functions In [51], Cremers et al. extend their two phase technique mentioned in Section 3.4.2 to a multiphase approach. Their objective is to integrate multiple competing shape priors into level set based segmentation schemes. The originality of their approach compared to the Vese's approach is they use labeling functions instead of level set functions to define the different phases. For that they define the following vector labeling function:

$$L : x \in \Omega \rightarrow R^n, L(x) = (L_1(x), ..., L_n(x)). \tag{3.17}$$

Each component $L_j(x)$ of $L(x)$ are binary. $L_j(x)$ can take the values -1 or 1. One phase contains the pixels (x,y) of Ω having the same value $L(x)$. As with the previous model, a labeling function with n components can define 2^n phases. The labeling function $L(x)$ is simultaneously optimized with a signed distance map function representing the active contour to jointly segment and partition the image domain between the objects of interest. For that each shape model ϕ_j is associate to a particular vector label $(L_1, ..., L_n)$. Then during the optimization, the value of $L_j(x)$ are modified in order that the indicator function χ_i (Equation 3.18) tends to 1 in areas where the level set function ϕ is similar to the prior shape model ϕ_j (region segmented with a prior shape) and 0 otherwise (regions segmented without prior shape).

$$\chi_i = \frac{1}{4^n} \Pi_{j=1}^{n} (L_j + l_j)^2, \tag{3.18}$$

Note that this multiphase scheme is designed to indicate where to apply which prior knowledge and not to segment connected objects.

In [110], Lie et al. have also extended their technique described in Section 3.4.2 to multi-phase segmentation with the Chan and Vese model. As the previous methods, they use n binary function to identify 2^n phases.

b. One Function The representation of several phases with one level set function ϕ was initiated in models to simulate thin film growth of material [37, 121]. These models are used for the fabrication of high speed semiconductor electronic devices. In this application, a large number of individual material interfaces at different layers have to be identified. The idea is to let $\phi = 0$ represent the interfaces of the first layer, $\phi = 1$ represent the interfaces of the second layer and so on. By using just one level set function rather than one per layer, the tracking algorithm is kept simple and memory costs are kept low.

In [111], Lie et al. propose an adaptation of this representation to image segmentation. Their technique consists to represent each phase by a constant value i. The set of these constant values build up a piecewise constant level set function ϕ.

$$\phi = i \in \Omega_i, i = 1, 2, ..., n, \tag{3.19}$$

In this representation, the active contours are modeled by the discontinuities of ϕ.

To integrate this labeling function in the Mumford-Shah functional they express ϕ by the following linear combination of basis functions ψ_i.

$$I = \sum_{i=1}^{n} c_i \psi_i, \tag{3.20}$$

where I is the piecewise-smooth image, $\psi_i(x) = 1$ for $x \in \Omega_i$ and $\psi_i(x) = 0$ elsewhere and $c_i = mean(\psi_i = 1)$. They add the following constraint to the functional to ensure that the function ϕ will keep its label values during its evolution,

$$K(\phi) = (\phi - 1)(\phi - 1)...(\phi - n) = 0, \tag{3.21}$$

This constraint also guaranties that there is no vacuum or overlap between each phase. If $K(\phi) = 0$ each point $x \in \Omega$ can belong to one and only one phase.

This lead to the following functional :

$$minE(c, \phi, K(\phi) = 0) = \int_\Omega |I - I_0|^2 dx + \beta \Sigma_{i=1}^n \int_\Omega |\nabla \phi_i| dx, \tag{3.22}$$

The large approximation errors are penalized by the fidelity term $\int_\Omega |I - I_0|^2 dx$. The penalization term corresponds to the sum of the length of the subdomain boundaries modeled by ϕ_i. The weight $\beta > 0$ controls the effect of both these terms. However, the authors mention that it would make the algorithm simpler if this regularization was done on ϕ directly. But in this case the total variation norm of ϕ would be related not only to the length of subdomain boundaries but also to the difference between the label values. Performing the regularization on the basis function permits to just penalize the length of the curves. Note that this method permits to over-estimate the total number of phases. The superfluous phases will disappear at convergence. Their corresponding basis function will be equal to 0.

Advantages of the Multi-Phase Scheme using one Labeling Function

- We just need one level set function to represent the phases. This permits to gain in storage capacity.
- It does not need a reinitialization procedure like the signed distance map function.

Its Limitations

- This representation needs constraints to avoid overlapping or vacuum problems betweem the basis function or that the label values are modified during the level set function evolution.

3.5 Search Strategy

In the state of the art, two active contour-based approaches are used to find the optimal solution of an image segmentation problem: *the variational approach* and *the PDE-based approach*. Figure 3.4 summarizes the classification of the active contour models done from these two classes.

3.5.1 The Variational-Energy Approach

This approach consists to derive the active contour evolution equation (PDE) from a functional F to minimize.

Two Types of Functional

There exist two types of functional.

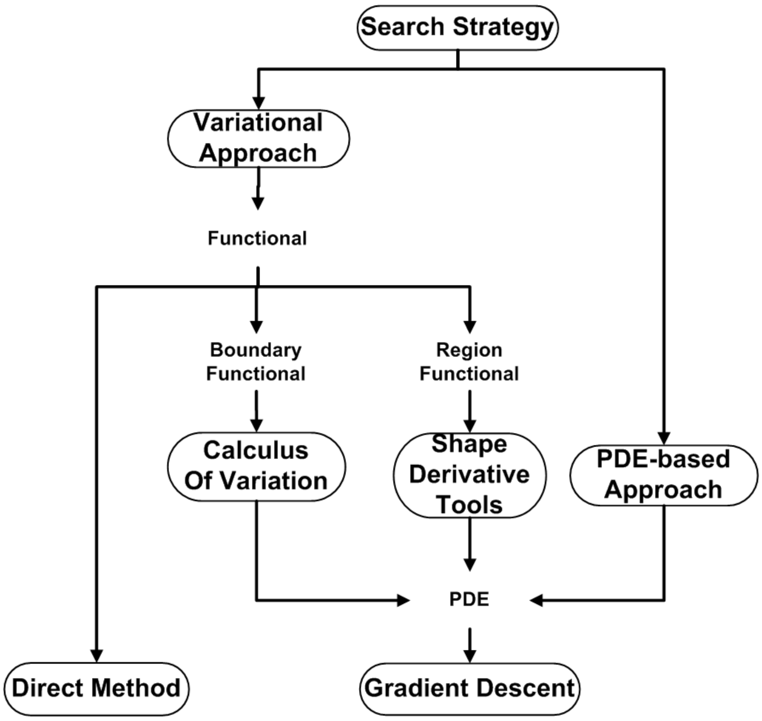

Figure 3.4: Classification of the active contour models according to their search strategy.

1. **The Boundary Functional** Boundary-based image segmentation models are linked to the following boundary (B) functional:

$$F_B(\partial\Omega) = \int_{\partial\Omega} f_B(\partial\Omega(s))ds, \tag{3.23}$$

where $\partial\Omega$ is the boundary of the region Ω. f_B is the descriptor of $\partial\Omega$. ds is the arc length/area element. The evolution equation is derived from this functional by the classical method of calculus of variations (see Section 3.5.1). Note that the boundary-based image segmentation models have been the first active contour segmentation models introduced in the literature [98].

2. **The Region Functional** Region-based image segmentation models are link to the following region (R) functional:

$$F_R(\Omega) = \int_{\Omega} f_R(x,\Omega)dx, \tag{3.24}$$

where f_R is the descriptor of Ω. The evolution equation of the boundary of regions are either derived directly from this functional by the shape gradient method proposed by Delfourd and Zolésio in [55] (see Section 3.5.1) or by passing through the Green-Riemann theorem in order to get a boundary functional.

General Functional

To partition an image in two regions, segmentation models are generally based on this general functional (F_G):

$$F_G(\partial\Omega, C) = \int_{\Omega_{in}} f_{R,in}(x,\Omega_{in})dx + \mu \int_{\Omega_{out}} f_{R,out}(x,\Omega_{out})dx + \nu \int_{\partial\Omega} f_B(\partial\Omega(s))ds, \tag{3.25}$$

where Ω_{in} and Ω_{out} are respectively the inner and the outer region of the closed active contour $C := \partial\Omega$ (see the *region competition algorithm* in Section 3.6.2), $f_{R,in}$ is the descriptor of the inside region and $f_{R,out}$ the descriptor of the outside region and f_B is the boundary descriptor. This functional is composed, as the Mumford-Shah model (Equation 3.1), of a linear combination of global measures (region-based terms) and local measures (boundary-based terms) concerning the regions to be segmented.

Links between the Boundary and Region Functional

Aubert et al. in [9, 10] and Jehan-Besson et al. in [92, 93] studied the links between the boundary and region functionals. They showed that boundary functionals are equivalent to region functionals by solving Poisson's or Helmotz's equation with well-chosen boundary conditions:

Theorem 1: Transformation of Region Functionals into Boundary Functionals Let Ω be a bounded open set with regular boundary $\partial\Omega$. Let $f_R : \bar{\Omega} \rightarrow R$ be a continuous function and u be the unique solution of Poisson's equation:

$$\begin{cases} -\Delta u & = f_R \in \Omega \\ u & = 0 \in \partial\Omega. \end{cases} \tag{3.26}$$

Then we have the following equality

$$\int_{\Omega} f_R(x, \Omega) dx = \int_{\partial\Omega} \nabla u \cdot \mathcal{N} ds, \tag{3.27}$$

where $\mathcal{N}$ is the inside pointing unit normal to $\partial\Omega$.

Theorem 2: Transformation of Boundary Functionals into Region Functionals Let Ω be a bounded open set with regular boundary $\partial\Omega$. Let $f_R : \bar{\Omega} \rightarrow R$ be a continuous function and u be the unique solution of Helmotz's equation:

$$\begin{cases} -\Delta u + u = 0 \in \Omega \\ \frac{\partial u}{\partial \mathcal{N}} = -f_B \in \partial\Omega. \end{cases} \tag{3.28}$$

Then we have the following equality

$$\int_{\partial\Omega} f_B(\partial\Omega(s)) ds = \int_{\Omega} u(x, \Omega) dx. \tag{3.29}$$

Hence, image segmentation problems can be studied either through a boundary functional by changing all region functionals into boundary functionals using Theorem 1 or through a region functional by changing all boundary functionals into region functionals using Theorem 2.

Functional derivation

Minimizing a functional involves the computation of its derivative. Two techniques have been developed. One to derive the boundary functional and another one to derive the region functional.

1. Calculus of Variations

The calculus of variation permits to find the optimal solution link to a boundary functional F_B. For that, F_B has to be continuous and differentiable. The method consists to compute the first variation of F_B to determine the *Euler-Lagrange equation*:

$$\frac{\partial F_B}{\partial u} = 0, \tag{3.30}$$

where u is the active contour representation. This equation gives a necessary condition to compute the optimizer $u*$ of F_B such that $\frac{\partial F_B}{\partial u}|_{u*} = 0$.

The fastest way to find the optimizer (usually a local optimizer) is to use the gradient descent by introducing an artificial time t such that:

$$\frac{\partial u}{\partial t} = \pm \frac{\partial F_B}{\partial u}, \tag{3.31}$$

and look for the steady state solution. The sign depends on the direction of the minimization.

2. Shape Derivative Tools

The shape derivative tools developed by Delfourd and Zolésio [55] permit to find the optimal solution link to a region functional F_R. Based on these tools, Aubert and Jehan-Besson have proposed in [10, 93] a general derivation model (Equation (6.4)) that considers the cases when the descriptor is region-independent or region-dependant. A descriptor is region-dependant when it evolutes with the deformation of the active-contours and thus of the regions. This is often the case of statistical descriptor computed on the image to segment like the mean, the variance or the histogram of a region. On the other hand, the descriptor is often region-independent when the statistical descriptor is computed on a reference image.

The Eulerian derivative in the direction $\mathbf{V}$ of the region functional F_R corresponds to:

$$< F_R, \mathbf{V} >= \int_{\Omega} \frac{\partial f_R(x, \Omega, \mathbf{V})}{\partial \tau} dx - \int_{\partial\Omega} f_R(x, \Omega))(\mathbf{V} \cdot \mathcal{N}) ds, \tag{3.32}$$

where $\frac{\partial f_R(x,\Omega,\mathbf{V})}{\partial \tau}$ is the shape derivative f'_R. It is defined by

$$f'_R = \lim_{\tau \to 0} \frac{f_R(x, \Omega(\tau)) - f_R(x, \Omega)}{\tau}. \tag{3.33}$$

The region integral considers the dependence of the criterion with the region Ω and the contour integral considers the dependence of the criterion with the contour $\partial\Omega$.

Equation (6.4) is easy to solve if it is rewrite with the Theorem 1 as the following boundary integral:

$$< F_R, \mathbf{V} >= - \int_{\partial\Omega} (A(x, \Omega) + B(x, \Omega))(\mathbf{V} \cdot \mathcal{N}) ds. \tag{3.34}$$

$A(x, \Omega)$ is the term coming from the dependance of the descriptor with the region and so from the evaluation of the shape derivative $\frac{\partial f_R(x,\Omega,\mathbf{V})}{\partial \tau}$. If $f_R(x, \Omega(\tau)) = f_R(x, \Omega)$, the descriptor f_R does not depend on the region Ω and the shape derivative $\frac{\partial f_R(x,\Omega,\mathbf{V})}{\partial \tau} = 0$. Thus, the Eulerian derivative in the direction $\mathbf{V}$ of the functional F_R corresponds simply to the boundary integral. When $A(x, \Omega)$ is region-dependant, the functional becomes more complicated to differentiate. We refer the reader to [10, 92–94] for the explicit formulation of $A(x, \Omega)$.

$B(x, \Omega)$ is a term coming from the dependance of the descriptor with the contour.

$$B(x, \Omega)) = f_R(x, \Omega). \tag{3.35}$$

According to the Cauchy-Schwartz inequality, the fastest way to decrease F_R s.t $< F_R, \mathbf{V} >= \int_{\partial\Omega} F(\mathbf{V} \cdot \mathcal{N})ds$ is obtained by choosing $\frac{\partial u}{\partial \tau} = -F\mathcal{N}$ which leads to the evolution equation:

$$\frac{\partial u}{\partial \tau} = ([A(I(x), \Omega) + B(x, \Omega)] + \lambda\kappa)\mathcal{N}, \tag{3.36}$$

where κ is the curvature of the active contour represented by u. This boundary term added to the region-based PDE in order to regularizes the evolving curve. λ weights the region and boundary terms.

Iterative Resolution

The PDE derived from the functional is then solved iteratively. At each iteration u is discretized as follows:

$$\frac{\partial u(x,t)}{\partial t} \simeq \frac{u(x,t+\Delta t) - u(x,t)}{\Delta t} \tag{3.37}$$

where Δt is the time step at which u is updated.

Equation (3.37) can be expressed as the following iteration equation:

$$u(x,t+\Delta t) = u(x,t) + \Delta t \frac{\partial u(x,t)}{\partial t}. \tag{3.38}$$

The time step Δt is an important parameter. A too low time step results in unnecessary computations. A high time step causes numerical instability. The Courant-Friedrichs-Levy (CFL) condition sets an upper bound to the time step by the requirement that u does not move more than the length of one pixel h during an iteration of the algorithm [152].

$$max_{x\in\Omega} F(x)\Delta t \leq h \tag{3.39}$$

This condition is generally used to compute automatically the optimal time step.

Advantages of the Variational Approach

- This way of determining the evolution equation guaranties that there exists a unique solution of the PDE and that the interface will converge towards this solution.

Its Limitations

- To find the optimal solution, the functional has to be continuous and differentiable.
- The CFL condition tends to slow down the algorithm. Because of this condition, the time step should be very small, thus the segmentation model needs a lot of iterations to converge.

The Direct Method

Some approaches like the one introduced in [159] propose to evolute the active contour without computing its evolution equation. This technique consists in calculating the energy directly. At each iteration, the position of the active contour is changed in order to minimize the energy.

Advantages of the Direct Method

- This method do not require to solve a PDE. This permits to avoid the numerical stability constraint (CFL) and thus to have a faster convergence.
- The functional F does not need to be differentiable.

- Such methods can converge in one sweep under suitable initial conditions.

Its Limitations

- With this heuristic approach, we can not guarantee that F has a unique solution.

3.5.2 The PDE-based Approach

The second approach is more intuitive. It consists to define directly the active contour evolution equation from Equation (5.17) or (5.8) without defining an energy to minimize (see [33] for example). Note that some segmentation models were first defined intuitively and then reformulated in a variational approach (for instance see [126, 127] for the PDE-based approach and [157] for the corresponding variational formulation).

The Advantages of the PDE-based Approach

- There is no need to compute derivatives of a functional F.

Its Limitations

- This method does not permit to guarantee that the segmentation problem has a unique solution.

3.6 Feature Space and Similarity Metrics

The active contour segmentation model consists to minimize an energy functional $E(C)$ designed to be minimal when the active contour has delineated the target objects. This energy is designed on a particular image feature characterizes by a function called *descriptor*. According to the feature space employed, we can identify two classes of models: *contour-based* and *region-based*. Each of these classes can be divided in *unsupervised* and *supervised* methods. A segmentation method is unsupervised when the descriptor is extracted from the image to segment. When the descriptor corresponds to a feature of reference (prior feature), the model is supervised. Figure 3.5 summarizes this classification.

3.6.1 Boundary-based Model

The first generation of active contour segmentation methods has been based on the detection of edges in an image. This technique consists to detect the closest contour(s) from an initial position.

Unsupervised model

There exist two non supervised contour-based models.

The Original Snake Model The first active contour segmentation model introduced by Kass et al. in [98] is a contour-based model. It is based on a parametrical representation of the curve. The evolution equation of this model is given by the minimization of the following energy functional:

$$E_{Kass}(C) = \alpha \int_0^1 |\frac{\partial C(p)}{\partial p}|^2 dp + \beta \int_0^1 |\frac{\partial^2 C(p)}{\partial p^2}|^2 dp + \lambda \int_0^1 g(|\nabla(G_\sigma * I)|))dp, \qquad (3.40)$$

where I is the image to segment. G_σ is the Gaussian function with standard deviation σ and $*$ is the convolution operator. I is often convolved with G_σ before the gradient computation,

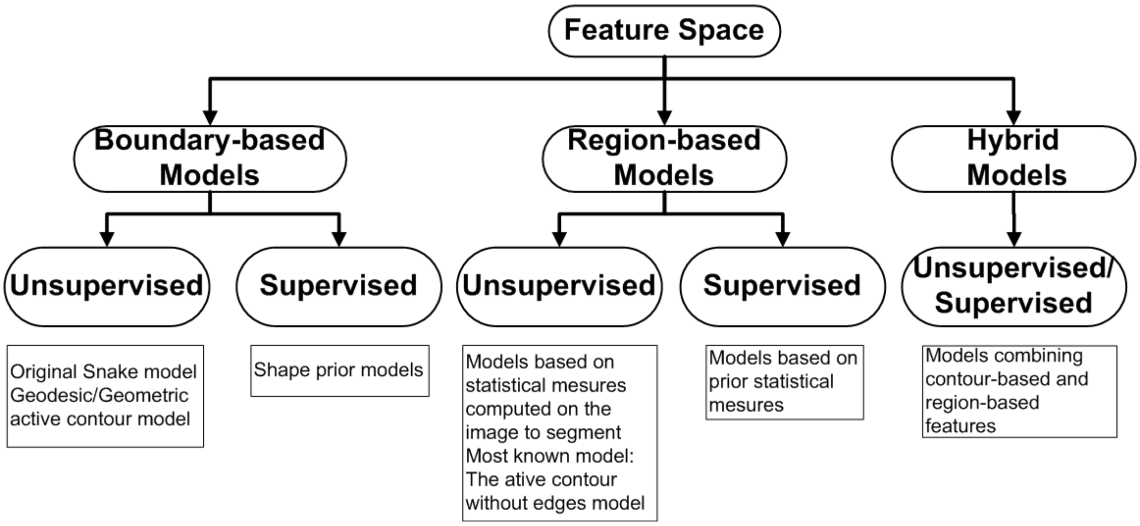

Figure 3.5: Classification of the active contour segmentation algorithms according to their feature space.

this operator being very sensitive to noise. This energy functional is composed of three terms weighted by the positive parameters α, β and λ. The first two terms are physics-based smoothness constraints based on the geometry of the curve. They correspond to the first and second derivative. The first derivative controls the tension of the curve. It gives to the snake the behavior of resisting to the stretch. The second derivative controls the rigidity. It makes the snake less flexible and thus smoother. If $\beta = 0$, the curve can have second order discontinuity and thus segment objects with sharp angles. The sum of both terms is called the internal energy. The third term, called the external energy, attracts the curve toward the boundaries of objects using an edge detecting function g defined by:

$$g(x) = \frac{1}{1+\gamma x^2}, \tag{3.41}$$

where γ is an arbitrary positive constant. Note that the value of the third term vanishes when $|G_\sigma * I|$ has a high value (contour position).

The Geodesic Active Contour Model Caselles et al. [34] and Kichenassamy et al. [104, 105] proposed a new energy, based on the Kass model, but by using the implicit curve parametrisation. This model is called geodesic or geometric active contour (GAC). The functional energy corresponding to this model is:

$$\begin{aligned} E_{GAC}(C) &= \int_0^1 g(|\nabla(G\sigma * I_T(C(p))|)|C_p|dp \qquad (3.42) \\ &= \int_0^{L(C)} g(|\nabla(G\sigma * I_T(C(s))|)ds. \end{aligned}$$

The left part is the functional corresponding to the non-parametric representation. It depends on dp, the parameter variation. The right part is the same functional corresponding to the non-parametric representation. It is depending to ds, the Euclidean element of length. $L(C)$ is the Euclidean length of the curve C defined by

$$L(C) = \int_0^1 |C(p)|dp = \int_0^{L(C)} ds. \tag{3.43}$$

Hence, the functional (3.42) is actually a new length obtained by weighting the Euclidean element of length ds by the function g, which contains information regarding the boundary of the objects lying in the image to segment I. The function g is the edge detecting function introduced in the previous section and defined e.g. by Equation (5.41). of Since this model is only based on the image gradient, one of the main limitation is that the initial contour has to be close enough to the object to segment in order to converge correctly. In [46], Cohen et al. proposed to artificially introduce a constant force in the geodesic active contour model, called a balloon force to partially alleviate the sensitivity to initial conditions. The balloon force also increases significantly the speed of convergence toward the steady state solution and allows the detection of non convex objects.

As the evolution of the unsupervised contour-based models depends on local image gradients, it is highly sensitive to noise, poor image contrast, fuzzy contours or texture edges.

Supervised Model

This model permits to integrate prior shape knowledge about the objects to segment. The shape constraints are generally included in the segmentation model by minimizing the distance between the shape of the current active contour and a prior shape. In the simplest case, this leads to the following shape energy:

$$E_{shape} = \int_{\Omega} (\phi(x) - \phi_0(x))^2 dx, \tag{3.44}$$

where ϕ is the current active contour and ϕ_0 the prior shape contour with an implicit representation. The prior shape ϕ_0 can correspond to a shape simply extracted from a reference image or a statistical shape model. The statistical model can simply correspond to the average shape of a training set [38, 39] or a shape model obtained by principal components analysis (PCA) [107, 108]. The energy (5.37) assumes that the position and the location of the object to segment are known. In a realistic segmentation problem, one generally does not know the position and location of objects of interest. In such case, a possible solution is to introduce a set of transformation parameters in the shape energy in order to optimize the alignment between the prior shape ϕ_0 and the active contour $\phi(x)$ [139, 140, 147].

Another supervised contour-based approach propose to incorporate prior fixed location (corresponding points) given by the user in the segmentation model [40].

Supervised contour-based models permits to segment the real shape of partially hidden object, to segment a part of an homogenous object (for example the right part of the lateral ventricles of the brain) or to help the object segmentation in presence of strongly cluttered background.

3.6.2 Region-based Model

Region-based model are based on global information about the regions to segment. This information is given by a statistical region descriptor.

Unsupervised Model

The first region-based model was proposed by Ronfard et al. in [146]. For this model, the authors have proposed to use region-based forces instead of the usual boundary-based forces in the original snake model of Kass [98]. The basic idea of the region-based model is that all the points of the active contour with a neighborhood that fits the region descriptor of the object are pushed outside by centrifugal forces. Conversely, all the points of the active contour with a neighborhood that fits the region descriptor of the background are pulled inside by centripetal forces. Later, the "region competition algorithm" of Zhu et al. in [180] define the notion of region competition linked to the region-based models. Their model is derived from the original snake model and the region growing algorithm. To segment an image, the region growing algorithm tests statistics measures inside a region. Its main limitation is it often generates segmentation results with irregular boundaries and small holes. It would need regularization constraints. Moreover, the design of the region growing algorithm is very intuitive. It is thus difficult to prove that it converges to the minimum of a cost function. Concerning the snake model, it relies only on edge information. Thus its convergence often fails when the active contour lies in an homogeneous region. It would need a more global criterion as regional statistic information. The region competition algorithm combines the advantages of both algorithm to minimize a global cost function. It consists to create a competition between the region inside the active contour Ω_{in} and the region outside the active contour Ω_{out} for the ownership of pixels. This competition is based on a statistical measure. When the active contour is closed to the contour to segment, the contour-based term contributes also to the segmentation. The regularization terms of the snake model assures the smoothness of the active contour during the whole segmentation process.

Probably the most well-known unsupervised region-based model is the 2-phase method based on the mean descriptor presented by Chan and Vese in [35]. In their model they propose to minimize the Mumford-Shah functional in the context of active contours. This model was called the *Active Contour Without Edges* (ACWE). The name of the Chan-Vese's model means that it is able to stop the curve evolution even in the absence of boundary whereas the standard snake model fails to stop. It can detect boundaries not defined by gradients. Its stopping criterion is thus independent of the image gradient ∇I. It is only based on the region competition.

The associated functional to minimize is as follow:

$$E_{ACWE}(\Omega_{in}, c_1, c_2) = Per(\Omega_{in}) + \int_{\Omega_{in}} (c_1 - I)^2 dx + \mu \int_{\Omega_{out}} (c_2 - I)^2 dx, \tag{3.45}$$

where c_1 and c_1 are respectively the mean values of Ω_{in} and Ω_{out} and $Per(\Omega_{in})$ is the perimeter of the region Ω_{in} Note that in this functional, the gradient-based term of the MS functional 3.1 was removed. This case corresponds to the piecewise-constant case of the Mumford-Shah model, also called the minimal partition problem. Its optimal solution is an image composed of regions of approximatively constant intensities equal to the mean value of intensities in the corresponding region.

Other statistical descriptors have been proposed for region-based models such the variance [176], the entropy-based and the joint-entropy-based measure [87, 88], or the mutual information [102, 103].

Supervised Model

Concerning the supervised region-based segmentation models, approaches are mainly based on probability distribution functions (pdfs). The first, presented by Paragios et al. in [138], proposes to include in a segmentation model, prior knowledge about the desired intensity properties of the different regions to detect, by minimizing an energy derived from an a posteriori density function. This density function defines the probability that a given pixel belongs to a particular region knowing its intensity value. In [95], Jehan-Besson et al. propose a different approach that consists in minimizing the "distance" between the pdfs of regions selected in the image to segment and pdfs of references. They propose to measure this "distance" with the Kullback-Leibler divergence measure, the Hellinger distance or the chi-2 function comparison function.

The Advantages of the Region-based Models

- It can stop the curve evolution even in the absence of boundary whereas the standard snake model fails to stop.
- It is more robust in presence of noise than the contour-based model.

Its Limitations

- It needs prior shape information to deal with occlusion problems, poor image contrast or presence of strongly cluttered background.

3.6.3 Hybrid Model

As we saw it in the general Functional (3.25), most of the active contour segmentation models combine region-based features with contour-based features. The region-based features are mainly used to drive the segmentation and the contour-based features are for the regularization of the curve or for introducing shape prior to improve the robustness of a segmentation model with respect to noise, poor image contrast and initial position of the contour[24].

3.7 Regularization

One of the main advantage of the variational segmentation techniques compared to other segmentation methods is that regularization constraints can be easily integrated in the segmentation process. This constraints permit to get smooth segmented contours. In the active contour models, the regularization is naturally based on the geometry of the curve. In this section, we distinguish the constraints used in the parametric and the non parametric models.

3.7.1 Parametric Models

As we saw in the original snake model (Equation 3.40), parametric models use two types of regularization terms which correspond to the first and the second derivative. See section 3.6 for the physical interpretation of these both terms.

3.7.2 Non parametric Models

In the majority of the non parametric models, the active contours are smoothed by minimizing their length. This is described by the well-known Total Variation functional (TV):

$$E_{TV}(\phi) = \int_{\Omega} |\nabla\phi| dx. \tag{3.46}$$

The corresponding evolution equation is:

$$\phi_t = F_{reg}|\nabla\phi| = \kappa|\nabla\phi|, \tag{3.47}$$

where κ is the anisotropic mean curvature of level sets defined by:

$$\kappa = \nabla \cdot (\frac{\nabla\phi}{|\nabla\phi|}). \tag{3.48}$$

This regularizer term was first introduced by Osher et al. in [135].

The drawback of the mean curvature term is that it is particularly sensitive to numerical instabilities. Thus it necessitates very small time steps.

In [79, 80], Gibou et al. proposed to simplify the Euler-Lagrange equation of the Chan-Vese model by ignoring this length regularization term. Their algorithm performs the regularization in a second step by anisotropic diffusion. This method permits to consider larger time steps and thus to speed up the segmentation process.

3.8 Multi-Resolution Approaches

As in the registration framework (Chapter 2) multi-resolution/scale approaches have also been proposed for the active contour segmentation model. These techniques permit first to reduce the required computational cost and secondly to decrease the risk of convergence to a local minimum. There exist two types of multi-scale approach.

3.8.1 The Spatial-based Approach

In this approach, the resolution/scale corresponds to the spatial resolution. This technique consists to solve the minimization problem using a coarse to fine resolution pyramid [137]. The different scales are obtained by downsampling the image to segment. The segmentation result obtained at one level is extrapolated and used as initial solution for the next level.

3.8.2 The Shape-based Approach

In this approach, the resolution/scale corresponds to the shape resolution. This technique consists to solve the minimization problem from the lowest shape complexity to the finest. This type of scale is also called scale of observation. The different scales of observation are obtained by a diffusion equation apply with different number of iterations on the image to segment. Again, the segmentation result obtained at one scale is used as initial solution for the next scale [85]. In [22, 23], Besson et al. propose a multiscale image segmentation model to simultaneously extract structures at different scales of observation/resolution. They define the interdependence between space and scale by a special tensors metric.

Note in more sophisticated approaches, the generation of the different scales is directly integrated in the segmentation model (see [69] for spatial multi-resolution and [5] for shape multi-resolution). With these methods there is no necessity for constructing in a previous step a multi-scale pyramid of the image to segment.

3.9 Conclusions

In this chapter, we have presented a survey on the active contour segmentation models. The basic idea of these models is to detect a particular object in an image from an initial position of its contours. The active contour models the successive estimations of the object contours. As the registration algorithm, the AC segmentation models are designed to solve an optimization problem. This problem consists to find the active contour position that optimizes an energy functional designed to be minimal when the active contour delineates the object contours. The differences between the multitude of existing AC segmentation models rely on the representation of the active contour and on the definition of the energy to minimize.

In this chapter we have defined three types of contour representation: the parametric representation, the non parametric representation and the constraint-based implicit representation. The choice between the parametric and the non parametric representation is a compromise between the computational cost and the accuracy of the modeling. Indeed, the computational cost of an active contour segmentation model is lower with a parametric representation. First the parametric representation is more compact. It is thus more efficient in memory. Then the contour displacements are only computed at control points. However the accuracy of the modeling and the segmentation result are strongly depending on the number of control points and on their position along the curve. Moreover this representation does not allow changes of topology. The non-parametric representation permits to model very accurately any types of shape, the solution is not depending on the curve parametrization and this representation allows topological changes. However it makes the segmentation model slower because it requires to store and calculate a large number of points. The non parametric representation was for a long time linked to the signed distance function. Currently, new models tend to replace it by a label function in order to avoid the reinitialization step due to the conservation of the signed distance property.

The 2 phase non parametric representation can be divided into two subclasses: the hard and the soft representation. The segmentation method linked to the hard representation classifies the image pixels trough the crossing of an interface. This segmentation method is thus very local. The particularity of this representation is it permits to localize an object of interest based on prior spatial knowledge. This prior spatial knowledge corresponds to the initial position of the contours and the detected object is the closest object to this initial contour position. The original signed distance function and the label function belong to this type of implicit representation. The segmentation method linked to the soft representation classifies the image pixels following their probability to belong to a particular region. This segmentation method segments all the objects in the image that match a particular feature. It is thus more global than the one derived from the hard representation. This second type of implicit representation was proposed to speed the segmentation process when we need to segment all the objects of the image that match particular features. The initial position of the contours permits to speed up the segmentation not to select a particular object.

The constraint-based implicit representation is a representation recently proposed to combine the low computational cost of the parametric representation and the possible topology change of the non-parametric representation. However this representation keeps the same limitation than the parametric representation: the accuracy of the segmented contour is strongly depending on the number of control points and on their distribution on the image.

We saw that the energy to minimize can lead to a supervised or unsupervised segmentation. The first active contour segmentation models were boundary-based. As the evolution of boundary-based segmentation methods depends on local image gradients, they are very sensitive to noise, fuzzy contours or texture edges. The region-based segmentation models are more robust because they use global information about the regions to segment. This information is given by a statistical region descriptor.

The main advantage of the active contour segmentation model compared to other segmentation models is its regularization constraint that permits to obtain smoothed segmented contours.

This active contour framework despite the fact that it was originally designed for segmentation seems particularly appropriate to integrate local constraints in a registration task. In the next chapter we will present the algorithms proposed so far to combine segmentation by active contour to registration.

Joint Registration and Segmentation Models

4

4.1 Introduction

This chapter aims to present the models proposed so far for joint image registration and segmentation. In this thesis, we have limited our attention to the non parametric approaches derived from the AC framework for the two following reasons. First, the AC framework is particularly well suited to define and implement local segmentation or contour regularization constraints. Secondly, the objects selected to drive the registration are represented in an implicit way (level set method [135]). This implies that the results will be independent of the contour representation and possible topology changes between objects to match will be implicitly handle.

This chapter is organized as follow. In Section 4.2, we describe the methods intuitively deduced from the general evolution equation of the level set function (PDE-based approach). We will see that these methods are based on level set tracking. Then, in Section 4.3, we present the methods directly derived from an energy to minimize (variational approach). This second type of methods is based on level sets registration. In Section 4.4, we present a model that combine the variational approach with the PDE-based approach. Finally, the advantages and the limitations of both approaches are discussed in Section 5.10. Figure 4.1 summarizes the different types of joint image registration and segmentation models presented in this chapter.

4.2 Models derived from a PDE-based Approach

In this section, we present two algorithms directly designed from the following level set evolution equation introduced by Osher and Sethian in [135]:

$$\frac{\partial \phi(x,t)}{\partial t} = v(\phi(x,t))|\nabla \phi(x,t)|, \tag{4.1}$$

where x is an image point, t is the time parameter, ϕ is the level set function, v is the velocity of the flow or speed function regarding to ϕ, and t is the time parameter. The derivation of this formula from the level set function motion was shown in Chapter 3.

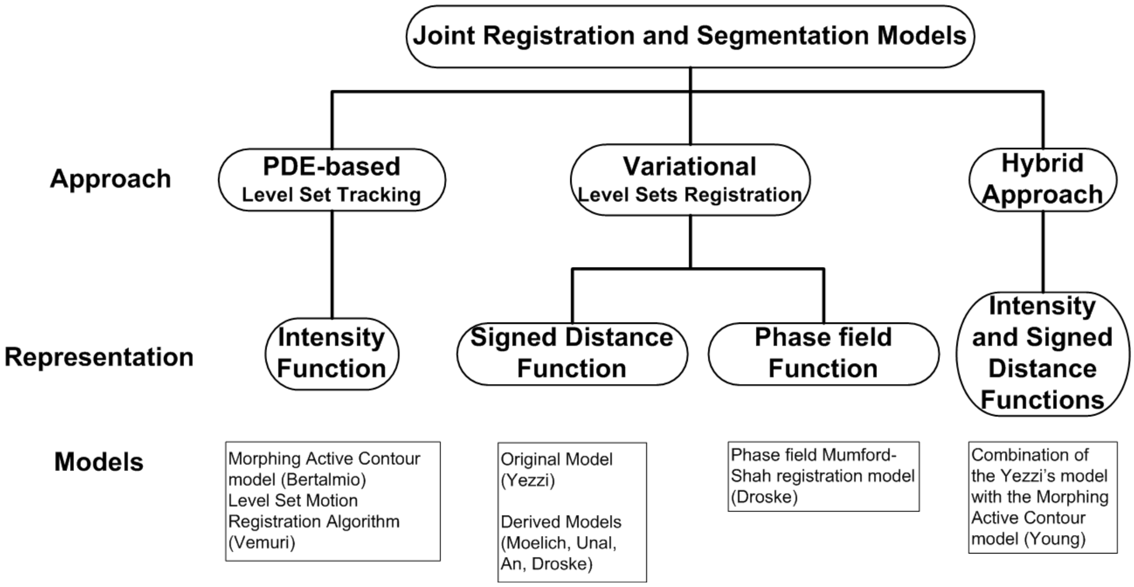

Figure 4.1: Classification of the joint registration and segmentation models according to the approach used.

4.2.1 The Morphing Active Contour model

This model was proposed by Bertalmio et al. in [16, 17]. In fact, this algorithm joints morphing instead of registration to active contour segmentation. That means that it deforms the moving image through the target image as in a registration process but the corresponding geometric transformation is not determined explicitly. However we chose to cite it as first reference of the PDE-based approach because it is based on a very similar method to the one used in the *Level Set Motion Registration Algorithm* described in the following section. Moreover it was designed for atlas-based segmentation.

The algorithm of Bertalmio assumes as data a moving image, a target image and a segmented contour that identifies an object of interest in the moving image. The segmented contour is represented implicitly as a zero contour of a signed distance function ϕ_d. Note that in the atlas-based segmentation method (Chapter 1), this contour would correspond to an atlas label. The goal of the morphing active contour model is to identify in the target image a contour that corresponds to the object segmented in the reference image. This is done by solving a system composed by the two partial differential equations (PDEs) described below.

1. The Morphing Equation

The first PDE is in charge of morphing the two images to each other. It is based on the original idea to consider as level sets of interest, the level sets naturally present in the moving image (the intensity contours). The authors propose thus to replace in (5.8) the level set function $\phi(x,t)$ by the intensity function of the moving image $\phi_{I,M}(x,t)$. This leads to the following evolution equation:

$$\frac{\partial \phi_{I,M}(x,t)}{\partial t} = v(\phi_{I,M}(x,t))|\nabla G_\sigma * \phi_{I,M}(x,t)|, \tag{4.2}$$

with $\phi_{I,M}(x,0) = \phi_{I,M}(x)$.

G_σ is a Gaussian kernel with standard deviation of σ and $*$ is the convolution operator. $\phi_{I,M}$ needs to be convolved with a Gaussian kernel G prior because the gradient computation is very sensitive to noise. As with the level set segmentation model, the morphing equation makes the level sets of $\phi_{I,M}$ evolve along their respective normal. The steady state solution is obtained when $\phi_{I,M}(x,t) = \phi_{I,T}(x)$ where $\phi_{I,T}(x)$ is the intensity function of the target image. As speed function, the authors chose the morphing term $v(\phi_{I,M}(x,t)) = \phi_{I,M}(x,t) - \phi_{I,T}(x)$.

Note that this morphing equation has three limitations:

1. In homogeneous regions of $\phi_{I,M}$, $|\nabla\phi_{I,M}(x,t)| = 0$ and the morphing process is stopped even if $\phi_{I,M}(x,t) \neq \phi_{I,T}(x,0)$. To cope with this problem, the morphing active contour algorithm assumes that the boundaries to track are not placed over regions where there is no information and thus flat gradient. This means that this algorithm can not track objects with fuzzy or sparse boundaries.
2. Since the speed function v measures gray-level differences, an histogram equalization of both image has always to be performed as a preprocessing operation. This operation could be avoided by computing the velocity on contrast invariant features like the image gradient.
3. This PDE assumes that the morphing image and the target image are consistent, i.e. they contain the same objects with similar intensity and position. The morphing active contour algorithm avoids inconsistencies problems by applying the morphing equation locally on a narrow band around the active contour. Naturally the active contour has to select a consistent object between both images.

In [16, 17], the authors intuitively deduced this morphing equation from the level set evolution equation (5.8). Below we show how this PDE can be computed from an optical flow or a variational approach.

a. The Optical Flow Approach The optical flow method is based on the assumption that the brightness of the moving image intensity function $\phi_{I,M}(x,t)$ stays constant for small displacements, and for a short period of time. In the usual optical flow approach, these small displacements are explicitly expressed by vectors. Here we will model them implicitly by the variation of the image contours dC. Note that this modeling links the optical flow approach and the active contour method.

$$\phi_{I,M}(C(t)+dC, t+dt) = \phi_{I,T}(C(0),0) \Rightarrow d\phi_{I,M}(C(t),t) = 0, \tag{4.3}$$

where $d\phi_{I,M}$ is the total derivative of $\phi_{I,M}$.

By deriving (4.12) with the chain rule, the optical flow constraint (4.3) can be rewritten as:

$$d\phi_{I,M}(x,t) = \underbrace{\frac{\partial\phi_{I,M}}{\partial C}}_{\nabla\phi I,M}\frac{\partial C(t)}{\partial t} + \frac{\partial\phi_{I,M}}{\partial t} = 0, \tag{4.4}$$

We saw in the active contour framework that the variation of a contour is depending of its unit normal vector $\mathcal{N}$ and the velocity v such as $\frac{\partial C(t)}{\partial t} = -vN$.

Here $\mathcal{N}$ is defined for each level set of the moving image intensity function, as follows:

$$\mathcal{N} = \mathcal{N}_{\phi_{\mathcal{I},\mathcal{M}}} = \frac{\nabla\phi_{I,M}}{|\nabla\phi_{I,M}|}. \tag{4.5}$$

The optical flow constraint is generally used to express the variation of the displacement $\frac{\partial C(t)}{\partial t}$. To obtain the morphing contour equation, we have here to express the intensity variation:

$$\frac{\partial\phi_{I,M}}{\partial t} = (\phi_{I,M}(x,t) - \phi_{I,T}(x,0))|\nabla\phi_{I,M}|, \tag{4.6}$$

Note that the optical flow approach often consider that $\phi_{I,M}(x,t)$ and $\phi_{I,T}(x,t)$ are separated by only one unit of time:

$$\frac{\partial \phi_{I,M}}{\partial t} = \phi_{I,M}(x,t) - \phi_{I,T}(x,t), \tag{4.7}$$

This imply that following the general level set formulation 5.8 , $v = \frac{(\phi_{I,M}(x,t) - \phi_{I,T}(x,t))}{|\nabla \phi_{I,M}|}$.

We will discuss the difference between both formulations in the description of our joint segmentation and registration method (Chapter 5).

b. The Variational Approach The morphing equation of Bertalmio (4.2) can also be derived from the following energy functional:

$$F(\phi_{I,M}) = \int_{\Omega} (\phi_{I,M}(x,t) - \phi_{I,T}(x,0))^2 dx. \tag{4.8}$$

Note that this type of energy functional is often used to introduce prior knowledge in variational segmentation models. For example it is used in the Shape-prior model or in the Mumford-Shah model to ensure that the moving contour/image will stay similar to a contour/image of reference (see Chapter 3).

2. The Tracking Equation

The second PDE aims to track a particular object deformed by the morphing equation. For that, it has to evolve the signed distance function ϕ_d with the same speed as the morphing equation. This lead to the following equation:

$$\frac{\partial \phi_d(x,t)}{\partial t} = (\phi_{I,M}(x,t) - \phi_{I,T}(x,0)) \mathcal{N}_{\phi_{I,M}}(x,t) \cdot \mathcal{N}_{\phi_d}(x,t) |\nabla \phi_d(x,t)|, \tag{4.9}$$

where $\mathcal{N}_{\phi_{I,M}}(x,t) = \frac{\nabla \phi_{I,M}}{|\nabla \phi_{I,M}|}$ and $\mathcal{N}_{\phi_d}(x,t) = \frac{\nabla \phi}{|\nabla \phi_d|}$. The scalar product between these two normals gives a sign that permits to evolute ϕ_d in the same direction of $\phi_{I,M}$. Indeed, as the implicit displacements are computed by both PDE on the same contour point, they will be collinear but because of local values (local image level gray for the morphing equation and local distance values for the tracking equation) they can have opposite direction. Thus, if we want the zero-level set of ϕ_d to track the evolution of the image points of I_M, we have to project the morphing velocity $\phi_{I,M}(x,t) - \phi_{I,T}(x,0) \mathcal{N}_{\phi_{I,M}}$ on the normal direction of the level sets of ϕ_d. Both PDEs are thus couple by their velocity. In [16, 17], no regularization term is mentioned to keep the level sets smooth during their evolution. We can suppose that they have used the common mean curvature term.

The authors propose to use their algorithm for active contour segmentation based on a reference image. This reference image gives an approximation of the object shape to segment and prior knowledge about its intensities. Potential applications would be contour tracking in a sequence of images or slice by slice segmentation of 3D images.

The Advantages of the Morphing Active Contour

- This technique uses shape and intensity prior knowledge without hypothesis concerning the object to track as usual prior model. It is thus more flexible.
- The signed distance function permits to select consistent objects between both images.
- Thanks to the implicit nature of the model, the object of reference can adapt its topology to the target object.

Its Limitations

- This model can only segment closed and disconnected contours.
- This joint matching and segmentation process necessitates to solve two PDEs: one to deform the image and another one to track the deformation.
- The initial contour has to be a level set of the moving image. This algorithm is thus limited to segment objects with not well defined boundary.
- This model requires that the moving image is locally consistent with the target image in the area around the active contour, i.e. same objects with similar position and intensities.

4.2.2 Level Set Motion Registration Algorithm

In [168], Vemuri et al. present a non-parametric non rigid registration algorithm inspired by the level set segmentation model. This algorithm is very close to the morphing active contour model of Bertalmio but dedicated to atlas registration instead of atlas morphing. The main difference is that the image matching is not anymore tracked by a level set function but by a dense deformation field u and that the matching and the tracking PDEs are combined into a single PDE. To get the segmentation of a particular object in the target image, this deformation is applied to the segmentation of the corresponding object in the moving image using the atlas-based approach.

The evolution equation of this model is the following:

$$\frac{\partial u(x,t)}{\partial t} = v(\phi_{I,M}(x,t)) \frac{\nabla G_\sigma * \phi_{I,M}(x,t)}{\sqrt{\nabla G_\sigma * \phi_{I,M}(x,t)^2 + \epsilon^2}}, \tag{4.10}$$

where ϵ is a small positive constant. This parameter permits to stabilize the numerical computation when $\nabla G_\sigma * \phi_{I,M}$ is close to zero. The intensity function $\phi_{I,M}$ at time t is given by the deformation field $u(x,t)$ and the initial intensity function $\phi_{I,M}(x,0)$ such that:

$$\phi_{I,M}(x,t) = \phi_{I,M}(x + u(x,t), 0), \tag{4.11}$$

which ensures that the evolution of the intensity function exactly corresponds to the current deformation.

As in the initial level set segmentation model, this matching equation makes the level sets of $\phi_{I,M}$ evolve along their respective normal with a speed v. Besides, the direction of the motion depends on the local intensity levels of the image: The motion goes from the highest intensity to the lowest intensity if $v(\phi_{I,M}) > 0$ and from the lowest to the highest if $v(\phi_{I,M}) < 0$.

In [168], the authors draw the attention that the existence and the uniqueness of the PDE (5.19) is difficult to prove and has to be further investigated.

The Vemuri's model also use an intensity difference term $v = (\phi_{I,M}(x,t) - \phi_{I,T})$ as speed function. We will show in the description of our model (Chapter 5) that the most used segmentation term of the AC framework, the region-based term, cannot be directly used in such model. Concerning the regularization of the deformation field, it is performed at the end of each iteration by isotropic diffusion (Gaussian filtering).

As in the Bertalmio's model, the authors intuitively deduced their registration equation from (5.8). Below we show how this PDE can be computed from an optical flow or a variational approach.

a. The Optical Flow Approach This time, the small displacements of the optical flow constraint are explicitly expressed by the variation of a dense deformation field du as in the usual optical flow approach. This lead to the following equation:

$$\phi_{I,M}(x + du, t + dt) = \phi_{I,T}(C(0), 0) \Rightarrow d\phi_{I,M}(C(t), t) = 0. \tag{4.12}$$

As before, the optical flow constraint (4.12) can be rewritten as:

$$d\phi_{I,M}(x,t) = \underbrace{\frac{\partial \phi_{I,M}}{\partial u}}_{\nabla\phi_{I,M}} \frac{\partial u}{\partial t} + \frac{\partial \phi_{I,M}}{\partial t} = 0. \tag{4.13}$$

This leads to the following vector flow evolution equation:

$$\frac{\partial u(x,t)}{\partial t} = -\frac{\phi_{I,M,t}}{|\nabla \phi_{I,M}|} \frac{\nabla \phi_{I,M}}{|\nabla \phi_{I,M}|}, \tag{4.14}$$

where $\phi_{I,M,t} := \frac{\partial \phi_{I,M}}{\partial t}$ is the variation of the intensity function.

As mention in the description of the Bertalmio's model, the optical flow approach often considers that $\phi_{I,M}(x,t)$ and $\phi_{I,T}(x,t)$ are separated by only one unit of time:

$$\frac{\partial \phi_{I,M}}{\partial t} = \phi_{I,M}(x,t) - \phi_{I,T}(x,t). \tag{4.15}$$

Through the active contour framework we have fund that

$$\frac{\partial \phi_{I,M}}{\partial t} = (\phi_{I,M}(x,t) - \phi_{I,T}(x,t))|\nabla \phi_{I,M}|. \tag{4.16}$$

By combining the level set evolution equation (4.16) with the optical flow equation (4.14) we obtain the evolution equation (5.19) of the Vemuri's model.

b. The Variational-Energy Approach The registration equation of Vemuri (5.19) can also be derived from an energy functional:

$$F(\phi_{I,M}) = \int_\Omega (\phi_{I,M}(x+u,t) - \phi_{I,T}(x,0))^2 dx. \tag{4.17}$$

Note that this equation is similar to the one proposed for the variational formulation of the Bertalmio's morphing equation expect that the evolution of the moving image is depending of geometrical transformation u.

The Advantages of the Level Set Motion Registration Algorithm

- The contours driving the registration and the contours segmented by the atlas-based method can be of any types: closed or open, connected or disconnected.
- The active contours (contours of the moving image) are modeled with only one function, the intensity function I_M.
- The deformation of all the moving image contours are tracked at the same time by the deformation field.
- The deformation of the moving image and its contours tracking are performed by solving only one PDE.
- The regularization of the deformation field by diffusion permits not only to smooth the evolving level set but also to diffuse their transformation on region with a flat gradient ($|\nabla I_M(x,t)| = 0$). Thus this method permits through an atlas projection to segment also fuzzy, sparse or even none visible contours.

Its Limitations

- As the algorithm considers all the contours presents in the moving image, possible inconsistences between the moving and the target image can lead to misregistration. This registration process requires thus that the whole moving image is consistent with the target image, i.e. they contain objects with similar position and intensities.

4.3 Models derived from a Variational-Energy Approach

In this section, we present algorithms designed from this general functional energy:

$$E(\phi, u) = \int_{\Omega} f(\phi, u) d\Omega, \tag{4.18}$$

where Ω is the image domain, ϕ is the level set function, u is a geometrical transformation and f is the image descriptor.

4.3.1 Yezzi's model

The first attempt of a model directly derived from an energy was presented by Yezzi and al. in [177]. This model consists first to define two segmentation energies (Equations (4.19) and (4.20)), one in the moving image I_M and another one in the target image I_T, that aim to segment the same object in both images. As energy, the authors have illustrated their method with the mean-based segmentation functional proposed by Chan et Vese in [35].

$$E_M(C_M) = \int_{C_{M,in}} (I_M(x) - mean(C_{M,in}))dx + \int_{C_{M,out}} (I_M(x) - mean(C_{M,out}))dx, \tag{4.19}$$

where C_M is the active contour segmenting the moving image. $mean(C_{M,in})$ and $mean(C_{M,out})$ are respectively the mean values of the inside and outside region.

$$E_T(C_T) = \int_{C_{T,in}} (I_T(x) - mean(C_{T,in}))dx + \int_{C_{T,out}} (I_T(x) - mean(C_{T,out}))dx, \tag{4.20}$$

where C_T is the active contour segmenting the moving image. $mean(C_{T,in})$ and $mean(C_{T,out})$ are respectively the mean values of the inside and outside region.

Then both energies are coupled by defining the active contour of the target image C_T as beeing the active contour of the moving image C_M under the rigid deformation u, i.e. $u(C_M) = C_T$.

The joint registration and segmentation energy to minimize is thus depending on the active contour C and on the transformation g.

$$\begin{aligned} E(C, g) &= E_M(C) + E_T(g(C)) \qquad (4.21) \\ &= \int_{C_{in}} (I_M(x) - mean(C_{M,out})))dx + \int_{C_{out}} (I_M(x) - mean(C_{M,out})))dx \\ &\quad + \int_{u(C_{in})} (I_T(x) - mean(C_{T,out})))dx + \int_{u(C_{out})} (I_T(x) - mean(C_{T,out})))dx. \end{aligned}$$

The integrals of Equation (4.21) can be simplified as:

$$\begin{aligned} E(C, g) &= E_M(C) + E_T(g(C)) \qquad (4.22) \\ &= \int_{C_{in}} (I_M(x) - mean(C_{in})) + (I_T(u(x)) - mean(u(C_{in})))dx \\ &\quad + \int_{C_{out}} (I_M(x) - mean(C_{out})) + (I_T(u(x)) - mean(u(C_{out})))dx. \end{aligned}$$

The derivation of this energy leads to $1 + N * 6$ PDEs where N is the image dimension. The first PDE updates the representation of the contour C. A mean curvature term was added to this PDE for the contour regularization. The other $N * 6$ PDEs update each parameters of the rigid transformation. These last PDEs does not require a regularization term, the regularization of the rigid transformation being implicit.

The Advantages of the Yezzi's model

- The active contour segmentation and the registration tasks are expressed in only one functional energy.
- Minimizing the Yezzi functional involves not only to segment one object of interest in both images but also to minimize the difference in position between these objects. Thus, the registration helps the active contour segmentation by combining the information of both images and the active contour segmentation helps the registration task by isolating a consistent object between both images.
- This model can combine multi-modal information as the segmentation energies are defined independently on both images.

Its Limitations

- The joint segmentation and registration process needs to solve $N * 6 + 1$ PDEs.
- The model was designed to segment one object in the target image (2 phase segmentation) and to recover only rigid transformation.
- It was shown in [124] that the segmentation results of this model is very sensitive to the initial conditions.

4.3.2 Models inspired by the Yezzi's model

Several authors have analyzed the Yezzi's model and proposed solutions for its limitations. We present below the four most relevant works.

1. **Initial conditions and Reconstruction of Objects from Partial Information** In [124], Moelich et al. first show that the Yezzi's model is very sensitive to the initial curve and deformation. To avoid local minima, the active contours of both images have to be well superposed to the objects of interest. To make the algorithm more robust, Moelich et al. propose to define the active contour of both images as beeing the initial curve under a particular deformation, not only for the target image like in the Yessi's model. They also introduce an initial registration step to find the best registration parameters that compensate in both images the difference of position between the initial curve and the objects of interest.

   Secondly, the authors show the ability of the Yezzi's model to reconstruct an object from partial information by combining the shape of the target object with the source object. Thus, they propose to replace the Chan and Vese segmentation model [35] that always results to the segmentation of the intersection of both objects (logical And) by the logic segmentation models of Sandberg and Chan [151]. That way if the objects in the source and target images have dissimilarities, their segmentation can be constrained to the intersection of both objects (logical And), to the union of both objects (logical Or) or to other types of logical operations.

2. **Extension to Non Rigid Registration** In [167], Unal et al. generalize the rigid framework of Yezzi to non rigid registration. For that, they replace the rigid deformation of the source contour by a non rigid deformation. As the authors were interesting to analyze the variation between shapes, their model computes the deformation field on the active contours only and not on the whole image.

3. **Moving Image seen as a Prior image** In [8], An et al. propose to consider the moving image of the Yezzi's model as a prior image. From this prior image, they extract a prior shape of

the object to segment in the target image. By using this prior shape as initial contour instead of any contours close to the target objects as in the Yezzi's model, permits to decrease the numerical calculation time. They also propose to include a prior segmentation term in the Yezzi's model that computes the difference of intensity between the prior shape and the shape segmented by the active contour in the target image. This term corresponds in fact to the matching image term used in the Bertalmio or in the Vemuri's model at the difference that it is computed inside the prior shape only.

4. **Sharp and Soft Contour-based Non Rigid Registration** In [60], Droske et al. present two joint registration and active contour segmentation models. The first one called "Sharp interface Mumford-Shad registration" is a model similar to Yezzi but as in the An's model [8], it uses a prior shape extracted from the moving image for the initial curve and as in the Young's model [178], it optimizes a non rigid deformation. The novelty of the Droske's model is it is boundary-based instead on intensity-based as the models presented above. It can thus register images of different modalities. Also the non rigid deformation computed on the contour is propagated to the whole image by a Finite Element Method (FEM). Droske et al. enhance that the limitation of the Yezzi's model is that the level set function can represent only closed and disconnected curves. To cope with this problem, they propose a second model called "Phase field Mumford-Shad registration". The particularity of this model is that the contours of both images are represented by a phase field. That means that a membership level to the two phases from 0.0 (background) to 1.0 (contours position) is attributed at each pixel. The authors have designed an energy functional that optimizes the detection of common contours between the source and target image as well as the non rigid deformation between them. Thus the matching is not perturb by possible inconsistences between both images. Also this soft model permits to consider close, open, connected and disconnected contours for the registration.

4.3.3 Other Types of Variational-Energy Models

In this section, we mention two other techniques that are close to the joint segmentation and registration model proposed by Yezzi.

Joint Optical Flow Estimation and Active Contour Segmentation These models aims to generate a dense but "discontinue" deformation field on the whole image. This transformation is not used for registration but for analyzing the motion between two images sequences (see [139], [28] or [7]). The basic idea is to use the active contours to partition the moving image in homogenous region and to compute the optical flow between the target and moving image separately on each partition.

Non rigid registration between Implicit Representation of Shapes In [140], Paragios et al. propose to extract the non rigid deformation u between 2D geometric shapes from their representation by a signed distance function. For that they design this functional.

$$E(g) = \int_{\Omega} (\phi_M(x+u) - \phi_T) dx \tag{4.23}$$

where $\phi_M(g(x))$ is the implicit representation of the moving shape and ϕ_T is the implicit representation of the target shape. This functional is minimize by optimizing rigid and non rigid registration parameters. The authors uses this model to compute a point to point correspondence on the shape contours only.

4.4 An Hybrid Model

In [178], Young et al. propose to combine in a two steps process, the joint segmentation and registration algorithm proposed by Yezzi with the morphing active contours algorithm. Their objective is to segment organs in 3D CT scans for radiotherapy treatment planning. The challenge with these organs is they have not well defined boundary because of their connection with other organs of same intensities. Prior knowledge is thus needed to delineate them. To do that, they chose to follow a slice by slice segmentation process where a segmented slice becomes the reference image for the segmentation of the next slice. By combining a segmentation based on semi-global image features (region means) with a rigid registration, the Yezzi's algorithm permits to obtain a global estimation of the object boundary with a shape very similar to the one of the reference image. The morphing algorithm is then used to refine this segmentation by using more local features, the pixel intensity. Note that in this second step, the accuracy segmentation can be improved only where the initial curve is on a contour. On homogenous region, the contour will keep the position given by the Yezzi's model. The authors fund that their algorithm can segment accurately no more than three consecutive slices. They propose thus to use it to automatically fill gaps between two manually segmented slice.

4.5 Discussion

In this chapter, we saw that the PDE-based and the variational approaches proposed so far for joint registration and segmentation use two different types of method.

The PDE-based approaches are based on level set tracking. They consider the intensity function of a reference image as a level set function. The level sets of this intensity function are deformed with the level set evolution equation to match corresponding contours in a target image. The idea is to track these level sets during their evolution. The methods presented in this chapter propose to perform this tracking by a second level set function (a signed distance function) or by a dense deformation field. The level set function permits to track selected contours that are consistent between both images but can consider only disconnected objects with close and well visible contours. The dense deformation field, through the atlas-based segmentation method, permits to segment any types of objects (connected, disconnected, close or open, with or without visible contours). However, as all the level sets of the reference image are considered, inconsistencies between both images can lead to missregistration.

The variational approaches are based on level sets registration. This method consists to segment corresponding objects in both images. The idea is to perform the registration not on the original images but on the level set representation of the active contours. Thus the registration is performed on consistent objects. Also the information of both images is combined by making the contour of the target image depending on the contour of the source image through the computed geometrical deformation. The segmentation of both images is thus influence by shape prior knowledge coming from the other image. This method can register multi-modal images because the registration is performed on segmented geometrical features and not on the image intensities. It can also segment object with sparse contours by combining the shape information of both images. However it is very sensitive to the initial position of the active contours and can segment close and disconnected objects only. Moreover, this method is often design to optimizes either a rigid transformation or a non rigid deformation but only computed on a narrowband around the objects contour. Only the model of Droske et al. [60] can perform a multi-phase segmentation and propagates the non rigid displacement of the active contours through the whole image but it is boundary-based and not region-based as the other models.

Part III

Contributions

Our Active Contour-Based Registration Model

5

5.1 Introduction

This chapter aims to introduce the model we propose to integrate local constraints in an atlas non rigid registration process. This model should allow:

- To base the registration on relevant geometrical objects* in order to increase the robustness of the algorithm regarding possible inconsistencies between the atlas and the image to segment (the target image).
- To exploit more local prior information than the one used in common atlas registration approaches. This prior information could concern the intensity distribution or the admissible shapes of objects selected to drive the registration.
- To impose the smoothness of the registered atlas contours.

As we saw in Chapter 3, the Active Contour (AC) framework [98] seems particularly well suited to define and implement such local constraints even if this technique was initially designed for image segmentation and not for image registration. However as we have already mentioned in Chapter 2, segmentation and registration are closely related. The segmentation of the source and target images can reduce their inconsistencies and thus improve their registration. Inversely, a better segmentation of these images may be obtained by combining their information. In order to best combine it, the images need to be perfectly aligned. The main objective of this thesis is to design a model that performs these two tasks jointly: the registration of the atlas and the segmentation of the target image based on AC techniques. In order to adapt the AC segmentation framework to atlas registration, we had to study the following points:

1. How to model the atlas contours (the active contours) selected to drive the registration?
2. Which scheme to use when these active contours have to register more than two regions?

---

*Remind that we consider as geometrical objects points, lines or surfaces.

3. How to explicitly track the active contours motion?
4. How to extend the explicit deformation of the active contours to the whole image?
5. How to get an accurate registration on the contours segmented by the active contour and far away from these contours?
6. How to define registration constraints on closed and open contours?
7. How to design a registration model that can use any type of local constraint defined in the active contour framework (supervised/unsupervised contour-based or region-based)?
8. How to indicate to the registration model which type of information to use in which region of the image?
9. How to get smooth and accurate registered contours as well as a smooth deformation field?
10. How to speed up and stop this joint registration and segmentation process?
11. How to deal with the main limitation of the active contours framework: the initial active contour has to be well superposed to the object to segment to converge correctly?
12. How to get a bijective transformation?

Through the different sections of this chapter, we will present our joint registration and segmentation model by successively proposing solutions to the above questions. First, Section 5.2 presents the two representations we have used to model the active contours driving the registration. Then Section 5.3 describes the technique we propose to extract the deformation from the tracking of the active contours motion. After, Section 5.4 presents the different types of forces coming from the AC framework. We will see that some of these forces are already used in non-parametric registration methods. Section 5.5 describes the two multiscale schemes that we use to speed up the computation time of our model, to decrease the risk of convergence to a local minimum and to progressively improve the alignment of the atlas contours with their target. Section 5.6 describes the two methods we have tested to interpolate the active contours deformation to the whole image. Section 5.7 presents the regularization constraints that our model uses to enforce the smoothness of both the deformation field and the registered contours. Section 5.8 proposes an analyze of the convergence of our algorithm and presents the design of a stopping criterion. In Section 5.9 we show that our active contour registration model has a lot of similarities with an algorithm widely used in atlas registration: the Demons algorithm of Thirion [166]. Finally, Section 5.10 concludes this chapter with a discussion on the proposed model.

5.2 Active Contours Representation

We start designing our model by representing the active contours (in our case the contours selected in the atlas) with a signed distance function representation. Based on this representation, we have mainly developed distance-based registration and interpolation models (see Section 5.6). However as we saw in Chapter 3, one of the weak point of the signed distance function representation is that it limits the model to a two-phase segmentation/registration. Here we propose a new multi-phase representation based on one label function. We first point out why the information contained in the signed distance function representation is particularly important for the computation of the region-based forces derived from the AC framework. Then we present the new multi-phase representation we have developed based on this information.

5.2.1 Signed Distance Function Representation ϕ_d

We saw in Chapter 3 that the signed distance function representation ([135], [152], [134]) models the active contours as follows:

$$\phi_d(x) = \begin{cases} 0 & x \in C \\ +d(x) & x \in \Omega_{in} \\ -d(x) & x \in \Omega_{out}, \end{cases} \tag{5.1}$$

where C is the modeled contour, $\phi_d(x)$ is its implicit representation at the image point x and d is the Euclidean distance to the closest contour point on C. The sign of this representation generates two types of information. First it classifies the image pixels in two regions, Ω_{in} and Ω_{out}. Ω_{in} and Ω_{out} are respectively the inside and the outside regions of C. Secondly the gradient computed on its level sets is always oriented towards the inside or the outside of C. With the sign convention used in (5.1), they are all oriented from the outside to the inside of C. We have called this information given by $\nabla\phi_d$, the *polarity information*. We explain in Section 5.4 that the AC framework uses this information for the computation of the region-based forces. We will see that such attractive forces cannot be used with the intensity function representation because it does not contain this type of polarity information. Note that the concept of polarity was already introduced by Thirion et al. in [166] to describe their diffusion-based registration algorithm (the Demons algorithm) (see Section 5.9). However, in the AC framework, the notion of polarity is defined regarding closed contours while for the Demons algorithm, the authors describe it regarding any type of contours (closed or open).

5.2.2 Label Function Representation ϕ_L

For the registration of multiple regions, we propose to represent the active contours selected in the atlas by a label function ϕ_L. This label function permits to define an arbitrary number of regions as follows:

$$\phi_L : x \in \Omega \rightarrow \phi_L(x) = k, k \in [1, .., n] \text{ if } x \in \Omega_k, \tag{5.2}$$

where Ω_k is the k^{th} labelled region and n is the number of regions. In this representation, the active contours are modeled by the discontinuities of $\phi_L(x)$.

The label function representation permits to distinguish n regions by using only one function. However, this representation has two main limitations. First it does not contain the polarity information necessary to compute the most used attractive forces of the AC segmentation framework, the region-based forces (see Section 5.4). Thus to use this type of representation, we have to explicitly model this information. Secondly, during the segmentation process, level set functions are updated with the following finite different equation derived from the discretization of $\frac{\partial\phi(x,t)}{\partial t}$:

$$\phi(x, t + \Delta t) = \phi(x, t) + \Delta t \frac{\partial\phi(x, t)}{\partial t}, \tag{5.3}$$

Note that this equation changes the values of the level set function. It changes the current active contour position by moving ϕ up or down at different location. The finite different equation suites well the signed distance function representation. The position of the zero level set is change by updating the distances values of the function. The problem with the label function representation is that the label values model the different regions. Thus to use this type of representation, the AC model needs a constraint to imposes that the label function keeps its n possible values during its evolution.

We saw in Chapter 3 that Lie et al. proposed a similar non parametric representation in [111]. The differences between their method and ours concern the techniques used to model what we have called the polarity information and to evolve the label function. Both approaches are described below.

Polarity Information To generate the polarity information, Lie et al. proposed to model the labeled representation by a linear combination of binary functions ψ_k as follows:

$$\phi_L(x) = \sum_{k=1}^{n} k\psi_k(x), \tag{5.4}$$

where $\psi_k(x) = 1$ if $x \in \Omega_{in}$ and $\psi_k(x) = 0$ if $x \in \Omega_{out}$. Here the polarity is model by the labels 0 or 1. Thus the gradient computed on the interface is always oriented toward the inside of the modeled region.

In our model, inspired by the signed distance function representation, we generate the polarity information with a sign function locally computed around ϕ_L discontinuities. The objective of this sign function is to adapt the orientation of the local gradient such that it gives the polarity of the current region. This method is described in detail in Section 5.3.

Label Function Evolution To segment the target objects, the model of Lie et al. evolved each binary functions with the usual finite difference equation 5.3. Due to the two label function limitations described above, they had to introduce the following constraint in their evolution equation.

$$K(\phi) = (\phi - 1)(\phi - 1)...(\phi - n) = 0. \tag{5.5}$$

This constraint preserves the values of the label function during its evolution. It also permits to avoid vacuum and overlap between the basis functions.

As the objective of our model is to generate a dense deformation field u, we use u to define the current label function position $\phi_L(x,t)$ such that:

$$\phi_L(x,t) = \phi_L(x + u(x,t), 0). \tag{5.6}$$

By deforming the level set function with a nearest neighbor interpolation instead of updating it with the finite difference scheme, the values of the label function do not change during the registration process. Moreover, as the evolution of the label function does not dependant on the evolution of basis functions, we do not have overlapping or vacuum problems.

5.3 Deformation Field Extraction

To register the atlas, we need to extract a dense deformation field u that tracks the motion of the level set function modeling the active contours selected in the atlas. We are thus looking for a Partial Derivative Equation (PDE) that determines the variation of the deformation field $\frac{\partial u(x,t)}{\partial t}$ regarding to the variation of the level set function $\frac{\partial \phi(x,t)}{\partial t}$. This can be formulated as:

$$\frac{\partial u(x,t)}{\partial t} = u(x,t)_t = f(\frac{\partial \phi(x,t)}{\partial t}), \tag{5.7}$$

where f is a functional containing the local constraints coming from the AC framework.

Remind that the motion/variation of the level set function is given by the following PDE introduced by Osher and Sethian in [135]:

$$\frac{\partial \phi(x,t)}{\partial t} = \phi(x,t)_t = v(\phi(x,t))|\nabla\phi(x,t)|, \tag{5.8}$$

where v is the velocity of the flow or speed function that contains the local segmentation and contour regularization constraints. This equation corresponds to the general formulation of the AC segmentation models. We saw in Chapter 3 that v can be designed intuitively (PDE-based approach) or derived from the following energy functional (variational-energy approach)[*]:

$$E = \int_{\Omega} F(\phi(x), \nabla\phi(x), x) d\Omega. \tag{5.9}$$

By solving the Euler-Lagrange equation linked to this functional with the gradient descent method we get the following PDE :

$$\frac{\partial\phi}{\partial t} = \pm(\frac{\partial F}{\partial\phi} - \nabla\frac{\partial F}{\partial\nabla\phi}). \tag{5.10}$$

This equation is equivalent to the general formulation (5.8).

In the formulation (5.8), the evolution of the level sets is described in a more intuitively way than in (5.10). This equation shows that the level sets evolve along their respective normal with a speed v. The direction of this displacement is depending on the local polarity information of the signed distance function. With the level set function described in (5.1), the motion generated by $|\nabla\phi_d(x,t)|$ goes always inside the contours. Thus, contour points move in if $v(x) > 0$ (Figure 5.1(a)) and out if $v(x) < 0$ (Figure 5.1(b)).

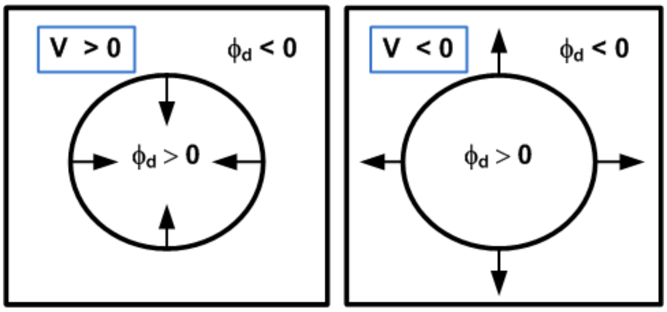

(a) (b)

Figure 5.1: In the AC framework, the direction of the active contour motion relies on the polarity information contained in the contour representation.

We present below two ways to derive the formulation (5.7) from (5.8). The first method is based on the optical flow approach (PDE approach) and the second one on a variational approach. First, we derive the formulation linked to the signed distance function representation ϕ_d. Then, we describe how to adapt the obtained evolution equation to the label function representation ϕ_L.

5.3.1 Signed Distance Function Model

Formulation derived from the Optical Flow

In this section, the desired formulation (5.7) is derived from the tracking of the signed distance function motion with the optical flow approach. This method assumes that the brightness of the moving

---

[*] The advantage of the variational-energy approach is that it permits to define an unified framework for an interpretation global of a processus in image processing as the image segmentation. The advantage of the PDE-based approach is that it offers more flexibity to solve segmentation problems because it allows more liberty in the choice of the terms composing the speed function.

image, here the isophotes of the level set function $\phi_d(x,t)$, stays constant for small displacements and a short period of time:

$$\phi_d(x,t) = \phi_d(x+du, t+dt) \Rightarrow d\phi_d(x,t) = 0, \tag{5.11}$$

where du is the instantaneous deformation vector field and $d\phi_d$ is the total derivative of ϕ_d.

By using the chain rule, the optical flow constraint (5.11) can be rewritten as:

$$\bigtriangledown \phi_d \frac{\partial u(x,t)}{\partial t} + \frac{\partial \phi_d}{\partial t} = 0. \tag{5.12}$$

As a result, we get the evolution equation of the vector flow from (5.12):

$$\frac{\partial u(x,t)}{\partial t} = -\frac{\phi_{d,t}}{\bigtriangledown \phi_d} = -\frac{\phi_{d,t}}{|\bigtriangledown \phi_d|}\frac{\bigtriangledown \phi_d}{|\bigtriangledown \phi_d|}, \tag{5.13}$$

where $\phi_{d,t}$, given by Equation (5.8), represents the variation of the level set function according to the desired constraints such as supervised segmentation, shape prior knowledge or contour regularization. Thus, by introducing the evolution equation of the level set segmentation model (5.8) with $\phi = \phi_d$ in (5.13), we obtain the following formula *merging the active contour segmentation framework with the image registration task*:

$$\frac{\partial u(x,t)}{\partial t} = -v(\phi_d(x,t))\mathcal{N}, \tag{5.14}$$

where $\mathcal{N} = \frac{\bigtriangledown \phi_d}{|\bigtriangledown \phi_d|}$ represents the unit normal vector of the level sets. Note that Equation (5.14) generates deformations radial to the active contours as Equation (5.8) generates radial active contour motion.

To evolve the level set function ϕ_d, we do not use the finite difference equation (5.3). Its position at time t is given by the deformation field $u(x,t)$ and the initial level set function $\phi_d(x,0)$ such that:

$$\phi_d(x,t) = \phi_d(x + u(x,t), 0), \tag{5.15}$$

with $\phi_d(x,0)$ is the initial active contours position. This ensures that the evolution of the level set function exactly corresponds to the current deformation.

Introducing Equation (5.15) in (5.14) yields to:

$$\frac{\partial u(x,t)}{\partial t} = -v(\phi_d(x+u(x,t),0))\frac{\bigtriangledown \phi_d(x+u(x,t),0)}{|\bigtriangledown \phi_d(x+u(x,t),0)|}, \tag{5.16}$$

This equation corresponds to *the general formulation of our active-contour registration model.* It defines a displacement vector (or force) at each point of the level set function where its gradient is not null. A large variety of segmentation/registration models can be derived from this formulation by using different speed functions or level set representation. Figure 5.2 shows the models that will be presented in this thesis.

Note that Equation (5.16) is very close to the evolution equation of the parametric AC models (see Chapter 3):

$$\frac{\partial C(q,t)}{\partial t} = -v(C(q,t))\mathcal{N}, \tag{5.17}$$

where $C(q)$ is the curve parameterized by q. But in 5.16 the computation of the forces is not done at control points but on a level set function. We will see in Section 5.4 that some forces can be computed on the whole level set function and others can only be computed on the level of interest (active contour position).

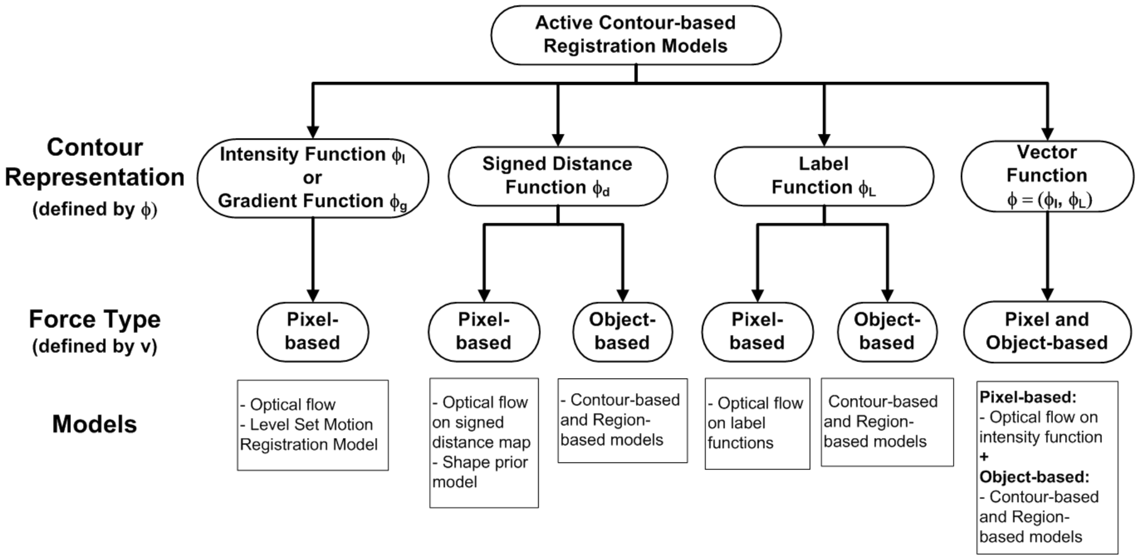

Figure 5.2: Classification of the active-contour registration models according to the contour representations ϕ_I (the intensity function), ϕ_g (the gradient function), ϕ_d (the distance function) and ϕ_L (the label function).

To stabilize the numerical computation when $\bigtriangledown\phi_d$ is close to zero, Equation (5.16) is modified as follows:

$$\frac{\partial u(x,t)}{\partial t} = -v(\phi_d(x+u(x,t),0))\frac{\bigtriangledown\phi_d(x+u(x,t),0)}{\sqrt{\bigtriangledown\phi_d(x+u(x,t),0)^2+\epsilon^2}}, \tag{5.18}$$

where ϵ is a small positive constant. This equation makes the level sets move along their respective normal with a speed v. In (5.18), we find again the dependance between the contour motion and the polarity information of the representation. With the level set function described in (5.1), a contour point move out if $v > 0$ and in if $v < 0$.

Note that the formulation of our active contour-based registration model has the same form of the evolution equation of the "level set motion registration algorithm" proposed by Vemuri et al. in [168] (see Chapter 4):

$$\frac{\partial u(x,t)}{\partial t} = v(\phi_I(x,t))\frac{\nabla G_\sigma * \phi_I(x,t)}{\sqrt{\nabla G_\sigma * \phi_I(x,t)^2+\epsilon^2}}, \tag{5.19}$$

with

$$\phi_I(x,t) = \phi_I(x+u(x,t),0), \tag{5.20}$$

and

$$v(\phi_I(x,t)) = \phi_{I,T}(x,t) - \phi_I(x,t), \tag{5.21}$$

where ϕ_I is the intensity function of the image to register.

The difference is that in our model, by keeping the original level set representation (the signed distance function ϕ_d) instead of using the image intensity function ϕ_I, we can directly use all the speed function v coming from the AC framework. As already mentioned for the Vemuri's model [168], the existence and the uniqueness of the result for PDEs of this type is difficult to prove.

Formulation derived from an Energy

We notice here that the deformation field variation $\frac{\partial u}{\partial t}$ can also be derived from the following general energy:

$$E = \int_{\Omega} F(\phi_d(u), \nabla\phi_d(u), u) d\Omega. \tag{5.22}$$

By solving the Euler-Lagrange equation linked to this functional with the gradient descent method, we get the following PDE:

$$\frac{\partial u(x,t)}{\partial t} = -\frac{\partial F}{\partial u} = -(\frac{\partial F}{\partial \phi_d} - \nabla \frac{\partial F}{\partial \nabla \phi_d})\nabla\phi_d. \tag{5.23}$$

We note that the formulation obtained with the optical flow method differs from the one obtained with the variational method by a factor of $| \bigtriangledown \phi|^2$. However both equations are mathematically equivalent. This is due to the fact that we do not change the steady state solution of a PDE by multiplying it with a positive function.

- Example with a first-order Energy:

$$E(u) = \int F(\phi_d(x+u)) d\Omega. \tag{5.24}$$

The PDE corresponding to this functional is:

$$\frac{\partial u}{\partial t} = -\frac{\partial F}{\partial u}. \tag{5.25}$$

If we have,

$$F = v(\phi_d(x+u)) = (\phi_d(x+u) - \phi_{d,0})^2. \tag{5.26}$$

where $\phi_{d,0}$ is a signed distance function of reference (see Section 5.4.2).

Then,

$$\frac{\partial F}{\partial u} = 2(\phi_d(x+u) - \phi_{d,0})\frac{\partial \phi_d}{\partial u}. \tag{5.27}$$

Note that,

$$\frac{\partial \phi_d}{\partial u} = \nabla\phi_d. \tag{5.28}$$

By combining combining Equations (5.29) with (5.26) and (5.28), we obtain the following evolution equation *:

$$\frac{\partial u}{\partial t} = -2(\phi_d(x+u) - \phi_{d,0})\nabla\phi_d. \tag{5.29}$$

5.3.2 Label Function Model

Formulation derived from the Optical Flow

In this Section, we show how to adapt the evolution equation derived from the signed distance function representation to the label function representation. We will see that this necessitates to add two constraints on the gradient computation. The resulting model was published in [63].

In the ϕ_L representation, the modeled contour does not correspond anymore to the zero level set but to the interface between two labeled regions. As ϕ_L is not a continuous function across its borders, we have to convolve it with a Gaussian kernel G_σ prior to the gradient computation.

---

[*] This evolution equation generates the Pixel-based registration forces presented in Section 5.4.2.

The AC region-based forces need that the gradient computed on both sides of the interfaces of ϕ_L indicates the polarity of the current region. Figures 5.3(a) and 5.3(b) show the gradient direction of the distance function representation with the two possible sign convention (sign + or - inside the modeled contour). The gradient direction is the same on both sides of the zero level set. The idea with the label function representation is to constraint the gradient to always indicates the outside of a given region. The gradient direction is thus opposite on both sides of each interfaces (Figure 5.3(c)).

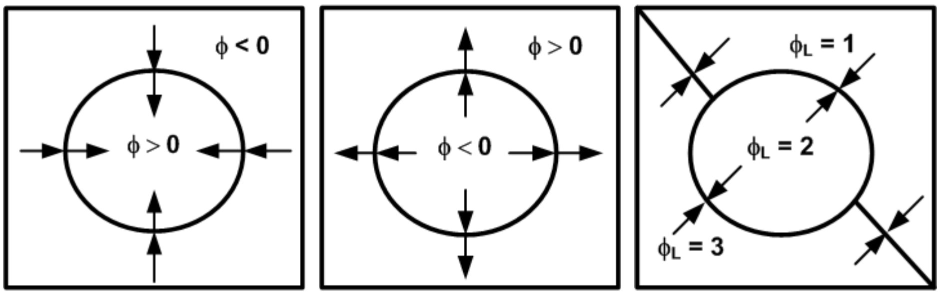

(a) (b) (c)

Figure 5.3: Gradient direction. a) and b) Distance function representation with the two different sign convention. c) Label function representation.

We have defined the following function S to determine the desired gradient direction based on the surrounding label values:

$$S(x) = \begin{cases} +1 & \text{if } \max_i \phi_L(x+x_i) > \phi_L(x) \\ -1 & \text{if } \min_i \phi_L(x+x_i) < \phi_L(x) \\ 0 & \textit{otherwise}, \end{cases} \tag{5.30}$$

where $x + x_i$, $i \in [1, 8]$ correspond to the 8-connected neighbors of pixel x. $\max_i \phi_L(x + x_i)$ and $\min_i \phi_L(x + x_i)$ are respectively the maximum and minimum values of function ϕ_L among the 8 neighbors of x. Figure 5.4 illustrates the function S. The green line enhances the interface between the light and dark regions. Each panel shows the current pixel (enhanced in bold) surrounding by its 8 neighbors. The arrow shows the initial direction of the gradient. If neighbors have values larger or equal to $\phi_L(x)$, the gradient is already in the right direction so $S(x) = 1$ (Figure 5.4(a)). If one neighbor has a value inferior to $\phi_L(x)$, the gradient direction will be change with $S(x) = -1$ (Figure 5.4(b)). Finally if the neighborhood has the same value of $\phi_L(x)$, the gradient is null which means $S(x) = 0$ (Figure 5.4(c)).

Thus, $\phi_d(x)$ is replaced by $\phi_L(x)$ in Equation (5.18) and the two constraints on the gradient are added such that we obtain the following evolution equation:

$$\begin{aligned} \frac{\partial u(x,t)}{\partial t} &= -S(x)v(\phi_L(x+u(x,t),0)) \cdot \\ & \qquad \frac{\nabla G_\sigma * \phi_L(x+u(x,t),0)}{\sqrt{\nabla G_\sigma * \phi_L(x+u(x,t),0)^2 + \epsilon^2}}, \end{aligned} \tag{5.31}$$

where v is the speed function given by an AC segmentation model.

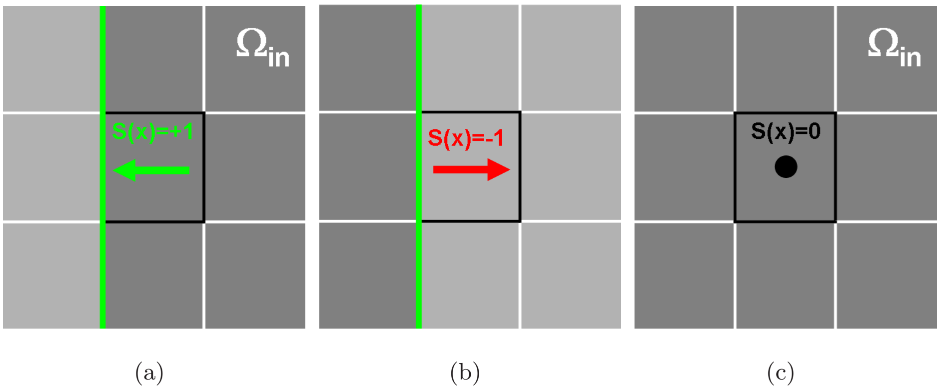

Figure 5.4: Illustration of the function S. a) $S(x) = 1$: Gradient is in the right direction. b) $S(x) = -1$: Gradient direction has to be changed. c) $S(x) = 0$: Gradient is null.

5.4 Driving Forces

In this section, we present the different types of forces of the AC segmentation framework and indicate with which type of contour representation they can be used.

We saw in the snake model (Chapiter 3) that active contour segmentation models are derived from the linear combination of two types of energy: the internal and the external energy. The internal energy E_{int} introduces regularization terms v_{reg} in the evolution equation. These terms generate forces that preserve the smoothness and the regularity of the active contour. The external energy E_{ext} introduces attractive terms v_{att} in the evolution equation. These terms generate forces that attract the active contour to the boundaries of the target object. We saw that these attractive terms can be boundary-based or region-based. Thus the segmentation by active contours corresponds to the steady state solution of the following energy minimization problem:

$$\underset{\phi}{min} E(\phi) = \alpha E_{int}(\phi) + \beta E_{ext}(\phi), \tag{5.32}$$

where α and β are positive constants weighting both energies.

Our active-contour-based registration model minimizes this energy functional with the following evolution equation:

$$\frac{\partial u(x,t)}{\partial t} = -\frac{(\alpha\phi_{reg,t} + \beta\phi_{att,t})}{|\bigtriangledown \phi|} \frac{\bigtriangledown \phi}{|\bigtriangledown \phi|} = -(\alpha v_{reg}(\phi) + \beta v_{att}(\phi))\frac{\bigtriangledown \phi}{|\bigtriangledown \phi|}, \tag{5.33}$$

where $\phi_{reg,t}$ is the level set variation coming from the internal energy and $\phi_{att,t}$ is the level set variation coming from the external energy. This equation is derived from the general formulation of our model (5.16).

In the following subsections we present the families of forces that belong to these two categories. Figure 5.5 summarizes this classification.

5.4.1 Regularization Forces

The most used regularization forces are the mean curvature forces. These forces smooth the level sets by minimizing their length. They are derived from the well-known Total Variation functional:

$$E_{reg}(\phi) = \int_{\Omega} |\nabla \phi| dx. \tag{5.34}$$

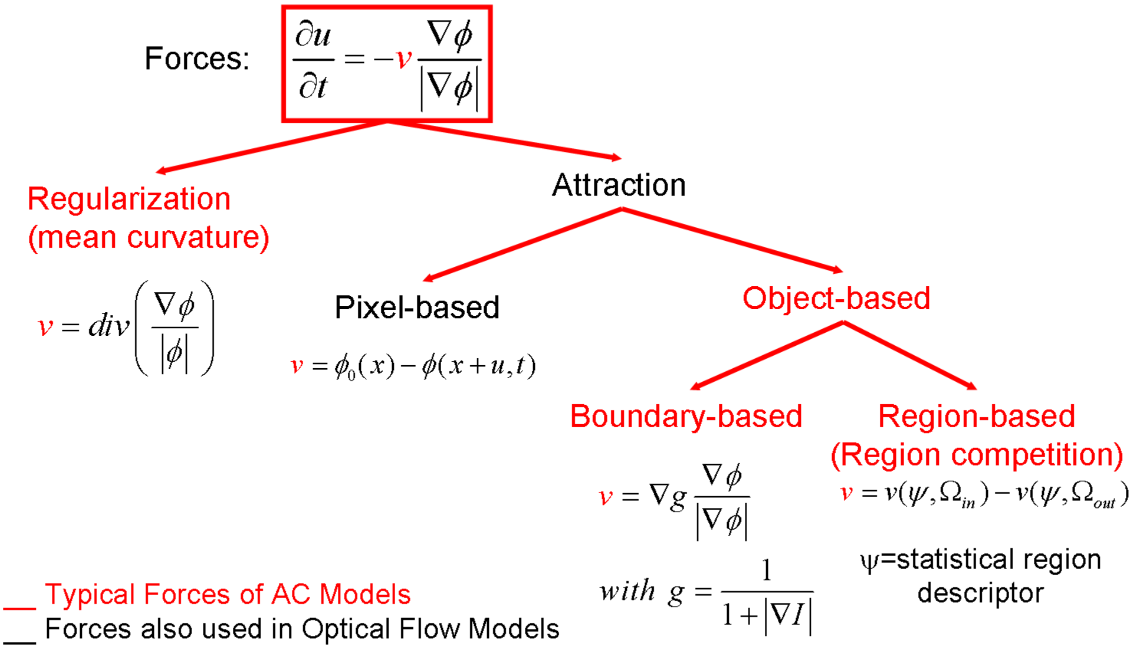

Figure 5.5: Classification of the AC forces according to their effect in a registration process.

The corresponding level set variation is:

$$\phi_t = \kappa|\nabla\phi|, \tag{5.35}$$

where κ is the curvature of the level sets defined by:

$$\kappa = \nabla\cdot(\frac{\nabla\phi}{|\nabla\phi|}). \tag{5.36}$$

These forces can be applied on any types of contour representation. For example we saw in Chapter 3 that the Mumford-Shah Model [128, 129] uses them on the intensity function representation and that the large majority of the active contour models apply them on the signed distance function representation [135].

5.4.2 Pixel-based Forces

These forces permit the local registration of the whole moving image domain or of selected regions. They are based on the smallest image feature, the pixel. This type of force is used to minimize the difference between the current level set function $\phi(x,t)$ and a level set function of reference $\phi_0(x)$. They are derived from the following energy:

$$E_{matching} = \int_\Omega (\phi_0(x) - \phi(x,t))^2 dx, \tag{5.37}$$

and this energy leads to the following level set variation:

$$\phi_t = (\phi_0(x) - \phi(x,t))|\nabla\phi|. \tag{5.38}$$

We note that the pixel-based forces are null when the active contours reach their target contours, i.e. when $\phi(x,t) = \phi_0(x)$.

Pixel-based forces are used in AC models but also in PDE-based registration models. In AC model, these forces permit to include intensity or shape prior knowledge in a segmentation process. For intensity prior knowledge, ϕ corresponds to the intensity function ϕ_I. For shape prior knowledge, ϕ corresponds to the signed distance function ϕ_d or to the gradient function $\nabla\phi_I$. In PDE-based registration models, these forces are used to match a source image to a target image. In these models, the level set function corresponds most often to the intensity function ϕ_I ([166], [168]) but we can find some algorithms that use ϕ_I simultaneously with the gradient function $\phi_g = \nabla\phi_I$ ([27], [7]).

The advantage of the pixel-based forces is they can match any type of contours (close or open) and can be used with any type of representation. However they are very sensitive to noise and are limited to recover small deformations.

5.4.3 Object-based Forces

These forces permit the global non rigid registration of regions or objects selected in the moving image by the level set function. There exist two types of object-based forces: the boundary-based and the region-based forces.

Boundary-Based Forces

These attraction forces are linked to the minimization of the following functional:

$$E_{bAtt}(\phi) = \int_{\Omega} g(I)|\nabla\phi|dx, \tag{5.39}$$

where ϕ is the implicit model of the curve, I is the image to segment and g is any general edge detector function. This functional means that the Euclidean length of the isophotes of ϕ is weighted by g, which contains information regarding the boundary of the objects lying in the given image.

Equation (5.39) leads to the following level set variation:

$$\phi_t = (v_{reg} + v_{att})|\nabla\phi| = g(I)\kappa + \nabla g(I) \cdot \nabla\phi. \tag{5.40}$$

In the first term, we recognize the curvature regularization term but weighted by $g(I)$. The second term is the advection term also depending on $g(I)$. $g(I)$ acts as a stopping function. Its goal is to stop the evolving curve when it reaches the object boundaries.

In [33], the authors choose:

$$g = \frac{1}{1 + |\nabla\hat{I}|}, \tag{5.41}$$

where $\hat{I}$ is a smoothed version of I, in order to remove noise. The term $|\nabla\hat{I}|$ is essentially zero except where the image gradient changes rapidly. In this case its value becomes large. This function g is close to unity away from boundaries, and drops to zero near sharp changes in the gradient image. The boundary-based forces assume that these changes correspond to the edges of the desired object to delineate.

Boundary-based forces have the following characteristics:

- It smooths the active contour. This smoothing is more important in homogenous area than on image contours.
- The contours of ϕ are attracted to the closest contours of I only in the area where $|\nabla\hat{I}| \neq 0$. The contour-based forces are often combined with the following balloon force in order to make the active contour move in homogenous area.

$$\phi_t = c|\nabla\phi| \tag{5.42}$$

where c is a constant. The sign of this constant will determine the direction of the active contour evolution. This term needs thus that the initial active contour is completely inside or outside of the object to segment.

Boundary-based forces present the following limitations:

- All the contours of ϕ located in a area where $|\nabla \hat{I}| \neq 0$ will be attracted to the closest contour of I. This means that if we apply this force on each point of the signed distance function ϕ_d every level set will collapse to their closest contour in I as shown in Figure 5.6. Thus to use it in registration, this force has to be computed only on the level set of interest, i.e. on the zero level set or on the interface between two labeled regions.

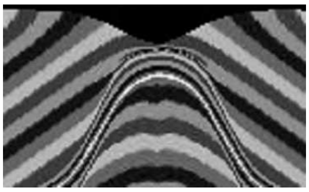

Figure 5.6: If we apply the boundary-based force on each point of the signed distance function, every level set will collapse to the closest target contour in the target image.

- These forces are only based on information extracted in the image to segment. Thus they can not exploit prior knowledge coming from a prior image expect the shape prior given by the initial position of the active contour.
- As this attraction force is based on local image gradient, it is thus very sensitive to noise.

In summary, contour-based forces can not be computed with the intensity function if this function contains many contours that can collapse to the same target contour. They can be used with the a signed or unsigned distance map function or a label function because these representations permits to select contours of interest. However for the distance function, they have to be computed on the zero level set only.

Region-based Forces

In this section, we study the attraction force of the region-based active contour models. We saw in Chapter 3 that these forces are no null at convergence. The steady state solution is found by region competition, i.e. by the balance between the force computed from the region inside the contour and the force computed from the region outside the contour:

$$v(x) = v_{in}(x) - v_{out}(x). \tag{5.43}$$

Region-based forces are the most used attractive forces of the AC framework because they are much less sensitive to noise than the boundary-based forces. Also they can perform supervised segmentation, i.e. they can use prior knowledge extracted from a reference image.

Below we describe two supervised forces we have designed for our model.

1. **Prior Mean-Based Forces** These prior mean-based forces are inspired by the first type of region-based segmentation model proposed by Chan et al. [35]. The design of these forces is quite simple but we show in Chapter 7 that they can be used successfully in a large number of applications.

The prior mean-based forces are derived from the following energy designed to be minimal when the mean of a region Ω defined in the target image by the evolving level set function is close to the mean of the corresponding region in the reference image:

$$E = \int_{\Omega_{in}} |I(x) - \mu_{in,prior}|^2 dx - \int_{\Omega_{out}} |I(x) - \mu_{out,prior}|^2 dx, \tag{5.44}$$

where μ_{prior} is the prior mean of a given region extracted from a reference image (the atlas) and I is the intensity function of the image to segment.

The derivation of functional (5.44) leads to the following level set variation:

$$\phi_t(x) = ((I(x) - \mu_{in,prior})^2 - (I(x) - \mu_{out,prior})^2)|\nabla\phi|. \tag{5.45}$$

This term assumes that corresponding regions between the reference and the target images have similar means. Note that μ_{prior} does not evolve during the registration process. Hence it is computed once on the reference image in a pre-process step. This substantially reduces the computation complexity making this model fast.

Note that the computation of this type of force is very close to the pixel-based forces expect that they do not compare the pixel values of the image to segment to the pixel values of the reference image but to the mean of regions defined in the reference image by the active contours. Moreover the region competition perform a local classification by evaluating to which region mean a pixel value is the closest.

2. **Prior Entropy-Based Forces** The prior entropy-based forces are inspired by the region-based segmentation model proposed by Herbulot et al. in [87]. They are based on the following energy designed to be minimal when the entropy of a region Ω defined in the target image by the evolving level set function is close to the entropy of the corresponding region in the reference image:

$$E(\Omega) = \frac{1}{|\Omega_{in}|} \int_{\Omega_{in}} -ln(q_{prior,in}(I(x), \Omega_{in}))dx - \frac{1}{|\Omega_{out}|} \int_{\Omega_{out}} -ln(q_{prior,out}(I(x), \Omega_{out}))dx, \tag{5.46}$$

where q_{prior} is the prior density distribution of a given region extracted from the reference image and I is the intensity function of the target image.

This term also assumes that corresponding regions between the reference and target images have similar intensity distributions and q_{prior} is computed once on the reference image in a pre-process step.

The pdf of a given region in the reference image is estimated using the Parzen windows method [141]:

$$p(\alpha, \Omega) = \frac{1}{|\Omega|} \int_{\Omega} G_\sigma(\alpha - I(x))dx, \tag{5.47}$$

where G is a Gaussian kernel with 0-mean and σ^2 variance.

The derivation of functional (5.46) leads to the following level set variation:

$$\begin{aligned} \phi_t(x) \quad &= \quad \frac{1}{|\Omega_{in}|}(ln(q_{prior,in}(I(x), \Omega))) \\ &\quad -\frac{1}{|\Omega_{out}|}(ln(q_{prior,out}(I(x), \Omega)))|\nabla\phi|. \end{aligned} \tag{5.48}$$

In fact this evolution equation classifies the image pixels following their probability to belong to the inside or the outside region. In [138], Paragios et al. have presented a similar supervised

AC segmentation model but directly deduced from the posteriori density function $q(\Omega_i|I(x))$ describing the membership of a pixel to a particular region Ω_i following its intensity $I(x)$. The difference is that in our model each term is weighted by the volume $|\Omega|$ of each region. This permits to give the advantage to the smallest region when the membership of a pixel is similar for both regions.

We have published this force and other types of supervised forces based on information theory in [64]. The design of these forces as well as the posteriori density function-based model of Paragios are presented in detail in Chapter 6.

General Notes on Object-based Forces

With the object-based forces, when an active contour reaches its target, the forces computed around the target contour are not zero but reversed. This is not a problem in a segmentation application because the final active contour position is given by the balance between these two opposite forces. On the other end, this is a limitation for a registration application. Indeed, we saw that object-based forces can be computed only on the interface. To get a dense deformation field, they have to be propagated on the whole image. Thus even if the active contour has reach its target, the propagation of the interface forces will continue to deform the rest of the images because they are not null. We need thus to detect when an active contour point reach a target contour point in order to cancel the corresponding interface force. For that, we propose to compute the interface force $v(x)$ on each radial side of the level set of interest. If both forces have opposite signs, $v(x)$ is set to zero:

$$\text{if } sign(v_+(.) \cdot v_-(.)) \leq 0 \text{ then } v(x) = 0, \tag{5.49}$$

where $v_-(.)$ and $v_+(.)$ are the forces computed on both sides of the level set of interest and $sign(.)$ is the sign function.

5.5 Multiscale Approaches

We describe below the two types of multiscale approach we have included in our model.

5.5.1 The Spatial Multiresolution Approach

We have already presented this approach in Chapters 2 and 3. We just remind here its basic idea. This method consists to register the atlas on a coarse to fine resolution pyramid of the images. The deformation field obtained at one resolution is extrapolated and used as initial solution for the next resolution. This technique permits first to reduce the required computational cost of the algorithm and then to decrease the risk of convergence to a local minima.

5.5.2 The Hierarchical Approach

The non rigid registration of the atlas is also performed following a hierarchical approach. We have published the hierarchical atlas concept in [91]. Figure 5.7 illustrates the registration process integrating this approach.

To register two images, we generally begin to align them globally with a parametric registration algorithm. This first step permits with a few degrees of freedom to put both images in the same position and thus to bring their corresponding contours closer. Then, a registration algorithm according much more degrees of freedom to its transformation is used to recover the variability between these corresponding contours. The hierarchical approach we propose permit to perform this second step progressively by limiting the number of objects to register in the atlas. The first layer of the hierarchy contains a subset of the atlas with the biggest and the more contrasted object contours. The resulting deformation field is then used as initial condition for the registration of the next layer including the contours of the first layer (in order to keep a constraint on their registration) and the contours of smaller objects with the condition that they are well superposed to their target. Finally the hierarchical registration end up with the registration of the smallest objects we can find in an image, the pixels. To register the contours of the first two layers, well-suited forces are the region-based forces because they can register selected regions and recover large displacements. Pixel-based forces are used for the local registration of the last layer. Pixel-based forces can be computed on the whole image domain if the atlas is consistent with the target image or if not on particular regions selected by a label function. The goal is that the registration of the objects of one hierarchical layer helps the segmentation of the objects of the next ones as in the usual process the global registration helps the local registration. While the contours of the objects concerned by the current layer are registered, the atlas contours of the objects defined in the next layers of the hierarchy are brought closer to their target contours. In medical images registration, particularly on 3D images, the experminents have confirmed the logical fact that the more rigid structures (like the bones) have to be registered first because their position determines the position of softer structures (like the tissues or the fluids). Figure 5.8 illustrates an example of geometrical features pyramid for the registration of neck CT images. It begins by the registration of the bones (the jaw and the vertebra) by region-based forces. Then the external contour of the neck and the trachea are also registered by region-based forces. Finally all the rest of the geometrical features of the image are registered by pixel-based forces.

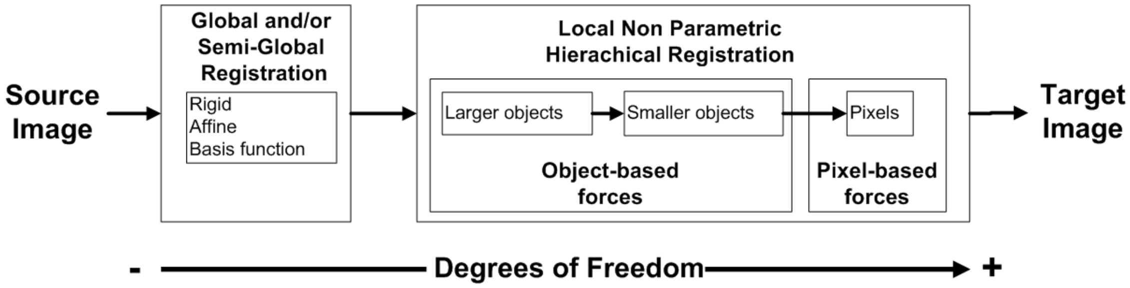

Figure 5.7: Registration process including the hierarchical approach.

5.6 Deformation Field Propagation

In this section, we describe the methods we have designed to propagate the explicit deformation of the active contours to the whole image domain.

5.6.1 Distance Function Methods

We propose below two methods based on the signed distance function representation.

Pixel-based Model

This method consists first to segment manually or automatically corresponding objects in the source and target images. In this thesis, we have used as automatic methods, active contour segmenta-

(a) (b) (c)

Figure 5.8: Geometrical features pyramid of a CT neck image. The registration is performed by increasing progressively the number of objects to match, from the more rigid structures to the softest: a) bones (jaw and vertebra) globally registered by region-based forces, b) bones, external contour of the neck and trachea globally registered by region-based forces, d) all the geometrical features of the image locally registered by pixel-based forces.

tion models and morphological operations. Then these segmented objects are registered and the deformation of their contours are propagated on the whole image by solving the following evolution equation:

$$\frac{\partial u(x,t)}{\partial t} = -(\phi_{d,T}(x) - \phi_{d,S}(x+u(x,t),t)) \frac{\nabla \phi_{d,S}(x+u(x,t),0)}{|\nabla \phi_{d,S}(x+u(x,t),0)|}. \tag{5.50}$$

This evolution equation is a particular solution of our general registration model (Equation (5.33)) with the signed distance function representation and the pixel-based forces. $\phi_{d,S}$ models the source objects and $\phi_{d,T}$ models the target objects. Due to the nature of the signed distance function representation, we assume that the modeled objects are disconnected. As initial condition we have $\phi_{d,S}(x,0) = \phi_{d,S}(x)$.

Figure 5.9 presents an example. Figures 5.9(a) and 7.22b) respectively show the segmentation of the source and target images. The objects on these images represent a sad and a happy face. The objective is to register the sad face to the happy face. Figures 5.9(c) and 5.9(d) are the signed distance functions corresponding to these images. Figure 5.9(e) shows the direction of the vector flow estimated by the normalized gradient of $\phi_d(x,t)$. Figure 5.9(f) shows the magnitude of the displacement estimated by the difference between the two signed distance functions $\phi_{d,T}(x)$ and $\phi_d(x,t)$ computed at each image point. The white areas correspond to extension motions, black areas to contraction motions and gray uniform areas to areas without motion. The extracted deformation field is globally quite smooth (see Figure 5.9(g)). This is due to the fact that the displacement generated by the active contours is perpendicular to these contours due to the gradient direction (see Figure 5.9(e)). Therefore, discontinuities appear on the skeleton of the image where two fronts reach themselves. Inspired by the optical flow regularization, a Gaussian filtering is applied on the deformation field at the end of each iteration. This permits to remove discontinuities while propagating the correction to the whole image (see Figure 5.9(h)). The Gaussian filtering necessitates to set a parameter σ. This parameter permits to limit the maximal elasticity of the deformation. During its evolution, $\phi_{d,S}$ deformed by u lost progressively its distance function property. The reinitialization of this function at each iteration permits to get a faster and more accurate convergence. Except the reinitialization coming from the AC framework, this model corresponds in fact to the optical flow approach applied on signed distance maps. In [140], Paragios et al. have also proposed to use the signed distance function representation in the non rigid registration of 2D geometric shapes. The difference with our work is that they optimize global transformations parameters simultaneously to the non rigid deformation and their deformation is only computed on a narrowband on the objects contour. It is not propagated on the whole image as in our approach.

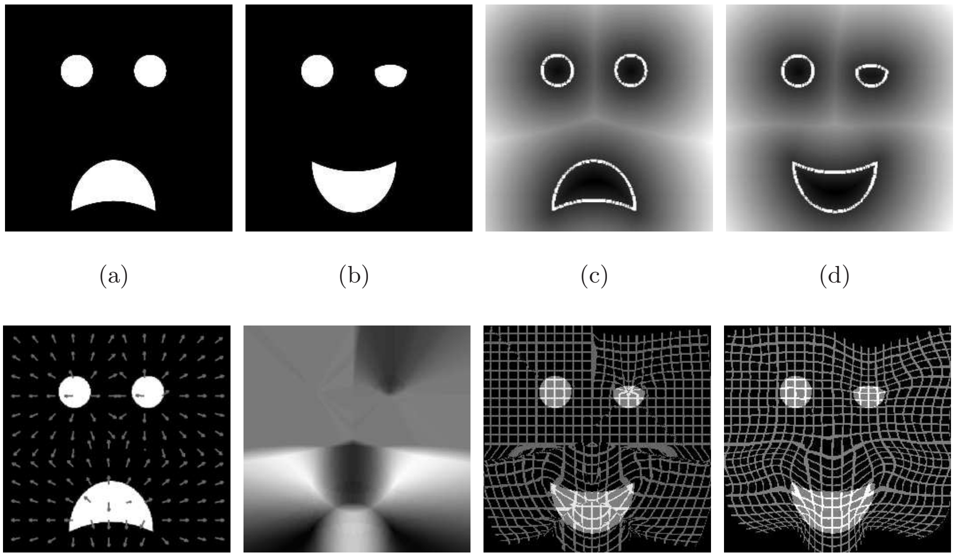

(a) (b) (c) (d)

(e) (f) (g) (h)

Figure 5.9: Deformation field extraction process on 2D synthetic data: (a) and (b) are the source and target binary images, (c) and (d) are their corresponding level set functions, (e) is the difference between the target level set function and the moving level set function (magnitude of the displacement), (f) is the normalized gradient computed on the moving level set function (direction of the displacement), (g) is the grid deformation without gaussian regularization, and (h) is the grid deformation with a gaussian regularization.

This registration model permits to match a contour modeled by $\phi_{d,S}(x,t)$ to its closest contour in $\phi_{d,T}(x)$. Thus, for the case of face matching presented above, the method does not put in correspondence the two corners of the mouth. To constraint particular points to match, a possible solution would be to use a second couple of signed distance functions $\phi_{d,PS}(x)$ and $\phi_{d,PT}(x)$ that just model these points. $\phi_{d,PS}(x)$ models the points in the source image and $\phi_{d,PT}(x)$ models the points in the target image. Of course, this method assumes that corresponding points between these two new distance functions are closer than other points. This leads to the following evolution equation[*]:

$$\frac{\partial u(x,t)}{\partial t} = -\frac{d2}{1+d2} d1 \mathcal{N}_1 - \frac{1}{1+d2} d2 \mathcal{N}_2, \tag{5.51}$$

where $\mathcal{N}_1 = \frac{\nabla \phi_{d,S}(x+u(x,t),0)}{|\nabla \phi_{d,S}(x+u(x,t),0)|}$ and $\mathcal{N}_2 = \frac{\nabla \phi_{d,PS}(x+u(x,t),0)}{|\nabla \phi_{d,PS}(x+u(x,t),0)|}$ are the normals of both moving distance functions. In the first term, $d1 = (\phi_{d,T}(x) - \phi_{d,S}(x+u(x,t),t))$ corresponds to the difference between the two distance functions modeling the objects contours. In the second term, $d2 = (\phi_{d,PT}(x) - \phi_{d,PS}(x+u(x,t),t))$ is the difference between the two distance functions modeling the corresponding points. The two fractions weight the contribution of both terms. Note that they give more importance to the second term near the points to match.

---

[*] I would like to thanks Dr Olivier Cuisinaire for the idea of this possible extension.

Different Types of Deformations

In this Section, we show that the pixel-based model can recover a large range of deformations. Most of these results were published in [61] and [62].

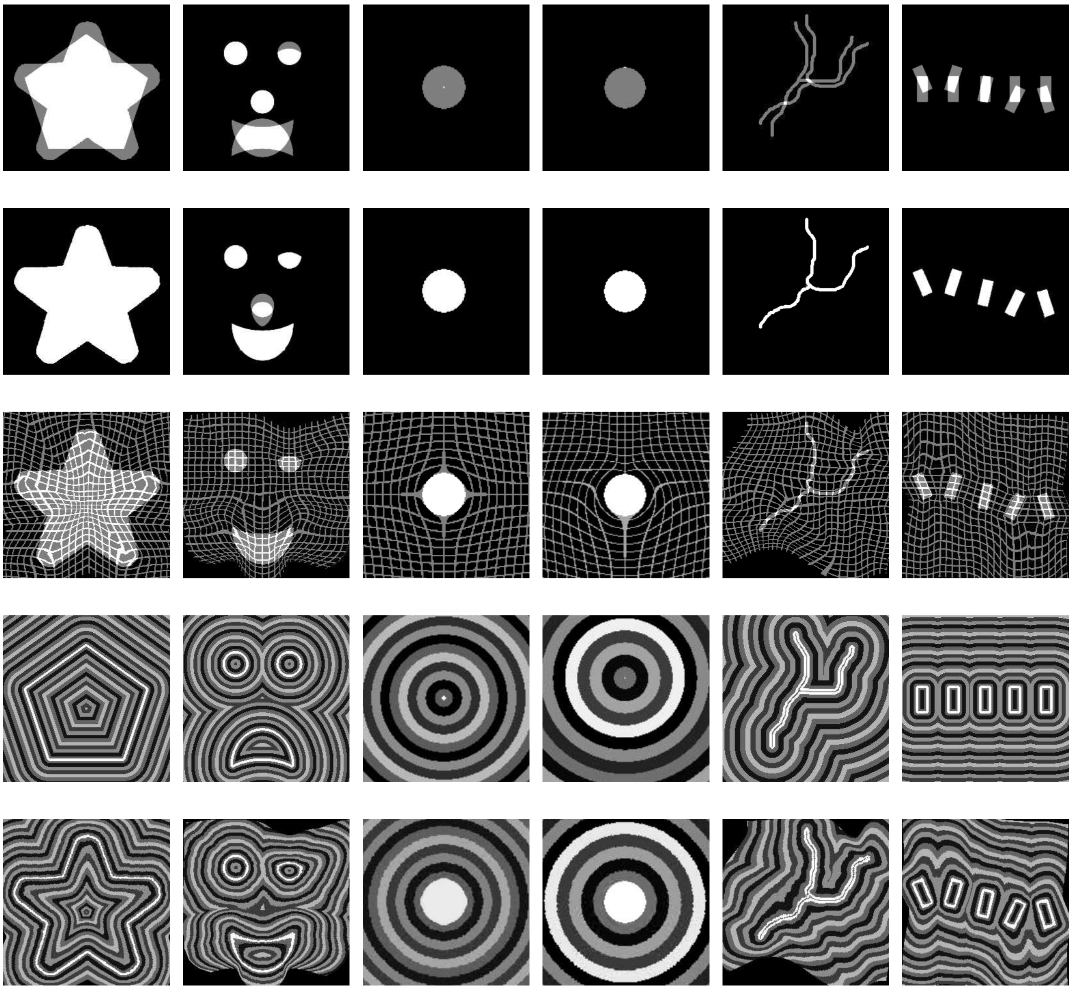

(z)

Figure 5.10: Deformation field extracted from different type of objects (closed contours, lines, points). Row (1): Initial difference. Row (2): Final difference. Row (3): Deformed regular grid. Row (4): Test image. Row (5): Deformed test image.

Figure 5.10 presents the non rigid registration results obtained on 2D synthetic images. The experiments consist to register mono-component and multi-components closed contours, to deform a point to a disc, to register lines and to recover rigid deformations. The registrations with point and lines represent new contributions. So far, in the AC framework, the distance function was always used to represent closed contours and neither points nor lines. At each column, row 1 shows the initial differences between the source and the target images (common sections are shown in white, regions that do not correspond are shown in gray). Row 2 shows these differences after having deformed the source image with the extracted non rigid transformation. Row 3 shows the transformation applied to a regular grid. Row 4 shows the modulo distance map of the source image (object contours are enhanced in white). Row 5 shows the test image of row 4 deformed with the computed transformation. The few gray regions of row 2 shows the accuracy of contour matching on 2D images. For the second case concerning face expressions, we note a difference on the nose. This registration was only based on the features defined by the eyes and the mouth. Thus, the nose of the source image has just followed the computed transformation. The deformed grid and the test image of rows 3 and 5 help in visualizing the regularity of the computed transformations. For the point matching experiment, the grid well shows the differences in the deformation when the point is placed in the center of the disc or on an extremity. In the first case, the deformation induced is radial with the same intensity in all direction. For the second case, the deformation is also radial but strongest at the opposite extremity of the disc and fades more we move away from this position.

These synthetic examples can be related to the particular applications in medical image registration illustrated in Figure 5.11. The first one corresponds to the registration of closed structures, the face matching experiment illustrates the estimation of non visible objects position from the local registration of visible objects, the point matching could model a tumor growth in an atlas, the lines matching could represent constraints on the registration of sulci, and the rigid objects matching could correspond to the registration of a spinal cord.

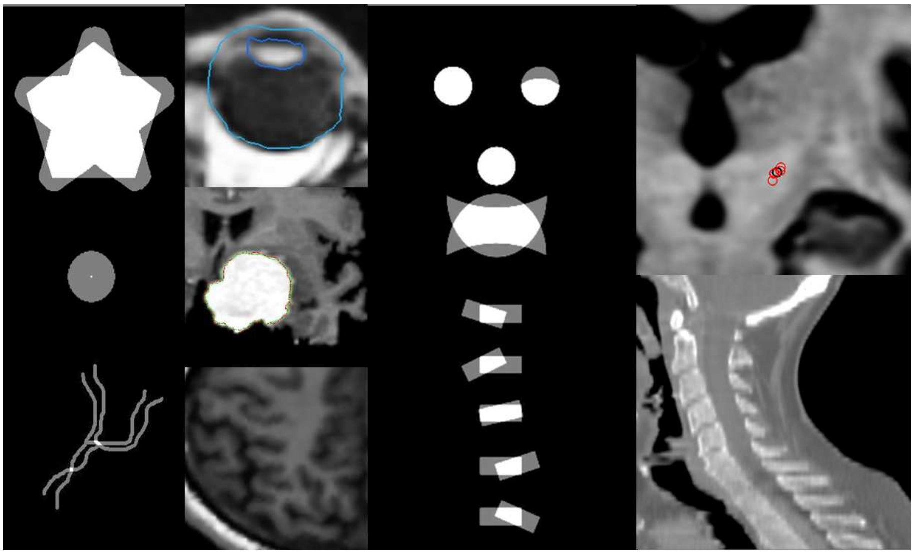

(a)

Figure 5.11: Related applications of the deformations shown in Figure 5.10 in medical image registration.

Object-based Model

In the previous method the segmentation of the objects of interest and their registration is performed in two steps. Here we propose a model also based on the signed distance function representation but which performs these two tasks jointly. The idea of this model is to compute contour-based or region-based forces on the zero level set and then to propagate the deformation to the whole image with the help of the signed distance function. In other words, we will track all the level sets of the level set function but the magnitude of the displacement (speed term value) corresponds to the one of the closest point on the zero level set.

In [83], Gomes et al. have demonstrated that when we apply an attraction term at each isophote of a signed distance function, all isphotes evolve toward the target contour to minimize their energy. This effect means that the level set function progressively lost its properties of signed distance map because the distance between two consecutive isophotes decreases when they reach the target contour. As we want that each point of the given image follow the displacement of the active contour, we have to employ a scheme to preserve the signed distance function during the evolution process.

A method often used in the active contour framework to maintain the level set function as close as possible to a distance map during its evolution, is to recompute it periodically from the current contour [41]. Unfortunately such reinitialization cannot be used in this object-based model. Indeed, with this method, only the zero level set stays at the same place. The position of all the other isophotes changes in order to respect the distance map property. Since here we are not only interested in the evolution of the zero level set, as in the standard active contour framework, but of all the isophotes, such sudden changes in the function would produce perturbations in their tracking. Moreover, this method does not prevent the isophotes from being attracted by the target contours. Thus, we need an approach that can be directly included in the evolution equation and that projects the displacement of the zero level set on the other levels.

In [83], Gomes and al. propose a method that fulfils this requirement perfectly. Their approach consists of introducing a new partial differential equation directly into the evolution equation to constrain the level set function to remain a distance map during its evolution. They demonstrate that the conservation of the signed distance map property, i.e. $|\nabla\phi_d(x)| = 1$, implies that the speed function v has to stay constant along the straight lines perpendicular to the isophotes. This leads to the following relation:

$$v(x) = v(x - \phi_d \bigtriangledown \phi). \tag{5.52}$$

By integrating the constraint (5.52) in the general evolution equation of our active contour model (5.18), we obtain the evolution equation of the object-based model using a distance-based interpolation:

$$\frac{\partial u(x,t)}{\partial t} = -v(x - \phi_d \bigtriangledown \phi)\frac{\bigtriangledown\phi_d(x + u(x,t), 0)}{\sqrt{\bigtriangledown\phi_d(x + u(x,t), 0)^2 + \epsilon^2}}. \tag{5.53}$$

To ensure that the isophotes of the level set function will stay well smooth during their evolution we add a mean curvature term to the evolution equation. However despite this regularization, discontinuities can occur where the gradient is not defined (on the skeleton of the level set function ϕ). These singularities result from the merger of two opposite displacement fronts. To obtain a well-smoothed deformation field overall, and thus avoiding discontinuities in the deformed image, we perform a local smoothing of the deformation field.

We proceed as follows. First, a mask of the skeleton is extracted from the level set function. For that, we use a method inspired by Gomes et al. in [83]. For 2D images, the method consists of forming the four possible estimators of $\nabla\phi$, $D^i\phi$ with $i = 1, .., 4$ namely:

$$\begin{aligned}
D^1\phi &= (D^{+x}\phi, D^{+y}\phi),\\
D^2\phi &= (D^{+x}\phi, D^{-y}\phi),\\
D^3\phi &= (D^{-x}\phi, D^{+y}\phi),\\
D^4\phi &= (D^{-x}\phi, D^{-y}\phi).
\end{aligned} \tag{5.54}$$

D^{+x} and D^{-x}, receptively D^{+y} and D^{-y}, are the forward and backward difference operators:

$$D^{+x}\phi = \frac{\phi(x+h,t)-\phi(x,t)}{h}, \tag{5.55}$$

$$D^{-x}\phi = \frac{\phi(x,t)-\phi(x-h,t)}{h}, \tag{5.56}$$

where h is the spatial step.

Then we look for pixels where these four estimators differ great by thresholding the following criterion:

$$\frac{1}{4}\sum_i \left(\frac{D^i\phi}{|D^i\phi|}, \frac{\overline{D\phi}}{|\overline{D\phi}|}\right) > T, \tag{5.57}$$

where $(.,.)$ is the scalar product and $\overline{D\phi} = \frac{1}{4}\sum_i D^i\phi$ and T the threshold value. Equation (5.57) can be interpreted as a measure of the mean variation of the direction of $\nabla\phi$ (which is large in the neighborhood of the skeleton). Note that the width and the quantity of skeleton detected strongly depends on the value of the spatial step h used to compute the backward and forward differences. Figure 5.12 shows the skeleton obtained on the brain image with h equal to 1 (Panel 5.12(a)) and h equal to 3 (Panel 5.12(b)). For this work, we use h equal to 3.

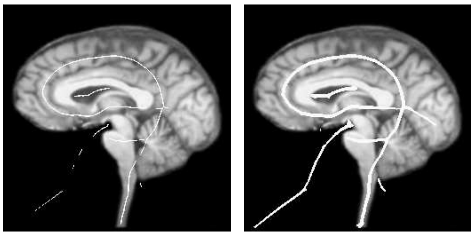
(a) (b)

Figure 5.12: Extracted skeleton superposed to the brain image. Rows: 1) h=1. 2) h=3.

Then, once the mask of the skeleton is extracted we use the following linear diffusion equation to smooth locally the deformation field:

$$\frac{\partial u_s(x,t)}{\partial t} = \Delta v(x,t), \tag{5.58}$$

with

$$v(x,t) = \begin{cases} u_s(x,t) & x \in \Omega_{skel} \\ u(x,t) & x \in \Omega \setminus \Omega_{skel}, \end{cases} \tag{5.59}$$

where u is the solution of Equation (5.53) at the point x, u stays thus unchanged here, u_s is the new deformation field, Ω_{skel} are the set of skeleton points and $\Omega \setminus \Omega_{skel}$ are the set of points outside the skeleton. Δ is the Laplacian operator. This equation is nothing but the well-known heat equation [68]. It corresponds to a Gaussian regularization [125]. At initial time, the deformation field located inside the skeleton mask is put to zero, i.e. $u_s = u(x,0), x \in \Omega_{skel}$. We use a time step Δt equal to 0.3 to solve equation (5.6.2). This smoothing is performed at each iteration but it is very fast since we have found experimentally that a number of iterations equal to the maximal width of the skeleton is enough to produce correct results and we process only the skeleton points.

Note that this local smoothing ensures not only the regularity of the deformation field but also permits diffusion of the computed displacement at places where the gradient is not defined.

In Figure 5.13, we show the effect of the curvature term on 2D real images. In the first row, we smooth the external contour of Saturn. In the second row, we smooth two contours in the brain image: the external contour and the ventricles. For each case, we show the initial position and the position after 200 iterations.

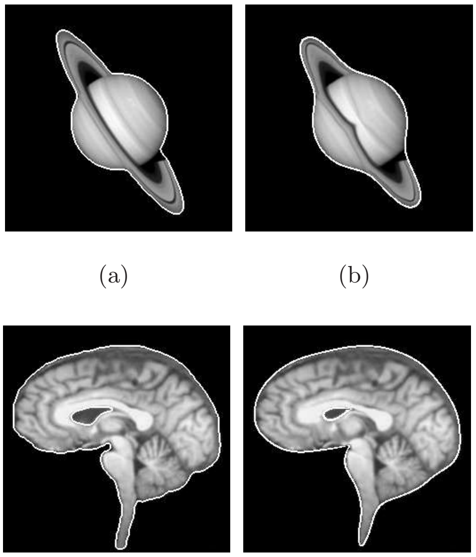
(a) (b)

(c) (d)

Figure 5.13: 2D real images deformed by the curvature term. Rows: 1) Saturn image, 2) brain image. Columns: a) Initial position, b) Position after 200 iterations.

Figure 5.14 shows two zooms on the deformation field obtained by the smoothing of Saturn's external contour. Panel 5.14(a) shows the center of the planet and Panel 5.14(a) shows one extremity of the ring. We can see that, thanks to the regularization scheme, opposite displacement fronts do not cause pixel crossing.

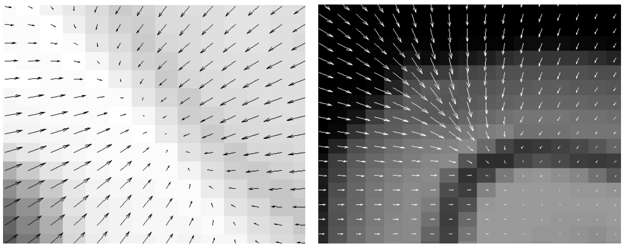
(a) (b)

Figure 5.14: Zoom on the deformation field of Saturn image.: a) center of the planet, b) one extremity of the ring.

In Figure 5.16, we register the external contours of the shell images along with the two object-based attraction forces. The first row shows the deformation computed by using the boundary-based forces and the second row shows the deformation obtained with the region-based forces. For each case, we show the initial position, an intermediate position and the final position. The target contours are copied in white onto all of these images. Figure 5.15 shows the final deformed level set functions. This figure shows that the deformations obtained with both attraction terms are quite

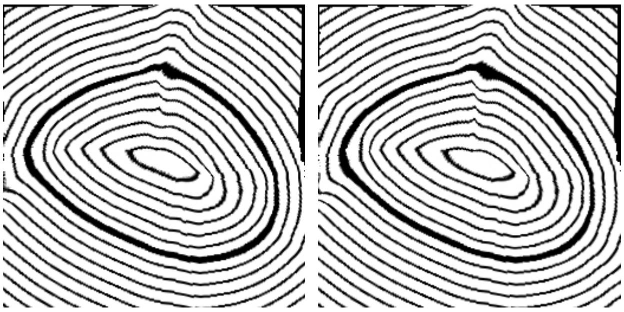

(a) (b)

Figure 5.15: Level set function of the shell deformed by the attraction terms: a) boundary-based, b) region-based.

similar. The displacement of each isophotes is smooth and follows the displacement of the zero level set. However, even if the deformation field is regular, the Panels of Figure 5.16 shows strange deformations in the shell texture. This is due to the fact that the natural deformation of a shell is radial but from its base and our registration technique, generates radial deformation from the skeleton of the active contours.

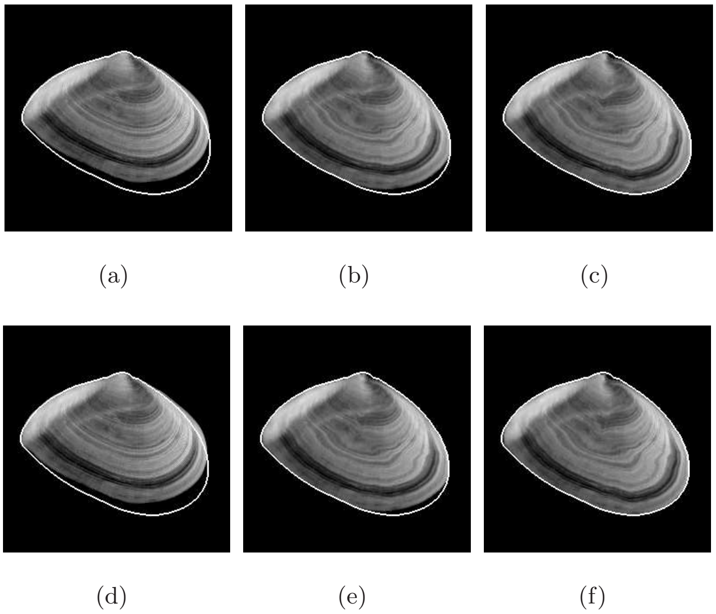

(a) (b) (c)

(d) (e) (f)

Figure 5.16: Attraction terms. Rows: 1) boundary-based, 2) region-based. Columns: 1) initial position, 2) intermediate position, 3) final position.

Advantages and Limitations of the Distance-based Methods

Let us highlight the main characteristics of the the pixel-based and object-based models presented above.

Two phase Representation The signed distance map representation limits the model to a two phase registration.

Texture The distance-based model interpolates radially the deformation of the active contour to the whole image. Such deformation can be an advantage to model a tumor growth for example or to interpolate the deformation on homogenous region. On the other hand, this type of model is not appropriate for the registration of regions containing texture. The generate deformation field is radial to the considered contours and thus does not follow the texture of the image.

Regularization The gaussian smoothing used in the pixel-based model ensures a smooth deformation field but do not act on contour smoothing. The mean curvature forces used in the object-based model acts on contour smoothing but impose a very small time step to avoid numerical instabilities. Thus to recover the same deformation, the model needs a much more higher number of iterations with the regularization by mean curvature forces than by gaussian smoothing.

5.6.2 Diffusion Model

This model was designed to combine the intensity function representation with the representation by label function. In other words, this model is based on the following vector level set function $\phi = \phi_I, \phi_L$. The concept of this model is to compute the attractive forces on the contours model by both level set functions and to diffuse the computed deformation to the whole image by diffusion. The label function permits to model the contours on which object-based forces can be applied. These object-based forces permit to register image region. The intensity function combined to the label function permits to select texture regions that are consistent between the reference and the target image. This texture regions are registered by pixel-based forces. Then the deformations computed on the active contour are extended on homogenous and inconsistent regions by linear diffusion:

$$\begin{aligned} \frac{\partial v(x,t)}{\partial t} &= \Delta v(x,t), \\ v(x,t=0) &= u_*(x), \end{aligned} \tag{5.60}$$

where u_* is the solution of the evolution equation of the active contour-based registration model and Δ is the Laplacian operator.

We illustrate this method on synthetic multi region data set. These images are shown in Figure 5.17. They correspond to multi-region images on which we have added different textures. The images of Column 1 are without noise and those of Column 2 are with a gaussian noise (0-mean and 20-variance). The moving and target images are respectively shown in Rows 1 and 2. In these images, we can distinguish the four regions shown in the label functions (Column 3). Three of these regions (the background, the left and right regions) are consistent between the moving and the target image, i.e. they have similar mean and texture. The last one (the central region) has a similar mean in both images but the orientation of the texture pattern is different. The target contours are copied onto the source and target images to visualize the initial differences. We note that the right region has much larger initial differences than the left region.

First we have registered these images with pixel-based forces. The registration process is thus very local. This has three consequences illustrated in the registration result shown in Figure 5.18. First the algorithm is quite sensitive to noise. Note that the center of the left region is less well registered on the noisy data (Figure 5.24(a)) than on the data without noise (Figure5.21(a)). Secondly, this algorithm presents some limitations when it has to recover large differences. In Figure 5.21(a)

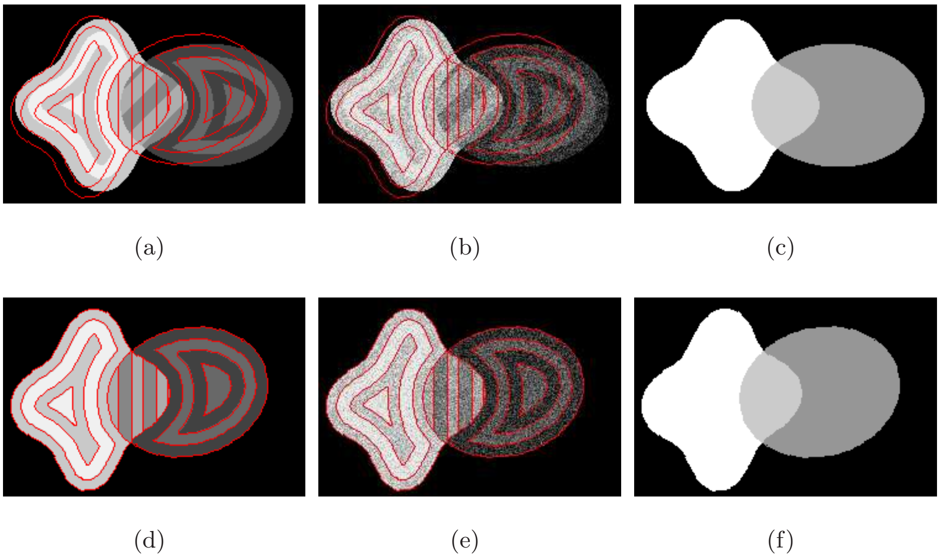
(a) (b) (c)

(d) (e) (f)

Figure 5.17: Multi-region data set. Column 1: Moving images without and with noise. Column 2: Target images without and with noise.

and 5.24(a), we see that the region with initial large differences (right region) presents large misregistrations. Finally, the algorithm has no scheme to prevent the registration of inconsistent regions, here the central region. The deformed grids helps to visualize the corresponding deformation field.

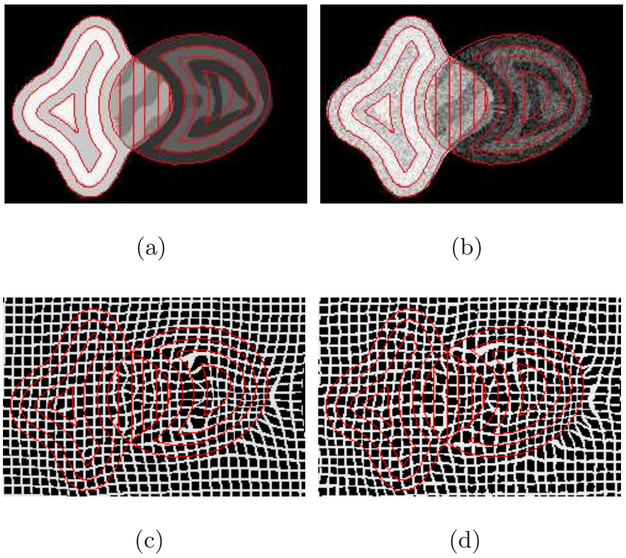
(a) (b)

(c) (d)

Figure 5.18: Pixel-based model results: (a) Data without noise. (b) Data with noise. (c) Deformation field.

Figure 5.19 shows the results obtained with object-based forces. We have used prior mean-based forces to register the four regions. Thanks to the constraints defined on the contours selected by the label function, the four region are well registered independently of the noise, of the amount of deformation to recover or of the differences in the texture. Nevertheless, the drawback of the contour/surface-based registration algorithm remains in this model. Indeed, as the deformation is only based on contours of interest, the probability of registration errors increases, the further one is from these contours. In fact, the level of accuracy is highly dependent on the number of objects considered. We can see in Figure 5.19 that we have more and more registration error in the texture more we are far away from the contours. Moreover with the label function, we can model only closed contours to drive the registration. On the other hand, pixel-based forces can consider every type of contours in the registration process.

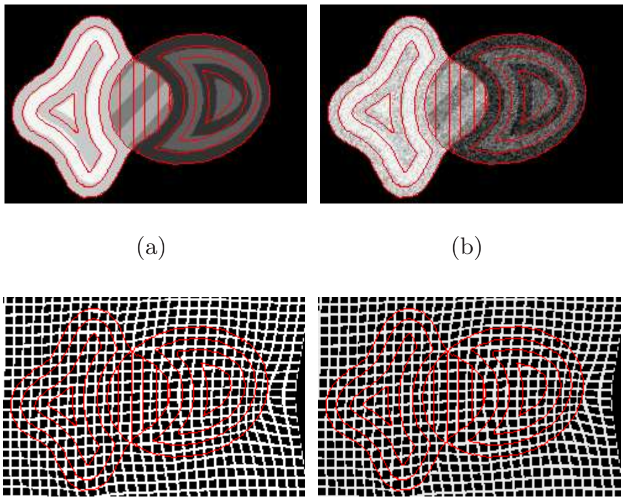
(a) (b)

(c) (d)

Figure 5.19: Object-based model results: (a) Data without noise. (b) Data with noise. (c) Deformation field.

Finally, the images were registered by a model combining pixel-based and object-based forces. This model uses the label function to determine where to compute which type of forces. Some image regions have to be registered globally. These are regions that have either no structures of interest to segment inside them or an inconsistent texture between both images to register. Thus for these regions, only object-based force are applied on their contours. Other regions have to be registered more locally. These are regions that contain features that can help the registration. Thus for these regions, object-based forces are applied on their contours and pixel-based forces are applied inside. If the deformation to recover is large, the registration process is performed hierarchically following the approach described in Section 5.5.2. First the regions modeled by the label function are globally registered by region-based forces and then locally registered by pixel-based forces. If the deformation to recover is small, both type of forces can be used simultaneously. Figure 5.20 shows the results obtained. This time the registration is performed on and far away from the selected contour. As the texture of the middle region is different between the moving and target image, we did not use pixel-based forces in it. The texture pattern is thus just following the deformation of the region contours.

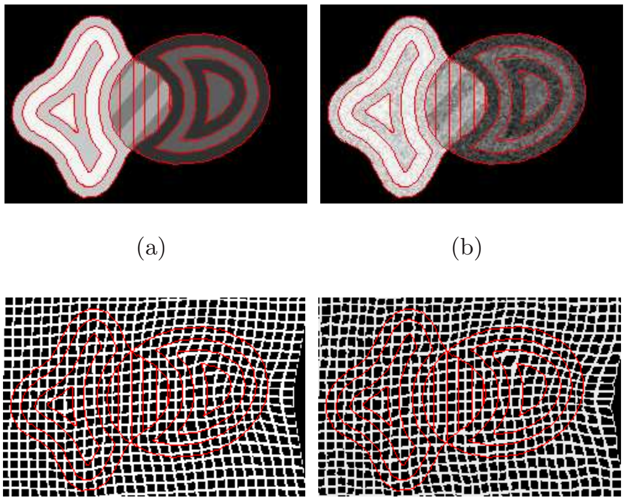

(a) (b)

(c) (d)

Figure 5.20: Pixel and Object-based model result: (a) Data without noise. (b) Data with noise. (c) Deformation field.

5.7 Regularization

In this section, we describe the smoothing and bijectivity constraints we have included in our active contour-based registration framework.

5.7.1 Smoothing constraint

The smoothing constraint of our model combines the smoothing techniques used in common diffusion registration algorithms and active contour segmentation models.

Linear diffusion

This smoothing technique is the most commonly used in diffusion registration algorithms (see [166], [168]). It is applied at the end of each iteration on the current deformation field. Its PDE corresponds to the heat equation. As mention in Section 5.6.2, this technique permits not only to smooth the deformation field but also to diffuse the contour deformation on a narrowband around it. The fastest way to perform this diffusion is to do it by filtering. The corresponding filter to the heat equation is the Gaussian filter. This filter depends on the parameter sigma setting the standard deviation of the Gaussian. Sigma acts as a elasticity parameter. The more sigma has a large value and the more the filtering will be performed on a larger neighbourhood. As a result the deformation field will be less elastic. The main limitation of this smoothing technique is it often lead to a compromise between the smoothness of the deformation field and the accuracy of the registration.

Mean Curvature

This regularization type is the most commonly used in active contour segmentation models. We have already described it in Section 5.4. Opposite to the linear diffusion smoothing technique, it acts directly in the evolution equation. Its goal is to constraint the evolving contours of the moving image to stay smoothed during their evolution. Its main limitation is it needs to be computed with a very small time step because it is very sensitive to numerical instabilities. Moreover it cannot interpolate the deformation through homogenous areas as the linear diffusion technique.

Combination of both Techniques

We show in the convergence analysis of our model (Section 5.8) that the limitation of the linear diffusion can be solved by the mean curvature and conversely. Indeed, as the mean curvature forces constraints the active contours to stay smooth, the evolution equation provides a smoother deformation field. Thus the deformation field can be smoothed with a smaller sigma. As the linear diffusion easily smooths the small irregularities of the deformation field, we can use a larger time step to compute the mean curvature forces.

5.7.2 Bijectivity Constraint

Analysis of the Bijectivity

We start this analysis by measuring the asymmetry of the transformation of our registration model with pixel-based forces and object-based forces. For this purpose we compute the deformation from the source image to the target image and from the target image to the source image on the noisy synthetic multiregion data set shown in Figure 5.17. Figure 5.21 shows the norm of the residual errors obtained by summing these two inverse transformations. With the pixel-based forces, the errors vary from 0 and 10.4 mm. With the object-based forces, the errors vary from 0 and 4.9 mm. An algorithm can be considered as bijective when these residual errors are close to zero.

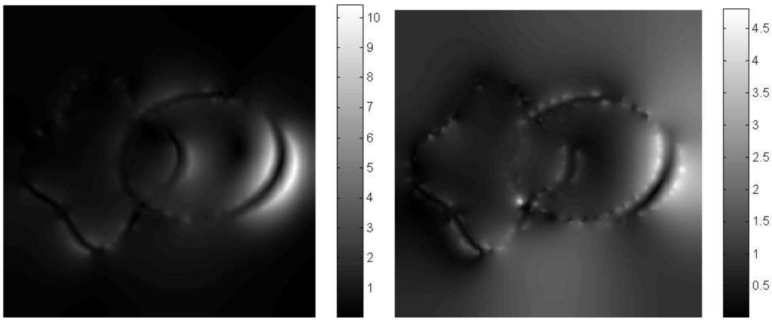

(a) (b)

Figure 5.21: Norm of the residual error vector: (a) Pixel-based forces. (b) Object-based forces.

Method

We have followed the approach proposed by Thirion et al. in [165]. This approach consists to compute at each iteration independently the forward transformation u and the backward transformation u^{-1}. Then their compatibility is maintained by equally distributing the residual deformation $R = u - u^{-1}$ onto the two deformation fields, i.e. $u' = u + R/2$ and $u'^{-1} = u^{-1} + R/2$ with u' and u'^{-1} are the corrected forward and backward transformations.

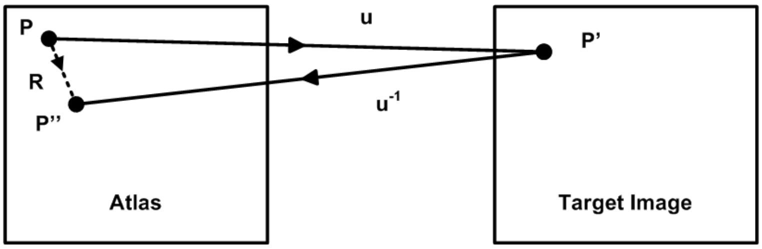

Figure 5.22: The bijectivity is imposed by the computation of the residual deformation $R = u \circ u^{-1}$ and the redistribution of a half of the residual to both transformations, at each iteration of the algorithm. Figure inspired from [166].

With our active contour-based model, to compute the backward transformation u^{-1}, we needs a second label function defined on the target image. Creating this second label function is straightforward when we need to register labeled images or if the contours of interest can be easily extracted from the target image by thresholding for example. When it is not the case we propose to avoid the manual segmentation of the target image by using a technique inspired by the Demon's algorithm [165]. This technique consists to compute the inverse transformation by diffusing the object of the target image through the contours of the source label image.

This lead to an equation similar to (5.32) expect that the label function is not deformed and the driving forces have an opposite sign because they do not have to attract the active contour to a target object (Figure 5.23(a)) but to diffuse the target object through the active contour (Figure 5.23(b)):

$$\frac{\partial u(x,t)}{\partial t} = S(x)F(L(x,0))\mathcal{N}. \tag{5.61}$$

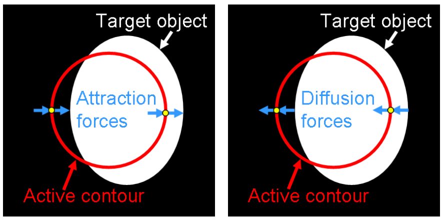

(a) (b)

Figure 5.23: Bijectivity constraint with one label function: (a) Forward transformation: Attraction forces. (b) Backward transformation: Diffusion forces.

Validation on Synthetic Data We have evaluated the quality of the registration with and without the bijectivy constraint on the noisy synthetic multiregion data set (Figure 5.17). For that we have used the following similarity measure to evaluate the difference between the target level set function ϕ_T and the moving level set function ϕ_M deformed by the obtained deformation field u.

$$MS = \frac{1}{|\Omega|}\Sigma_\Omega[\phi_T(x) - \phi_M(x + u(x), 0)]^2, \tag{5.62}$$

where MS is the Mean Square Error. $|\Omega|$ is the number of image pixels.

Table 5.1: Registration without Bijectivity constraint.

$Model$	P	O	OP
MSL	416	130	130
MSI	536	387	342

Table 5.2: Registration with Bijectivity scheme.

$Model$	P	OL	OD	OPL	OPD
MSL	496	195	197	118	127
MSI	614	426	426	328	328

Tables 5.3 and 5.2 respectively summary the results obtained without and with bijectivity. The first line of these tables indicates the model used: P= Pixel based forces, O= Object based forces, OL = Object-based forces with the label function approach for the reverse transformation, OD = Object-based forces with the diffusion approach for the reverse transformation, OPL = Object-based and Pixel-based forces with the label function approach for the reverse transformation, OPD = Object-based and Pixel-based forces with the diffusion approach for the reverse transformation. The columns gives the RMS values for each model: MSL is the similarity computed between the label functions and MSI values is the similarity between the intensity functions. For the initial data, MSEL is 2685 and MSEI is 2363. For the bijectivity results, the residual error is 0 because we perform the deformation field correction after the Gaussian filtering. Figures 5.24 and 5.25 respectively shows the registration results and transformation obtained without and with the bijectivity constraint.

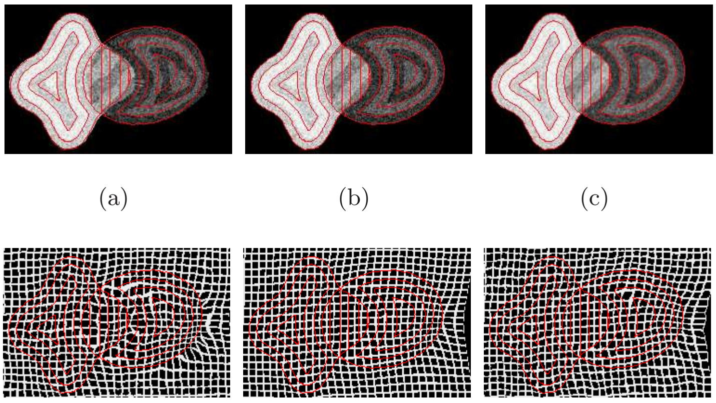
(a) (b) (c)

(d) (e) (f)

Figure 5.24: Registration without bijectivity constraint. Row 1: a) Pixel-based forces, b) Object-based forces, c) Pixel and Object-based forces Row 2: Corresponding deformation field.

From these results we can draw several conclusions. First the bijectivity scheme do not influence significantly the accuracy of the registration. We obtained similar qualitative and quantitive results. Secondly, the results obtained with the label function approach and the

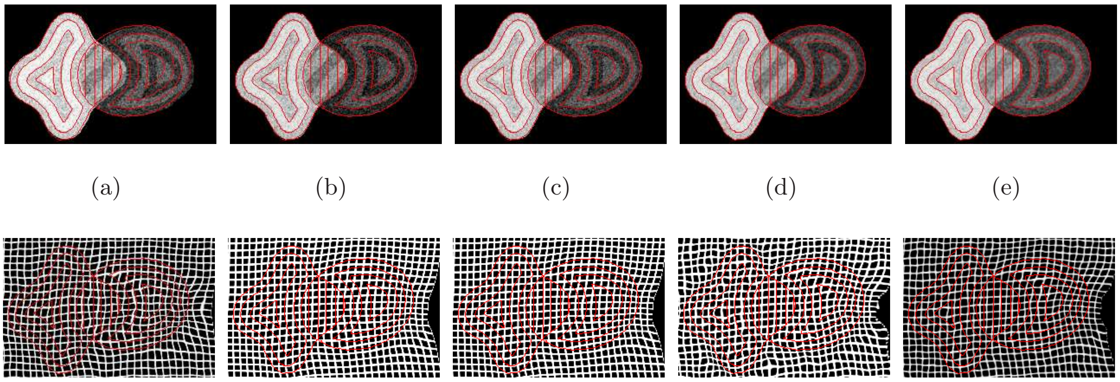
(a) (b) (c) (d) (e)

(f) (g) (h) (i) (j)

Figure 5.25: Registration with bijectivity constraint. Row 1: a) Pixel-based forces, b) Object-based forces (reverse with label function), c) Object-based forces (reverse by diffusion) d) Pixel and Object-based forces (reverse with label function) e) Pixel and Object-based forces (reverse by diffusion) Row 2: Corresponding deformation field.

diffusion approach are very close.

5.8 Analysis of the convergence

In this Section, we analyze and compare the convergence of the Pixel-based model (P), the Object-based model (O) and the couple Pixel and Object-based model (PO). The object-based forces were computed with the prior mean-based term. Note that the convergence of these three models is depending on the same parameters: the elasticity parameter σ, the number of scales and the number of iterations at each scale. To set the elasticity parameter, a compromise has generally to be done between the desired deformability and the smoothness of the deformation field. The number of scales is fixed in a way that the global morphology of the object has still to be identifiable at the lowest resolution scale. The optimal number of iterations at each scale should permit to obtain a good matching with a minimum computation time. Because of the registration models behavior complexity, the necessary number of iterations is difficult to predict intuitively. Therefore, we propose a stopping criterion to estimate the number of iterations of each scale during the registration process. This criterion was designed regarding to the conclusions of the convergence analysis.

We have compared the convergence of the three models by analyzing the evolution of the following similarity measure computed on the whole image domain Ω:

$$\alpha_i = \frac{1}{|\Omega|}\Sigma_{\Omega}[\phi_{I,T}(x) - \phi_{I,M}(x + u(x,t), 0)]^2, \tag{5.63}$$

where α is the Mean Square Error (MSE). It measures the difference between the target intensity function $\phi_{I,T}$ and the current moving intensity function, $\phi_{I,M}(x + u(x,t), 0)$ at each iteration i. $|\Omega|$ is the number of image pixels. In this study we do not measure separately the convergence of the regions defined by the label function as we did it for the analyze of the bijectivity (see Section 5.7.2). We considered the region convergence as implicit in the whole image convergence.

During the registration process, the MSE decreases until all points of the deformable model match the intensity of the corresponding points in the target image. Below we describe the convergence conditions of each model for the instantaneous displacement $\frac{\partial u(x,t)}{\partial t}$:

Pixel-based model: The instantaneous displacement decreases to zero when the intensities match perfectly.

Object-based model: The instantaneous displacement decreases to zero when the prior means of the inside and outside region match the target intensities on both side of an active contour point.

Pixel and Object-based model: The instantaneous displacement decreases to zero when the convergence conditions of both models are fulfilled.

We illustrate below the convergence of the algorithms described above on two examples, one on synthetic and one on real data.

5.8.1 Convergence on Synthetic Data

The two synthetic images of Figures 5.26(a) and 5.26(b) have been registered with the Pixel-based and the Object-based model. Figure 5.26(c) shows the difference between both images. Each image has dimension of 256x256 pixels and pixel dimensions are 1x1 mm^2. To better compare the convergence of both models we chose images that can be well registered by both methods, i.e. without noise, inconsistencies, open contours or texture. Thus the pixel-based forces will be computed on the same contours than the object-based forces. The registrations were performed with 4 scales and 100 iterations per scales.


(a) (b) (c)

Figure 5.26: Multi-region data set: (a) Source image, (b) Target image, (c) Difference between (a) and (b).

The resulting MSE evolutions are plotted as a function of the current scale in Figures 5.27 and 5.28. Each scale was enhanced by a different color. The coarsest one is shown in blue and the finest one in red. These two figures permit to compare the MSE evolutions without and with the bijectivity scheme. To compute the object-based forces, we used as label function the image 5.26(a) for the direct transformation and the image 5.26(b) for the reverse transformation. In each figure, Row 1 corresponds to the Pixel-based model and Row 2 to the Object-based model. Column 1 shows the MSE obtained with $\sigma = 2mm$ and Column 2 those obtained with $\sigma = 1mm$. The final MSE value is indicated under each panel. Finally, we show in Figures 5.29 and 5.30 the difference between the registration results and the target image.

Several conclusions can be drawn from these figures:

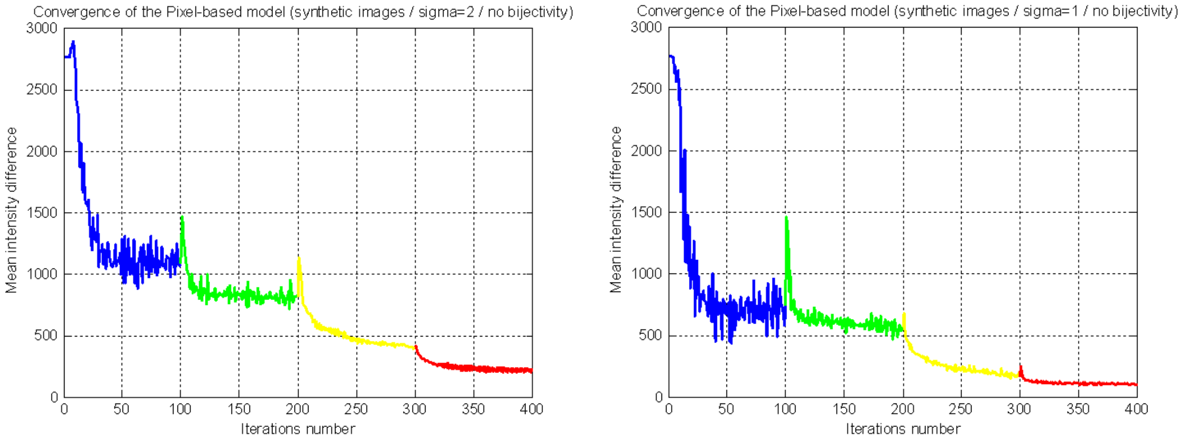

(a) Final MSE = 234

(b) Final MSE = 103

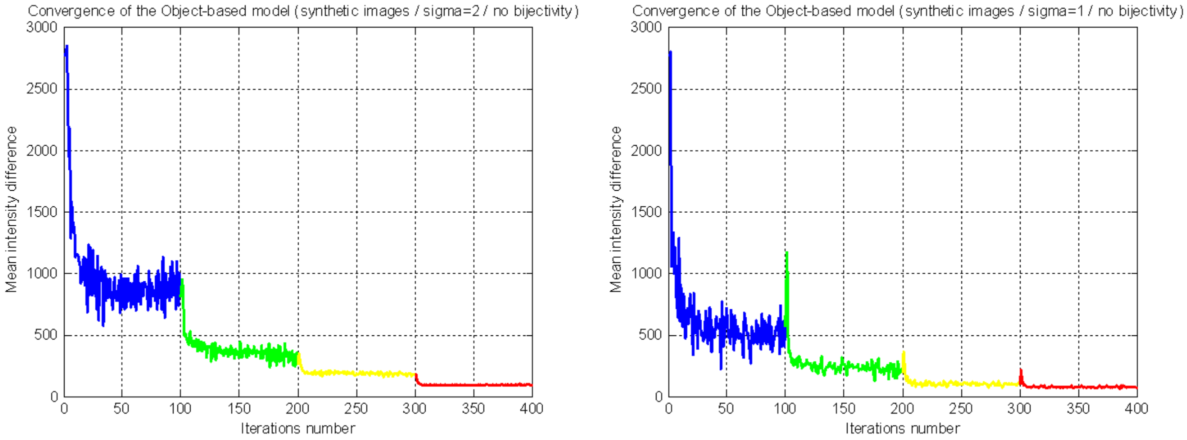

(c) Final MSE = 94

(d) Final MSE = 74

Figure 5.27: MSE evolution. Models without bijectivity scheme. Row 1: Pixel-based model. Row 2: Object-based model. Column 1: $\sigma = 2mm$. Column 2: $\sigma = 1mm$.

- First, notice the differences in the convergence evolution between the scales. The convergence is less variable in the finest scales than in the coarsest ones. Also at the coarsest scale (in blue), the evolution sometimes increases after having reach a global minima (for example see Figure 5.28(a)). We have thus to design a stopping criterion that will be more restrictive in the finer scales and that stop eventual divergence at the coarsest scale.

- Secondly, note that the MSE often presents a discontinuity when switching of scale. Actually, MSE increases with respect to the last error obtained at previous scale. This effect is due to the fact that the image resolution has increased and new errors appear at the new pixel locations.

- Then, notice that the constraints applied on the deformation tend to slow down the convergence. The MSE values are higher with $\sigma = 2mm$ than $\sigma = 1mm$ or with the bijectivity

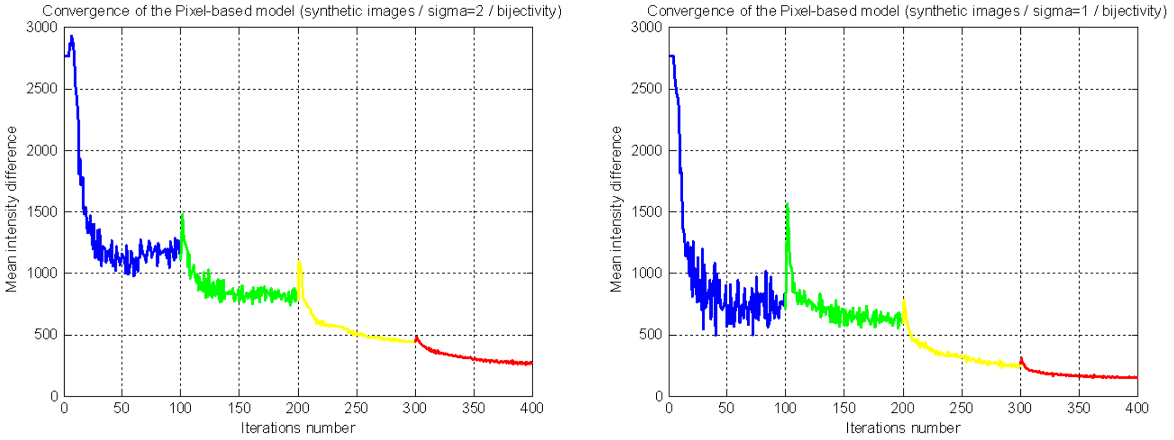

(a) Final MSE = 260 (b) Final MSE = 151

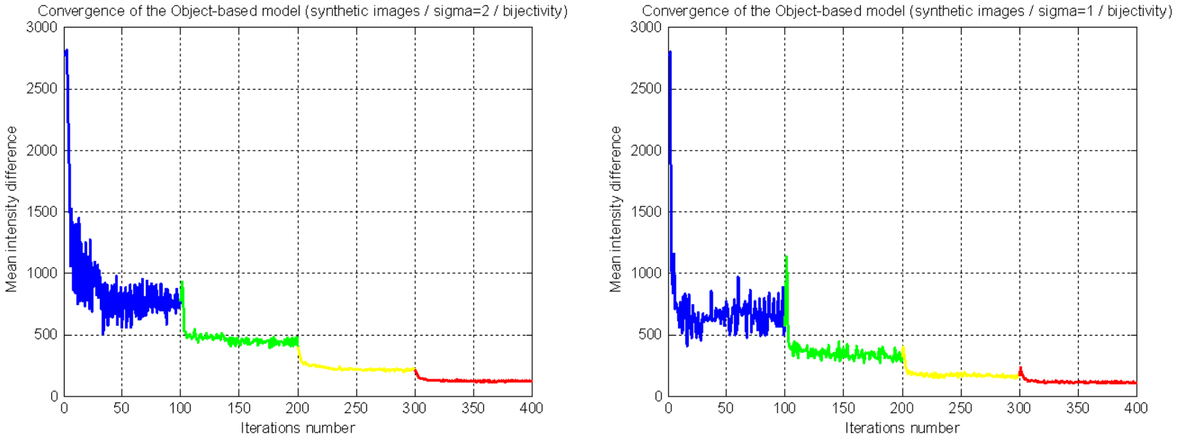

(c) Final MSE = 126 (d) Final MSE = 112

Figure 5.28: MSE evolution. Models with bijectivity scheme. Row 1: Pixel-based model. Row 2: Object-based model. Column 1: $\sigma = 2mm$. Column 2: $\sigma = 1mm$.

scheme.

- After, at each scale the MSE functions of the Object-based model reach more quickly a lower stable state (MSE values quasi-constant) than those of the Pixel-based model. The object-based force necessitates thus less iterations than the pixel-based forces to converge.
- Finally, notice on the difference images that the Pixel-based model did not converge enough at the location of the highest difference between both synthetic images. For the Object-based model the differences are just due to the contour smoothness.

5.8.2 Proposed Stopping Criterion

A stopping criterion is proposed in what follows. The idea is to stop the iteration process and switch to the next scale, when the MSE function reaches a stable state or a global minima. This stopping

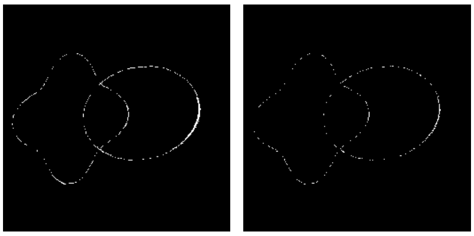

(a) Final MSE = 234 (b) Final MSE = 103

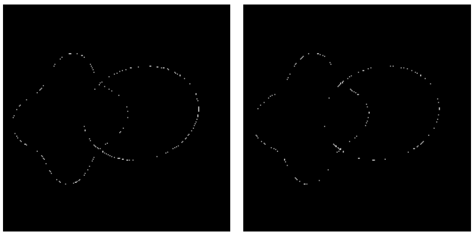

(c) Final MSE = 94 (d) Final MSE = 74

Figure 5.29: Difference images. Models without bijectivity scheme. Row 1: Pixel-based model. Row 2: Object-based model. Column 1: $\sigma = 2mm$. Column 2: $\sigma = 1mm$.

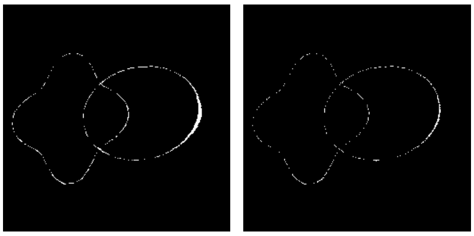

(a) Final MSE = 260 (b) Final MSE = 151

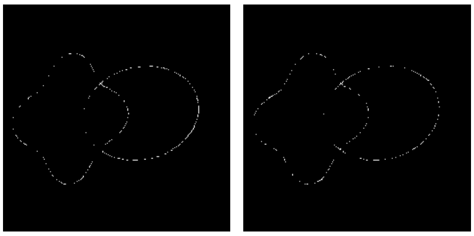

(c) Final MSE = 126 (d) Final MSE = 112

Figure 5.30: Difference images. Models with bijectivity scheme. Row 1: Pixel-based model. Row 2: Object-based model. Column 1: $\sigma = 2mm$. Column 2: $\sigma = 1mm$.

criterion was inspired by the one presented in [12].

First we use a mean filter to smooth the MSE function:

$$\alpha_i = \frac{1}{M}\Sigma_{k=i-M}^{i}\alpha_k, \tag{5.64}$$

where m_i is the mean of the M previous MSE values α_k. M is arbitrarily set as function of the scale, that is, more iterations are averaged in the coarsest than in the finest scales to be more robust in front of the MSE convergence variability.

Then the following expression is checked from the M^{th} iteration:

$$m_i - m_{i-M} >= 0. \tag{5.65}$$

In the implementation we rounded the mean values to not consider the decimals in their comparison.

In conclusion, this stopping criterion assumes that the algorithm has converged when the MSE values do not change significantly or increase during M consecutive iterations.

Convergence using the Stopping Criterion

The stopping criterion was integrated in the registration process of the synthetic images with the following parameters: $\sigma = 1mm$, 4 scales, bijectivity scheme and $M = 16, 16, 8, 8$ from the coarsest to the finest scale. The maximum number of iterations per scale was limited to 100. The results obtained with the Pixel-based model and the Object-based model are shown in Figure 5.31. The black line corresponds to the MSE function smoothed by the mean filter. The red triangles show the stopping point of each scale. Column 1 shows the stopping points proposed by the stopping criterion when it is applied on the MSE function of the Figures 5.28(b) and 5.28(d). Column 2 shows the MSE functions obtained when both algorithms are run with the stopping criterion. The number of iterations per scale and the final MSE are indicated under each panel.

In this example, we see that the stopping criterion has permit to reduce the number of iterations per scale and thus the computational time as well as the final MSE. In particular with the Pixel-based model, by avoiding the divergence of the coarsest scale, the stopping criterion has permit to improve considerably the final MSE. In Figure 5.32, we show the final result corresponding to the MSE function of the contour-based model (Figure 5.31(d)). The red contours correspond to the target contours.

5.8.3 Results on Real Data

In this section we analyze the convergence of the Pixel-based model, the Object-based model and the Pixel and Object-based model on 2D MRI brain images. For the last model, we did not use the hierarchical approach because of the small deformation to recover between both images.

Brain Data Set

This data set, shown in Figure 5.33, contains 2D MRI brain images. Figure 5.33(a) and 5.33(b) respectively show the source and target images. Figure 5.33(c) shows the initial differences between both images. Figures 5.33(d) and 5.33(e) show the label functions used to compute the object-based forces. These label functions were obtained from the MRI images by thresholding. Each image has dimensions of 256x256 pixels and pixel dimensions are 1x1 mm^2. All the results were computed with the bijectivity scheme, 4 scales and 100 iterations per scale. In this example, we analyze and compare the effect of the elasticity parameter σ and the curvature term on the convergence. The curvature term permits to assure the smoothness of the contour during the registration process.

The resulting MSE functions computed without the curvature constraint are plotted in Figure 5.34. Those computed with the curvature constraint are plotted in Figure 5.35. For each Figure, Row 1 corresponds to the Pixel-based model, Row 2 to the Object-based model and Row 3 to the Pixel and Object-based model. Column 1 shows the MSE obtained with $\sigma = 2mm$ and Column

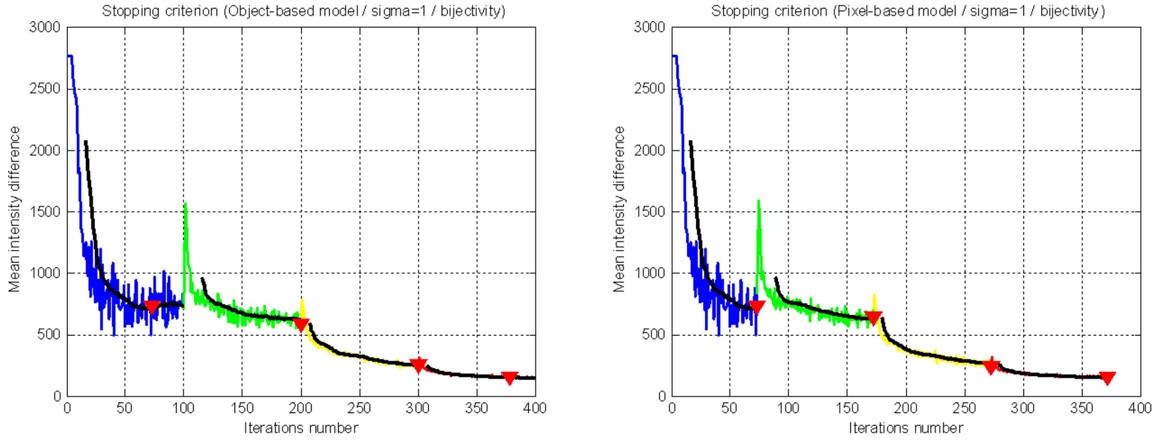

(a) Stop proposed after 73 / 100 / 100 / 79 iterations. Final MSE = 273.

(b) Stop after 73 / 100 / 100 / 100 iterations. Final MSE = 157.

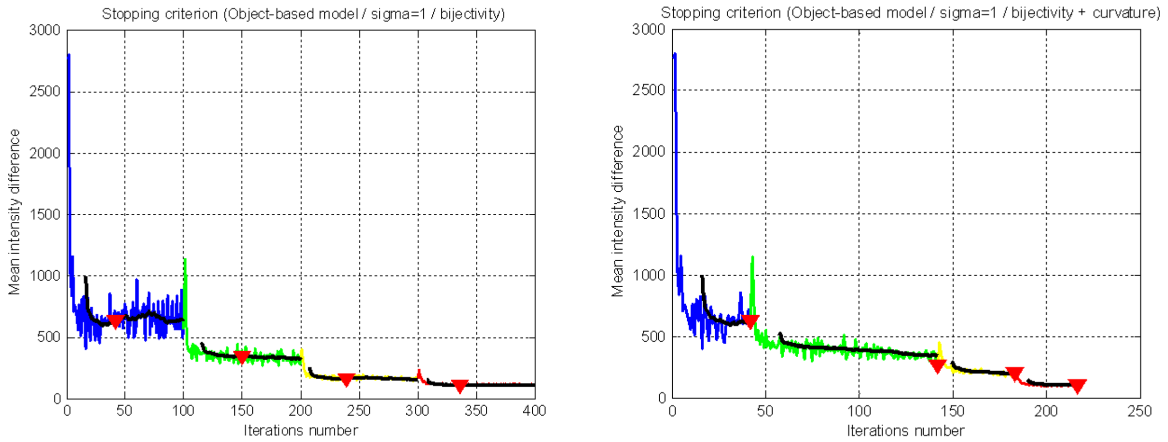

(c) Stop proposed after 37 / 43 / 34 / 26 iterations. Final MSE = 112.

(d) Stop after 42 / 100 / 42 / 37 iterations. Final MSE = 109.

Figure 5.31: Stopping criterion applied on the MSE function. Row 1: Pixel-based algorithm. Row 2: Object-based model. Column 1: Proposed stopping point. Column 2: Convergence with stopping criterion.

2 those obtained with $\sigma = 1mm$. Figures 5.36 and 5.37 show the corresponding difference images between the final registration result and the target image.

First we note that with these images, the MSE tends to diverge considerably at the coarsest scale. The Figure 5.38 illustrates what happened with the case of the Object-based model (sigma 1 without curvature term). Row 1 shows the registration result after 1 scale at resolution 32x32. Row 2 shows the registration result after 1 scale at resolution 64x64. Column 1 and column 3 show the initial moving image and the target image. Column 2 shows the registration results after 100 iterations. The initial and final MSE are indicated under each row. The green contours are those of the target image. At resolution 32x32, the algorithm succeed to improve the registration

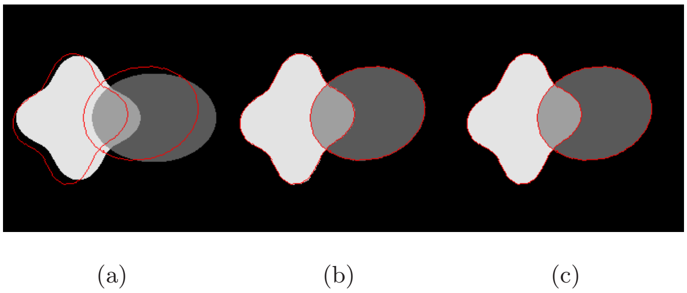
(a) (b) (c)

Figure 5.32: Registration result with the Object-based model. $\sigma = 1mm$, bijectivity and stopping criterion. (a) Initial moving image. (b) Registration result. (c) Target image.

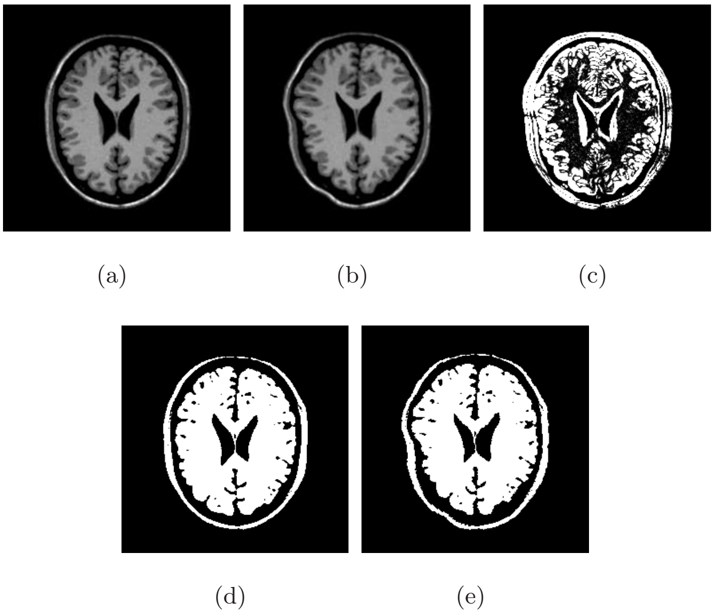
(a) (b) (c)

(d) (e)

Figure 5.33: Brain data set: (a) Source image, (b) Target image, (c) Difference between (a) and (b), (d) and (e) Label functions.

of some part of the brain like the ventricles but other part almost aligned in the original images get completely misregistrated (see for example the bottom of the skull). On the other hand, at resolution 64x64, the algorithm converges normally. This is due to the following reason. More the resolution is small more the different contours of the image are closed. Thus through the gaussian interpolation the motion of one contour will influence a larger ray of the surrounding contours especially if their instantaneous displacement is close to zero. To avoid this divergence, the registration of this images should be run with 3 scales. Otherwise, we will see that the stopping function we have designed will stop these divergences and thus improve the final result. Note that the use of the curvature term permits to reduce the amount of divergence and even sometimes transform it in convergence (compare Figure 5.36(b) to Figure 5.37(b)).

Figures 5.34 and 5.35 clearly show that for both sigma values, the curvature constraint speed up the convergence of the Pixel-based and the Pixel and Object-based model. The Pixel-based model

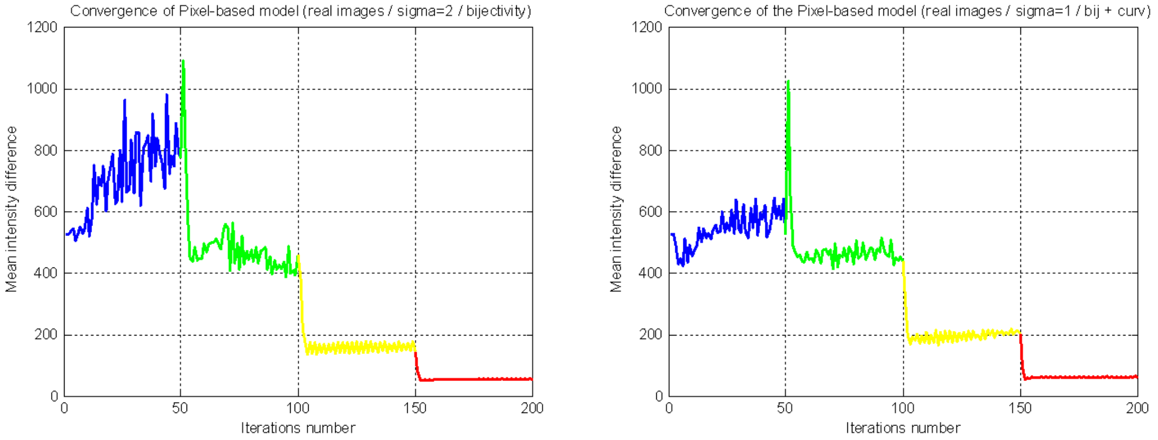

(a) Final MSE = 59 (b) Final MSE = 54

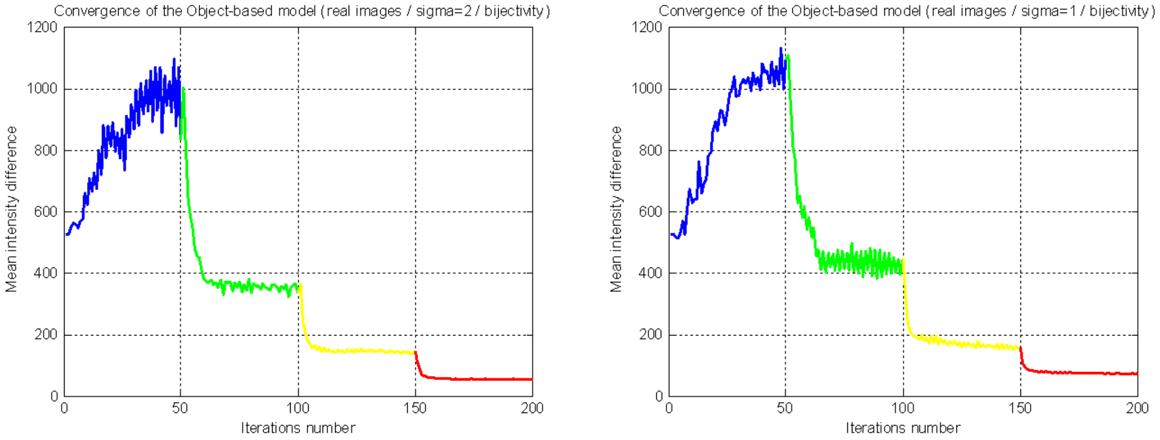

(c) Final MSE = 73 (d) Final MSE = 54

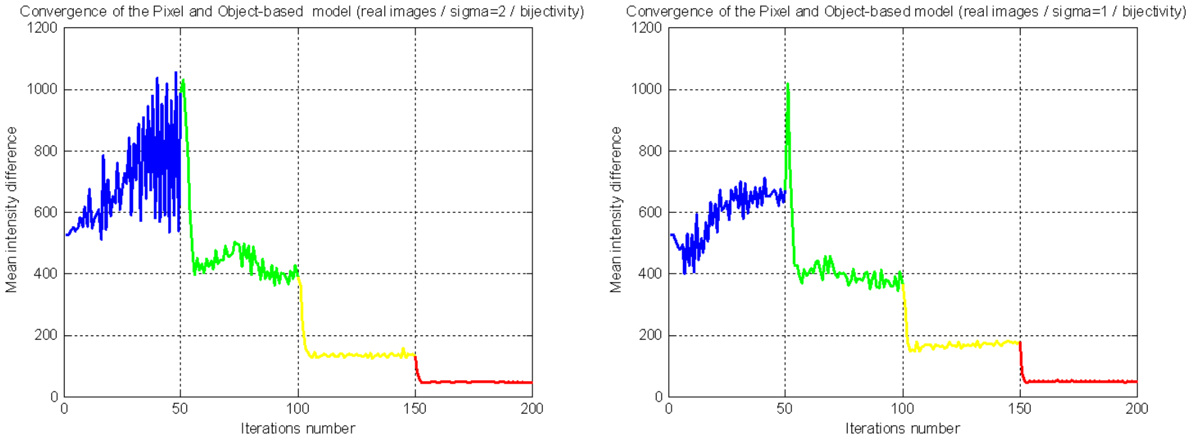

(e) Final MSE = 49 (f) Final MSE = 45

Figure 5.34: MSE evolution without curvature constraint. Row 1: Pixel-based algorithm. Row 2: Object-based model. Row 3: Pixel and Object-based model. Column 1: $\sigma = 2mm$. Column 2: $\sigma = 1mm$.

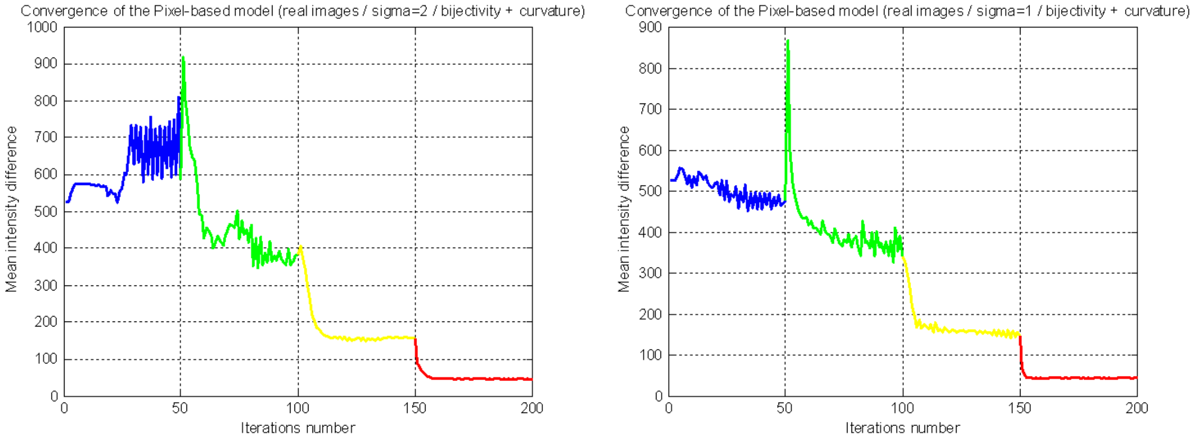

(a) Final MSE = 46

(b) Final MSE = 44

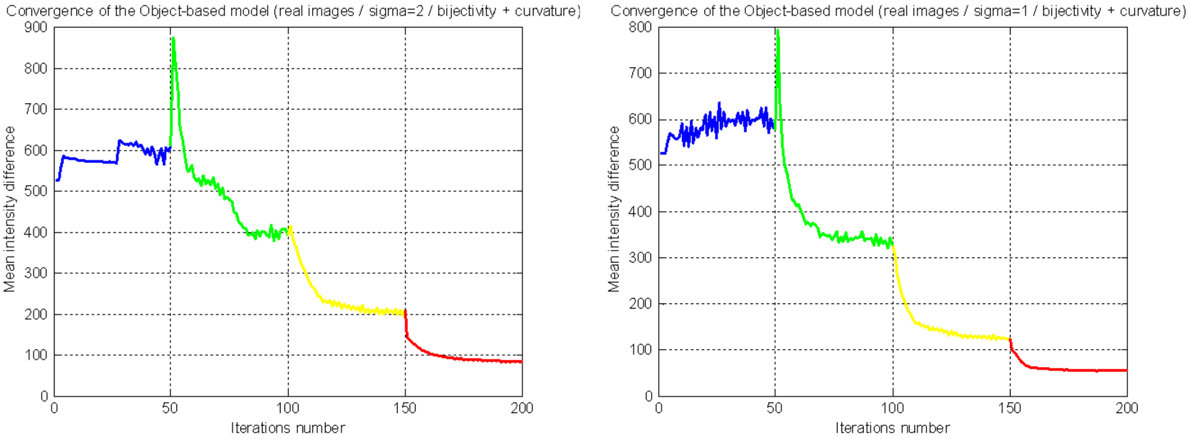

(c) Final MSE = 84

(d) Final MSE = 55

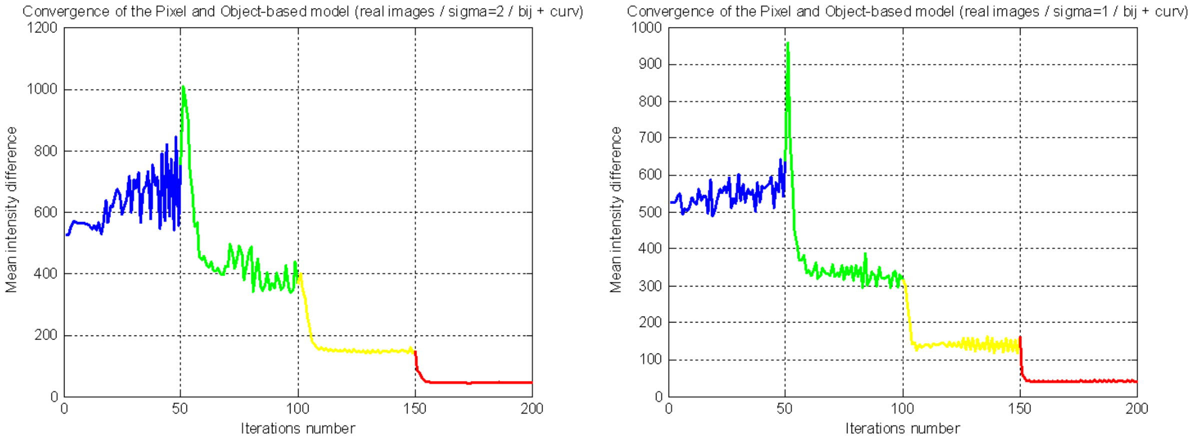

(e) Final MSE = 43

(f) Final MSE = 42

Figure 5.35: MSE evolution with curvature constraint. Row 1: Pixel-based model. Row 2: Object-based model. Row 3: Pixel and Object-based model. Column 1: $\sigma = 2mm$. Column 2: $\sigma = 1mm$.

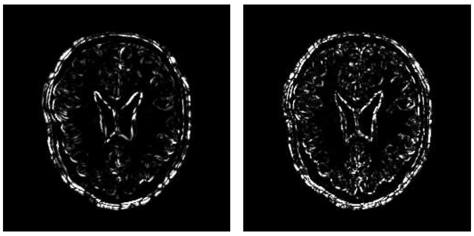

(a) Final MSE = 59 (b) Final MSE = 54

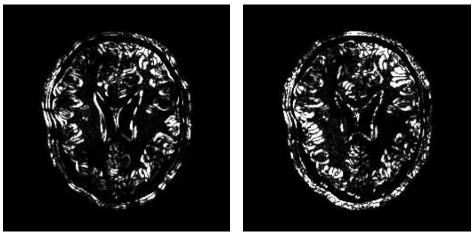

(c) Final MSE = 73 (d) Final MSE = 54

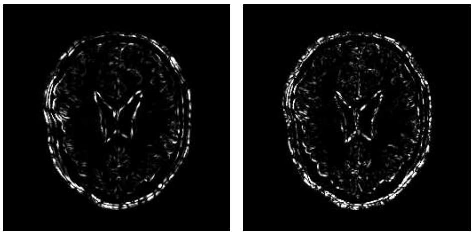

(e) Final MSE = 49 (f) Final MSE = 45

Figure 5.36: Difference images without curvature constraint. Row 1: Pixel-based model. Row 2: Object-based model. Row 3: Pixel and Object-based model. Column 1: $\sigma = 2mm$. Column 2: $\sigma = 1mm$.

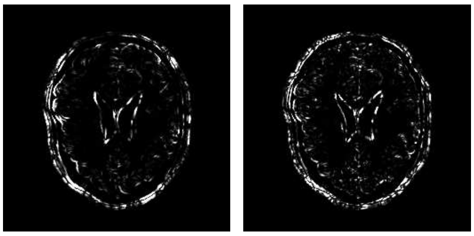

(a) Final MSE = 46 (b) Final MSE = 44

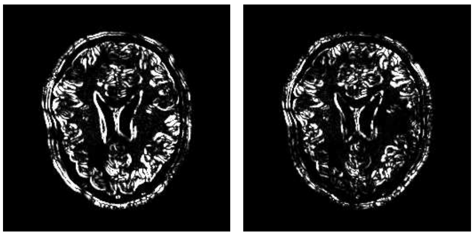

(c) Final MSE = 84 (d) Final MSE = 55

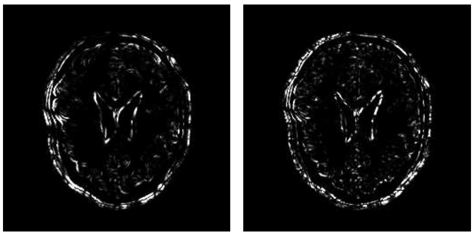

(e) Final MSE = 43 (f) Final MSE = 42

Figure 5.37: Difference images with curvature constraint. Row 1: Pixel-based model. Row 2: Object-based model. Row 3: Pixel and Object-based model. Column 1: $\sigma = 2mm$. Column 2: $\sigma = 1mm$.

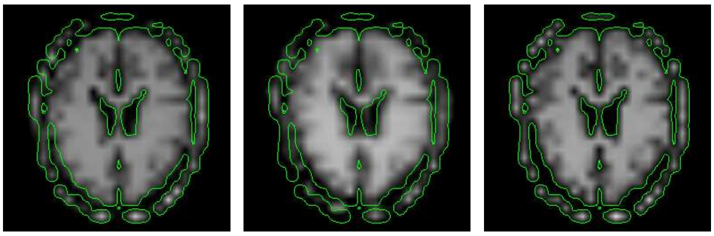

(a) Initial MSE = 525 (b) Final MSE = 1106 (c)

(d) Initial MSE = 558 (e) Final MSE = 360 (f)

Figure 5.38: Divergence at coarsest scale. Study with the Object-based model. Row 1: Resolution: 32x32. Row 2: Resolution: 64x64. Row 3: Pixel and Object-based model. Column 1: Initial moving image. Column 2: Registration result. Column 3: Target image.

presents the largest improvement of the final MSE. Conversely, the convergence of the contour-based model is slow down. In Figure 5.39, we show the effect of the curvature term on the Pixel-based model. To better see the registration differences in function of the parameters used, we zoomed in on the ventricles. The first and the last column show the initial moving image and the target image. Columns 2 and 3 show the moving image deformed with $\sigma = 2mm$ with and without the curvature constraint. Columns 4 and 5 show the moving image deformed with $\sigma = 1mm$ with and without the curvature constraint. In the first row we compared the contour of the moving image with those of the target images (green contours). We note that the accuracy of the different registration results are very similar. In the second row we show the same images but without the target contours in order to better see the border of the ventricles. Here we can see that the difference between all these results concerns the smoothness of the contours. We get smoother contours with a higher sigma and/or by using the curvature term. The advantage of the curvature term is that it constraints the contours to be smooth despite a high transformation deformability (small sigma value). Also it contributes to speed up the convergence by keeping the contours deformed by the pixel-based forces smooth during the registration process.

Finally, in Figures 5.36 and 5.37, we see that even if the contour-based model registers only the contours, the initial difference on the rest of the image is also reduced thanks to the transformation interpolation.

Convergence using the Stopping Criterion

The stopping criterion was integrated in the registration process of the real images with the following parameters: $\sigma = 1mm$, 4 scales, bijectivity scheme, $M = 16, 16, 8, 8$ from the coarsest to the finest

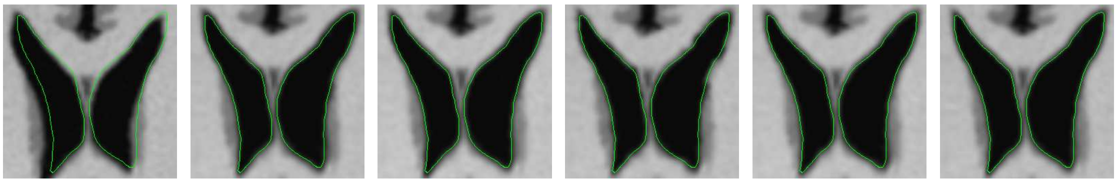

(a) Source (b) $\sigma = 2$ (c) $\sigma = 2$+Curv (d) $\sigma = 1$ (e) $\sigma = 1$+Curv (f) Target

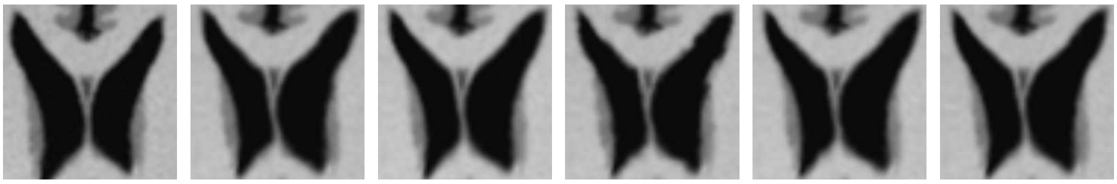

(g) Source (h) $\sigma = 2$ (i) $\sigma = 2$+Curv (j) $\sigma = 1$ (k) $\sigma = 1$+Curv (l) Target

Figure 5.39: Effect of the curvature constraint (Curv) on the smoothness of the ventricles contours. Results obtained with the Pixel-based model. Row 1: Deformed source image with the target contour superposed in green. Row 2: Same images without the target contours to better see the effect of the curvature term. For example Panels (j) and (k) well show the effect of the curvature term for a same sigma value.

scale and the curvature constraint. The maximum number of iterations per scale was limited to 50. The MSE functions obtained with the Pixel-based model and the Object-based model are shown in Figure 5.40. On the real data, the stopping criterion has also permit to reduce the number of iterations per scale all in keeping a similar final MSE.

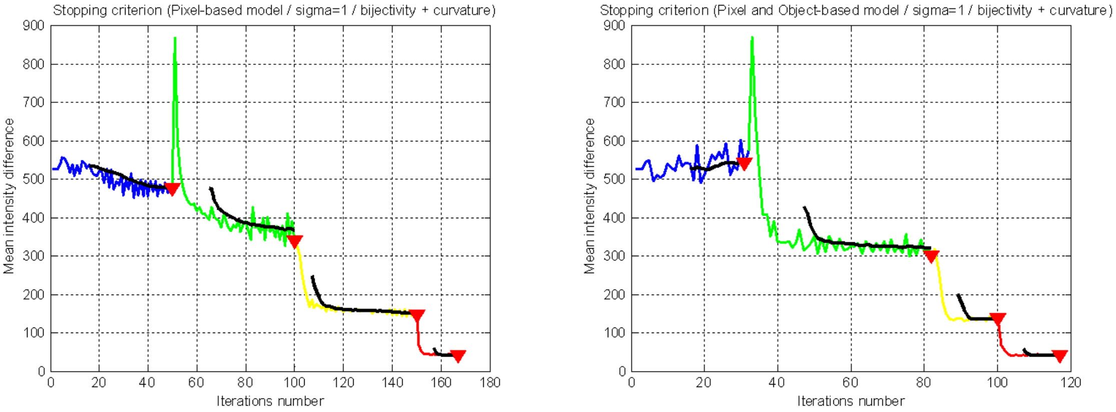

(a) Stop after 49 / 50 / 50 / 17 iterations. Final MSE = 43.

(b) Stop after 30 / 50 / 18 / 17 iterations. Final MSE = 42.

Figure 5.40: Stopping criterion with $\sigma = 1mm$ and the curvature constraint. (a) Pixel-based model, (b) Pixel and Object-based model.

5.8.4 Conclusions

In this section we have showed that:

- The constraints applied on the transformation (elasticity, bijectivity) slow down the convergence.
- The constraints applied on the speed term (object-based forces, mean curvature forces) contributes to speed up the convergence related to the pixel-based forces.
- The curvature term by preserving the smoothness of the contours permits to allow a higher deformability to the transformation (smaller sigma value).

Concerning the number of iterations, in order to speed up the algorithm computation, it would be logical to apply more iterations at coarser scales, as suggested in [165]. However, we saw that divergence can happen at the coarsest scale. The stopping criterion permits not only to estimate the optimal number of iterations at each scale but also to switch to the next scale in case of divergence.

5.9 Comparison with the Demons Algorithm

The closest work to our active contour-based registration model is probably the well-known diffusion algorithm widely used for atlas registration: the Demons algorithm of Thirion [166]. This section aims to enhance the differences and similarities between both approaches.

5.9.1 Different Sources of Inspiration

Inspired by the Maxwell's demons in thermodynamic, Thirion proposes in [166] an original viewpoint for image registration. This method considers object boundaries selected in the target image as semipermeable membranes. The moving image is then diffused through these interfaces. This diffusion is obtained by the action of effectors (the demons) situated within the membranes. The Demons algorithm is thus designed to match selected contours.

Our model also bases its registration on selected contours. It is derived from the active contour framework, a technique originally designed for image segmentation. Our method considers object boundaries selected in the moving image (the atlas) as active contours. The atlas is registered by the attraction of these contours through their corresponding contour in the target image. This attraction is obtained by the minimization of an energy functional.

5.9.2 Extraction of the Contours Considered for the Registration

Thirion presents three versions of his algorithm that mainly differ by the extraction of the contours driving the registration. The first method, called *Demons 1*, selects all pixels where $\nabla\phi_{I,T} \neq 0$ with $\phi_{I,T}$ is the intensity function of the target image. In the second method, *Demons 2*, an edge detector is used to extract these contours. *Demons 3* addresses a particular non rigid registration problem where the moving and the target image are already segmented, i.e. a label which refers to a given structure has been assigned to each point of these images. In this case, the contour points of the target image are points between adjacent pixels whose labels are different. The advantage of the *Demons 1* and *Demons 2* models is that connected, non connected, closed and open contours can drive the registration. The limitation is that all contours of the target image are considered. We will show in Section 6.3 that this can create mismatching in presence of inconsistencies between the moving and the target image. In *Demons 3*, only closed contours can be represented in the labeled version of the moving and target image but this method permits to eliminate possible inconsistencies.

In our registration approach, the contours to match are selected manually or with a segmentation method in the moving image (the atlas). Then these active contours are represented implicitly by a level set function. We have first tested our model with a signed distance function ϕ_d [135]. The limitation of this representation is that one level set function can represent several objects in an image but these objects can not be connected. In the segmentation framework, connected contours are usually represented by the intersection of two signed distance functions. We have then proposed to use a label function ϕ_L to define an arbitrary number of connected or non connected closed objects. Opposite to ϕ_d, ϕ_L permits to represent closed and connected objects by only one function. As in *Demons 3*, the level set function allows to select the contours that have to drive the registration. The advantage of our model is that this label function can be defined on the moving image only.

5.9.3 Computation of the Driving Forces

The Polarity Information

In the Demons algorithm, the action of a demon is modeled by a vector normal to the object's contours of the target image. A convention defines this vector as oriented from the inside of the object to the outside. Practically, these object contours can be closed or open and the vector corresponds simply to the gradient of the target image. Thus the inside of the object is the side of the contour with the lowest intensity and the outside is the side with the highest intensity. Then the demon pushes locally the moving image inside the object if the amplitude of the force computed at this point is negative, and outside if the amplitude of the force is positive. The sign of the diffusing forces gives the direction of the registration. Their magnitude sets the speed of the registration. To speed up the process, the amplitude of the diffusion forces are threshold to a constant when the moving contours are far away from their target contour and decrease then the moving contours get close to their target.[*]. Thus the definition of a demon relies on a polarity information as the region-based forces of the AC framework (see Figure 5.41). Thirion had noticed this analogy. In [166], he had mentioned that the closest work to his algorithm was the snake model of Ronfard et al. [146]. This snake model proposes to use region-based forces instead of the usual boundary-based forces of the original Kass model [98]. The basic idea of this model is that all the points of the active contour with a neighborhood that fits the object are pushed outside by centrifugal forces. Conversely, all the points of the active contour with a neighborhood that fits the background are pulled inside by centripetal forces.

Evolution Equation derived from an Energy

In [166], the design of the evolution equation of the Demons algorithm was intuitively derived from the optical flow formulation. In the literature one may find some attempts to reformulate this approach in a variational framework. In [32], it was shown that Demons can be viewed as a low-order approximation to the partial derivation equation (PDE) derived from the sum of squared intensity differences energy. The evolution equation of the most common version of the Demons algorithm corresponds to:

$$\frac{\partial u(x,t)}{\partial t} = v(\phi_I(x+u(x,t))\frac{\bigtriangledown G_\sigma * \phi_{I,T}(x)}{\mid \bigtriangledown G_\sigma * \phi_{I,T}(x) \mid}, \tag{5.66}$$

where $v = \phi_{I,T}(x) - \phi_I(x+u(x,t)$. $\phi_{I,T}$ needs to be convolved with a Gaussian kernel G prior because the gradient computation is very sensitive to noise.

---

[*] We have followed the same approach in the implementation of the forces used in our active contour registration model.

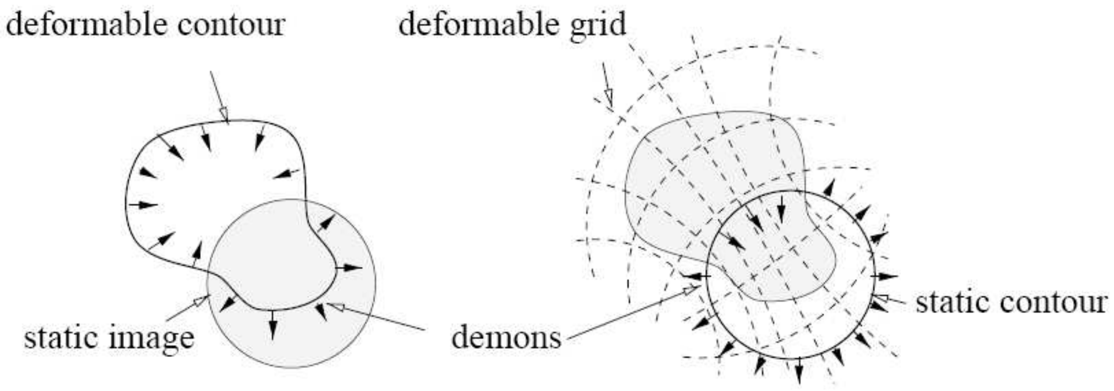

Figure 5.41: AC region-based forces and the attractive forces of the Demons algorithm are both based on polarity information. Left, a region-based active contour model for image segmentation; right, the Demons model used to perform image-to-image matching. Note that these images are reproduced from [166].

We note that the Demons algorithm uses pixel-based forces. It cannot use boundary-based forces because ϕ_I does not select the contours to match and region-based forces because the polarity information is not defined related to a closed object/region.

Advantages and Limitations

Figure 5.42 illustrates the initialization problem. Figure 5.42(a) illustrate the importance of the polarity information in attractive forces. In this example, non corresponding side of two triangles to register are close to each other. Attractive forces that do not use the polarity information, i.e. an indication about the inside and outside the contour, will match closest contour and thus will get trapped in a local minimum. For example, this would be the case with the optical flow registration approach if these triangles were represented by a binary mask or a unsigned distance function. On the other hand, the optical flow approach applied on a signed distance map or a signed label function or with the Demons algorithm on any types of representation, the convergence will be correct. This example shows that the success of a registration can sometimes depend on the polarity of the objects to register.

Figure 5.42(b) illustrates the case where the two contours to match (here the two discs) does not overlap initially. In this case the Demons algorithm and our model will fail the registration. The region-based forces of our model will make the moving disc disappear. In the demons algorithm, the target circle will diffuse the background outside its interface. In other word, the background matter will grow trough its interface. Such bad initialization is generally recovered by registering in a previous step both images with a parameter transformation (rather rigid or affine). Our AC-based registration model could also be used with a signed distance function representation and pixel-based forces. The distance function would permit to interpolate the information concerning the contour position trough the whole image and its sign indicates where is the inside and the outside of the shapes (polarity information). Finally a quite rigid deformation can be optimized by choosing a large sigma value for the gaussian regularization of the deformation field.

In both registration models, the forces computed on the contour are extending to the whole image by linear diffusion. Also both models apply a Gaussian filter (sigma) to $u(x,t)$ at each iteration to get a regular displacement field and speed up their registration with a multi-resolution approach.

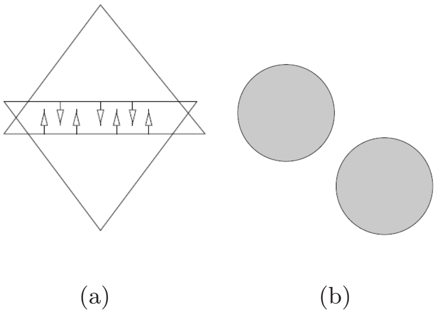
(a) (b)

Figure 5.42: Example of problematic initializations: Left, with attraction forces that does not take the polarity into account, the model can get trapped in a local minimum. Right, the Demons algorithm and the region-based forces of our model can not register objects that do not overlap. Note that these images are reproduced from [166].

5.9.4 Results

Fig. 5.43 shows atlas-based segmentation results obtained on 2-D neck CT images with the Demons algorithm and our model using region-based forces and the label function representation. Both algorithms were used with the same number of iterations and with a sigma of 1 mm. Each CT image has dimensions of 256x256 pixels and voxel dimensions are 1x1 mm^2. The atlas used for the segmentation is shown in Column 1. The contours driving the registration in our algorithm are enhanced by different colors: the external contour of the neck in green, the trachea in yellow, the jaw in red and the vertebra in blue. Fig. 5.43(f) shows the label function defining the three regions (in black, white and gray) that our algorithm has to consider. This label function was obtained from the level gray atlas (Fig. 5.43(a)) by thresholding and morphological operations. Fig. 5.43(k) shows the variability between the contours selected in the atlas and their corresponding contours in the patients. This variability is particularly large for the jaw and the vertebra. Columns 2 to 5 show the segmentations obtained on the patient images. The blue contours correspond to the Demon results and the red ones correspond to the AC model results. We see that the segmentations provide by our model are clearly more accurate than those obtained by Demon. The deformed grids help to visualize the corresponding deformation defined on the whole image domain by Demon (row 2) and the AC model (row 3). The deformation fields computed by our model are also clearly smoother than the ones obtained by Demons.

All these results were analyzed quantitatively by structure and by algorithm in Table 5.3. Two methods have been used to compare the automatic contours to manual segmentation of the patient images [57].

The first one is the following overlapping measure S:

$$S = \frac{2N(C1 \cap C2)}{N(C1) + N(C2)}, \tag{5.67}$$

with N(C1) and N(C2) are the number of pixels respectively included in the automatic and manual contours. The S value ranges from zero to one, with zero indicating no overlap and one indicating a perfect agreement between two contours.

The second similarity measure compares contours on a point-by-point basis. First a narrowband of one pixel on the inside and one pixel on the outside of the manual contours is computed. Then we compute the percentage of pixels in the automatic contours that fall within this band (Pts_in).

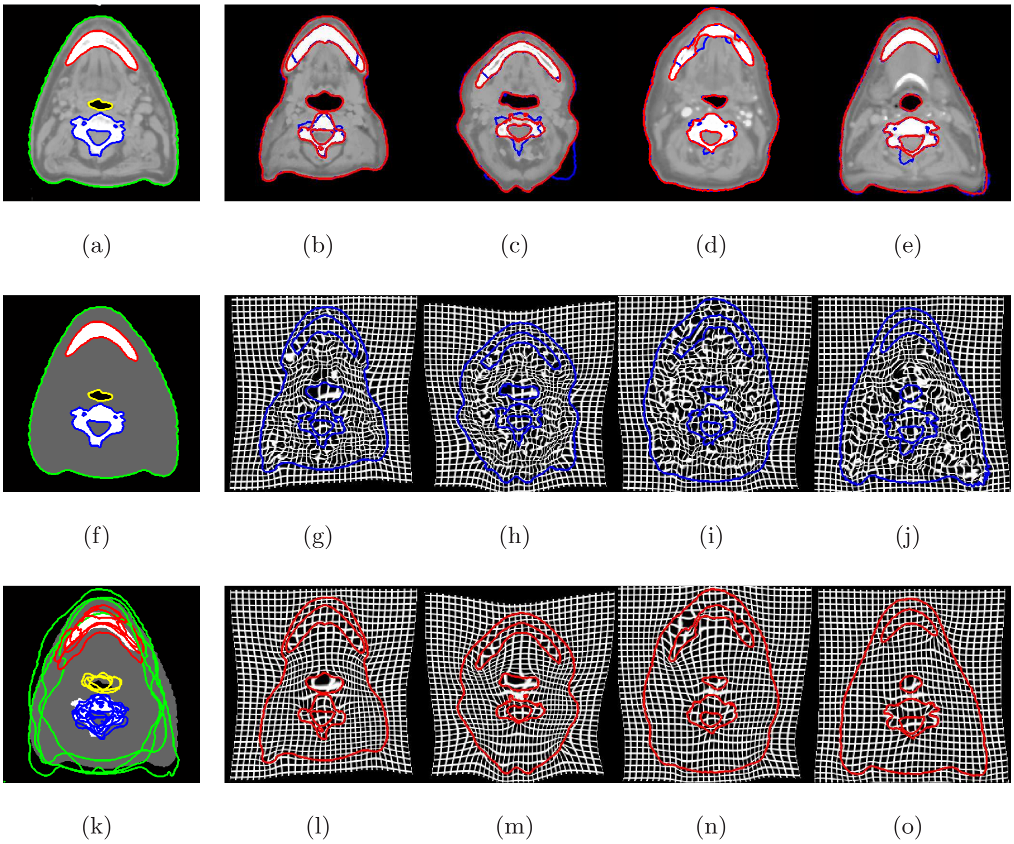
(a) (b) (c) (d) (e)

(f) (g) (h) (i) (j)

(k) (l) (m) (n) (o)

Figure 5.43: Neck CT images segmentation. Columns: 1) Atlas (MRI image, Label function, Variability of the target contours). 2)-5) Patients images. Rows: 1) On the patients images, delineations obtained by the Demons (blue) and the AC model (red). 2)-3) Deformation fields corresponding respectively to the Demon and the AC model.

Table 5.3: Mask and contour-based comparisons between the delineations obtained with the Demons algorithm (Dem.) and our AC model (Our M.).

Struct.	Mask Sim.		*Area* $[mm^2]$	Contours Sim.						*Perim* $[mm]$
				Pts_in[%]		Mean[mm]		Max[mm]		
	Dem.	*OurM.*		*Dem.*	*OurM.*	*Dem.*	*OurM.*	*Dem.*	*OurM.*	
Ext. cont.	0.99	1.00	28309	95.12	96.80	3.28	0.81	6.14	1.25	596
Trachea	0.97	0.98	599	99.12	100.00	0.38	0.00	0.50	0.00	90
Jaw	0.89	0.98	1708	85.87	97.80	3.71	0.52	8.22	1.25	243
Vertebra	0.81	0.93	1322	67.51	90.35	3.58	0.71	10.31	1.41	251

The mean and maximum distance from this band for pixels that fall outside it are also computed. We also indicated the area and the perimeter of each structure. Table 5.3 presents the average of the values obtained for each patient. Two main conclusions can be drawn from these results. First the Thirion's algorithm is trying to perform a pixel-based registration of every structures of the images even if they do not correspond between the atlas and the patient as the arteria, muscles and fat (gray area of Fig. 5.43(a)). This perturbs obviously the registration of the common structures. The proposed AC-based registration model performs a region-based registration of the structures selected in the atlas only. Then the segmentation results of the structures with large variability (jaw and vertebra) are much more accurate with the AC model. Thus, our model can recover larger deformation than the Demons algorithm.

The main advantage of our model is its capacity to register globally regions selected in the atlas while keeping local accuracies. These results show that our model can recover larger deformation than the Demons algorithm.

5.10 Discussion

In this chapter we have described the joint registration and segmentation model that we propose to integrate active contour-based constraints in a non parametric atlas registration process. The particularity of our model compared to the state of the art methods presented in Chapter 4 is that it was designed to use any type of forces coming from the AC framework. Our model is closer to the PDE-based approach proposed by Bertalmio [17] and Vemuri [168] than the variational technique proposed by Yezzi [177]. The first approach consists to extract the deformation field from the tracking of a level set function. The second approach propose to jointly segment both images and register their segmentation. We found that the first approach was more appropriated to introduce local constraint directly on the computation of the deformation field than the second one.

The general formulation of our model is derived from the usual implicit contour representation of the AC framework, the signed distance function and the well-known non parametric registration algorithm, the optical flow method. This way, we have obtained an evolution equation very close to the one used in the parametric AC segmentation model. The originality of this equation is that the evolution of the implicit contour representation is depending on a dense force field. In the usual level set framework, the active contour converges to the contour of the object to segment by iteratively pushing up or down the values of its implicit representation.

In particular we have pointed out the notion of polarity information contained in the signed distance function representation. This information is given by the gradient of the implicit representation. It indicates where is the inside and the outside of the modeled contour. This information is important for the computation of the region-based forces of the AC segmentation framework. From this information, we have proposed a multi-phase representation based on one label function.

We have also presented the different type of forces we can find in common AC segmentation model. There exist two types of forces: the regularization forces and the attractive forces. The regularization forces ensure that the contours stay well smooth during their evolution. The most commonly used are the mean-curvature forces. The attractive forces attract the active contours to their target contour. Some of these attractive forces use pixel-based information. We have thus called them the pixel-based forces. The advantage of the pixel-based forces is that they can perform very local registration. However they are very sensitive to noise and are limited to recover small deformation. The other type of attractive forces use boundary-based or region-based information. We have called them the object-based forces. This type of forces is very particular to the AC framework. They can recover larger deformation than pixel-based forces and are more robust to noise. Their main limitation is they are very sensitive to the initial contour position. The contour they drive can disappear if it is not initially superposed to its target object. We saw that regularization and pixel-based forces can be computed at each point of any type of contours representation. The boundary-based forces and region-based forces can be computed only on the interface of contours representation that can select driving contours in the moving image. Finally region-based forces needs a contour representation that indicates the polarity of the modeled regions.

We saw in Chapter 2 that usual registration processes match two images with a global to local registration. The global registration puts both images in the same position and brings thus their corresponding contour close. The local registration recover the local variabilities of these corresponding contours. Inspired by this strategy, we have proposed a hierarchical atlas registration process permitting to combine the advantages of the pixel-based forces and the object-based forces. First we use object-based forces to globally register selected image regions. Then pixel-based forces are used to register the images locally. It is sometimes useful to decompose the region registration into two hierarchical layers. The registration of a region can help the registration of its depending regions. For example we will see in Chapter 7 that the deformation generated by a tumor growth can push surrounding structures close to their target contour.

To obtain a dense deformation field, the displacement of the active contours has to be interpolated to the whole image. For that, we have proposed two types of interpolation. The first one consists to interpolate the contours deformation by using the different levels of the signed distance function representation. This method propagates the deformation on the whole image in a quasi linear way. However, the nature of this representation limits the model to a two phases registration and the generated dense deformation field is always radial to the considered contours. This technique can lead to a reasonable approximation of the deformation on homogenous region but we saw that it is not appropriated for texture regions. In the second method, we propose to perform this interpolation by diffusion as it is done in common optical flow algorithms. This method permits to use the label function representation and to constraint the interpolation thought texture region by pixel-based forces. As we are working with an image-based algorithm, on homogenous regions, we do not have visual indication on how interpolate the contour deformations. The only constraint we have concern the smoothness and the bijectivity of the deformation field. In medical imaging, we find registration model using interpolation techniques that propagate the displacement of selected image contours according to a physical model of the mater deformation. These types of interpolation are used in the elastic models [14], the fluid models [45] and the biomechanical finite-element models [70, 71, 122]).

Finally, we showed that our active contour registration algorithm using region-based forces has a lot of similarities with the well-known Demons algorithm [166]. The main advantage of our model is its capacity to register globally regions selected in the atlas while keeping local accuracies. Moreover results have shown that our model can recover larger deformation than the Demons algorithm.

However our registration model using region-based forces keeps a limitation of the AC framework: the atlas contours have to overlap the target contour otherwise they disappear.

In the next chapter, we present supervised forces based on information theory. These forces could be used in our active-contour based registration model to drive the non rigid registration of the atlas.

Supervised Models based on Information Theory

6

6.1 Introduction

In this chapter, we present two region-based models for supervised segmentation of scalar images using active contours and information theory. This work was published in [64]. Note that for the result presented in this chapter, these models have been used to perform an atlas-based segmentation by contour morphing but they could be included in our active-contour based registration model (Chapter 5) to drive the non rigid registration of the atlas.

A model is unsupervised when the region descriptor is only extracted from the image to segment. When the region descriptor is based on a feature of reference (prior knowledge), the model is supervised. So far, three types of supervised segmentation models have been presented. In the first model proposed by Bertalmio et al. [17], the prior knowledge comes from the deformation of a reference image to the image to segment by a morphing partial differential equation (PDE). The deformation of contours of interest selected in the reference image by an active contour are simultaneously tracked by a second PDE. This technique has been described in details in Chapter 4. The second model presented by Paragios et al in [138], consists to include in a segmentation model, prior knowledge about the desired intensity properties of the different regions to detect, by minimizing an energy derived from an a posteriori density function. This density function defines the probability that a given pixel belongs to a particular region knowing its intensity value. The last model was presented by Jehan-Besson et al. in [95]. They propose a different approach that consists in minimizing the ”distance” between the pdfs of regions selected in the image to segment and pdfs of references. They propose to measure this ”distance” with the Kullback-Leibler divergence measure, the Hellinger distance or the chi-2 function comparison function. In this paper, we investigate another important information theoretical measures, the entropy and the joint-entropy, to carry out a two-phase segmentation of scalar images in a supervised way.

In our first supervised model, we propose to carry out a region competition by optimizing an energy designed to be minimal when the entropy of the inside and outside regions of the evolving active contour are close to those of a reference image. The probability density functions (pdfs) used by this model can be computed in a preprocessing step on a reference image. This substantially reduces the computational complexity making this model fast. On the other hand, this implies that the reference image and the image to segment have similar pdfs. When the pdfs are too different or both images are not from the same modality we propose a second segmentation model computationally more expensive but more robust to intensity differences. This second model is based on an information measure extensively used for image registration, the joint entropy. The performance of both models is demonstrated on a variety of 2D synthetic data and medical images. They are also compared in term of segmentation accuracy and computational cost with an entropy-based unsupervised segmentation model recently proposed.

The remainder of this Chapter is organized as follow. In section 6.2.1, we present the two unsupervised models that Herbulot et al. [87, 88] have proposed for unsupervised segmentation of scalar and vectorial images (color images or motion vector fields). These models are the main source of inspiration for this work. In section 6.2.2, we show how we adapt these models to perform the segmentation of scalar images based on a reference image. We will see that one of these models used in a supervised way leads to the minimization of energy that has a very close form to the one proposed by Paragios. In section 6.3, we compare on a variety of 2D synthetic and medical images the performance of the two supervised models we propose with the unsupervised model for scalar image segmentation in [87]. Finally, these three segmentation models are discussed and conclusions are drawn in section 6.4.

6.2 Method

6.2.1 The Unsupervised Segmentation Models of Herbulot

In [87, 88], Herbulot et al. propose to carry out the segmentation of gray-scale and vectorial images composed of an object and a background by minimizing the entropy (H) of each region. In this context, the entropy is used to measure the homogeneity of a region.

Segmentation of Scalar Images

Following the Shannon definition [153] and the non parametric approximation of Ahmad and Lin [4], the marginal entropy* on a fixed region Ω is computed as follow:

$$H(q(\Omega)) = \int_{\Omega} \varphi(q(I(x), \Omega))dx, \tag{6.1}$$

with

$$\varphi(q(I(x), \Omega)) = -\frac{1}{|\Omega|} ln[q(I(x), \Omega))], \tag{6.2}$$

where $\varphi(.)$ as a region descriptor, $q(I(x), \Omega)$ is the probability density functions (pdf) associated with an observation $I(x)$ for a fixed region Ω at a given moment and $|\Omega|$ is the area of Ω. In this approach, the image intensity $I(x)$ is considered as a random variable.

The pdf of intensity of the region Ω is estimated in a non-parametric way using the Parzen windows method [141]:

$$q(I, \Omega) = \frac{1}{|\Omega|} \int_{\Omega} G_{\sigma}(I - I(\hat{x}))d\hat{x}, \tag{6.3}$$

where G_{σ} is the Gaussian kernel with 0-mean and σ^2 variance.

---

[*] The entropy was defined with the neperian logarithm because this logarithm has the simplest derivative: $ln(q)' \rightarrow \frac{1}{q}$.

Minimizing functional (6.1) involves the computation of its derivative. By using the shape derivative tool [10, 93], the Eulerian derivative in the direction $\mathbf{V}$ of the criterion (6.1) corresponds to:

$$< H, \mathbf{V} >= \int_{\Omega} \frac{\partial \varphi(I(x), \Omega, \mathbf{V})}{\partial \tau} dx - \int_{\partial\Omega} \varphi(I(x), \Omega))(\mathbf{V} \cdot \mathcal{N}) ds, \tag{6.4}$$

where $\frac{\partial \varphi(I(x), \Omega, \mathbf{V})}{\partial \tau}$ is the shape derivative. The region integral considers the dependence of the criterion with the region Ω and the contour integral considers the dependence of the criterion with the contour $\partial\Omega$.

It is demonstrated in [87, 88] that Equation (6.4) can be rewrite as the following contour integral:

$$< H, V >= -\int_{\partial\Omega} (A(I(x), \Omega) + B(I(x), \Omega))(\mathbf{V} \cdot \mathcal{N}).ds \tag{6.5}$$

$A(I(x), \Omega)$ is a term coming from the dependance of the descriptor with the region and $B(I(x), \Omega)$ is a term coming from the dependance of the descriptor with the contour.

In our case,

$$\begin{aligned} A(I(x), \Omega) = -\frac{1}{|\Omega|} \int_{\Omega} \frac{\partial \varphi(q(I(x), \Omega))}{\partial q} [q(I(x), \Omega) - \\ G_{\sigma}(I(x) - I(\hat{x}))] d\hat{x}, \end{aligned} \tag{6.6}$$

with

$$\frac{\partial \varphi(q(I(x), \Omega))}{\partial q} = -\frac{1}{|\Omega|} \frac{1}{q(I(x), \Omega)}, \tag{6.7}$$

and

$$B(I(x), \Omega) = \varphi(I(x), \Omega). \tag{6.8}$$

According to the Cauchy-Schwartz inequality, the fastest way to decrease $H(q(\Omega))$ s.t $< H, \mathbf{V} >= \int_{\partial\Omega} F(\mathbf{V} \cdot \mathcal{N}) ds$ is obtained by choosing $\frac{\partial C}{\partial \tau} = -F\mathcal{N}$ which leads to the evolution equation:

$$\frac{\partial C}{\partial \tau} = ([A(I(x), \Omega) + \varphi(I(x), \Omega)] + \lambda\kappa)\mathcal{N}. \tag{6.9}$$

where κ is the curvature of the contour C which regularizes the evolving curve and λ is a weight.

To produce two regions with two pdfs as homogenous as possible, the functional (6.1) is minimized by using the region competition approach introduced by Zhu and Yuille in [180]. Thus we look for the regions that minimize the following energy:

$$E_H(q_{in}, q_{out}) = H(q(\Omega_{in})) + H(q(\Omega_{out})) + \lambda \int_{\partial\Omega} ds, \tag{6.10}$$

where Ω_{in} is the object region and Ω_{out} is the background region. q_{in} and q_{out} are their corresponding pdfs and $\int_{\partial\Omega} ds$ is the regularization energy.

The energy (6.10) leads to the following evolution equation:

$$\begin{aligned} \frac{\partial C}{\partial \tau} &= ([A(I(x), \Omega_{in}) + \varphi(I(x), \Omega_{in})] + \\ &\quad [A(I(x), \Omega_{out}) + \varphi(I(x), \Omega_{out})] + \lambda\kappa)\mathcal{N}. \end{aligned} \tag{6.11}$$

Solving Equation (6.11) implies the segmentation of two homogenous regions, which are here the object of interest and the background. In the following of this paper, this marginal entropy-based unsupervised segmentation model will be called ME.

Segmentation of Vectorial Images

For the segmentation of vectorial images, Herbulot proposes another segmentation model based on the joint-entropy. The joint-entropy of a fixed region Ω is computed as follows:

$$H(q(I_1, I_2, \Omega)) = \int_\Omega \varphi(q(I_1(x), I_2(x), \Omega))dx, \tag{6.12}$$

with

$$\varphi(q(I_1(x), I_2(x), \Omega)) = -\frac{1}{|\Omega|} ln[q(I_1(x), I_2(x), \Omega))], \tag{6.13}$$

and

$$\begin{aligned} q(I_1(x), I_2(x), \Omega) = \frac{1}{|\Omega|} \int_\Omega \\ G_\sigma(I_1(x) - I_1(\hat{x}), I_2(x) - I_2(\hat{x}))d\hat{x}, \end{aligned} \tag{6.14}$$

where $q(I(x_1), I(x_2), \Omega)$ is the joint probability density functions (pdf) associated with the observations $I(x_1)$ and $I(x_2)$ for a fixed region Ω at a given moment. $G_\sigma(.,.)$ is the Gaussian kernel in 2D.

Note that the derivative of the joint-entropy functional (6.12) is similar to the one of the entropy functional (6.1). Thus we can directly deduce the evolution equation corresponding to the joint-entropy-based segmentation model by replacing in (6.11) the probability distribution $q(I(x), \Omega)$ by the joint probability distribution $q(I(x_1), I(x_2), \Omega)$:

$$\begin{aligned} \frac{\partial C}{\partial \tau} &= ([A(I_1(x), I_2(x), \Omega_{in}) + \varphi(I_1(x), I_2(x), \Omega_{in})] + \\ &\quad [A(I_1(x), I_2(x), \Omega_{out}) + \varphi(I_1(x), I_2(x)), \Omega_{out}] + \lambda\kappa)\mathcal{N}, \end{aligned} \tag{6.15}$$

where

$$\begin{aligned} A(I_1(x), I_2(x), \Omega) = -\frac{1}{|\Omega|} \int_\Omega \frac{\partial \varphi(q(I_1(x), I_2(x), \Omega))}{\partial q} \cdot \\ [q(I_1(x), I_2(x), \Omega) - G_\sigma(I_1(x) - I_1(\hat{x}), I_2(x) - I_2(\hat{x}))]d\hat{x}, \end{aligned} \tag{6.16}$$

with

$$\frac{\partial \varphi(q(I_1(x), I_2(x), \Omega))}{\partial q} = -\frac{1}{q(I_1(x), I_2(x), \Omega)}. \tag{6.17}$$

In [87, 88], these two entropy-based models were presented to perform unsupervised segmentation, i.e without prior knowledge on the pdfs of the regions to segment. Their pdfs have thus to be recomputed at each iteration of the process to correspond to the regions defined by the current position of the active contour.

6.2.2 Our Supervised Segmentation Models

In this section, we propose to use the models presented in the previous section to include in a segmentation model prior knowledge about the intensity distribution of the regions to detect. In this work, these prior intensity distributions are extracted from a reference image in which we know the segmentation of the object of interest. This reference image can be either a source image globally put in correspondence to the image to segment with an affine registration (as in the atlas-based segmentation methods [116, 118]) or the previous frame in a video sequence. Note that the reference image gives also to the active contour an initial position close to the target contour. In this supervised segmentation framework, we will call the reference image "atlas" and the image to segment "target image".

Atlas-based Marginal Entropy Model (ABME)

Let q_{prior} be the prior pdf of a fixed region Ω extracted from the atlas.

Inspired by the entropy definition (6.1), we define the following functional energy $E_{q_{prior}}$ that aims to segment regions having entropies close to the corresponding regions in the reference image:

$$H(q_{prior}) = \int_{\Omega_{in}} \varphi(q_{prior,in}(I(x)))dx + \int_{\Omega_{out}} \varphi(q_{prior,out}(I(x)))dx, \tag{6.18}$$

with

$$\varphi(q_{prior}(I(x)) = -\frac{1}{|\Omega|} ln[q_{prior}(I(x))], \tag{6.19}$$

where $I(x)$ is an intensity value of the target image. Thus if the minimization of the energy (6.18) leads to a perfect segmentation of Ω_{in} and Ω_{out} in the target image, then $q_{in} = q_{prior,in}$ and $q_{out} = q_{prior,out}$.

As q_{prior} is constant, the descriptor $\varphi(.)$ does not depend on the region Ω. Thus, shape derivative $\frac{\partial \varphi(q_{prior}(I(x))}{\partial \tau}$ is equal to zero. The Eulerian derivative in the direction $\mathbf{V}$ of the criterion (6.18) corresponds simply to the contour integral:

$$< E_{q_{prior}}, \mathbf{V} >= - \int_{\partial\Omega_{in}} \varphi(q_{prior,in}(I(x)))(\mathbf{V} \cdot \mathcal{N})ds - \int_{\partial\Omega_{out}} \varphi(q_{prior,out}(I(x), \Omega))(\mathbf{V} \cdot \mathcal{N})ds. \tag{6.20}$$

With the region competition and the regularization term we obtain the following evolution equation:

$$\frac{\partial C}{\partial \tau} = -(\varphi(q_{prior,in}(I(x))) - \varphi(q_{prior,out}(I(x))) + \lambda\kappa)\mathcal{N}. \tag{6.21}$$

This segmentation model assumes that corresponding regions between the reference and target images have similar intensity distributions. When these distributions are too different we propose to use the model described in section 6.2.2.

Related Work to ABME

In [138], Paragios et al. presents an energy that has a very close form to the entropy-based energy with prior knowledge (6.18). The main difference is that they deduce their energy from the a posteriori density function $q(P(\Omega)|I(x))$ describing the membership of a pixel to a particular region following its intensity $I(x)$. $P(\Omega) = \{\Omega_{in}, \Omega_{out}\}$ represents the partition of the image domain into two non-overlapping regions $\{\Omega_{in} \cap \Omega_{out} = \varnothing\}$.

With the Bayes rule, this density function can be rewritten as:

$$q(P(\Omega)|I(x)) = \frac{q(I(x)|P(\Omega))}{q(I(x))} q(P(\Omega)). \tag{6.22}$$

By assuming that all the partitions are a priori equally possible they ignore the constant terms $p(I(x))$ and $p(P(\Omega))$. Thus the density function (6.22) becomes:

$$q(P(\Omega)|I(x)) = q(I(x)|P(\Omega)) = q(I_{in}(x)|P(\Omega_{in}))q(I_{out}(x)|P(\Omega_{out})). \tag{6.23}$$

By assuming that the points within each region are independent they obtain:

$$\begin{aligned} q(I_{in}(x)|P(\Omega_{in})) &= \prod_{\Omega_{in}} q_{prior}(I(x),\Omega_{in}) \\ q(I_{out}(x)|P(\Omega_{out})) &= \prod_{\Omega_{out}} q_{prior}(I(x),\Omega_{out}) \end{aligned} \tag{6.24}$$

Finally, as the maximization of an a posteriori probability is equivalent with the minimization of the $-log()$ function of this probability they get the following functional energy:

$$E(q_{prior}) = -log\left[\prod_{\Omega_{in}} q_{prior,in}(I(x)) \prod_{\Omega_{out}} q_{prior,out}(I(x))\right] \tag{6.25}$$

$$= -\int_{\Omega_{in}} \varphi(q_{prior,in}(I(x)))dx - \int_{\Omega_{out}} \varphi(q_{prior,out}(I(x),\Omega))dx$$

In conclusion, our a priori entropy-based Energy (6.18) differs from the a posteriori density function-based Energy (6.25) by the normalization by the region area.

Atlas-based joint Entropy Model (ABJE)

In the reference work [88], I_1 and I_2 of the joint entropy-based segmentation model (Equation 6.15) correspond to two channels of a color image or the components of a 2D dense deformation field. In the model presented here, I_1 corresponds to the target image and I_2 corresponds to the atlas. To be able to compute the joint probability (6.14), the atlas has to be deformed to follow the evolution of the active contour. During the segmentation process, the atlas I_2 at time t will be thus given by the dense deformation field $u(x,t)$ and the initial reference image $I_2(x,0)$ such that:

$$I_2(x,t) = I_2(x + u(x,t), 0). \tag{6.26}$$

$u(x,t)$ is extracted by tracking the active contour motion. To compute it, we use our active contour registration model using pixel-based forces and the signed distance function representation ϕ_d (Chapter 5). In this method, $u(x,t)$ is extracted from the implicit representation of the contour by the level set function ϕ of Osher and Sethian [135]. Let $\phi_{d,T}(x)$ be the level set representation of the current active contour and $\phi_d(x,0)$ be the level set representation of the initial contour. $u(x,t)$ is obtained by solving the following partial derivative equation (PDE):

$$\frac{\partial u(x,t)}{\partial t} = -v\frac{\bigtriangledown\phi}{|\bigtriangledown\phi|}, \tag{6.27}$$

where

$$F(x,t) = (\phi_{d,T}(x) - \phi_d(x,t)), \tag{6.28}$$

and

$$\phi_d(x,t) = \phi_d(x + u(x,t), 0). \tag{6.29}$$

In fact, $v(x,t)$ measures the distance between the contour represented by $\phi_d(x,t)$ and the target contours represented by $\phi_{d,T}(x)$. Note that when the level set function is carried over by the current deformation field as in (6.29), the property of signed distance function will be violated as soon as the registration starts and thus causes numerical inaccuracy. In order to avoid this, the level set function $\phi_d(x,t)$ is re-initialized at each iteration.

Inspired by the optical flow regularization where a Gaussian filtering G_σ is applied on the deformation field at each iteration, the total deformation field is obtained as follows:

$$u(x, t+1) = (u(x,t) + \frac{\partial u(x,t)}{\partial t}) * G_\sigma, \tag{6.30}$$

where $*$ is the convolution operator. This Gaussian filtering permits to remove discontinuities that appear on the skeleton of the $\phi_d(x,t)$ due to the distance map property while propagating the correction to the whole deformation field. The Gaussian filtering necessitates to set a parameter σ.

By including the deformation of the reference image in the joint-based segmentation model (6.15), we obtain the following evolution equation:

$$\begin{aligned} \frac{\partial C}{\partial \tau} &= ([A(I_1(x), I_2(x+u,0), \Omega_{in}) + \varphi(I_1(x), I_2(x+u,0), \Omega_{in})] \qquad (6.31) \\ &+ [A(I_1(x), I_2(x+u,0), \Omega_{out}) + \varphi(I_1(x), I_2(x+u,0), \Omega_{out})] + \lambda\kappa)\mathcal{N}. \end{aligned}$$

6.3 Results

Figure 6.1 shows the segmentation results obtained on 2D synthetic images (Rows 1, 2 and 3) and 2D medical images (Rows 4, 5 and 6) with the two supervised models we have presented. Each image has dimensions of 100x100 pixels and pixel dimensions are 1x1 mm^2. These results are compared with those obtained with the unsupervised model for the segmentation of scalar image proposed by Herbulot et al. in [87]. The atlas and the target images are respectively shown in Columns 1 and 2. Column 3 shows the result obtained with the marginal entropy model (ME) (Equation (6.11)). Column 4 shows the results obtained with the atlas-based marginal entropy model (ABME) (Equation (6.21)) and Column 5 shows the results obtained with the atlas-based joint-entropy model (ABJE) (Equation (6.31)). The initial position of the active contour is shown in green on the atlas (Column 1). The segmentation result is shown in green on the images of Columns 3, 4 and 5. The target contours are copied in red onto all of these images to visualize the initial differences and the quality of the segmentation. These target contours, considered as ground truth, were obtained from the target image by manual segmentation. The two values under the images of Columns 3, 4 and 5 represent respectively the number of iterations necessary to obtain the corresponding result and the mask overlap ratio between this automatic segmentation and the ground truth. The value of this ratio ranges from zero to one, with zero indicating no overlap and one indicating a perfect agreement between both masks (for more detail about this mask similarity measure see [57]).

Concerning the results on synthetic images. Row 1 presents synthetic images with two regions gray and black. The corresponding regions between the atlas (Panel 6.1.1) and the target image (Panel 6.1.2) have same pdfs. Panels 6.1.1 shows that the object of interest contains one region, the gray one. In this case, the three models gives similar segmentation results (see Panels 6.1.3, 6.1.4 and 6.1.5). The fastest one is the ABME model because it uses pdfs computed in a preprocessing step on the atlas. Row 2 presents synthetic images containing 3 regions (white, gray and black). Again the corresponding regions between the atlas (Panel 6.1.6) and the target image (Panel 6.1.7) have same pdfs. Panel 6.1.6 shows that the object of interest contain two regions (white and gray). In this case, the ME model segments only the gray region (Panel 6.1.8). Note that the gray region was the region the most important inside the initial contour (Panel 6.1.7). The two supervised models segment the same regions that the object of interest in the atlas (see Panels 6.1.9 and 6.1.10). Row 3 presents also synthetic images containing three regions but this time the corresponding regions between the atlas (Panels 6.1.11) and the target image Panel 6.1.12) have different pdfs. Note that the background of the atlas has the same pdf that the big circle in the target image and conversely.

Again, the unsupervised model segments the region the most important inside the initial contour (Panel 6.1.13). On the other hand, the ABME model segments the background and some points of the object of interest that belongs to its pdfs of reference (Panel 6.1.14). In this case, only the ABJE model succeeds in the segmentation of the object of interest (Panel 6.1.15).

Concerning the results on real images. Row 4 presents results on computed tomography (CT) of the neck area. The object to segment in the target image is the jaw. The corresponding regions between the atlas (Panel 6.1.16) and the target image (Panel 6.1.17) have similar pdfs. The best results were obtained with the supervised segmentation models (Panels 6.1.19 and 6.1.20). The ABME model was the most fast and the most accurate. On the other hand, the ME model segments some homogeneous parts of the tissue surrounding the jaw. Row 5 presents results on brain MR images. The objects to segment in the target image are the lateral ventricles. The reference image (Panel 6.1.21) and the target image (Panel 6.1.22) beeing of different modalities (T1 and T2) the corresponding regions have different pdfs. This time, the ME model and the ABJE model succeed in the segmentation of the ventricles. With the ABME model, the active contour tends to disappear as there is no intensity value corresponding to the reference pdf of the ventricles. Row 6 presents results on an anatomical slide. The objects to segment in the target image is the eye. The target image (Panel 6.1.27) by deforming the atlas with rigid deformation and by changing its window level. Thus it has different pdfs compare to the atlas (Panel 6.1.26). The best segmentation result was obtained by the ABME model (Panel 6.1.30). The ME model divides the image in two homogenous regions. Thus the segmented object include part of the tissues surrounding the eyes and presents holes inside the eye. The ABME model segments only the parts of the eye with intensities corresponding to the pdf of reference.

6.4 Discussion and Conclusions

In this Chapter, we have presented two supervised models based on information theory for the segmentation of scalar images. They permit to segment an object in an image by using prior knowledge coming from a reference image or atlas. This prior knowledge is an initial position for the active contour close to the target contours and prior pdfs concerning the two regions to detect in the target image. The first model based on the entropy addresses the cases where the pdfs of the objects and the background in the reference image are similar to those to segment in the target image. The second model uses the joint-entropy to deal with the cases when these pdfs are too different. Both models are compared with an unsupervised entropy-based model recently proposed by Herbulot et al in [87, 88]. Results showed that when these pdfs are similar the supervised entropy-based model has the lowest computational cost because the pdfs of reference can be computed in a preprocessing step. When these pdfs are too different the supervised joint-entropy based model is the most robust model. On the other hand, this method is more expensive computationally because the joint pdfs have to be computed at each iterations and a second PDE have to be solve to find the deformation field that deforms the reference image to follow the evolution of the active contour. The unsupervised model is faster to deal with different pdfs but the result is very sensitive to the initial position of the contours and the object or the background to segment in the target image have to satisfy the homogeneity criterion. In [120], we illustrate the use of our entropy-based models for an application in 3D medical images segmentation and coding. In [63], the marginal entropy-based model was used to drive the non rigid registration of an atlas.

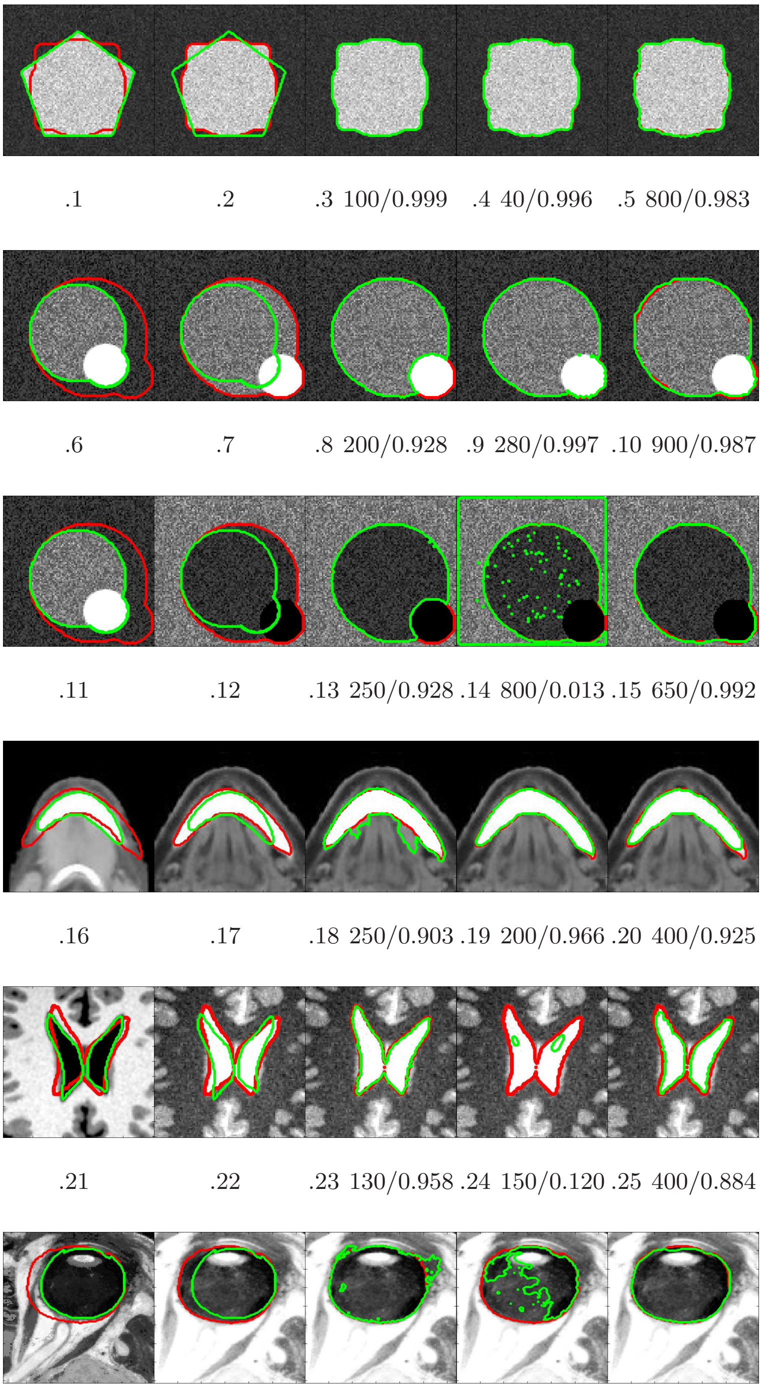

.1 .2 .3 100/0.999 .4 40/0.996 .5 800/0.983

.6 .7 .8 200/0.928 .9 280/0.997 .10 900/0.987

.11 .12 .13 250/0.928 .14 800/0.013 .15 650/0.992

.16 .17 .18 250/0.903 .19 200/0.966 .20 400/0.925

.21 .22 .23 130/0.958 .24 150/0.120 .25 400/0.884

.26 .27 .28 150/0.962 .29 500/0.676 .30 800/0.983

Figure 6.1: Segmentation results. Columns: 1) Reference image. 2) Image to segment. 3) Unsupervised marginal entropy model (ME). 4) Atlas-based marginal entropy model (ABME). 5) Atlas-based joint-entropy model (ABJE). Rows: 1) Synthetic images: 2 regions, same pdfs. 2) Synthetic images: 3 regions, same pdfs. 3) Synthetic images: 3 regions, different pdfs. 4) Neck CT images: similar pdfs. 5) T1/T2 Brain MR images: different pdfs. 6) Anatomical eye images: different pdfs. Values under the images of Columns 3, 4, 5: Number of iterations/Mask overlap measure.

Part IV

Applications

7

Potential Applications in Medical Imaging

7.1 Introduction

The main objective of this thesis is to design an algorithm for atlas-based segmentation which combines the advantages of the dense deformation field computed by the registration algorithms, with local segmentation constraints coming from the active contour (AC) framework. In Chapter 5, we have presented the general formulation of a non parametric model from which we can derive a large variety of segmentation/registration algorithms. These algorithms differ by their type of registration forces and by the representation of the contours driving the registration. We have proposed to classify these derived active contour-based registration models in three categories: the Pixel-based models, the Region-based models and, the Region-based and Pixel-based models[*]. This chapter aims to present segmentation problems in medical imaging that suit well to each one of these categories of model[†].

Figure 7.1 shows the organization of this Chapter. The presented applications are divided in three sections according to the type of active contour-based registration model used.

1. **Pixel-based Models** Section 7.2 is dedicated to the Pixel-based model using the signed distance function representation. This Section begins to present on real 2D data, different examples of constraints that this model allows to include in a registration process. Then, we show how this model can be used to grow a large space occupying tumor in an atlas and to propagate the deformation generated by this tumor on the surrounding structures. After that, we demonstrate on neck CT images that the position of the hardest tissues determines the po-

---

[*] In this Chapter, we have omitted the Boundary-based models because of their large sensitivity to noise and their limitation to exploit the prior knowledge coming from an atlas.

[†] The active contour-based registration models have been implemented in the ITK environment [104]. For the application on 3D images, we will give the average processing time related to the image registration. The algorithms have been run on a computer having the following characteristics: Intel(R) Pentium(R), 4 CPU, 2.8 GHz, 1.00 GB of Ram. Note that these processing times could be certainly reduced by optimizing the programming codes.

sition of the softer surrounding tissues. The hierarchical registration approach requires thus that the hardest anatomical tissues are registered first. Finally, we present an atlas-based application for a statistical study on neuronal connections. In this application, our active contour-based registration model has been used to estimate the position of regions of interest on the surface of the left and right thalami (small structures of the brain).

2. **Region-based Models** Section 7.3 is dedicated to the Region-based model using the label function representation. We will see that the deep brain simulation (DBS) application is well suited for this type of model. It requires to estimate from an atlas, the position of the subthalamic nucleus (STN). The STN is a very small structure of the brain that is not always clearly visible on MR images.

3. **Region-based and Pixel-based Models** Section 7.4 is dedicated to the Region-based and Pixel-based model using the label and intensity function representation. First, we present the preliminary results that we have obtained on 2D real images for the atlas registration on a brain image with a large space occupying tumor. Then, we show on 3D images, how this model can compensate intra-operative brain shift.

The results obtained for these different atlas-based segmentation applications are discussed in Section 7.5.

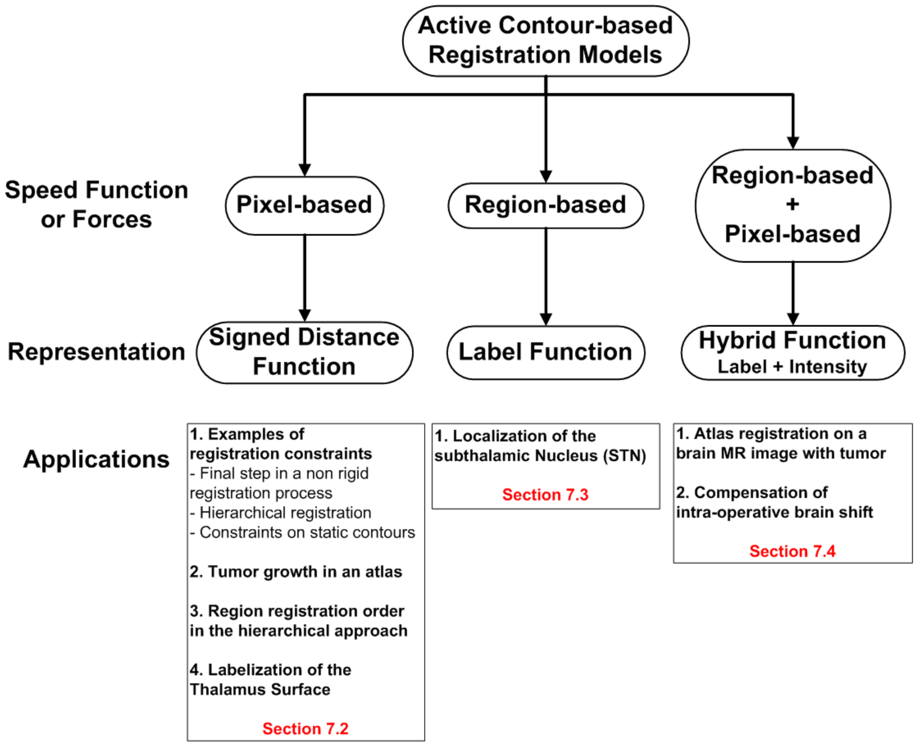

Figure 7.1: Organization of this chapter.

7.2 Pixel-based Model

This Section shows medical applications related to the Pixel-based model using the signed distance function representation. This first category of model requires the segmentation of the target image.

We propose thus to use this Pixel-based model when the targeting objects are easy to segment (for example bones in CT images) or to add constraints on manually segmented objects. Note that the results of this model depend strongly on the quality of the segmentation of both images. The deformation computed by our model have been propagated to the whole image with a distance-based interpolation in the *Examples of Registration Constraint* (Sections 7.2.1) and *Tumor Growth Model* (Section 7.2.2). The results of the *Hierachical Approach on Neck CT Images* (Section 7.2.3) and *Thalamus labelization application* (Section 7.2.4) have been generated by using a diffusion-based interpolation. We will show in Section 7.3 that the diffusion-based interpolation seems to be more appropriated to propagate the non rigid deformation of anatomical structures.

7.2.1 Examples of Registration Constraints

We have first tested our Pixel-based model on three types of 2D medical images: neck CT images, brain MRI images and Prostate MRI images. These images have been created by extracting two similar slices of two different patient volumes after an affine registration. Their size is 256x256.

Final Step in a Non Rigid Atlas Registration Process

The first experiment (Figure 7.2) consists in registering two CT slices of the neck region using four structures: the external neck contours, the vertebra, the trachea and the jaw. To show the accuracy of the registration during the process, the contours of interest have been drawn on the patient image and copied on all the other panels. Panel 7.2.1 shows the atlas image after an affine registration. Panel 7.2.2 shows the result after a global registration performed by a BSpline algorithm. This global non rigid registration allows to have a better initial alignment between corresponding contours. Panel 7.2.3 shows the result obtained with the Pixel-based model. This experiment shows that our active contour-based registration model can complete in a second step, the deformation of an intensity-based non rigid algorithm to get a more accurate registration.

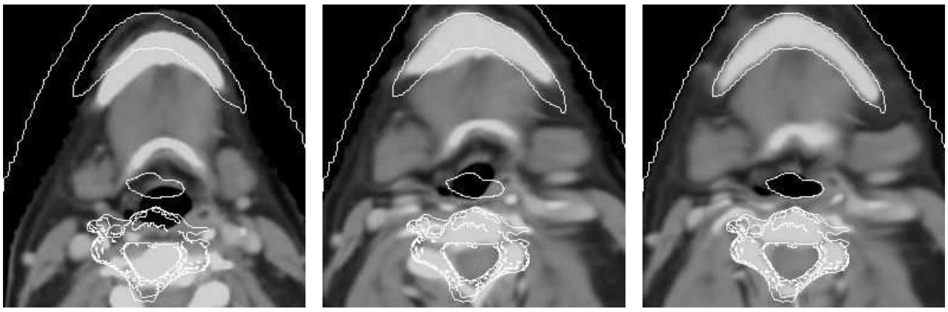

.1 Affine .2 Bspline .3 AC

Figure 7.2: Complement to a Global Non Rigid Atlas Registration Process. Atlas-based registration of a neck axial slice.

Hierarchical Registration

The second experiment (Figure 7.3) consists in registering brain sagittal slices using five structures: the external contours of the brain, the ventricles, the brainstem, the cerebellum and the corpus callosum. In this case, we have performed the registration with two hierarchical layers. In the first layer, we have registered the external contours of the brain and the ventricles. This registration has improved the corresponding contours alignment of the second layer structures: the brainstem, the cerebellum and the corpus callosum. The patient contours have also been copied on all the panels. Panel 7.3.1 shows the atlas after the affine registration. Panel 7.3.2 shows the result after the local registration of the brain external contours and the ventricle. Panel 7.3.3 shows the final result after the local registration of the corpus callosum, the brainstem and the cerebellum. This experiment shows that the hierarchical approach can help the registration of complex structures based on objects easier to segment. In Section 7.2.3, we will illustrate on 3D images, the importance of the structure registration order in the hierarchical approach.

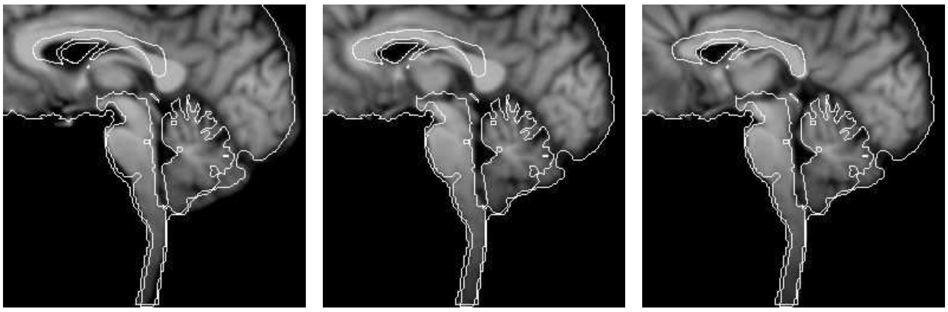

.1 Affine .2 Layer 1 .3 Layer 2

Figure 7.3: Atlas hierarchical registration of a brain sagittal slice.

Constraints on Static Contours

The third experiment (Figure 7.4) consists in registering the rectum between two MR slices of the prostate area. Panel 7.4.1 shows the atlas after the global non rigid registration. Panel 7.4.2 shows the patient image. The contours in red correspond to the patient contours. We note that only the rectum has really moved between these two images. The deformation of the surrounding structures is practically null. Row 2 and row 3 respectively shows the rectum registration results with and without constraints on the surrounding muscles contours (dark structures). The objective of these constraints is to prevent the surrounding muscles from being deformed by the movement of the rectum. Column 1 and 2 show the moving and target level set function used. We see that the constraints on the surrounding contours only consists in introducing the contours that have not to move in the level sets used for extracting the deformation field. Column 3 shows the deformed atlas. Column 4 shows the corresponding transformation. We can see on panel 7.4.5 that without constraint, the left muscle is strongly attracted by the deformation of the rectum. On the other hand, for the result 7.4.9, the constraints on the surrounding muscles have prevent the left muscle to follow the rectum motion. This third experience shows that local constraints on contours that have not to be deformed during the registration process can easily be introduced in our signed distance function tracking method.

7.2.2 Tumor Growth in an Atlas

This experiment concerns the registration of an atlas on a brain presenting a large-space occupying tumor. Such registration is challenging because: (1) the lesion does not exist in the atlas, (2) large deformations have to be recovered. However we decide to use this case for our preliminary results on

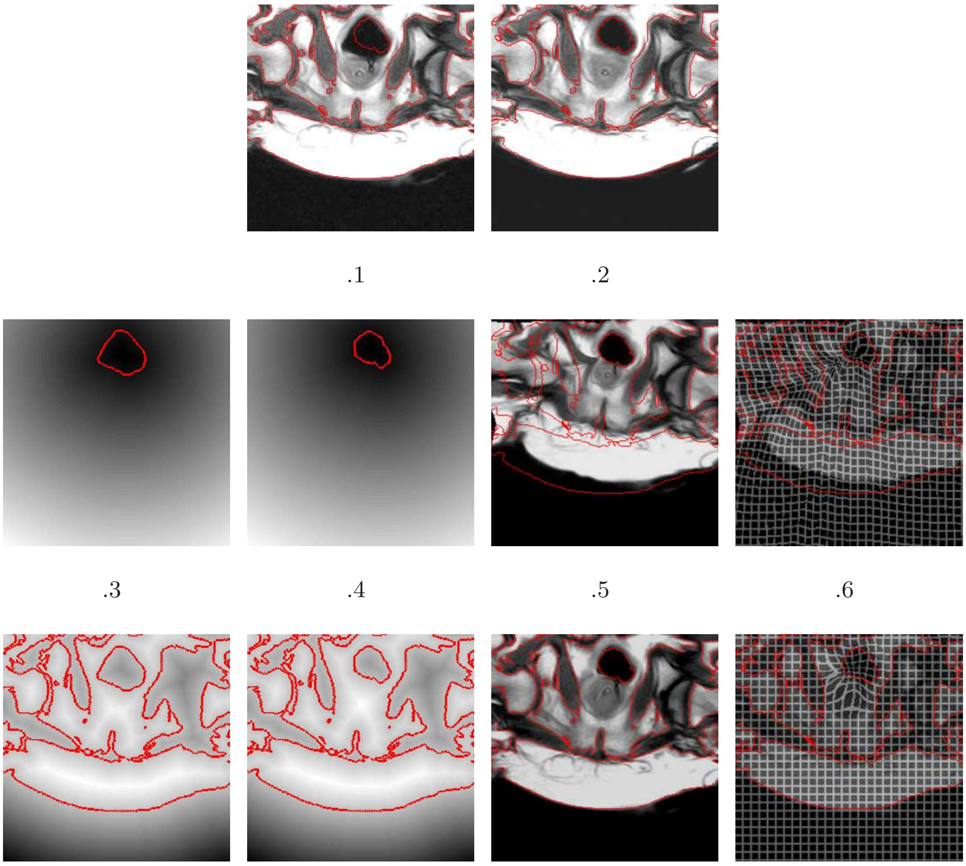

.1 .2

.3 .4 .5 .6

.7 .8 .9 .10

Figure 7.4: Constraints on Static Contours. Atlas-based registration of a prostate axial slice. Row 1: a) Atlas, b) Patient. Row 2 and 3: Registration without and with constraint on the surrounding structures. Column 1: Moving level set function. Column 2: Target level set function. Column 3: Deformed atlas. Column 4: Deformed grid.

3D real data because we can model two types of deformations: surface matching and tumor growth by matching a point (seed) to a volume (segmented tumor). The patient image used in this study has been retrieved from the Surgical Planning Laboratory (SPL) of the Harvard Medical School & NSG Brain Tumor Database [99]. The digital atlas also comes from the SPL [101]. These images have been registered with an affine transformation.

The features used for the registration can be classified in two categories:

1. The features to limit the propagation of the deformation: head and brain contours.
2. The features to catch the most of the deformation due to the pathology: lateral ventricles and tumor.

Two different segmentation techniques are used to segment these features: level set methods for contrasted structures (head and ventricles) and mathematical morphology to extract the brain. The level set-based registration is then performed on the binary images generated by these segmentations.

With this technique, to obtain a correct radial tumor growth, the seed has to be the only object placed inside the tumor area of the patient. As the lateral ventricles overlap this area, they are registered in a second step. So, we have to perform a hierarchical registration process with two layers (first layer: head, brain and tumor, second layer: lateral ventricles) following the approach proposed by Houhou et al. in [91].

Figure 7.5 shows the difference of position between the source and target binary images used during the registration process for the sagittal view (raw 1) and the axial view (raw 2). Columns 1 and 2 show respectively the initial and final position.

The objective of atlas registration is to automatically segment the patient image. The raw 3 of Figure 7.5 shows how two other structures of the atlas, the cerebellum and the caudate nucleus (white contours), follow the deformation interpolated from the features registration (gray contours). The column (a) shows the atlas contours superposed to the patient image. The column (b) shows these contours deformed by the computed transformation.

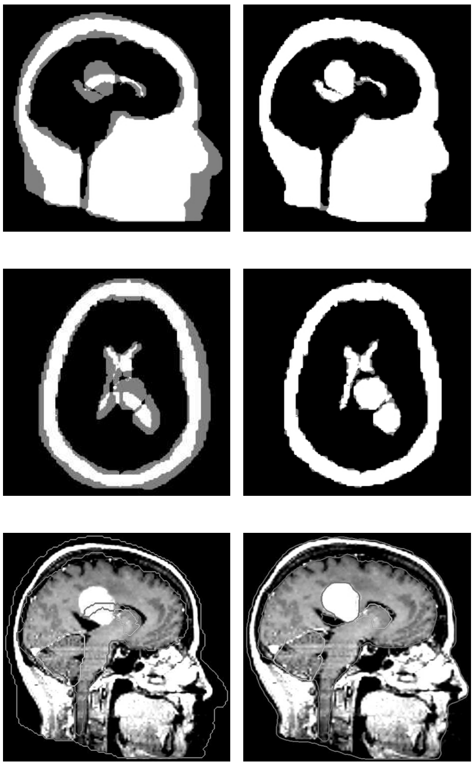

Figure 7.5: Geometrical feature-based atlas registration. Row 1: Axial view. Row 2: Sagittal view. Column (a): Initial differences. Column (b): Final differences. Row 3: Atlas based segmentation of a brain image with large tumor. Column (a): Initial atlas contours on patient image. Column (b): Deformed atlas contours.

Figure 7.6 shows the effect of the tumor growth on the surrounding structures of the atlas. Panel (a) shows the atlas. Panel (b) shows the atlas just after the tumor growing (after the registration of layer 1). Panel (c) shows the patient image. Contours of the tumor and lateral ventricles have been drawn on the patient image and copy on the other panels to show how the structures follow the deformation generated by the tumor growing. We note that the deformation generated by the tumor growth already gives to the lateral ventricles and the corpus callosum a shape similar to the patient's structures. This deformation is related to the position of the seed. Thus, the seed has been placed in the atlas following the knowledge of an expert about the real origin of the tumor.

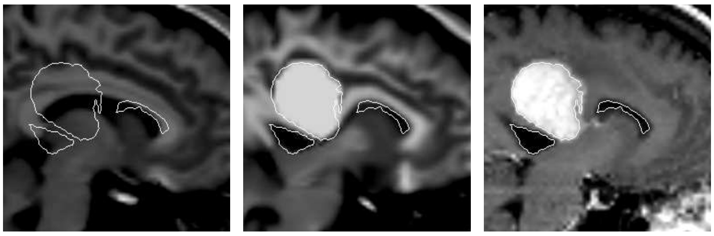

.1 .2 .3

Figure 7.6: Tumor growing. (a) Atlas. (b) Atlas deformed. (c) Patient image.

7.2.3 Region Registration Order in the Hierarchical Approach

This section aims to show the importance of the region registration order in the hierarchical approach, especially in 3D image registration. The principle of the hierarchical approach is that the registration of the main image objects helps the registration of depending objects. We will see on 3D neck CT images which order in the anatomical structure registration is the best to follow this principle.

Data

The data used are shown in Figure 7.7. Row 1 shows the intensity atlas and row 2 shows the patient image. The original size of these images are 512x512x62 with a pixel size of 0.9375x0.9375x4.0 mm. To reduce the computation time, we have subsampled and cropped these images to a size 120x150x28 (pixel size 1.875x1.875x8 mm). The images shown in Figure 7.7 have been registered with an affine registration. The contours drawn on the panels correspond to the target contours. They permit to visualize the level of matching between both images. The red contours are the contours of the target bones and the yellow contours are the contours of the external contour of the neck. We note that the contours of both images are initially quite well superposed.

Method

For this experiment, we have performed two types of region-based registration. In the first type, the image registration is driven by the external contour of the neck. In the second type, we chose the hardest tissue of the neck, the bones, to drive the registration. The goal is to see how the other structures of the neck follow the registration of the selected structures. The neck and bones have been segmented on both images by using a threshold-based method and morphological operations. The processing time for these registrations is in average 15 minutes (40 iterations without using a multi-resolution approach).

Results

The results are shown in Figure 7.8. Row 1 corresponds to the result of the external contour-based registration. Row 2 corresponds to the result of the bones-based registration. The effect obtained with both these registration are discussed below.

External Contour-based Registration Even if the initial differences between the external contour of the atlas and the patient image was quite small, we note that their registration has provoked large changes in the position of the internal structures. This is notably the case for

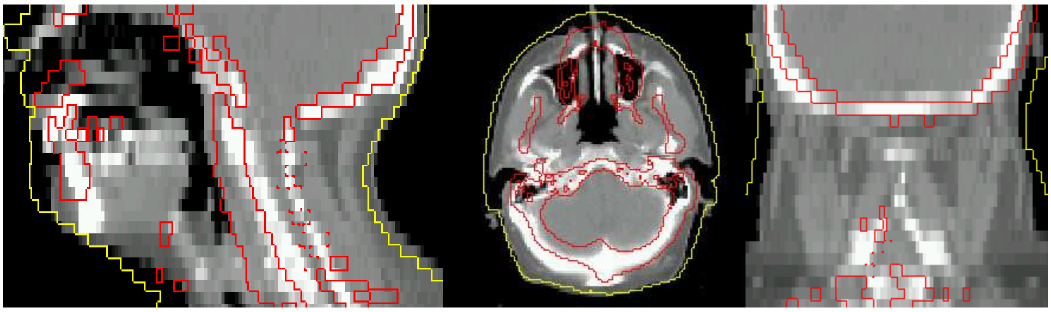

Atlas

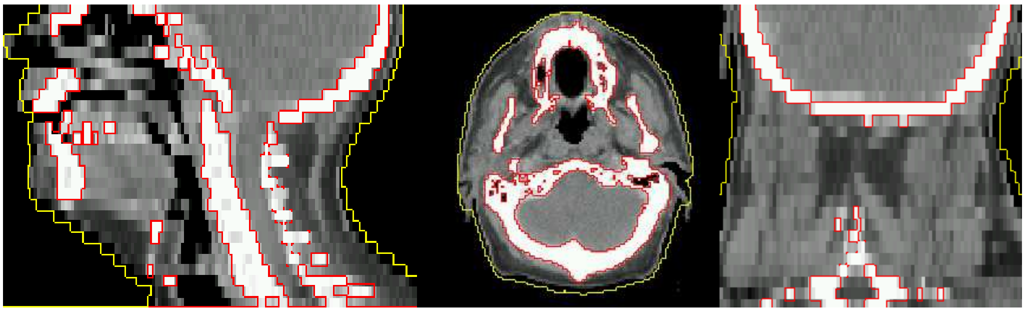

Patient image

Figure 7.7: Region registrations order in the hierarchical approach. Initial data: 3D neck CT images (the 3 columns respectively show the sagittal, axial and coronal views).

the position of the vertebra and the trachea. Moreover the contours of both these structures are become less well aligned than the initial position they had after the affine registration. This registration has not followed the principle of the hierarchical approach.

Bone-based Registration In the result of this registration, we can see that the alignment of the bones are brought the surrounding structures closer to their target contours. This registration has followed the principle of the hierarchical approach.

In conclusion, in the hierarchical approach we have to be careful to the order of the anatomical structures to register. We have to follow the physical dependency that exists between anatomical structures. In neck images, it seems logical that the hardest structures should be registered first because they influence the position and shape of the softest surrounding structures (muscles, fat, arteria).

7.2.4 Labelization of the Thalamus Surface

To investigate Schizophrenia disease, our research group is performing a study on the neuronal connectivity between the cerebral cortex and the right and left thalami. According to metabolic and post-mortem studies [136] [143] [109], the total number of fibers is expected to be less important with schizophrenic subjects than with normal subjects. This seems to be especially the case for the thalamo-frontal bundles.

In this project, we propose to analyze the thalamo-cortical connectivity by using Diffusion MRI. First, we will quantify the number of connections between regions of interest (Rois) selected on the

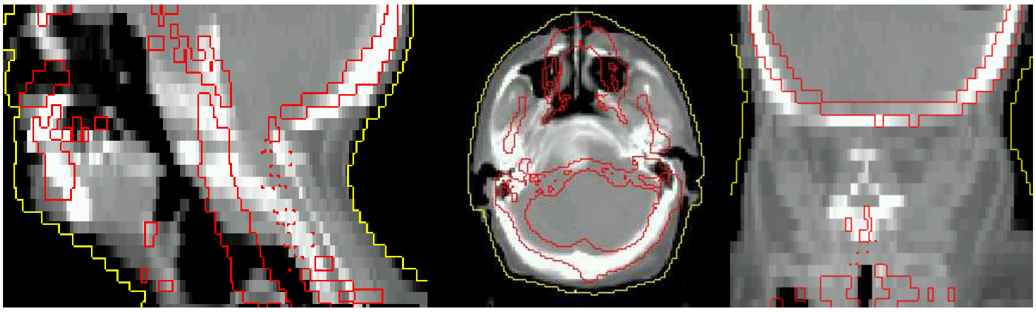

External contour registration

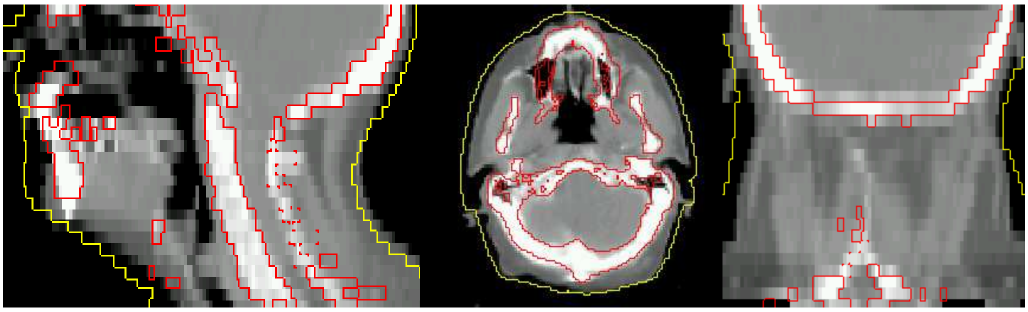

Bones registration

Figure 7.8: Region registrations order in the hierarchical approach. Registration results (the 3 columns respectively show the sagittal, axial and coronal views).

cortex surface and on the right and left thalamus surfaces. These measures will be carried out on normal and schizophrenic subjects. Then by comparing the results obtained for both groups, we will be able to see if the neuronal connections are less important in schizophrenic patients and eventually to localize the fibers reductions.

Labelization Method

To perform this statistical study, the Rois defined on the cortex and thalamus surfaces have to be anatomically at the same place in each subject's brain. We propose to solve this surface labelization problem by projecting the Rois defined on an atlas on the surfaces to be labeled (atlas-based segmentation approach via registration).

As atlas, we use the MNI305 atlas, a statistical brain atlas built by the Montreal Neurological Institute from 305 normal MRI scans [67]. To test our labelization method, we have divided its cortex into N labeled Rois by the automatic cortex labelization method proposed in [72] [56] and available in the FreeSurfer software package [158]. The surface of its thalami was randomly divided into 10 Rois of similar size with a region growing-based method. Note that for the statistical study, all these Rois will correspond to anatomically meaningful cortex regions (cerebral cortex areas/gyri) and thalamus regions (subthalamic nuclei).

To compute the deformation field between the atlas and the patients cortex, we have used the mesh to mesh registration algorithm proposed by Fishl et al. in [73] [74] (also available in the FreeSurfer software package [158]). This algorithm was designed to register two cortex based on their meaningful curvature.

Opposite to the cortex surface, the curvature of the thalamus surface is not enough significant to help to the registration of Rois. We propose here to perform this registration with our active contour-based registration model. Figure 7.9 illustrates the atlas-based segmentation problem for the thalamus labelization. Panel 7.9a shows the MNI atlas with its right thalamus labeled and Panel 7.9b shows the MRI image of a subject with its right thalamus to be labeled.

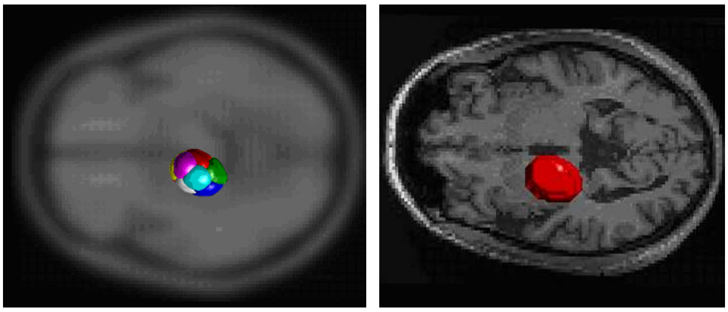

a b

Figure 7.9: The thalamus labelization problem suits well the atlas-based segmentation approach via registration. a) Labelled thalamus of the MNI atlas. b) Thalamus of the patient.

Thalamus Registration

Our model was tested to label the right and left thalami of 11 subjects. The MNI atlas has a size of 128x128x91 with a pixel size of 2x2x2. The Diffusion MR images of the subjects to be labeled have a size of 128x128x68 with a pixel size of 2x2x2. The MNI atlas has been aligned to each subject with an affine registration to compensate their differences in position. The thalami of the Diffusion MR images have been delineate with the level set-based method proposed by Jonasson et al. [97]. To reduce the computation time, we have performed the non rigid registration on a region of interest of 30x30x30 around the thalami to be registered.

Our registration model was used with pixel-based forces. As we have to delineate virtual structures, we use it with a bijectivity scheme. The contours of the thalami have been modeled with two types of contour representation: the unsigned distance function and the signed distance function. The goal was to see if, for this application, the polarity information contained in the second type of representation could influence the results of the labelization. For the registration, we did not use a multi-resolution scheme as the images to register are initially quite small. During the registration, the sigma value of the Gaussian filtering is progressively reduced from 5 to 1 mm. This permits to begin the registration process with a quite rigid transformation in order to recover the global difference of position between both thalami and then to allow progressively more and more elasticity to the transformation*. The sigma value is adjusted according to the similarity value measured be-

---

*This approach could be compared to the registration methods using basis functions. The registration process of these parametric methods begins with a few number of basis function of large size to recover global deformations. Then, the number of basis function is progressively increased and their size proportionally decreased during the registration process to get a more local registration

Table 7.1: Mask and contour-based comparison between the registration results obtained with the unsigned distance function (Unsigned DF) and the signed distance function (Signed DF) for the right thalamus.

Representation	MaskSim. $[mm^3]$	Area $[mm^3]$	Contours Sim.			Perim $[mm]$	Radius $[mm]$
			Pts_in[%]	Mean$[mm]$	Max$[mm]$		
Unsigned DF	0.90	2374.18	98.20	1.84	2.36	673.09	6.55
Signed DF	0.90		97.8	1.03	1.14		

tween both distance maps to be registered. The processing time for these registrations is in average 8 minutes (20 iterations with bijectivity scheme).

Figure 7.10 and 7.11 respectively show one example of thalamus registration using the unsigned distance function and the signed distance function. Here the unsigned distance function is represented by a contour and the signed distance function by a mask. In both Figures, the red contours/masks represent the atlas thalamus and the green contours/masks represent the subject thalamus. The common parts between both contours/masks are in orange. Row 1 shows the initial position between both thalami and row 2 shows the position after registration.

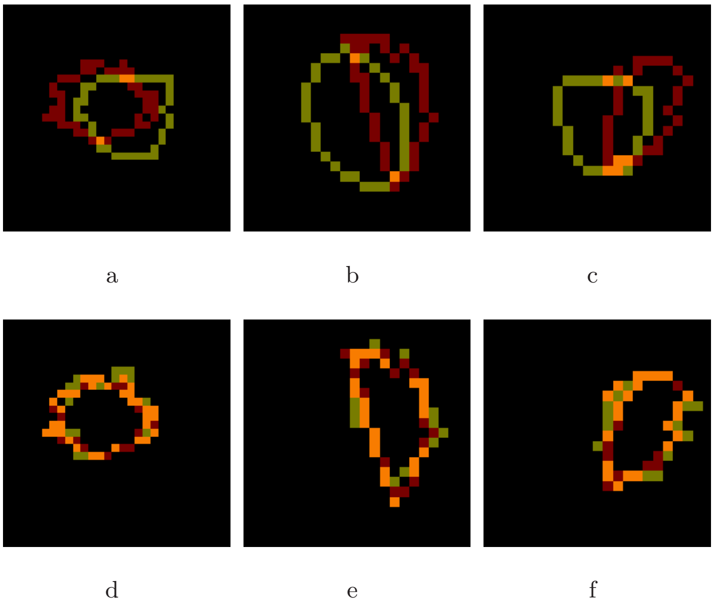
a b c

d e f

Figure 7.10: Thalamus registration using the unsigned distance function (the 3 columns are respectively coronal, sagittal and axial views). Red contours: atlas thalamus. Green contours: subject thalamus. Orange parts: common parts. Row 1: Initial position. Row 2: Position after the registration.

The registration results were quantitatively analyzed regarding to the contour representation in Table 7.1 and 7.2. Table 7.1 shows the results for the labelization of the right thalamus and table 7.1 shows the results for the labelization of the left thalamus.

The registration accuracy was quantified with the following mask and contour similarity measures (Note that these measures were already described at the end of Chapter 5):

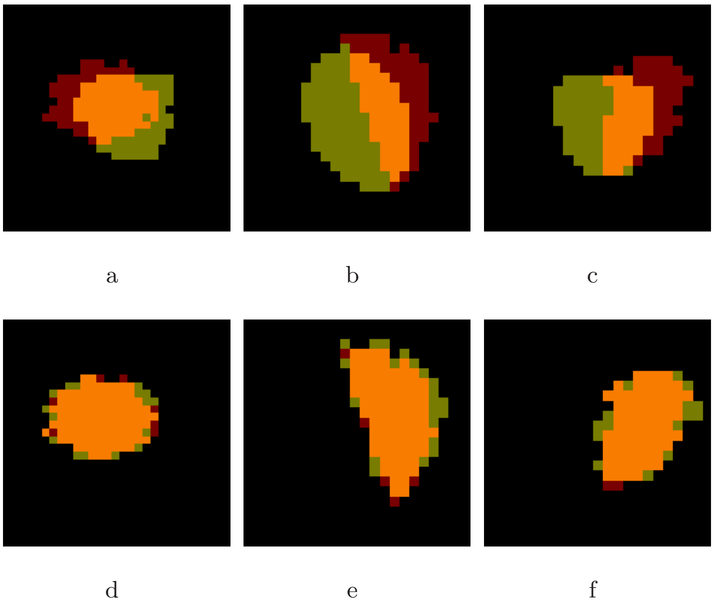
a b c

d e f

Figure 7.11: Thalamus registration using the signed distance function (the 3 columns are respectively coronal, sagittal and axial views). Red masks: atlas thalamus. Green masks: subject thalamus. Orange parts: common parts. Row 1: Initial position. Row 2: Position after the registration.

Table 7.2: Mask and contour-based comparison between the registration results obtained with the unsigned distance function (Unsigned DF) and the signed distance function (Signed DF) for the left thalamus.

Representation	MaskSim. $[mm^3]$	Area $[mm^3]$	Contours Sim.			Perim $[mm]$	Radius $[mm]$
			Pts_in[%]	Mean$[mm]$	Max$[mm]$		
Unsigned DF	0.91	2125.40	98.70	1.84	1.90	616.54	6.14
Signed DF	0.92		99.01	2.22	2.28		

1. **Mask Similarity Measure** This measures corresponds to the following equation:

$$S = \frac{2N(C1 \cap C2)}{N(C1) + N(C2)}, \tag{7.1}$$

   with N(C1) and N(C2) are the number of pixels respectively included in the deformed atlas thalamus and in the subject thalamus. The S value ranges from zero to one, with zero indicating no overlap and one indicating a perfect agreement between two contours.

2. **Contours Similarity Measure** This measure compares the thalamus contours on a point-by-point basis. First, a narrowband of one pixel on the inside and one pixel on the outside of the contours to labeled is defined. Then, we compute the percentage of pixels in the automatic contours that fall within this band (Pts_in). The mean and maximum distance from this band for pixels that fall outside it are also computed. Moreover, we indicated the area, perimeter and maximal radius of the right and left thalamuses. The tables present the average of the values obtained for each patient.

Two main conclusions can be drawn from these quantitative results. First the accuracy of these registrations would be sufficient for a number of atlas-based applications but for this surface labelization problem, the thalamus contours of the atlas needs to perfectly match the thalamus contours of the subject to be labeled. In the next section, we will show the effect of the registration errors and describe the solution we propose to cope with this problem. Then for this application, the polarity information seems to not make significant differences in the quality of the registration.

Thalamus Labelization

In this section, we show how the computed deformation fields are used to project the labels of the atlas thalami to the subject thalami.

Row 1 of Figure 7.12 shows the axial, sagittal and coronal views of the right labeled atlas thalamus (the labels are represented by different colors). Row 2 shows the result obtained if we apply a dense deformation field matching the atlas thalamus to the thalamus of a given subject directly on this image. We note in Panels 7.12d and 7.12f that the obtained labeled regions are disconnected at some places. Moreover, the position of the labels does not correspond exactly to the subject contours due to the registration errors mentioned in the previous section.

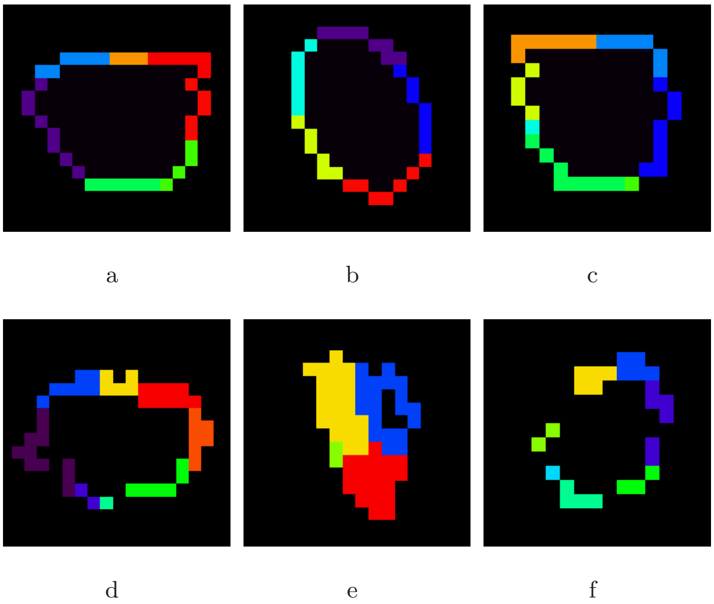

Figure 7.12: Thalamus labelization with the contour labeled image (coronal, sagittal and axial views). Row 1: Labeled thalamus of the atlas. Row 2: Result of the labelization.

To cope with this problem, we have created from the labeled images of the right and left atlas thalami, new labeled images as the one shown in Row 1 of Figure 7.13. The light contours correspond to the original contours of the atlas thalamus. These labeled images were obtained by radially projecting the labels of the thalamus atlas on each side of its contours. Once these labeled images are deformed by their corresponding deformation field, the desired labelization is obtained by superposing them with the contours of the right and left subject thalami. Row 2 of Figure 7.13 shows that the obtained labeled contours are this time continuous. Moreover, the result perfectly matches the patients contour to be labeled.

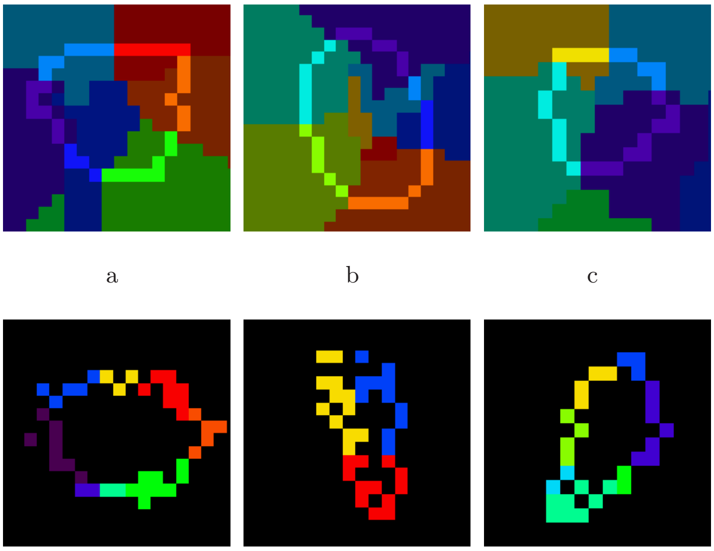
a b c

d e f

Figure 7.13: Thalamus Labellisation with the whole labeled image (coronal, sagittal and axial views). Row 1: Labeled image. Row 2: Labelization result. Note that the initial atlas contours are superposed in light on the labeled image.

Results

Figure 7.14 and 7.15 respectively show the labelization of the right and left thalami of a subject. The first line shows the result obtained with the model using the unsigned contour representation and the second line shows the result obtained with the model using the signed contour representation.

In Figure 7.16, we can see a 3D rendering of the labeled right and left thalami of the atlas. Figures 7.17 and 7.2.4 respectively show the results obtained by projecting the atlas labels to the right and left thalami of four different subjects. Row 1 corresponds to the result obtained with the model with the unsigned representation and row 2 corresponds to the result obtained with the model with the signed representation.

Visually there are not significative differences in the labelization obtained with both contour representations. The positions of the labeled region (Rois) are globally similar. We just note small differences along their interface.

Future Work

To validate our thalamus labelization method, we need now to constitute a data set of thalami where meaningful Rois (the subthalamic nuclei) have been delineated by medical experts. This way, we could compare our results with ground truths.

7.3 Region-based Model

This Section is dedicated to the Region-based model using the label function representation. This second category of model does not require the segmentation of the target image as the first one but

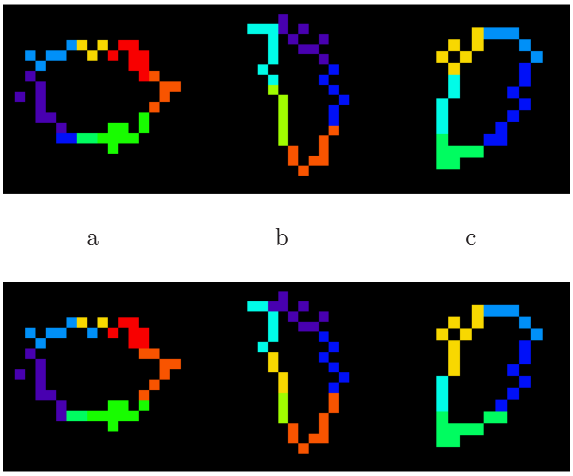

a b c

d e f

Figure 7.14: Right thalamus labelization (coronal, sagittal and axial views). Row 1: Result obtained with unsigned contour representation. Row 2: Result obtained with the signed contour representation.

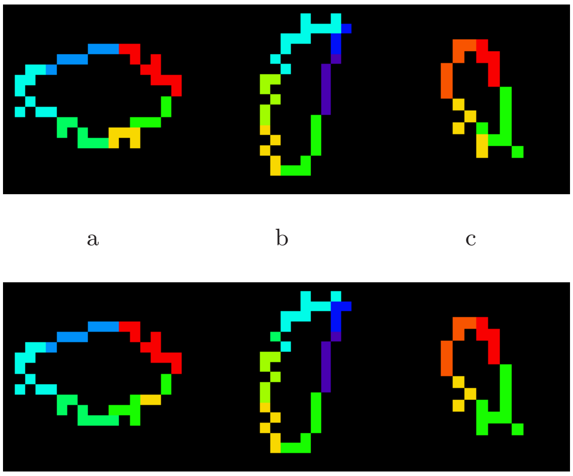

a b c

d e f

Figure 7.15: Left thalamus labelization (coronal, sagittal and axial views). Row 1: Result obtained with unsigned contour representation. Row 2: Result obtained with the signed contour representation.

have no registration constraints on the image contours located far away from the closed contours selected to drive the registration.

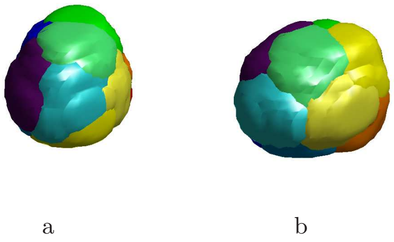

Figure 7.16: 3D rendering of the atlas thalamus. a) Right thalamus. b) Left thalamus.

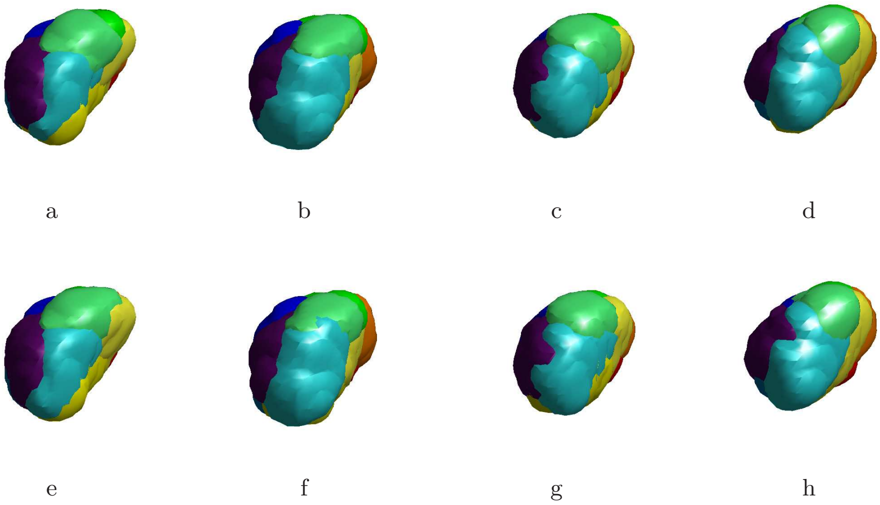

Figure 7.17: 3D rendering of the right labeled thalamus of 4 subjects. Row 1: Unsigned contour representation. Row 2: Signed contour representation.

7.3.1 Localization of the Subthalamic Nucleus (STN)

Subthalamic nucleus (STN) targeting is needed in the treatment of Parkinson disease and other movement disorders [142]. STN is a very small structure (in average 10 x 6 x 3 mm^3) that is not always clearly visible in MRI. Its localization is often performed by atlas-based segmentation [58] [149]. The position of the STN on the patient image is estimated by projecting two points indicating the position of the right and left STN in the atlas.

For the non-rigid registration of the atlas, Sanchez et al. propose to register only the relevant structures surrounding the STN [149]. They show that the local registration of the lateral and third ventricles (see Figure 7.19) permits to get not only a faster process but also more accurate results than those obtained by registering the whole atlas.

This atlas registration problem suits particularly well our approach. Indeed, instead of segmenting the structures of interest in the source and target image and registering the binary masks as in [149], our model by using region-based forces can perform these segmentation and registration tasks in one step. In [149], the registration of the binary masks was performed by a free-form deformation algorithm similar to the method proposed by Rueckert [148].

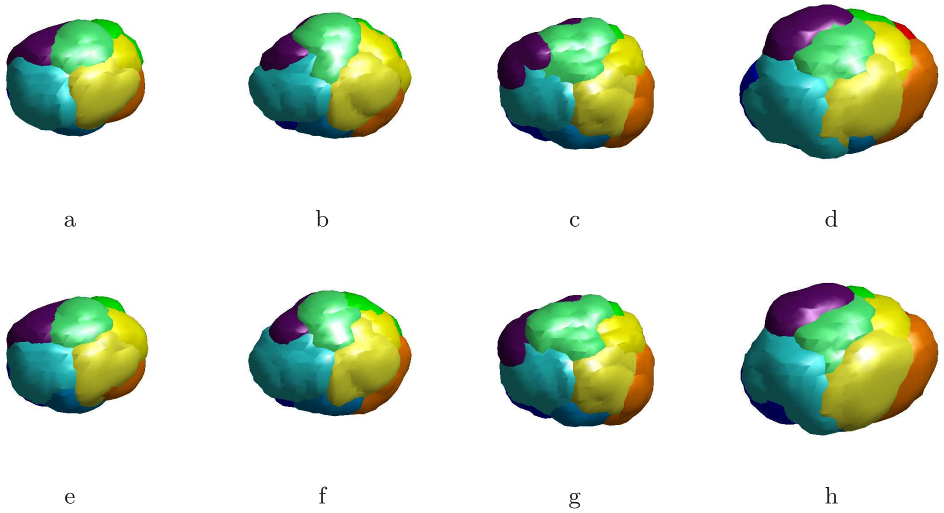

Figure 7.18: 3D rendering of the left labeled thalamus of 4 subjects. Row 1: Unsigned contour representation. Row 2: Signed contour representation.

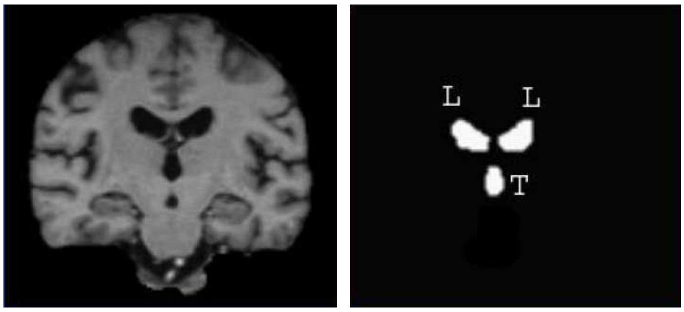

a Intensity atlas

b Selected structures

Figure 7.19: Structures used to estimate the position of the STN: lateral ventricles (L) and third ventricle (T) (coronal view). Note that these Figures are reproduced from [149].

Method

Data Set We test our atlas registration algorithm on two 0.5 Tesla MR images of the brain (image size: 128x128x122, voxel size: 1.1718x1.1718x1.3963 mm^3). We know the location of the right and left STN on both images. These ground-truths correspond to the mean of the STN location given by two medical experts. One of these images has been considered as the atlas (the STN position of this image is considered as a reference). The other image has been considered as the patient image (the image where we need to estimate the STN position). These two images have been aligned with an affine transformation to compensate the global change of position. The lateral and the third ventricles have been segmented on both images with a semi-automatic segmentation method based on thresholding. To reduce the computation time of the non rigid registration process, both images have been cropped to a size of 90x60x80 around the area of interest, i.e. around the lateral and third ventricles and the known positions of the STN.

Models We performed this atlas registration by testing the five following models derived from the general formulation of our active contour-based registration algorithm:

***PIDiff* Model** Pixel-based model using an intensity function representation with a diffusion-based interpolation. This model performs the registration on the whole MR images.

***PLDiff* Model** Pixel-based model using a label function representation with a diffusion-based interpolation. This model performs the registration on the ventricles masks.

***PDDist* Model** Pixel-based model using a signed distance function representation with a distance-based interpolation. This model performs the registration on the signed distance function computed from the ventricles contours.

***PDDiff* Model** Pixel-based model using a signed distance function representation with a diffusion-based interpolation. This model performs the registration on the signed distance function computed from the ventricles contours.

***RLDiff* Model** Region-based model using a label function representation with a diffusion-based interpolation. This model bases its registration process on the inside and outside ventricles regions selected on the MR images by the label function.

As we need to estimate the position of virtual structures, all these models are used with a bijectivity scheme. The model based on the signed distance function and on the label function based their registration process on the ventricles only while the *PIDiff* model use all the contours of the intensity atlas.

We also consider a sixth model that we have called *PDDiffTrue*. This last model corresponds to the *PDDiff* model but its signed distance function represents not only the ventricles but model also the points corresponding to the known position of the STN in both images. In this work, we use this model to have an idea of the level of precision that we can obtained with our registration model. Note that it would be interesting for this application to use this type of model to generate a prior deformation field model. This model could compute the deformation fields between the atlas and a data set of patients where we know the position of the STN. Then the application of principal component analysis (PCA) to the obtained deformation fields should permit one to get the characteristic modes of deformation modeling the variation of the STN position related to the variation of the ventricles position. See [36] for an example of such prior shape model derived from a PCA applied on deformation fields.

The processing time for these registrations is in average 12 minutes (40 iterations with 3 resolutions).

Results

The results obtained with the six active-contour based registration models are shown in Figure 7.20. The level gray images respectively show the sagittal, coronal and axial views of the patient image. The positions of the STN are represented by the center of circles. On the presented views, the size of these circle varies in function of the position of their center. We also show the contour of the lateral and third ventricles. The red contours are considered as ground truths, i.e. the STN position given by an expert and the segmentation of the ventricles obtained by the semi-automatic segmentation method. In Row 1, the blue contours show the initial position of the ventricles and STN of the atlas. The next rows show the positions found by the registration models. The name of the considered model is written under the first panel of each row. The numbers under the third column indicated for each registration models, the overlap mask values (this measure was described in Section 7.2) between the deformed atlas ventricles and the segmented patient ventricles. The numbers located under the fourth column are the distance in mm between the STN position and the ground truth STN position. The left number correspond to the left STN and the right number correspond to the right STN.

These results lead to the following conclusions:

- By comparing the results obtained with the *PDDist* and *PDDiff* models, we see that diffusion interpolation better corresponds to the brain deformation than the distance-based interpolation.
- We obtained better overlap masks values with the distance-based model because these models directly match the segmentation of the patient image used as ground truth. The registration process of the other models is based on the intensity of the target image.
- By comparing with the results obtained by the *RLDiff* and the *PIDiff* models we note that the *RLDiff* models lead to better results. The difference between both models is that *RLDiff* has based its registration only of the structures of interest, the lateral and third ventricles and *PIDiff* has considered all the contours of the MRI images. Moreover we have shown in Chapter 5 that the *RLDiff* model is more robust to noise and can recover larger transformations than the *PIDiff* model.

Future Work

In this section, we test different models derived from the general formulation of our active contour-based registration model on the STN localization application. Among the models that does not need the segmentation of the target image, this feasibility study gives more satisfying results with the region-based model that only use the ventricles to drive the registration than the pixel-based model that bases its registration on all the image contours. The obtained results are promising for the model using region-based forces but not relevant because it was tested on one set of images only. This possible application for our model necessitates now a validation on a larger amount of cases and a comparison with other non rigid registration algorithm usually used to register the STN atlas. At present, we are planning to compare the *RLDiff* model with the Affine, AC-PC, BSpline and Demons registration methods. For this comparison, we will follow the validation process used by Sanchez et al. in [150].

7.4 Region-based and Pixel-based Model

This section is dedicated to the Region-based and Pixel-based model using the label and intensity function representation. This model allows to be accurate on the contours model by the label function thanks to the Region-based forces and far away of these contours thanks to the Pixel-based forces. The registration forces used by the Region-based model are the prior mean-based forces.

7.4.1 Atlas Registration on a Brain MR Image with Tumor

Figure 7.21 show preliminary results obtained in a tumor growth application. These results illustrate the effect of the Pixel-based registration forces, the Region-based registration forces and, the combination of the Region-based and Pixel-based registration forces. The atlas and the patient images are respectively shown in Figures 7.21a) and 7.21b). These images correspond to 2D slices extracted

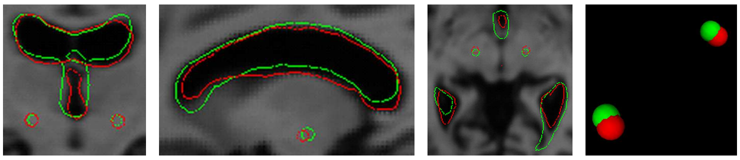

.1 Initial Data .2 .3 0.82 .4 1.47 / 1.53

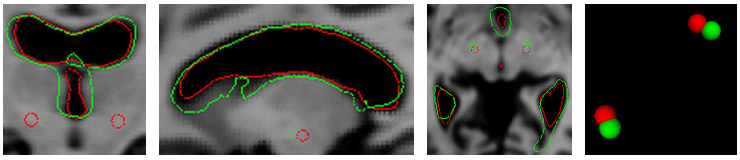

.5 PIDiff .6 .7 0.82 .8 2.39 / 3.20

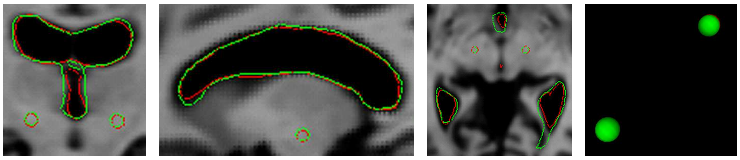

.9 PLDiff .10 .11 0.92 .12 0.44 / 0.62

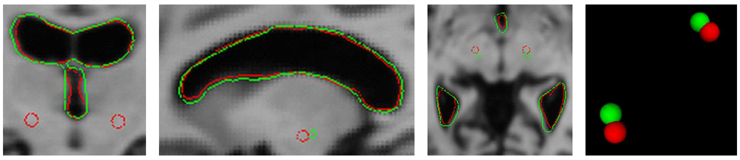

.13 PDDist .14 .15 0.92 .16 3.33 / 2.87

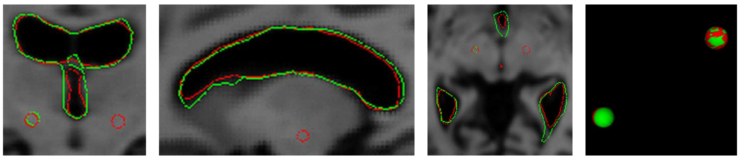

.17 PDDiff .18 .19 0.90 .20 0.62 / 0.00

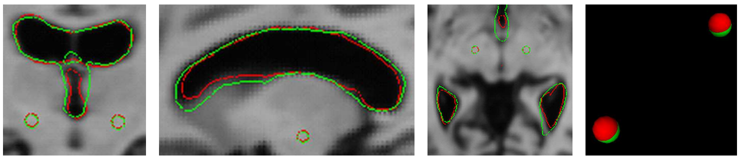

.21 RLDiff .22 .23 0.86 .24 0.44 / 0.44

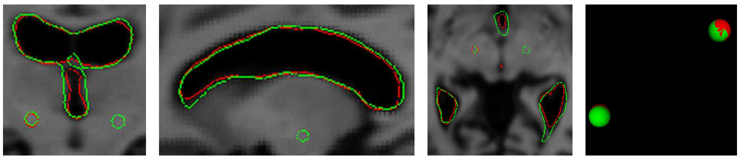

.25 PDDiffTrue .26 .27 0.90 .28 0.44 / 0.00

Figure 7.20: Estimation of the STN Position by six models derived from the general formulation of our atlas-based registration algorithm.

from 3D brain MR images. We note that the patient image contains a tumor not present in the atlas. There is also some noise around its skull. Figure 7.21c) shows the label image that has been used to impose Region-based registration constraint for the matching of the skull. A seed (a pixel-size point) has been inserted inside this label image to generate the growth of a new region inside the atlas which is the tumor. The green contours copied on all these images are the target contours. They help to visualize the initial difference and the accuracy of the registration. Column 2 shows the registration obtained with three different types of active contour-based registration models. The first panel corresponds to the result of the Pixel-based model using the intensity function representation. We note that this model has locally good results (see the sulci registration inside the red circle) but the registration of the external contour of the brain is disturbed by the noise. The second panel corresponds to the result of the Region-based model using the label function representation. This model has allowed to obtain a better registration result with the external contour and to growth a tumor from the seed in the atlas image. However, registration errors subsist far away of the contour considered for the registration (see inside of the red circle). For the last registration result, we have combined Pixel-based and Region-based forces. The registration result of this model is accurate on the contour model by the label function thanks to the Region-based forces and far away of these contours thanks to the Pixel-based forces. Column 3 shows the deformed grids corresponding to each one of these models.

7.4.2 Compensation of Intra-Operative Brain Shift

Image-guided surgery aims at bringing pre-operative information to the surgeon during the procedure. Most often, this involves registering pre-operative images with the patient in the operative room. A number of methods have been developed for this purpose. Until late 80's, these have involved rigid body registration techniques. Although rigid body techniques have proven clinically useful, there is a body of literature that shows that brain deforms during the procedure [100, 131, 144]. The main factors causing this deformation include the loss of cerebrospinal fluid (CSF), the injection of anaesthetic agents, and the actions of the neurosurgeon (such as resection and retraction). When this is the case, rigid body transformations are not sufficient to register accurately pre- and intra-operative information. These deformations can significantly diminish the accuracy of neuronavigation systems. Therefore, it is of great importance to be able to quantify and correct these deformations by updating preoperative imaging during surgery.

This has lead several research groups to develop methods and techniques that can compensate for intra-operative brain shift. These methods fall into two categories.

Image-based Models Image-based models involves that intraoperative imaging are available (for instance interventional MR [130, 132], ultrasound [29, 81], or CT [114]). These methods tends to establish correspondences between image structures and interpolate between them either in a arbitrary way [148, 166] or with a fluid or elastic deformation models [14, 44, 45]. Their main limitation concerning this application is that they often consider the image globally. They are generally not designed to add local registration constraint on the main structures affected by the brain shift.

Biomechanical Models These models have the advantage to not need intraoperative images. Their goal is to propagate displacements measured at the surface of the brain through the entire volume. Surface displacements are measured with a tracked probe [77] or a tracked laser range scanner (LRS) [123]. The propagation is computed from prior biomechanical knowledge about the deformability of the brain. The main drawback of these models is that it remains difficult to accurately estimate all the forces and boundary conditions that interact with the

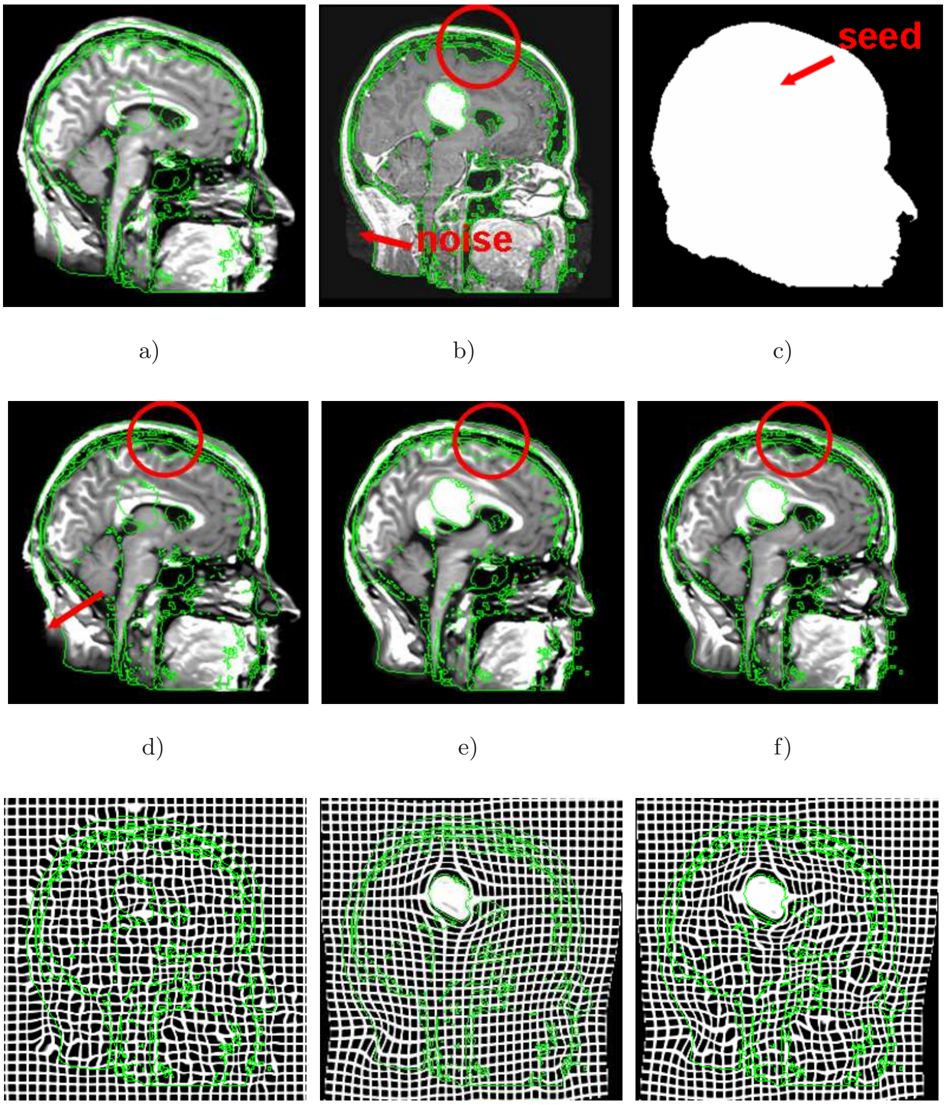

a) b) c)

d) e) f)

g) h) i)

Figure 7.21: Atlas registration on brain MR image with tumor. Row 1: Data Set a) Intensity atlas, b) Patient image, c) Label function with position of the seed. Row 2: Registration results d) Pixel-based forces, e) Region-based forces, f) Pixel-based and Region-based forces. Row 3: Corresponding deformation field.

model during neurosurgery. Recently, Ferrant et al [70, 71] have proposed to introduce more local constraints in biomechanical models based on intraoperative images. Their method consists to track key surfaces of objects, as the cortical surface or the lateral ventricles, using a deformable surface matching algorithm. Then the displacements at the boundary surfaces is propagated to the rest of the brain with a biomechanical model. This new registration algorithm is more constraint but still cannot take into account all the possible forces that can deform the brain during the surgical intervention.

Here, we show the results obtained with our active contour-based registration model on this application. Our model belongs to the category of the image-based models. It computes the deformation based on visual image features. Its main advantage compared to other models of this type is that as the Ferrant's algorithm, it can track key surfaces of objects to recover the largest deformations due to the brain shift. Then, it can finalize the registration based on more local image features by using pixel-based forces.

Data Set

Our model was tested on the two intraoperative 0.5 Tesla MR brain images shown in Figure 7.22 * (image size: 256x256x60, voxel size: 0.9375x0.9375x2.5 mm^3). Column 1 shows a coronal and axial view of the source image. Column 2 shows a coronal and axial view of the target image. Both these images have been aligned with an affine registration algorithm to account for patient movement within the magnet. The contours of the target image have been copied in green of all the Panels to visualize the deformation due to the brain shift. One can very well observe the shift in the direction of the gravity, as well as the shrinking of the lateral ventricles.

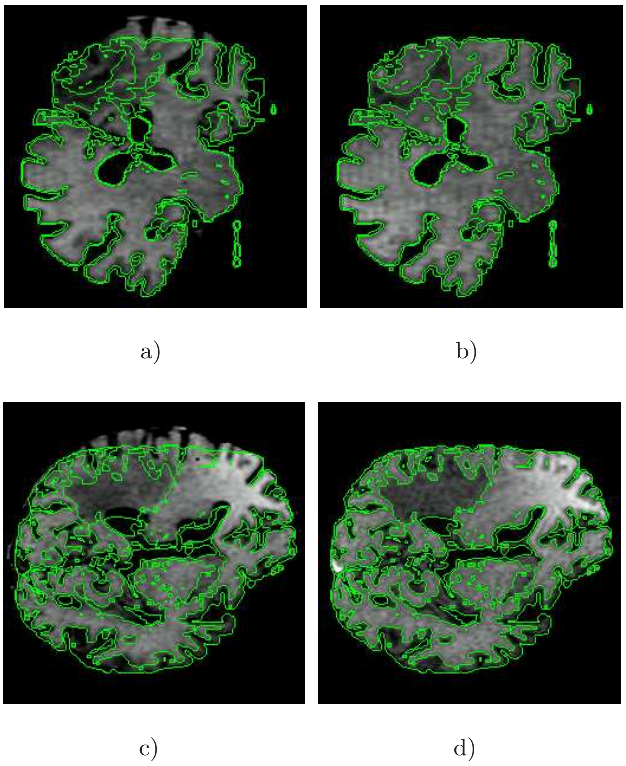
a) b)

c) d)

Figure 7.22: Initial Data. Columns: 1) Source image. 2) Target image. Rows: 1) Coronal view. 2) Axial view.

Both these images have been segmented by thresholding and morphological operation in order to extract the cortical surface and the lateral ventricles. From these segmentations, we have generated the binary masks shown in Figure 7.23. These masks correspond in fact to the white and gray

---

[*] These images come from the Surgical Planning Laboratory (SPL) of the Harvard Medical School. We would like to thanks the Prof. Simon Warfield for having giving us the access to those data.

matter of the brain. They have been used as label function for our active contour-base algorithm. Row 1 shows the coronal and axial views of the label function of the source image. Row 2 shows the coronal and axial views of the label function of the target image. Row 3 shows the initial differences between both label functions.

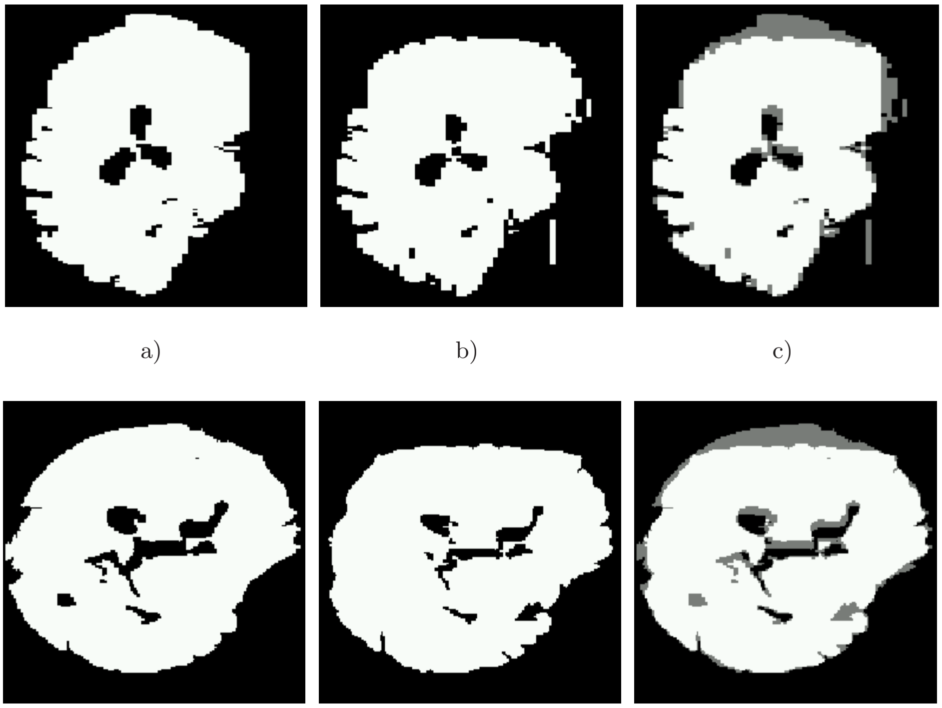

a) b) c)

d) e) f)

Figure 7.23: Label functions. Columns: 1) Source image. 2) Target image. 3) Difference Image. Rows: 1) Coronal view. 2) Axial view.

Models

We have performed this registration by testing the five following models derived from our general formulation:

PI Model Pixel-based model using an intensity function representation. This model performs the registration by considering the whole MR images.

PL Model Pixel-based model using a label function representation. This model performs the registration of the binary masks modeling the cortical surface and the lateral ventricles contours.

PD Model Pixel-based model using a distance function representation. This model performs the registration of the signed distance function computed from the cortical surface and the lateral ventricles contours.

RL Model Region-based model using a label function representation. This model bases its registration process on the inside and outside of the white and gray brain matters selected on the MR images by the label function.

All these models are used with an diffusion interpolation, 3 resolutions and a bijectivity scheme. Note that the PL, PD and RL models due to their level set representation, performed a region-based registration of the images. The PI model perform a more local registration. For the results obtained with the PL, PD and RL models, to be also accurate far away of the considered contour, we have applied these models on the 2 coarsest scales and the PIDiff model on the highest scale following the hierarchical approach. The computing time is in average 50 minutes (120 iterations).

Results

The source images deformed by the above models are presented in Figures 7.24 and 7.25. Figure 7.24 shows a coronal view and Figure 7.25 shows an axial view. In both Figures, the first Panel of Row 1 shows the initial source image. The following panels of the same row show the results obtained with the region-based registration model, i.e. with the PL, PD and RL models. Row 2 shows the results obtained after applying the PI model on the results shows in Row 1 of the same Column.

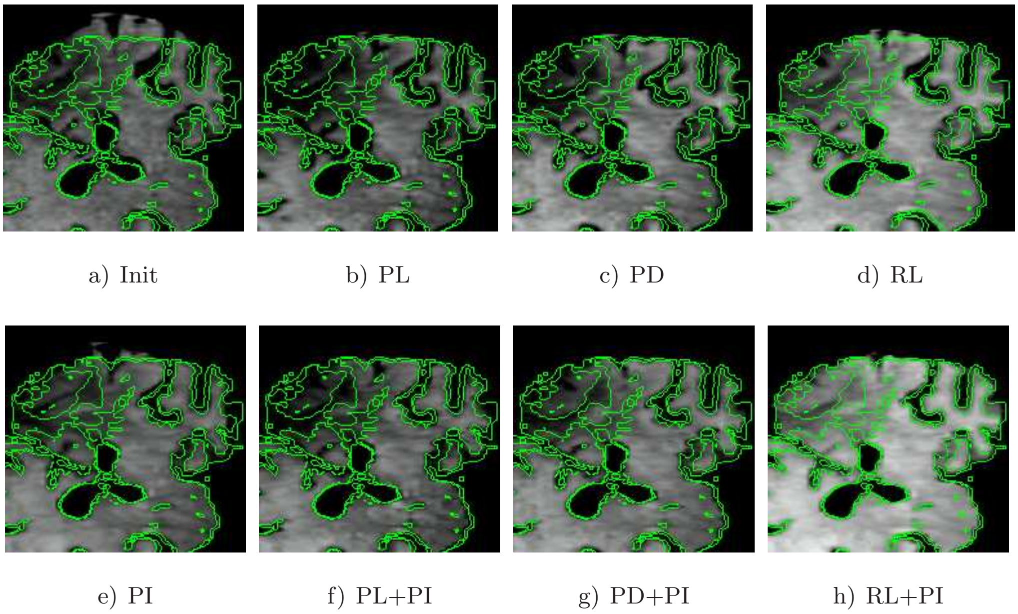

a) Init b) PL c) PD d) RL

e) PI f) PL+PI g) PD+PI h) RL+PI

Figure 7.24: Coronal view of the registration results (Target contours in green). Row 1: Initial Data (First panel). Global Registration (Next Panels). Row 2: Local Registration. The name of the registration model used is indicated under each panel.

We have compared quantitatively the results of these different models by using landmarks. Figure 7.26 shows in red the landmarks that we have manually selected in the source image and in green the landmarks that we have manually selected in the target image. Note that the landmarks 1 to 3 have been selected on the cortical surface. The landmarks 4 and 5 on the ventricles, the landmarks 6 and 7 on internal sulci and the landmark 8 on the border of the edema. The eventual errors due to the manual selection of these landmarks have to be taken into account in the analysis of these quantitative results.

Tables 7.3 and 7.4 present for each landmarks the measurements of the Euclidean distances between the deformed source landmarks and the landmarks manually placed on the target image.

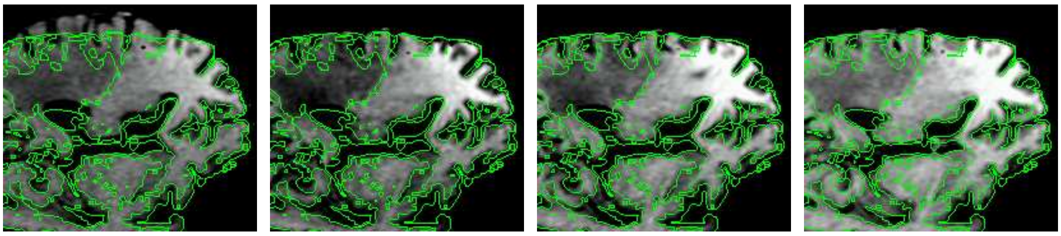

a) Init b) PL c) PD d) RL

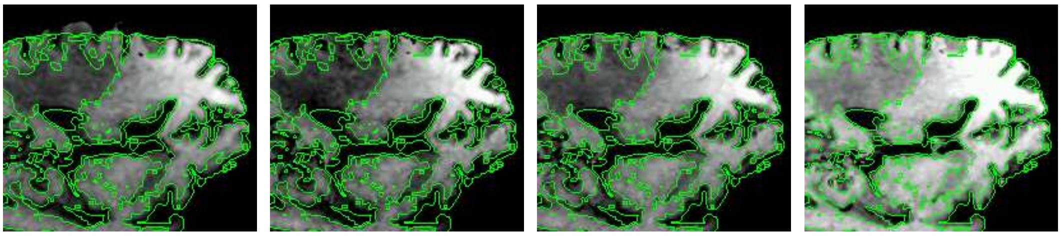

e) PI f) PL+PI g) PD+PI h) RL+PI

Figure 7.25: Axial view of the registration results (Target contours in green). Row 1: Initial Data (First panel). Global Registration (Next Panels). Row 2: Local Registration. The name of the registration model used is indicated under each panel.

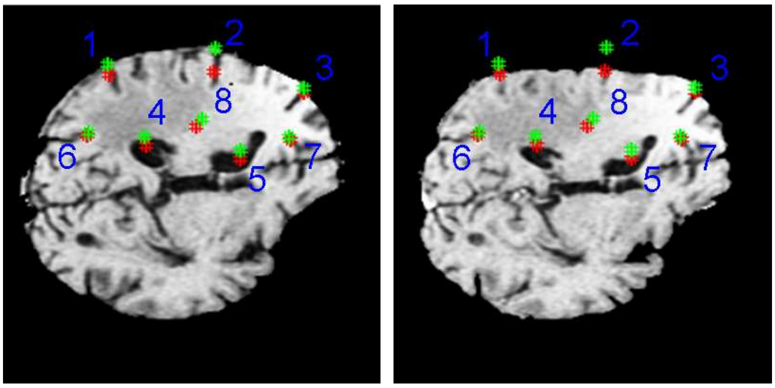

a) b)

Figure 7.26: Landmarks points. a) Source landmarks in green. b) Target landmarks in red.

These distances are given in *mm*. Tables 7.3 indicates in its first line the initial distances betwen the source and target landmarks. The following rows show the distance obtained after applying the region-based registration model indicated on left of the table. Table 7.3 shows the final distance after having applied the pixel-based registration.

From these results we can draw the following conclusions:

- We can see in Table 7.3 that the region-based registration allows to reduce significantly the differences between landmarks even far away from the contour driving the registration.

Table 7.3: Distances in mm between the deformed source landmarks after the region-based registration and the landmarks manually placed on the target image.

Location	Cortical Surface			Ventricles		Internal Sulci		Edema Border
Landmark number	1	2	3	4	5	6	7	8
Initial Distances	5.12	11.20	1.86	3.78	4.39	2.24	2.39	4.48
PL	1.18	5.11	1.59	2.45	2.75	1.71	1.67	2.81
PD	0.88	3.16	0.62	2.24	2.49	1.34	1.24	1.96
RL	1.18	3.26	1.59	1.71	3.33	2.02	2.11	2.49

Table 7.4: Final distances in mm between the deformed source landmarks after pixel-based registration and the landmarks manually placed on the target image.

Location	Cortical Surface			Ventricles		Internal Sulci		Edema Border
Landmark number	1	2	3	4	5	6	7	8
PI	4.28	7.92	1.71	3.32	2.20	1.18	1.18	2.11
PL+PI	1.00	4.09	1.18	2.45	2.20	1.33	1.70	2.44
PD+PI	1.24	3.10	1.75	1.76	1.24	1.39	1.24	1.86
RL+PI	1.18	3.26	1.33	2.45	2.45	1.71	1.71	2.26

- The combination of the region-based and pixel-based models give similar results. The advantage of the RL-PI model is that it does not requires the segmentation of the target image.
- We note a clear differences between the PI and the other models for the landmarks located in the middle of the shifted cortical surface, i.e. the landmarks number 1 and 2. Thus, the brain shift has been better recovered by applying a region-based registration before the pixel-based registration.

Future Work

For the next step of this work, we would like to compare in accuracy and in computation time, the results of our image-based model with those of the biomechanical model proposed by Ferrant et al. in [70, 71] that also track the deformation of key structures for the registration. The advantage of our model is that it computes the deformation based on the visible features of the images. Its drawback is that its interpolation is arbitrary. The advantage of the Ferrant's model is that its interpolation is based on the biomechanical modeling of the deformation of the brain. Its drawback is that it cannot take into account all the forces that interact with the brain during the intervention.

7.5 Conclusion

A lot of segmentation problems in medical imaging can be solved by using prior knowledge coming from an atlas. The formulation of our active contour-based registration algorithm is enough general to be easily adaptable to various types of segmentation problems. This represent an important advantage. In this chapter, we use our model to integrate different types of local constraints in a registration process, to model a tumor growth in the atlas, to label the surface of an anatomical structure, to register a neck atlas based on its external contours or based on its bones (object-based registration linked to the hierarchical registration approach), to localization the subthalamic nucleus (STN) or to compensate the intra-operative brain shift. The results obtained with our model on these different applications are very promising. We are now mainly focused on the validation of our algorithm. We would like to compare our algorithm with the non rigid registration algorithms currently used to register atlases. We are also planning to adapt our model to a particular application in radiation therapy planning of the neck. Both these future works are explained more in details in Chapter 8.

Part V

Conclusions

General Conclusions

8

In this chapter, we review the most important issues and contributions of this thesis. Following that, we present the future works.

8.1 Review of the discussed Topics

Below are short summaries on the different topics studied in this thesis.

Prior Knowledge in Segmentation The applications presented in Chapter 7 show that a lot of segmentation problems that we can find in real applications need prior knowledge to be solved. This is especially the case when the objects to delineate do not have real contours in the image. The thalamus labelization or the localization of the subthalamic nucleus (STN) are two relevant examples. The atlas-based segmentation algorithm that we have presented in this thesis extracts this prior information from a reference image which is the atlas.

Object-based Information contained in the Atlas We note in publications on the comparison of non rigid registration methods for particular atlas-based applications (for example, see the validations presented in [54] and [150] on the STN localization) that the evaluated methods to register the atlas are general image registration algorithms. That means that they are not specially designed to exploit the object-based information particular to the atlas. This object-based information comes from the combination of the intensities atlas with its labeled version. This information concerns the features of the object to segment in the target image as well as the features of its neighboring objects. Among the segmentation techniques, we found that the active contour (AC) method is particularly appropriated to exploit such information, especially thanks to their region-based forces. Region-based forces are segmentation forces that delineate the desired region by creating a competition between its own features and the features of its neighborhood.

Polarity Information To introduce region-based forces in a multi-phase registration process, we had to study the polarity information contains in the signed distance function representation.

In the AC framework, the polarity information is defined regarding a closed contour. Its goal is to indicate where are the inside and the outside of a given contour. In [166], Thirion had already pointed out the importance of the polarity information in non rigid registration. For that matter, his well-known non rigid registration algorithm is based on such type of information. However in this algorithm, the polarity information is not defined regarding close contours like in the AC framework but regarding local intensities.

Spatial Dependance between Structures Region-based forces allow the non rigid registration of closed regions. It is obvious that the registration of selected regions has an influence on the position of their surrounding objects. To take benefit of this spatial dependance in the registration process, we had to define the hierarchical atlas registration approach.

8.2 Achievements and Publications

In this thesis we have proposed:

1. **A Joint Registration and Segmentation Model** This model permits to integrate active contour segmentation constraints in a non parametric atlas registration process. Its main advantage is that it has been designed to use any types of force coming from the AC framework. Moreover, this model is very flexible. We saw that it can be easily adaptable to various types of applications by changing the type of contour representation, the type of segmentation force and by defining the position of these segmentation forces regarding to a label function. The general formulation of our model was first presented in [62]. Note that the derived model using a distance-based representation and pixel-based forces was previously described in [61].

2. **A Multi-Phase Active Contour Registration** To cope with the limitations of the traditional signed distance-based function representation (2 phase segmentation and reinitialisation problems), we have proposed a multi-phase registration model based on one label function. This representation is derived from the study of the polarity information role contained in the signed distance-based function, in the active contour segmentation. The adaptation of the label function representation to our atlas registration model was published in [63].

3. **A Hierarchical Atlas Registration Approach** Region-based registration forces lead us to define the hierarchical atlas registration approach. This approach consists to register the main structures of the image in order to improve the initial atlas contour position for the registration of depending structures. The concept of hierarchical atlas was published in [91].

4. **An Analogy to the Demons of the Thirion's Algorithm** The analogy between the region-based forces of our model and the Demons of the Thirion's algorithm was mentioned in [63].

5. **Supervised Segmentation Forces based on Information Theory** After the description of our atlas-based registration model, we have presented a study concerning segmentation forces based on marginal and joint prior distributions. The idea behind this work is to integrate such supervised forces in our model to drive the registration of an atlas. Moreover, in this thesis we have applied our atlas registration model on mono-modal applications only. Registration forces based on joint prior distributions could permit one to segment images with a different modality than the one of the atlas. These supervised segmentation forces derived from the information theory was published in [64]. In [120], we describe how these supervised forces can be used for a slice by slice segmentation of 3D medical images.

8.3 Future Works

In this Section, we present possible lines of future research regarding the development of our active contour-based algorithm and a particular application in medical imaging.

8.3.1 Possible Development of the Algorithm

We have defined below three areas of research:

1. **Supervised Registration Forces** The new registration framework that we have defined in this thesis, implies to design active contour-based registration forces that exploits the prior knowledge of a reference image. For the applications shown in this thesis, we have mainly used the prior mean-based forces inspired by the region-based segmentation model proposed by Chan et al. [35]. The design of these forces is quite simple, but we have shown that they can be used successfully in a large number of segmentation problems. In Chapter 6, we have presented a study on supervised forces based on prior probability distribution. It would be now interesting to include segmentation terms based on the joint probability like the joint entropy or mutual information in our registration algorithm. This way, we could also address the registration of multi-modal images. It is interesting to note that our registration framework considers indirectly the joint distribution between 3 images (the intensity atlas, the labeled atlas (or a label function) and the image to segment). The role of the labeled atlas is in fact to condition spatially the joint distribution of the intensity atlas and the image to segment. Usual multi-modal registration approach generally consider only the joint distribution between the intensity atlas and the image to segment. These 2D and 3D joint distributions are illustrated in Figure 8.1.

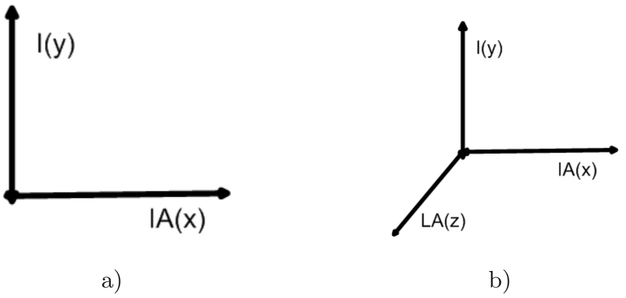

Figure 8.1: Joint image distributions for atlas registration. a) Usual registration approach: joint distribution between the intensity atlas (IA) and the image to segment (I). b) Our registration framework: joint distribution between the intensity atlas (IA), the image to segment (I) and the labeled atlas (LA).

   In this thesis, we did not show examples with shape prior models. Future work concerning the application described in Section 8.3.2 would be more oriented in this direction. The last possible research line we propose here, would be to consider the registration forces that have been designed in the active contour framework to segment particular textures.

2. **Hierarchical Atlas Registration Approach** The atlas registration algorithm developped in this thesis led us to an object-based registration framework. This framework implies to study the existing physical dependances between the objects contained in the image. We saw, for

example, that the bones have to be registered first on neck images. It would be interesting for future research on the hierarchical registration approach to describe (by using trees for example) the dependance in position between anatomical structures in different types of medical image.

3. **Applications** In this thesis, we mainly show applications in medical imaging. We have mentioned in the introduction that other application areas in computer vision, like objects tracking in video sequences, often resort to a very similar atlas-based segmentation method. It would be then interesting to test on segmentation problems in video sequence. A well suited application would be for example the detection and the localization of facial paralyzis. The method recently proposed by Shu et al. in [156] consists first to localize relevant facial regions like the eyebrows, the eyes, the nostril and the mouth. After that, the motion of these features are extracted between two successive frames with the optical flow method. The deformation fields thus obtained allows then to detect and localize facial paralyzis by comparing the motion between the left and right part of the face. Our model could perform these segmentation and registration tasks in one step by directly tracking the relevant face elements.

8.3.2 Particular Application

Atlas-based Segmentation of CT neck images for Radiation Therapy Planning plan to use the registration model developed in this thesis for an atlas-based application on CT Neck Images. The objective of this work is to segment virtual contours for radiation therapy planning. For this purpose, we need to study the following points:

- **Contour Representation** The choice of contour representation depends on the object types we need to model. We saw that the signed distance map function is particularly useful to minimize the distance between the contours of binary objects. This type of representation could be exploited to introduce manual constraints in the registration process. The label function allows to select the disconnected or connected closed regions that have to drive the atlas registration. The intensity function is useful when we need to register texture inside selected regions. This last type of contours representation should not be used inside quasi-uniform region like the image background, the bones or the trachea.
- **Atlas Hierarchical Approach** This approach requires decomposing the atlas of the neck in different registration layers. For this neck registration application, it would be interesting to first determine which structures would influence the position of the objects of interest. This study would be similar to the one performed in our lab on the STN application [149]. The results have shown that the STN position can be estimated by registering the ventricles only. Moreover, neck CT images have generally a rather large size (512x512x62 in average). Registering the area of interest only would permit to save a lot of processing time. Besides this, we have shown in Chapter 7 that hardest tissues like bones should be registered first. Indeed, it seems logical that the position of harder tissues determines the position of softer surrounding tissues.
- **Segmentation Forces** The type of region forces also depends on the object type we have to register. In this thesis, we have used prior mean-based forces for the registration of the main neck structures (bones, trachea and its external contours). We found satisfying results on 2D images. On the other hand, the registration on 3D images was more challenging because mobile structures like the trachea or the spinal cords present a very

large variabilities between two patients. However, our atlas registration model was only tested on the whole neck images. Registering only the regions of interest should allow to reduce considerably the amount of variability to recover and then improve the results in 3D.

The deformation field computed by our model gives an estimation of the position of the virtual objects. We are currently building prior shape model from training sets in order to enforce the accuracy of this estimation. The goal of these prior models is to introduce in the registration process the landmarks used by medical experts to draw such structures.

Validation To evaluate the accuracy of our atlas registration model, it is now important to compare its results with algorithms currently used to register atlases. The strength of our algorithm compared to other image-based algorithm is that, thanks to the region-based forces coming from the active contour framework, it can perform an object-oriented registration.

We are planning to first validate our registration model on the STN localization application. For this purpose, we will compare our model with the Affine and AC-PC registration, as well as the BSpline and Demons follow the validation method published by our lab in [150]. Our algorithm should lead to a lower computation time, because it can consider only the lateral ventricles that are relevant to find the STN position. Moreover, we expect that our model will be more robust, because its registration will be not perturbed by possible inconsistent structures between the atlas and the patient image.

Bibliography

[1] *Berkeley Segmentation Data Set*. URL `http://www.eecs.berkeley.edu/`.

[2] The visible human project. 1991.

[3] D. Adalsteinsson and J. Sethian. A fast level set method for propagating interfaces. *J. Computational Physics*, 118:269–277, 1995.

[4] I. A. Ahmad and P. Lin. A nonparametric estimation of the entropy for absolutely continuous distributions. *IEEE Transactions on Information Theory*, 22(3):372–375, 1976.

[5] C. Alvino. Multiscale active contour methods in computer vision with applications in tomography. *Georgia Institute of Technology Theses*, 2005. URL `http://smartech.gatech.edu/handle/1853/6896`.

[6] L. Ambrosio and V. Tortorelli. Approximation of functionals depending on jumps by elliptic functionals via γ-convergence. *Comm. Pure. Appl. Math*, 43:999–1036, 1990.

[7] T. Amiaz and N. Kyriati. Piecewise-smooth dense optical flow via level sets. *International Journal of Computer Vision*, 68(2):111–124, 2006.

[8] J. An, Y. Chen, F. Huang, D. Wilson, and E. Geiser. A variational pde based level set method for a simultaneous segmentation and non-rigid registration. *MICCAI*, pages 286–293, 2005.

[9] G. Aubert, M. Barlaud, O. Faugeras, and S. Jehan-Besson. Image segmentation using active contours: Calculus of variations or shape gradients. *Technical Report INRIA/I3S RR-4483*, 2003.

[10] G. Aubert, M. Barlaud, O. Faugeras, and S. Jehan-Besson. Image segmentation using active contours: calculus of variations or shape gradients. *SIAM J. Appl. Math*, 63(6):2128–2154, 2003.

[11] A. Azar, C. Xu, X. Pennec, and N. Ayache. An interactive hybrid non-rigid registration framework for 3d medical images. *ISBI*, pages 824–827, 2006.

[12] M. Bach Cuadra. Atlas-based segmentation and classification of magnetic resonance brain images. *THÈSE NO 2875, École Polytechnique Fédérale De Lausanne*, 2003.

[13] M. Bach Cuadra, M. De Craene, V. Duay, B. Macq, C. Pollo, and J. Thiran. Dense deformation field estimation for atlas-based segmentation of pathological mr brain images. *Methods and Programs in Biomedicine*, 84(2-3):66–75, 2006.

[14] R. Bajcsy and S. Kovacic. Multiresolution elastic matching. *Computer vision, Graphics and Image Processing*, 46:1–21, 1989.

[15] H. G. Barrow, J. M. Tenenbaum, R. C. Bolles, and H. C. Wolf. Parametric correspondence and chamfer matching: Two new techniques for image matching. *Proceedings of the Fifth International Joint Conference on Artificial Intelligence*, pages 659–663, 1977.

[16] M. Bertalmio, G Sapiro, and G. Randall. Morphing active contours: A geometric approach to topology-independent image segmentation and tracking. *Proceedings of ICIP'98*, 1998.

[17] M. Bertalmio, G Sapiro, and G. Randall. Morphing active contours. *IEEE Transaction on Pattern Analysis and Machine Intelligence*, 22(7):733–736, 2000.

[18] A. Bois dAische, M. De Craene, X. Geets, V. Gregoire, B. Macq, and S. K. Warfield. Efficient multi-modal dense field non-rigid registration: alignment of histological and section images. *Medical Image Analysis, ITK special issue*, 2004.

[19] F. Bookstein and al. Principal warps: Thin-plates splines and the decomposition of deformations. *IEEE Transactions on Pattern Analysis and Matching Intelligence*, 11:567–585, 1989.

[20] R.P. Brent. *Algorithms for Minimization Without Derivatives.* Prentice-Hall, 1973.

[21] X. Bresson. Image segmentation with variational active contours. *THÈSE NO 3283, École Polytechnique Fédérale De Lausanne*, 2005.

[22] X. Bresson, P. Vandergheynst, and J.-P. Thiran. Multiscale active contours. *LTS-REPORT-2004-009*, 2004.

[23] X. Bresson, P. Vandergheynst, and J.-P. Thiran. Multiscale active contours. *International Journal of Computer Vision*, 70(3):197–211, 2006.

[24] X. Bresson, P. Vandergheynst, and J.-P. Thiran. Variational model for object segmentation using boundary information and shape prior driven by the mumford-shah functional. *International Journal of Computer Vision*, 28(2):145–162, 2006.

[25] M. Bro-Nielsen and C. Gramkow. Fast fluid registration of medical images. *In Höhne, K. H. and Kikinis, R. (eds), Visualization in Biomedical Computing VBC"96, Lecture Notes in Computer Science*, pages 267–276, 1996.

[26] L. Brown. A survey of image registration technique. *ACM Computing Surveys*, 24(4):326–376, 1992.

[27] T. Brox, A. Bruhn, N. Papenberb, and J. Weickert. High accuracy optical flow estimation based on a theory for warping. *Proc. 8th European Conf. Computer Vision, Part IV: Lecture Notes in Computer Science*, 3024:25–36, 2004.

[28] T. Brox, A. Bruhn, and J. Weickert. Variational motion segmentation with level sets. *ECCV*, pages 471–483, 2006.

[29] D. J. Burr. The correction of stereotactic inaccuracy caused by brain shift using an intraoperative ultrasound device. *Lecture Notes in Computer Science: CVRMED-MRCAS*, 1205: 459–466, 1997.

[30] D. J. Burr. A dynamic model for image registration. *Computer Graphics and Image Processing*, 15:102–112, 1981.

[31] C. C. Baillard, P. Hellier, and Barillot C. Cooperation between level set techniques and 3d registration for the segmentation of brain structures. *International Conference on Pattern Recognition (ICPR)*, pages 991–994, 2000.

[32] P. Cachier. Fast non rigid matching by gradient descent: Study and improvements of the "demons" algorithm. *RR 3706, INRIA*, 1999.

[33] V. Caselles, F. Catte, T. Coll, and F. Dibos. A geometric model for active contours. *Numerische Mathematik*, 66:1–31, 1993.

[34] V. Caselles, R. Kimmel, and G. Sapiro. Geodesic active contours. *International Journal of Computer Vision*, 22(1):61–79, 1997.

[35] B. Chan, T. F. and L. Vese. Active contours without edges. *IEEE Transactions on Image Processing*, 10(2):266–277, 2001.

[36] G. Charpiat, O. Faugeras, and R. Keriven. Shape statistics for image segmentation with prior. *CVPR*, 2007.

[37] S. Chen, B. Merriman, M. Kang, R. E. Cafilsch, C. Ratasch, L.-T. Cheng, M. Gyure, R. P. Fedkiw, and S. Osher. Level set method for thin film epitaxial growth. *tech. rep. CAM 00-03, UCLA Math. Depart.*, 2000.

[38] Y. Chen, H. D. Tagare, S. Thiruvenkadam, F. Huang, D. Wilson, and E.A. Geiser. On the incorporation of shape priors into geometric active contours. *Workshop on Variational and Level Set Methods in Computer Vision,*, pages 145–152, 2001.

[39] Y. Chen, H. D. Tagare, S. Thiruvenkadam, F. Huang, D. Wilson, K.S Gopinath, R.W. Briggsand, and E.A. Geiser. Using prior shapes in geometric active contours in a variational framework. *International Journal of Computer Vision*, 50(3):315–328, 2002.

[40] Y. Chen, W. Guo, F. Huang, D. Wilson, and E.A. Geiser. Using prior shape and points in medical image segmentation. *Energy Minimization Methods in Computer Vision and Pattern Recognition, LNCS 2683*, pages 291–305, 2003.

[41] D.L. Chopp. Computing minimal surfaces via level set curvature flow. *Jour. of Comp. Phys.*, pages 77–91, 1993.

[42] G. E. Christensen and H. J. Johnson. Consistent image registration. *IEEE Transaction on Medical Image Analysis,*, 20(7):568–582, 2001.

[43] G. E. Christensen, M. I. Miller, and M. Vannier. A 3d deformable magnetic resonance textbook based on elasticity. *AAAI Spring Symp. Series: Applications of Computer Vision in Medical Image Processing*, pages 153–156, 1994.

[44] G. E. Christensen, R. D. Rabbitt, and M. I. Miller. 3d brain mapping using a deformable neuroanatomy. *Phys. Med. Biol.*, 39:609–618, 1994.

[45] G. E. Christensen, R. D. Rabbitt, and M. I. Miller. Deformable templates using large deformations kinematics. *IEEE Transactions on Image Processing*, 5(10):1435–1447, 1996.

[46] L. Cohen and I. Cohen. Finite element methods for active contour models and balloons for 2-d and 3-d images. *IEEE Trans. PAMI*, 15(7):1131–1147, 1993.

[47] A. Collignon, D. Vandermeulen, P. Suetens, and G. Marchal. 3d multi-modality medical image registration using feature space clustering. *Computer Vision, Virtual Reality, and Robotics in Medicine, N. Ayache, Lecture Notes in Computer Science, Springer-Verlag, Berlin*, 905: 195–204, 1995.

[48] D.H. Cooper, C.J. Cootes, T.F.and Taylor, and J. Graham. Active shape models - their training and application. *Computer Vision and Image Understanding*, 2(61):38–59, 1995.

[49] T.F. Cootes, C. Beeston, and C.J. Edwards, G.J.and Taylor. A unified framework for atlas matching using active appearance models. *MICCAI*, 2:927–934, 2005.

[50] D. Cremers, N. N. Sochen, and C. Schorr. Towards recognition-based variational segmentation using shape priors and dynamic labeling. *Scale-Space'03, LNCS 2695*, pages 388–400, 2003.

[51] D. Cremers, N. N. Sochen, and C. Schorr. Multiphase dynamic labeling for variational recognition-driven image segmentation. *Int. J. of Comp. Vision*, 66(1):67–81, 2006.

[52] O. Cuisenaire. Automatic registration of 3d mr images with a computerized brain atlas. *SPIE Medical Imaging,*, 1719:438–449, 1996.

[53] C. A. Davatzikos, J. L.. Prince, and R. N. Bryan. Image registration based on boundary mapping. *IEEE Trans. Med. Imag.*, 15, 1996.

[54] B. M. Dawant, R. Li, E. Cetinkaya, C. Kao, J. M. Fitzpatrick, and P E. Konrad. Computerized atlas-guided positioning of deep brain stimulators: A feasibility study. *WBIR*, pages 142–150, 2003.

[55] M. C. Delfourd and J.-P. Zolésio. Shapes and geometries: Analysis, differential calculus, and optimization. *Advances in Design and Control. SIAM*, 2001.

[56] R. S. Desikan. An automated labeling system for subdividing the human cerebral cortex on mri scans into gyral based regions of interest. *NeuroImage*, 31(3), 2006.

[57] P.-F. D'Haese. Automatic segmentation of brain structures for radiation therapy planning. *SPIE Medical Image Processing*, pages 517–526, 2003.

[58] P. F. D'Haese, E. Cetinkaya, P. E. Konrad, C. Kao, and B. M. Dawant. Computer-aided placement of deep brain stimulators: From planning to intraoperative guidance. *IEEE Transactions on Medical Imaging*, 24(11):1469–1478, 2005.

[59] Directories. URL `http://www.directories.ch`.

[60] M. Droske, W. Ring, and M. Rumpf. Mumford-shah based registration. *Computing and Visualization in Science (CVS)*, 2007.

[61] V. Duay, N. Houhou, and J.-P. Thiran. Atlas-based segmentation of medical images locally constrained by level sets. *ICIP*, 2005.

[62] V. Duay, M. Bach Cuadra, , X. Bresson, and J.-P. Thiran. Dense deformation field estimation for atlas registration using the active contour framework. *European Signal Processing Conference (EUSIPCO)*, 2006.

[63] V. Duay, X. Bresson, N. Houhou, M. Bach Cuadra, and J.-P. Thiran. Registration of multiple regions derived from the optical flow model and the active contour framework. *EUSIPCO*, 2007.

[64] V. Duay, S. Luti, G. Menegaz, and J.-P. Thiran. Supervised segmentation for scalar images based on active contours and information theory. *EUSIPCO*, 2007.

[65] S. Esedoglu and Y. H. R. Tsai. Threshold dynamics for the piecewise constant muford-shah functional. *Technical report, CAM report (04-63)*, 2004.

[66] M. Esiri and Morris J. The neuropathology of dementia. *Cambridge University Press*, 2002.

[67] A. C. Evans, D. L. Collins, S. R. Mills, and R. L.and Peters T. M. Brown, E. D.and Kelly. 3d statistical neuroanatomical models from 305 mri volumes. pages 1813–1817, 1993.

[68] L. C. Evans. Partial differential equations. 1998.

[69] P. Perez F. Heitz and P. Bouthemy. Multiscale minimization of global energy functions in some visual recovery problems. *CVGIP: Image Under-standing*, 59:125–134, 1994.

[70] M. Ferrant, A. Nabavi, B. Macq, P. M. Black, F. A. Jolesz, R. Kikinis, and S. K. Warfield. Registration of 3-d intraoperative mr images of the brain using a finite-element biomechanical model. *IEEE Transactions on Medical Imaging*, 20(12):1384–1397, 2001.

[71] M. Ferrant, A. Nabavi, B. Macq, P. M. Black, F. A. Jolesz, R. Kikinis, and S. K. Warfield. Serial registration of intraoperative mr images of the brain. *IEEE Medical Image Analysis*, 6 (4):337–359, 2002.

[72] B. Fischl. Automatically parcellating the human cerebral cortex. *Cerebral Cortex*, 14:11–22, 2004.

[73] B. Fischl. Cortical surface-based analysis ii: Inflation, flattening, and a surface-based coordinate system. *NeuroImage*, 9(2):195–207, 1999.

[74] B. Fischl. High-resolution inter-subject averaging and a coordinate system for the cortical surface. *Human Brain Mapping*, 8:272–284, 1999.

[75] M. Fornefett, K. Rohr, and Siegfried Stiehl H. Elastic registration of medical images using radial basis functions with compact support. *CVPR*, pages 402–407, 1999.

[76] R. Fritsch and G Fritsch. The four-color theorem. *History, Topological Foundations and Idea of Proof. Springer*, 1998.

[77] Macuinas R.J. Bass W.A. Carpini W. Galloway, R.L. Optical localization for interactive, image-guided neurosurgery. *Medical Imaging*, 2164:137–145, 1994.

[78] M. Gastaud, M. Barlaud, and G. G. Aubert. Tracking video objects using active contours. *Workshop on Motion and Video Computing*, pages 90–95, 2002.

[79] F. Gibou and R. Fedkiw. A fast hybrid k-means level set algorithm for segmentation. *Stanford Report*, 2002.

[80] F. Gibou and R. Fedkiw. A fast hybrid k-means level set algorithm for segmentation. *Proceedings of 4th Annual Hawaii International Conference on Statistics and Mathematics*, pages 281–291, 2005.

[81] D.G. Gobbi. Ultrasound/mri overlay with image warping for neurosurgeryg. *MICCAI*, (1935): 106–114, 2000.

[82] D.E. Goldberg. Genetic algorithms in search, optimization, and machine learning. *Addison-Wesley Publishing Company, Reading, MA*, 1989.

[83] J. Gomes and O. D. Faugeras. Reconciling distance functions and level sets. *Scale-Space*, pages 70–81, 1999.

[84] C. Goodall. Procrustes methods in the statistical analysis of shape. *Journal of Royal Statistical Society*, 53(2):285–339, 1991.

[85] Laura Gui, Xavier Bresson, and Jean-Philippe Thiran. Multiscale image segmentation using active contours. *LTS-REPORT-2005-022*, 2005.

[86] P. Hellier and Barillot C. Coupling dense and landmark-based approaches for non-rigid registration. *IEEE Transactions on Medical Imaging*, (2):217–227, 2003.

[87] A. Herbulot, S. Jehan-Besson, Barlaud M., and Aubert G. Information theory for image segmentation using shape gradient. Technical report, 2004.

[88] A. Herbulot, S. Jehan-Besson, Barlaud M., and Aubert G. Segmentation of vectorial image features using shape gradients and information measures. Technical Report 3, 2006.

[89] K. et al. Hohne. Using points and surfaces to improve voxel-based non-rigid registration. *MICCAI*, 2(2489):565–572, 2002.

[90] K. et al. Hohne. A volume based anatomical atlas. *IEEE Computer Graphics and Applications*, 12(4):72–78, 2005.

[91] N. Houhou, V. Duay, A. S. Allal, and J.-P. Thiran. Medical images registration with a hierarchical atlas. 2005.

[92] M. Jehan-Besson, Barlaud and G. Aubert. Dream2s: Deformable regions driven by an eulerian accurate minimization method for image and video segmentation. *Technical Report I3S RR-2001-14*, 2001.

[93] M. Jehan-Besson, Barlaud and G. Aubert. Dream2s: Deformable regions driven by an eulerian accurate minimization method for image and video segmentation. *International Journal of Computer Vision*, 53:45–70, 2003.

[94] S. Jehan-Besson. Modèles de contour actifs basés regions pour la segmentation d'images et de vidéo. *Laboratoire I3S Sophia Antipolis Thesis*, 2003.

[95] S. et al. Jehan-Besson. Shape gradients for histogram segmentation using active contours. *International Conference on Computer Vision*, 2003.

[96] H. J. Johnson and G. E. Christensen. Consistent landmark and intensity-based image registration. *IEEE Transactions on Medical Imaging*, 21(5), 2002.

[97] L. Jonasson, P. Hagmann, C. Pollo, X. Bresson, Wilsona C., R. Meuli, and J.-P. Thiran. A level set method for segmentation of the thalamus and its nuclei in dt-mri. *Signal Processing*, 87:309–321, 2007.

[98] M. Kass, A. Witkin, and Terzopoulos D. Snakes: active contour models. *First international conference on computer vision*, pages 259–268, 1987.

[99] M. R. et al. Kaus. Segmentation of meningiomas and low grade gliomas in mri. *MICCAI99*, pages 1–10, 1999.

[100] P.J. Kelly, B.A. Kall, S.J. Goerss, and F.I. Earnest. Computer-assisted stereotaxic laser resection of intra-axial brain neoplasms. *Journal of Neurosurgery*, (64):427–439, 1986.

[101] R. Kikinis. A digital brain atlas for surgical planning, model driven segmentation and teaching. *IEEE Trans. on Visual. and Comput. Graph.*, 2(3), 1996.

[102] J Kim, J. W. Fisher III, A. Yezzi, Jr. M. Cetin, and A. S. Willsky. Nonparametric methods for image segmentation using information theory and curve evolution. *IEEE International Conference on Image Processing (ICIP)*, pages 797–800, 2002.

[103] J Kim, J. W. Fisher III, A. Yezzi, Jr. M. Cetin, and A. S. Willsky. Incorporating complex statistical information in active contour-based image segmentation. *IEEE International Conference on Image Processing (ICIP)*, 2003.

[104] Ibanez L., Schroeder W., L. Ng, and J. Cates. The itk software guide. *Kitware*, 2005. URL `http://www.itk.org`.

[105] K. V. Leemput, F. Maes, D. Vandermeulen, and P. Suetens. Automated model-based bias field correction of mr images of the brain. *IEEE Transactions on Medical Imaging*, 18(10): 897–908, 1999.

[106] A. Leow, P. Thompson, H. Protas, and S. C. Huang. A surface-based technique for warping three-dimensional images of the brain. *IEEE Trans. Med. Imag.*, 15:1–16, 1996.

[107] M. Leventon. Statistical models for medical image analysis. *Ph.D Thesis*, 2000.

[108] M. Leventon. Statistical models for medical image analysis. *IEEE International Conference of Computer Vision and Pattern Recognition*, pages 316–323, 2000.

[109] D. A. Lewis, D. A. Cruz, D. S. Melchitzky, and J. N. Pierri. Am j psychiatry. 158(1411), 2001.

[110] J. Lie, M. Lysaker, and X.-C. Tai. A binary level set model and some applications to mumford-shah image segmentation. *IEEE Transactions on Image Processing*, 15(5):1171–1181, 2006.

[111] J. Lie, M. Lysaker, and X.-C. Tai. A variant of level set method and application to image segmentation. *Mathematics for Computation*, 75(255):1155–1174, 2006.

[112] T. Lindeberg. Scale-space theory: A basic tool for analysing structures at different scales. 21 (2):224–270, 1994.

[113] D. Louis Collins, G. Le Goualher, , and A. Evans. Non-linear cerebral registration with sulcal constraints. *MICCAI*, pages 974–984, 1998.

[114] L.D. Lunsford and A.J. Martinez. Stereotactic exploration of the brain in the era of computed tomography. 22:222–230, 1984.

[115] F. Maes and A. Collignon. Multimodality image registration by maximization of mutual information. *IEEE Transactions on Medical Imaging*, 16, 1997.

[116] J.B. Maintz and A. Viegever. A survey of medical image registration. *IEEE Transaction on Medical Image Analysis,*, 2(1):1–36, 2001.

[117] R. Malladi, J. Sethian, and B. C. Vemuri. Shape modeling with front propogation: a level-set approach. *IEEE Transactions on Pattern Analysis and Machine Intelligence*, 17(2):158–175, 1995.

[118] C. R. Maurer and J. M. Fitzpatrick. *A review of medical image registration.* 1993.

[119] J. C. Mazziotta, A. W. Toga, and R. S. J. Frackowiak. Brain mapping: The disorders. *Academic Press*, 2000.

[120] G. Menegaz, S. Luti, V. Duay, and J.-P. Thiran. An interactive toolbox for atlas-based segmentation and coding of volumetric images. SPIE, 2007.

[121] B. Merriman, R. Caflisch, Osher S., Ratsch C., S. Chen, M. Kang, and M. Gyure. Island dynamics and level set methods for continuum modeling of epitaxial growth. pages 145–171. Applied and industrial mathematics, Venico-2, 1998, Kluwer Acad. Publ., Dordrecht, 2000.

[122] M. I. Miga. Initial in-vivo analysis of 3d heterogeneous brain computations for model-updated image-guided neurosurgery. *MICCAI98*, 2(1):743–752, 1998.

[123] M.I. Miga, T.K. Sinha, D.M. Cash, R.L. Galloway, and R.J. Weil. Cortical surface registration for image-guided neurosurgery using laser range scanning. *IEEE Transactions on Medical Imaging*, 22(8):973–985, 2003.

[124] M. Moelich and T. Chan. *Joint Segmentation and Registration using Logic Models.* 2003.

[125] J.-M. Morel and S. Solimini. Variational methods in image segmentation. *Progress in Nonlinear Differential Equations and Their Applications*, 1995.

[126] Liu W. Yoo T. Morse, B. and Subramanian K. Active contours using a constraint-based implicit representation. *CVPR*, pages 285–292, 2005.

[127] M. Mullan, R. Whitaker, and J. Hart. Procedural level sets. *NSF/DARPA CARGO Meeting*, 2004.

[128] D. Mumford and J. Shah. Boundary detection by minimizing functionals. *Proceedings of the International Conference on Computer Vision and Pattern Recognition*, pages 12–49, 1985.

[129] D. Mumford and J. Shah. Optimal approximations of piecewise smooth functions and associated variational problems. *Communications on Pure and Applied Mathematics*, 42:577–685, 1989.

[130] A. Nabavi. Image-guided therapy and intraoperative mri in neurosurgery. minimally invasive therapy and allied technologies. *Computerized Medical Imaging and Graphics*, (9):277–286, 2000.

[131] H.J. Nauta. Error assessment during image guided and imaging interactive stereotactic surgery. *Computerized Medical Imaging and Graphics*, (18):279–287, 1994.

[132] C. Nimsky, O. Ganslandt, M. Buchfelder, and R. Fahlbusch. Intraoperative magnetic resonance tomography - experiences in neurosurgery. *Computerized Medical Imaging and Graphics*, (71):987–994, 2000.

[133] J. Nocedal and S. J. Wright. Numerical optimization. *Springer-Verlag*, 2000.

[134] S. Osher. Geometric level set methods in imaging, vision and graphics. *eds. S. Osher and N. Paragios, Springer-Verlag, NY*, pages 3–20, 2003.

[135] S. Osher and J.A. Sethian. Fronts propagating with curvature-dependent speed: Algorithms based on Hamilton-Jacobi formulations. *Journal of Computational Physics*, 79:12–49, 1988. URL `citeseer.nj.nec.com/osher88fronts.html`.

[136] B. Pakkenberg. *Arch Gen Psychiatry*, 47(1023), 1990.

[137] N. Paragios and R. Deriche. Coupled geodesic active regions for image segmentation. *Rapport de recherche de l'INRIA*, 1999.

[138] N. Paragios and M. Rousson. Geodesic active regions: A new paradigm to deal with frame partition problems in computer vision. *Computer Vision. Journal of Visual Communication and Image Representation*, 13(1-2):249–268, 2002.

[139] N. Paragios, M. Rousson, and V. Ramesh. A shape-to-area variational approach for global-to-local registration. *European Conference on Computer Vision*, pages 775–790, 2002.

[140] N. Paragios, M. Rousson, and V. Ramesh. Non-rigid registration using distance functions. *Computer Vision and Image Understanding*, 89:142–165, 2003.

[141] E. Parzen. On estimation of a probability density function and mode. *Ann. Math. Stat.*, 33: 1065–1076, 1962.

[142] J. Perlmutter and Mink J. Deep brain stimulation. *Annual Review of Neuroscience*, 29: 229–257, 2006.

[143] G. J. Popken, W. E. Bunney, S. G. Potkin, Jr., and E. G. Jones. *Proc Natl Acad Sci U S A*, 97(9276), 2000.

[144] D.W. Roberts, A. Hartov, F.E. Kennedy, M.I. Miga, and K.D. Paulsen. Intraoperative brain shift and deformation: a quantitative analysis of cortical displacement in 28 cases. *Journal of Neurosurgery*, 32:749–760, 1998.

[145] G. K. Rohde, A. Aldroubi, and B. M. Dawant. The adaptive bases algorithm for intensity-based nonrigid image registration. *IEEE Transactions on Medical Imaging*, 22(11):1470–1479, 2003.

[146] R. Ronfard. Region-based strategies for active contour models. *Int. J. Comp. Vision*, 13: 229–251, 1994.

[147] M. Rousson and N. Paragios. Shape priors for level set representations. *ECCV*, 2:78–92, 2002.

[148] D. Rueckert, L.I. Sonoda, C. Hayes, D. L. G. Hill, M. O. Leach, and D. J. Hawkes. Nonrigid registration using freeform deformations: application to breast mr images. *IEEE Transactions on Medical Imaging*, 18(8):712–721, 1999.

[149] F. Sanchez Castro, C. Pollo, J. G. Villemure, and Thiran J. P. Feature-segmentation-based registration for fast and accurate deep brain stimulation targeting. *Proceedings of the 20th International Congress and Exhibition in Computer Assisted Radiology and Surgery*, 2006.

[150] F.J. Sanchez Castro, C. Pollo, J. G. Villemure, and Thiran J. P. Validation of experts versus atlas-based and automatic registration methods for subthalamic nucleus targeting on mri. *International Journal of Computer Assisted Radiology and Surgery*, 1(1):5–12, 2006.

[151] B. Sandberg02 and Chan T. Logic operators for active contour on multi-channel images. Technical report, 2002.

[152] J. A. Sethian. Level set methods and fast marching methods. *Cambridge University Press*, 1999.

[153] C. Shannon. A mathematical theory of communication. *Bell Sys. Tech. J.*, 27:379–423, 1948.

[154] J. Shen. γ-convergence approximation to piecewise constant mumford-shah segmentation. *Int'1 Conf. Advanced Concepts Intell. Vision Systems*, pages 499–506, 2005.

[155] J. Shen. A stochastic-variational model for soft mumford-shad segmentation. *International Journal of Biomedical Imaging*, pages 1–14, 2006.

[156] H. Shu, J. J. Soraghan, and B. F. O'Reilly. Automatic motion feature extraction with application to quantitative assessment of facial paralysis. *ICASSP*, 1:I–441 – I–444, 2007.

[157] G. Slabaugh, Q. Dinh, and G. Unal. A variational approach to the evolution of radial basis functions for image segmentation. *CVPR*, 2007.

[158] FreeSurfer software package. URL `http://www.martinos.org/freesurfer`.

[159] B. Song and T. Chan. A fast algorithm for level set based optimization. *UCLA CAM Report*, 02(68), 2002.

[160] J.C. Spall, S.D. Hill, and D.R. Stark. Theoretical comparisons of evolutionary computation and other optimization approaches. *Proceedings of the Congress on Evolutionary Computation*, pages 1398–1405, 1998.

[161] J. A. Stark and W. J. Fitzgerald. Model-based adaptive histogram equalization. *Signal Processing*, pages 193–200, 1994.

[162] C. Studholme, D. L. G. Hill, and D. J. Hawkes. Multiresolution voxel similarity measures for mr-pet registrationn. *Information Processing in Medical Imaging*, pages 287–298, 1995.

[163] J. Talairach and P. Tournoux. Co-planar stereotaxic atlas of the human brain: 3-dimensional proportional system - an approach to cerebral imaging. *New York, NY: Thieme Medical Publishers*, 1998.

[164] P. Thevenaz, Ruttimann U. E., and M. Unser. A pyramid approach to subpixel regisration based on intensity. *IEEE Transactions on Image Processing*, 7(1):1–15, 1998.

[165] J.-P. Thirion. Fast non-rigid matching of 3d medical images. *Tech. Rep. 2547*, 1995.

[166] J.-P. Thirion. Image matching as a diffusion process: an analogy with maxwell's demons. *IEEE Transaction on Medical Image Analysis*, 2(3):243–260, 1998.

[167] G. Unal and G. Slabaugh. Coupled pdes for non-rigid registration and segmentation. *IEEE Computer Society Conference on Computer Vision and Pattern Recognition (CVPR)*, 1:168–175, 2005.

[168] B. C. Vemuri, J. Ye, Y. Chen, and C. M. Leonard. Image registration via level-set motion : Applications to atlas-based segmentation. *IEEE Transaction on Medical Image Analysis*, 7 (1):1–20, 2003.

[169] L. A. Vese and T. F. Chan. A multiphase level set framework for image segmentation using the mumford and shah model,. *UCLA CAM Report 01-25*, 2001.

[170] L. A. Vese and T. F. Chan. A multiphase level set framework for image segmentation using the mumford and shah model. *International Journal of Computer Vision*, 50(3):271–293, 2002.

[171] P. Viola and W.M. Wells. Alignment by maximization of mutual information. *Fifth Int. Conf. on Computer Vision*, pages 16–23, 1995.

[172] R. T. Whitaker, X. Xue, and G. Sapiro. A level-set approach to 3d reconstruction from range data. *International Journel of Comp. Vision*, 10(3):203–231, 1998.

[173] Wikipedia. URL `http://www.wikipedia.org/`.

[174] P. P. Wyatt and J. A. Noble. Map mrf joint segmentation and registration of medical images. *Medical Image Analysis*, 7(4):539–552, 2003.

[175] C. Xiaohua, M. Brady, and D. Rueckert. Simultaneous segmentation and registration for medical image. *Proc. MICCAI*, pages 663–670, 2004.

[176] A. Yezzi, A. Tsai, and A. Willsky. A statistical approach to snakes for bimodal and trimodal imagery. *International Conference of Computer Vision*, pages 898–903, 1999.

[177] A. Yezzi, L. Zollei, and T. Kapur. A variational framework for joint segmentation and registration. *Proceedings of the IEEE Workshop on Mathematical Methods in Biomedical Image Analysis (CVPR-MMBIA)*, pages 44–49, 2001.

[178] Y.-N. Young and D. Levy. Registration-based morphing of active contours for segmentation of ct scans. *Mathematical Biosciences and Engineering*, 2(1):79–96, 2005.

[179] H.-K. Zhao, T. Chan, B. Merriman, and S. Osher. A variational level set approach to multiphase motion. *Journal of Computational Physics*, 127(1):179–195, 1996.

[180] S. C. Zhu and A. Yuille. Region competition: Unifying snakes, region growing, and bayes/mdl for multiband image segmentation. *IEEE Transactions on Pattern Analysis and Machine Intelligence*, 18(9):884–900, 1996.

[181] B. Zitova and J. Flusser. Image registration methods: a survey. *Image and Vision Computing*, pages 977–1000, 2003.

Curriculum Vitæ

Valérie DUAY

EPFL Electrical Engineer, PhD Student

Route des Charmilles 16
1963 Vétroz / VS
SWITZERLAND
Phone: +41 (0)27 346 34 23
Mobile: +41 (0)77 460 22 05
valerie.duay@epfl.ch

Swiss
July 25th 1975
Single

Education

- ***2003 -*** : **PH. D. Thesis in Biomedical Image Analysis**
  Signal Processing Institute (ITS), Swiss Federal Institute of Technology (EPFL), Lausanne / VD, Switzerland
  Research Areas: Non rigid atlas image registration, PDE and level set methods.
  Adviser: Prof. Jean-Philippe Thiran, Email: JP.Thiran@epfl.ch
- ***2002***: **Master's degree in Electrical Engineering**, EPFL
  Diploma Project: Principal component analysis models for the segmentation of medical images.
- ***1995***: **Elementary School Teacher Diploma**,
  Ecole Normale, Sion / VS, Switzerland

Academic Experience

- ***2003 -*** : **Research Assistant at EPFL**
  Areas: Signal Processing, Image Processing, Pattern Recognition.
  Duties: Assistantship for exercises or computer lab sessions, preparation of exercises sessions or exams, oversight of master thesis projects, some replacements for lectures, oral presentations for lab visitors and conference paper reviews.

- ***2002 - 2003***: **One year training period in USA**
  Medical Image Processing Laboratory, Vanderbilt University, Nashville, TN/USA
  Project: Radiotherapy planning via autosegmented brain structures.
  Adviser: Prof. Benoit Dawant, Email: Benoit.Dawant@vanderbilt.edu

Post-graduate Education

- ***2005***:
  - Advanced Virtual Reality Systems and Telepresence, Prof. D. Thalmann, Doctoral School, EPFL.

- ***2004***:
  - 6th IEEE EMBS International Summer School on Biomedical Imaging, Berder Island, Brittany, France.
  - Speech Processing and Recognition, Prof. H. Bourlard, Doctoral School, EPFL.
  - Modern Approaches to Machine Learning, Prof. W. Gestler, Doctoral School, EPFL.

Languages

French:	Native
English:	Advanced (1 year in USA (2002-2003), OISE English Courses: 2 weeks in Cambridge/UK (2005) and 3 weeks in San Francisco/USA (2006))
German:	Intermediate

Computer Skills

Operating Systems User:	UNIX, Linux, Windows 95/98/NT/XP, MacOS.
Programming languages:	C/C++, Java, Python, VTK/ITK, IDL, QT, OpenGL, VRML, HTML.
Tools:	MS Office, Latex, Matlab, Mathematica, LabView.

Hobbies

- Piano, Swimming, Diving, Tennis, Ski.

Publications

Journal Papers

2006:

- M. Bach Cuadra, M. De Craene, V. Duay, B. Macq, C. Pollo and J.-Ph. Thiran. **Dense Deformation Field Estimation for Atlas-based Segmentation of Pathological MR Brain Images**, *Computer Methods and Programs in Biomedicine*, Vol. 84, Nr. 2- 3, pp. 66-75, 2006.

2005:

- T. Sinha, B. Dawant, V. Duay, D. Cash, R. Weil and M. Miga. **A method to track cortical surface deformations using a laser range scanner**, *IEEE Transactions on Medical Imaging*, Volume: 24, Issue 6, pp. 767- 781, 2005.

2003:

- P. D'Haese, K. Niermann, A. Cmelak, E. Donnelly, V. Duay, R. Li, B. Dawant. **Neuroanatomical automatic segmentation in brain cancer patients.** , *International Journal of Radiation Oncology Biology Physics*, Volume: 57, Issue 2, pp. S205, 2003.

Book Chapters

2008:

- M. Bach Cuadra, V. Duay and J.-Ph. Thiran. **Atlas-based Segmentation**, *Biomedical Image Analysis: Methodologies and Applications*, with N. Ayache, N. Paragios and J. Duncan, Springer, 2008. (To appear)

Conference Papers

2008:

- V. Duay, X. Bresson, F. J. Sánchez Castro, C. Pollo , M. Bach Cuadra and J.-Ph. Thiran. **An Active Contour-based Atlas Registration Model for Automatic Subthalamic Nucleus Targeting on MRI: Method and Validation**, *5th IEEE International Symposium on Biomedical Imaging (ISBI)*, Paris, France, 2008. (Submitted)

2007:

- V. Duay, M. Bach Cuadra, N. Houhou, X. Bresson and J.-Ph. Thiran. **Registration of Multiple Regions Derived from the Optical Flow Model and the Active Contour Framework**, *15th European Signal Processing Conference (EUSIPCO)*, Poznan, Poland, 2007.
- V. Duay, S. Luti, G. Menegaz and J.-Ph. Thiran. **Active Contours and Information Theory for Supervised Segmentation on Scalar Images**, *15th European Signal Processing Conference (EUSIPCO)*, Poznan, Poland, 2007.
- G. Menegaz, S. Luti, V. Duay and J.-Ph. Thiran. **An interactive toolbox for atlas-based segmentation and coding of volumetric images**, *SPIE Medical Imaging, San Diego*, USA, Volume 6512, 2007.

2006:

- V. Duay, M. Bach Cuadra, X. Bresson and J.-Ph. Thiran. **Dense Deformation Field Estimation for Atlas Registration using the Active Contour Framework**, *14th European Signal Processing Conference (EUSIPCO)*, Florence, Italy, 2006.

2005:

- V. Duay, N. Houhou and J.-Ph. Thiran. **Atlas-Based Segmentation of Medical Image Locally Constrained by Level Sets**, *IEEE International Conference on Image Processing (ICIP)*, Genova, Italy, 2005.

- N. Houhou, V. Duay, A. Allal and J.-Ph. Thiran. **Medical Images Registration with a Hierarchical Atlas**, *13th European Signal Processing Conference (EUSIPCO)*, Antalya, Turkey, 2005.

2004:

- V. Duay, P. D'Haese, R. Li and B. Dawant. **Non-Rigid Registration Algorithm with Spatially Varying Stiffness Properties**, *IEEE International Symposium on Biomedical Imaging (ISBI)*, Arlington, USA, vol. 1, pp. 408-411, 2004.

2003:

- P. D'Haese, V. Duay, T. Merchant, B. Macq and B. Dawant. **Atlas-based segmentation of the brain for 3-dimensional treatment planning in children with infratentorial ependymoma**, *International Conference on Medical Image Computing and Computer Assisted Intervention (MICCAI)*, Montréal, Canada, pp. 627-634, 2003.
- T. Sinha, V. Duay, B. Dawant and M. Miga. **Cortical Shift Tracking Using a Laser Range Scanner and Deformable Registration Methods**, *International Conference on Medical Image Computing and Computer Assisted Intervention (MICCAI)*, Montréal, Canada, pp. 166-174, 2003.
- V. Duay, T. Sinha, P. D'Haese, M. Miga and B. Dawant. **Non-rigid registration of serial intra-operative images for automatic brain shift estimation**, *Second International Workshop on Biomedical Image Registration (WBIR)*, Montréal, Philadelphia, PA, USA, pp. 61-70, 2003.
- P. D'Haese, V. Duay, R. Li, A. du Bois d'Aische, T. Merchant, A. Cmelak, E. Donnelly, K. Niermann, B. Macq and B. Dawant. **Automatic Segmentation of Brain Structures for Radiation Therapy Planning**, *SPIE Medical Imaging*, San Diego, USA, pp. 517-526, 2003.

2001:

- E. Solanas, V. Duay, O. Cuisenaire and J.-Ph. Thiran. **Relative Anatomical Location for Statistical Non-Parametric Brain Tissue Classification in MR Images**, *IEEE International Conference on Image Processing (ICIP)*, pp. 885-888, 2001.